Development of Cavity Enhanced Differential Optical Absorption Spectroscopy (CE-DOAS) and application to laboratory and field measurements of trace gases and aerosols

by

RYAN MILLER THALMAN

B.S., Brigham Young University, 2007

A dissertation submitted to the

Faculty of the Graduate School of the

University of Colorado in partial fulfillment

Of the requirement for the degree of

Doctor of Philosophy

Department of Chemistry and Biochemistry

2013

This dissertation entitled:

Development of Cavity Enhanced Differential Optical Absorption Spectroscopy (CE-DOAS) and application to laboratory and field measurements of trace gases and aerosols.

Written by Ryan Miller Thalman

Has been approved for the Department of Chemistry and Biochemistry

_____

Rainer Volkamer

_____

Geoffery Tyndall

Date:_____

The final copy of this thesis has been examined by the signatories, and we find that both the content and form meet acceptable presentation standards of scholarly work in the above mentioned discipline.

Abstract

Thalman, Ryan Miller (Ph.D. Chemistry, Department of Chemistry and Biochemistry)

Development of Cavity Enhanced Differential Optical Absorption Spectroscopy (CE-DOAS) and application to laboratory and field measurements of trace gases and aerosols.

Dissertation directed by Assistant Professor Rainer M. Volkamer.

Cavity Enhanced Differential Optical Absorption Spectroscopy (CE-DOAS) can measure gases and aerosols relevant in the atmosphere. Human activity and natural processes contribute constituents to the atmosphere that effect air quality, health and climate. Primary pollutants and secondary products of the chemistry (O_3, aerosol) of these pollutants have impacts on human health (photochemical smog and aerosols increase mortality and morbidity rates), quality of life (visibility) and global climate. CE-DOAS utilizes a high finesse cavity consisting of a pair of highly reflective mirrors between which light makes many passes before leaking out of the cavity and being detected to realize long path lengths (5-30 kilometers) over a small cavity length (1m) leading to enhanced sensitivity. The work is presented as follows: (a) Design, construction and characterization of CE-DOAS as well as data analysis development; (b) Temperature dependent measurements of O_4 cross-sections in the ultra-violet and visible wavelength range; (c) Measurements of Rayleigh Scattering cross-sections at UV and visible wavelengths; (d) Instrument inter-comparisons of CE-DOAS with other techniques; (e) mechanistic studies of the chemistry of isoprene oxidation; and (f) deployment of CE-DOAS for field measurements.

To my wife Jenny for all of her unfailing support and trust that I would eventually finish.

Acknowlegements

The work of this Ph.D. dissertation was supported by Graduate fellowships for RT by NASA (2008-2011) and CIRES (2011-2012), as well as funding to Rainer Volkamer through start-up funds provided by CU-Boulder, NSF CAREER award ATM-0847793, California Air Resource Board contract 09-317 (Cal-Nex 2010), EUROCHAMP-2 for travel support for the AlDiIn inter-comparison campaign and the Department of Energy Office of Science award DE-SC0006080.

The author would like to acknowledge, for Chapter 2, Eleanor Waxman and Barbara Dix for assistant with WinDOAS fitting, Christa Hasenkopf for assistance with Mie codes and aerosol scattering calculations, Rebecca Washenfelder and Steve Brown for useful help with cavity construction, Jose Jimenez and Maggie Tolbert with the loan of aerosol generation and classification equipment.

For the work of Chapter 3 I would like to acknowledge Geoff Tyndall, John Orlando and Jim Burkholder for useful discussions about their previous works on the topic as well as Veronica Vaida and for the loan of one set of cavity mirrors centered at 630 nm.

The work of Chapter 4 was done in conjunction with Kyle Zarzana and Maggie Tolbert.

The work of Chapter 5 and 6 completed at the National Center for Atmospheric Research was done in conjunction with Geoff Tyndall, John Orlando, Thomas Karl, Saewung Kim and Roger Seco, Luping Su and Jon Mak of the State University of New York- Stony Brook and Eleanor Waxman from CU.

The work of Chapter 6 completed at EUPHORE was done in collaboration with Maria Teresa Rodrigez of Universidad de Castilla la Mancha, Spain, Mila Rodenas, and Amelia Munoz from CEAM, Steve Ball, Mark Thomas and Iain Goodall of the University of Leicester, Andrew Rickard of the University of Leeds, Frank Keutsch and Samuel Henry of the University of Wisconsin and Eleanor Waxman of CU.

TABLE OF CONTENTS

List of Tables

List of Figures

Chapter I

1. Introduction

The composition of Earth's atmosphere affects many areas of our lives, from the cleanliness of the air we breathe, visibility, to increased early mortality, higher exposure to UV radiation and the changing climate of the Earth. Pollution, or unwanted/adverse additions to Earth's atmosphere from anthropogenic (human) origin, affects the quality of life that we enjoy. Atmospheric Chemistry is the study of the sources, composition and chemical processing of organic and inorganic trace constituents of the atmosphere, and encompasses compounds in the gas and particle phases. In this introductory chapter a brief overview will be given of (1) atmospheric oxidation chemistry of volatile organic compounds with radicals and (2) optical spectroscopy for the detection of trace gases.

1.1 Atmospheric Oxidation Chemistry

A great deal of the research on the troposphere (lower layer of the atmosphere) in the past 40 years has been centered on the production of ozone from the oxidation of volatile organic compounds (VOC) such as isoprene, benzene and toluene. This has stemmed from the observable effects of ozone on human health and its regulation through the Clean Air Act(2008). VOCs are emitted by the biosphere as well as part of vehicle and industrial emissions. As shown in Figure 1, VOC's react with oxidants in the atmosphere (OH, O_3 or NO_3) or are photolyzed by solar radiation to form radical compounds (RO_2) which further react with nitric

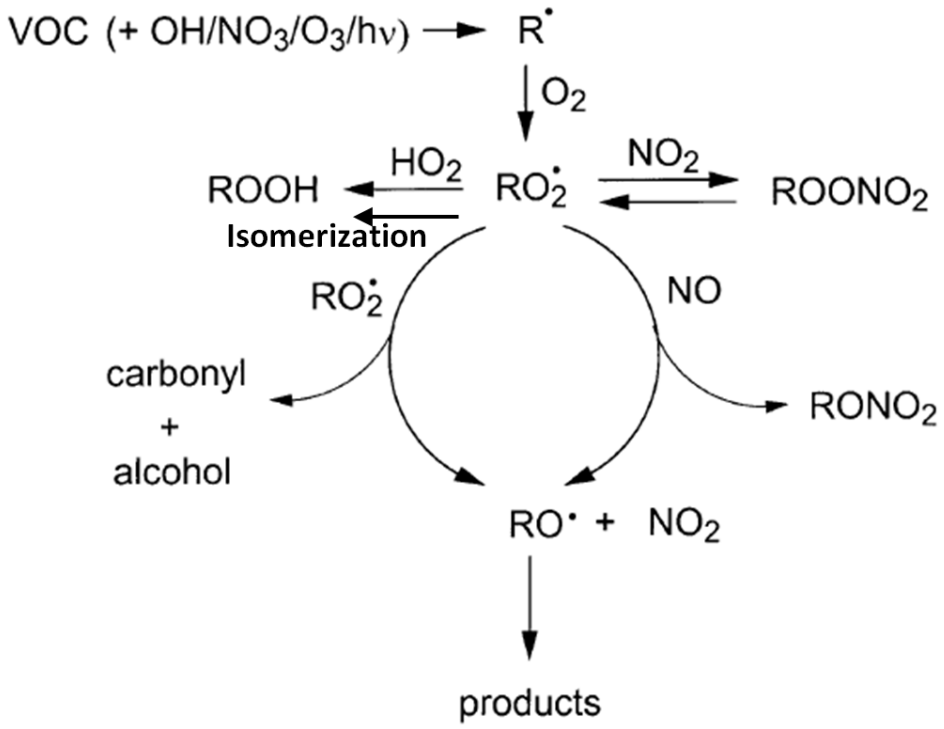

Figure 1.1: Scheme of atmospheric oxidation of VOCs. Peroxy radicals (RO_2) have several possible fates in the atmosphere, dependent on the conditions. In urban areas VOCs react to form ozone catalyzed by NO_x and by RO_2 and HO_2 in remote environments. [Adapted from Atkinson and Arey (2003)]

oxide (NO) to form nitrogen dioxide (NO_2); NO_2 photolyzes to reform NO along with an oxygen radical which upon reaction with O_2 forms ozone. In this series of reactions, NO is regenerated catalytically by the photolysis of NO_2 and the VOC functionalizes or fragments through successive oxidation steps.

VOCs in the atmosphere come from a variety of sources and each source has a characteristic composition of specific organic compounds. Industrial and automobile emissions are typically predominantly aromatic compounds such as benzene, toluene and the xylenes (Hildebrandt et al., 2009). Industrial and automobile emissions generally consist of aromatics and NOx (Hildebrandt et al., 2009). Biogenic VOCs (BVOC) are predominantly isoprene, monoterpenes (e.g. pinenes) and sesquiterpenes (Guenther et al., 2012).

Isoprene emitted by the biosphere is the largest single compound of biogenic origin in the global budget of volatile organic compounds (VOC) contributing an estimated 400-500 Tg annually (Guenther et al., 2012), which is half of all biogenic VOC. Isoprene is emitted by plants and is dependent on sunlight and heat stress. The fate of isoprene in the atmosphere is dominated by reaction with hydroxyl radical (OH). Isoprene is also a dominant sink for OH reactivity in biogenic regions (Karl et al., 2009), and the dominant primary sink for OH in some urban areas such as Los Angeles (Washenfelder et al., 2011). The oxidation of VOCs in the atmosphere contributes to the creation of ozone and secondary organic aerosol (SOA) (Carlton et al., 2009). Aerosols are known to contribute to an increase in overall mortality and are known mutagens (Pope and Dockery, 2006; Villalobos-Pietrini et al., 2007).

Reaction of isoprene with OH forms formaldehyde (HCHO), methacrolein (MACR), and methyl vinyl ketone (MVK) as major first generation products (Tuazon and Atkinson, 1990).

While the mono and di-subsituted carbonyl compounds hydroxyacetone (HACET), glycolaldehyde (GLYC), glyoxal (GLYOX) and methyl glyoxal (MGLYOX) do not make up a large part of the prompt or later generation reaction products, they are known to contribute significantly to the formation and growth of SOA (Kroll et al., 2005; Liggio et al., 2005; Galloway et al., 2009). Isoprene is responsible for 46% and 78.5% of the global production of glyoxal and methyl glyoxal respectively (Fu et al., 2008). Taking this into account, changes in the yields of these small molar yield products can make a very large difference to their global budgets. In order to better understand oxidation of isoprene as well as aromatic compounds we here investigate optical methods of detection for important oxidation products utilizing the method of Differential Optical Absorption Spectroscopy (DOAS) combined with optical cavities.

1.2 Differential Optical Absorption Spectroscopy

1.2.1 Lambert-Beer Law

Molecules and particles attenuate light -when passing through a volume- by scattering or absorption. The sum of scattering and absorption constitutes extinction. The following Lambert-Beer Law describes the absorption of light for one absorbing or scattering species:

$$I(\lambda) = I_0(\lambda)e^{-\sigma(\lambda)cL} \tag{1.1}$$

where $I_0(\lambda)$ is the initial light intensity with respect to wavelength, $I(\lambda)$ is the attenuated light intensity with respect to wavelength and the distance traveled, $\sigma(\lambda)$ is the wavelength dependant absorption cross-section of the absorbing species (cm^2 $molecule^{-1}$), c is the concentration of the species (molecule cm^{-3}) and L(cm) is the length along which the absorption takes place, as depicted in Figure 1.2.

For small optical depths (optical depth(τ) = $\ln(I_0/I)$) the Lambert-Beer's law Absorbance (optical depth) correlates with concentration and can be used to measure the concentrations of compounds in liquid phase solutions or in the gas phase. A typical bench-top instrument would use a poly-chromatic light source with a fixed absorbance path defined by either a fill-able gas cell or a liquid phase cuvette. The reference light intensity (I_0) would be intensity of the light through the cell or cuvette without the absorber added. A better detection sensitivity of compounds can be achieved by either the compound having a large molecular absorption cross-section or by increasing the length over which the light interacts with the molecule. Applications using long light paths in the atmosphere use analysis techniques which account for unknown extinctions and variations.

1.2.2 The DOAS Method

The Differential Optical Absorption Method (DOAS) was first introduced in 1979 (Perner and Platt) and has found a wide variety of spectroscopic applications (Platt and Stutz, 2008), and is a numerical high-pass treatment of the data. In the atmosphere it is possible to realize long light paths by either collecting scattered solar radiation or by sending light through an open volume of the atmosphere. In these applications it is difficult to record I_0 (that includes all portions of the light path (optics, mirrors, similar portion of the atmosphere) in the absence of the absorber of interest), either because the light source is inaccessible (scattering solar radiation), or is highly variable (long light paths with an active light sources (Xe-arc lamps)). In addition, the attenuation of light over long light-paths becomes more complicated when accounting for scattering on gases (Rayleigh type scattering) and aerosols (Mie type scattering) as well as atmospheric turbulence which contribute broad-band losses that are relatively unstructured with respect to wavelength. Accounting for these considerations as well as fluctuation of the light

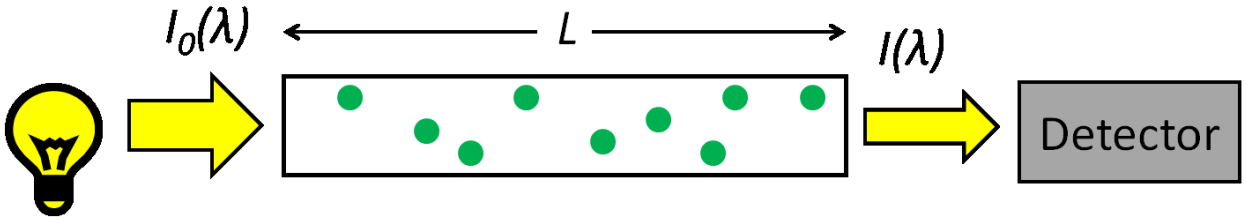

Figure 1.2: Simple diagram of the Lambert-Beer law. Light of initial intensity I_0 passes over a distance L through a medium which it interacts with and is attenuated by a molecule (green circles), and is observed with intensity I at a detector.

source, the Lambert-Beer law can be rewritten as follows:

$$I(\lambda, L) = I_0(\lambda)\exp\left(-\int_0^L [\sum_i \sigma_i(\lambda)c_i(l) + \epsilon_R(\lambda, l) + \epsilon_M(\lambda, l)]dl\right). \quad (1.2)$$

In this expression several absorbers *i* are considered and *i* denotes a specific molecule for which an absorption cross-section σ_i and concentration c_i are given, $\epsilon_R(\lambda, l)$ is the extinction due to Rayleigh, $\epsilon_M(\lambda, l)$ is the extinction due to Mie scattering of aerosols, and all of these are integrated over the absorption length. In this notation the optical density can be written as:

$$\tau = ln\left(\frac{I_0(\lambda)}{I(\lambda)}\right) = \sum_i \sigma_i(\lambda) \int_0^L c_i(l)dl. \quad (1.3)$$

With the slant column density being defined as:

$$S = \int_0^L c_i(l)dl. \quad (1.4)$$

The solution to the issues discussed at the beginning of this section (inaccessible or unknown I_0, light source fluctuation) lies in being able to access changes to *differential* absorption structures independently from *broad-band* absorption or extinction processes, giving Differential Optical Absorption Spectroscopy (DOAS):

$$I(\lambda, L) = I_0(\lambda)\exp\left(-\int_0^L [\sum_i \sigma_i'(\lambda)c_i(l) + \sum_i \sigma_{0i}(\lambda)c_i(l) + \epsilon_R(\lambda, l) + \epsilon_M(\lambda, l) + T(\lambda)]dl\right)$$

$$= I_0(\lambda)\exp\left(\int_0^L [\sum_i \sigma_i(\lambda)c_i(l) + polynomial]\, dl\right). \quad (1.5)$$

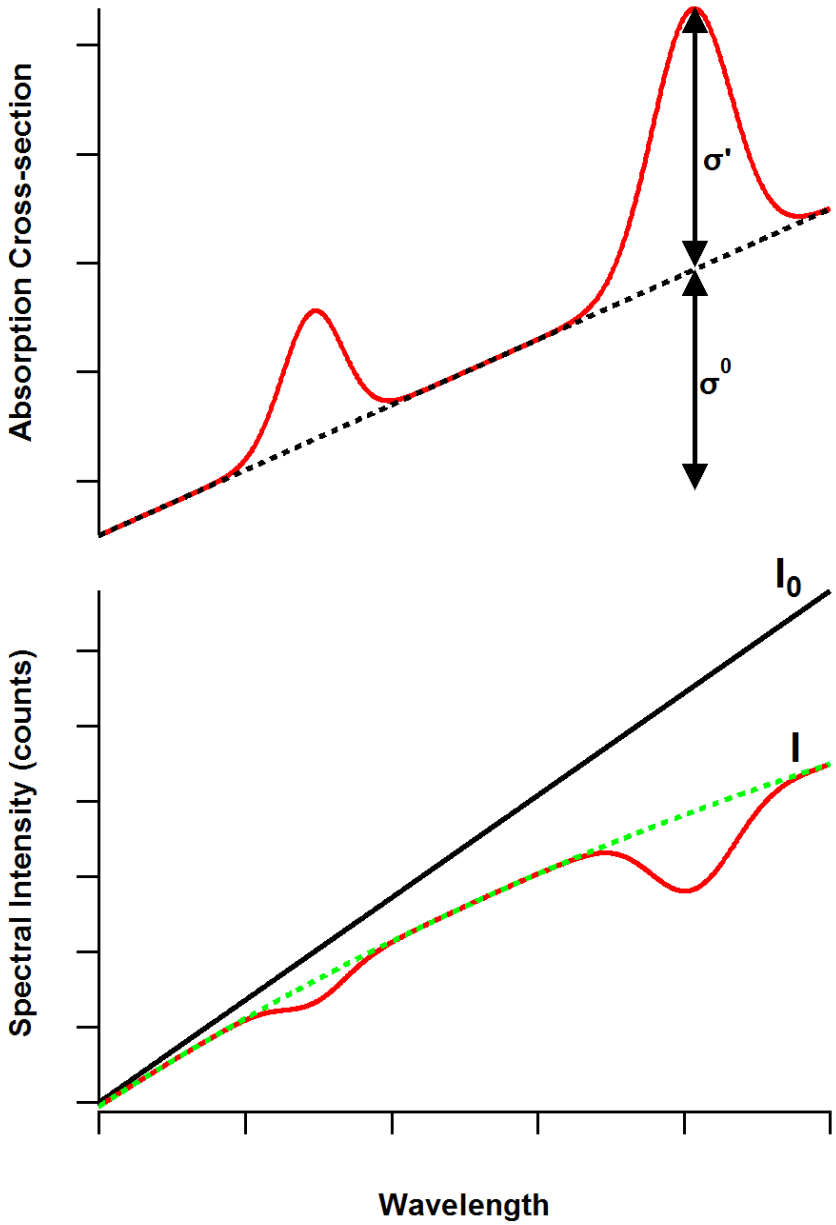

Figure 1.3: Depiction of the DOAS principle at work, where the absorption cross-section differential (σ') and broad-band (σ^0) parts can be separated by the fitting of a polynomial or high-pass filtering (bottom panel showing the two types of absorption in intensity space).

Where the cross-section is divided into its differential (σ') and broad-band components (σ_0) and adding $T(\lambda)$, which is the transfer function of the instrument (fibers and detector) for the as given in Eq. 1.2. In this analysis, highly structured, or differential features are able to be retrieved independent of fluctuations in any broad, or unstructured extinction processes.

The polynomial is used to approximate all of the broad-band processes (Rayleigh, Mie, Transfer function and broad-band absorption), and allows for selective fitting of the differential absorbers as shown in Figure 1.3. The polynomial serves as a high-pass filter and thus the minimizing non-linear least-squares fit of a set of absorbers to this expression is only sensitive to changes in the concentrations of the finely structured absorbers. The application of the DOAS method to high-finesse cavity instruments (Cavity Enhanced Absorption Spectroscopy, CEAS) offers long path-lengths, coupling to active light sources and a sample volume that is easily purge-able. In the balance of this work we will explore the advantages of applying the DOAS method to Cavity Enhanced Spectroscopy measurements and its application to the study of trace gases in the atmosphere, specifically the use of light emitting diodes (LEDs) and the advantage of DOAS retrievals over traditional intensity retrievals for CEAS (see section 2.4.3).

Chapter II

2 LED-CE-DOAS

This chapter published as: Thalman, R. and Volkamer, R.: Inherent calibration of a blue LED-CE-DOAS instrument to measure iodine oxide, glyoxal, methyl glyoxal, nitrogen dioxide, water vapour and aerosol extinction in open cavity mode, Atmos.Meas.Tech., 3, 1797-1814, 2010.

The combination of Cavity Enhanced Absorption Spectroscopy (CEAS) with broad-band light sources (e.g. Light-Emitting Diodes, LEDs) lends itself to the application of cavity enhanced Differential Optical Absorption Spectroscopy (CE-DOAS) to perform sensitive and selective point measurements of multiple trace gases and aerosol extinction with a single instrument. In contrast to other broad-band CEAS techniques, CE-DOAS relies only on the measurement of relative intensity changes, i.e. does not require knowledge of the light intensity in the absence of trace gases and aerosols (I_0). We have built a prototype LED-CE-DOAS instrument in the blue spectral range (420-490 nm) to measure nitrogen dioxide (NO_2), glyoxal (CHOCHO), methyl glyoxal (CH_3COCHO), iodine oxide (IO), water vapour (H_2O) and oxygen dimers (O_4). We demonstrate the first direct detection of methyl glyoxal, and the first CE-DOAS detection of CHOCHO and IO. The instrument is further inherently calibrated for light extinction from the cavity by observing O_4 or H_2O (at 477 nm and 443 nm) and measuring the pressure, relative humidity and temperature independently. This approach is demonstrated by experiments where laboratory aerosols of known size and refractive index were generated and their extinction measured. The measured extinctions were then compared to the theoretical extinctions calculated using Mie theory (3-7 x 10^{-7} cm^{-1}). Excellent agreement is found from both the O_4 and H_2O

retrievals. This enables the first inherently calibrated CEAS measurement at blue wavelengths in open cavity mode (mirrors facing the open atmosphere), and eliminates the need for sampling lines to supply air to the cavity, and/or keep the cavity enclosed and aerosol free. Measurements in open cavity mode are demonstrated for CHOCHO, CH_3COCHO, NO_2, H_2O and aerosol extinction. Our prototype LED-CE-DOAS provides a low cost, yet research grade innovative instrument for applications in simulation chambers and in the open atmosphere.

2.1 Introduction

Light-Emitting Diode (LED) light sources coupled with Cavity Enhanced Absorption Spectroscopy (CEAS) and Differential Optical Absorption Spectroscopy (DOAS) retrievals hold great potential for a light-weight, low-power and portable instrument to enable the sensitive and selective measurement of numerous atmospheric trace gases and aerosol extinction with a single instrument. In the last ten years several high-finesse cavity techniques have expanded on the principles of Cavity Ring-Down Spectroscopy (CRDS) (O'Keefe and Deacon, 1988; Brown, 2003). CRDS, CEAS, and integrated cavity output spectroscopy (ICOS) have in common the use of a high–finesse optical cavity consisting of two highly reflective mirrors to increase the absorption path length over that of conventional White-type (White, 1942), Herriott-type (Herriott and Schulte, 1965) or astigmatic (McManus et al., 1995) multi-reflection cells by several orders of magnitude (paths of 10-200 m). The long path length leads to greatly increased sensitivities of these techniques. CEAS works on many of the same principles as CRDS, but can be coupled with broad band (non-laser) light sources, either in the form of thermal emitters (Incoherent Broadband CEAS) or LEDs (LED-CEAS). CEAS techniques have been used to measure a wide variety of atmospheric trace gases including: nitrogen dioxide (NO_2) (Ball et al., 2004; Langridge et al., 2006; Venables et al., 2006; Triki et al., 2008; Washenfelder et al., 2008;

Gherman et al., 2008; Langridge et al., 2008a; Langridge et al., 2008b; Wu et al., 2009), the nitrate radical (NO_3) (Ball et al., 2004; Langridge et al., 2006; Venables et al., 2006; Triki et al., 2008; Gherman et al., 2008; Meinen et al., 2008; Langridge et al., 2008a; Langridge et al., 2008b; Schuster et al., 2009), dinitrogen pentoxide (N_2O_5) (Schuster et al., 2009), nitrous acid (HONO) (Gherman et al., 2008), water vapor (H_2O) (Venables et al., 2006; Washenfelder et al., 2008; Langridge et al., 2008a; Langridge et al., 2008b), ozone (O_3) (Venables et al., 2006; Chen and Venables, 2010), oxygen dimer (O_4) (Langridge et al., 2006; Wu et al., 2009; Chen and Venables, 2010), iodine (I_2) (Ball et al., 2004; Vaughan et al., 2008; Dixneuf et al., 2009), iodine monoxide (IO) (Vaughan et al., 2008), iodine dioxide (OIO) (Vaughan et al., 2008), bromine oxide (BrO), sulfur dioxide (SO_2) (Chen and Venables, 2010), and glyoxal (CHOCHO) (Washenfelder et al., 2008). CEAS techniques have also been used to measure the rather 'broad band' absorption cross section spectra of acetone, 2-butanone, and 2-pentanone (Chen and Venables, 2010). Available CEAS instruments to measure atmospheric trace gases in the blue spectral range (420-490 nm) are shown in Table 2.1. These techniques have incorporated both Xe-arc lamps and LEDs as light sources.

Traditional CEAS techniques rely on absolute intensity measurements to determine trace gas extinctions (Fiedler et al., 2003). Such measurements are susceptible to lamp drifts. Additionally, the ability of existing CEAS techniques to separate and quantify the temporal variability of extinction losses due to aerosols, turbulence, and changes in the mirror reflectivity and/or cavity alignment from the trace gases of interest remains poorly developed. CEAS measurements to date require frequent calibration measurements, which are time consuming and

Table 2.1. Summary of previous CEAS instruments in the blue spectral range.

Light Source	Mirror Reflectivity	Useable Spectral Range (nm)	Detected Species	Reference
Xe Arc	1. 0.999 2. 0.9998	1. 415-450 2. 427-450	IO IO	(Vaughan et al., 2008)
Xe Arc	0.99996	440-465	CHOCHO, NO_2, H_2O	(Washenfelder et al., 2008)
LED	0.99976	440-460	NO_2, O_4[a]	(Langridge et al., 2006)
LED	0.9997	420-480	NO_2, O_4[a]	(Ball and Jones, 2009)
LED	0.997	450-490	NO_2, O_4[b]	(Wu et al., 2009)
LED	0.99996	420 – 490	CHOCHO, CH_3COCHO, IO, NO_2, O_4[c], H_2O	This work

[a] in pure O_2 at 446 (25 times enhancement of O_4 over ambient conditions); [b] in pure O_2 at 477 nm; [c]in ambient air at 446 and 477 nm

reduce the duty cycle of measurements. Further, the temporal variability of aerosol extinction in the atmosphere poses a major challenge to measurements in open cavity mode, and aerosols often need to be removed from the cavity by means of filtration in sampling lines to enable quantitative measurements. Cavity Enhanced Differential Optical Absorption Spectroscopy (CE-DOAS) is a novel CEAS technique under development (Meinen et al., 2008; Platt et al., 2009). CE-DOAS in principle holds promise to retrieve both aerosol and trace gas information simultaneously, but this potential had as of yet not been systematically exploited. CE-DOAS and other CEAS techniques have in common the use of a high finesse optical cavity coupled to a broad band light source; broad areas of the spectrum (several 10nm) are simultaneously measured by means of a single detector (multiplexing advantage). DOAS retrievals are inherently insensitive to variations in the absolute light intensity (Platt and Stutz, 2008), as DOAS relies on measuring narrow band (<3-5nm FWHM) "differential" absorption features of trace gases; the differential absorption is independent of intensity variations, i.e., does not require knowledge of the light intensity in the absence of absorbers, I_0. In particular, lamp drifts or the presence of aerosols, both broadband processes, do not affect the fitting of narrow band structures, which a DOAS retrieval separates from broad band extinction by means of numerical high-pass filtering of the spectra. First attempts have coupled CEAS hardware with a DOAS retrieval algorithm (Meinen et al., 2008), and discussed the peculiarities of differential retrievals in optical cavities (Platt et al., 2009). Platt et al. (2009) showed that the average (1/e) path length in the cavity is given by the following equation:

$$\overline{L_{eff}}(\lambda) = \frac{d_0}{1-R(\lambda)+\varepsilon_{Ray}(\lambda)d_0+\varepsilon_{Mie}(\lambda)d_0+\sum \sigma_i c_i d_0} \qquad (2.1)$$

where d_0 is the cavity length, R is the mirror reflectivity, ε_{Ray}, is the extinction due to Rayleigh scattering, ε_{Mie} is the extinction due to aerosols and σ is the absorption cross-section of a trace

absorber. The various extinction processes (denominator of Eq. (2.1)) contribute to the reduction in path length; However past CE-DOAS configurations did not have the means to quantitatively account for the reduction in path length caused by temporally variable aerosol extinction, or other causes for variable cavity throughput. The strong sensitivity of Eq. (2.1) towards aerosol extinction is illustrated in Fig. 2.1, where the individual extinction losses are shown for our cavity. As the extinction loss becomes larger than the mirror loss or the Rayleigh loss, the effective path length decreases. Furthermore, the different contributions to the overall extinction have different wavelength dependencies. The effective wavelength dependent path length is thus no longer determined exclusively by R, and α_{Ray}, and their known wavelength dependencies. Aerosols are highly variable in the atmosphere, and as a result the effective path length becomes time dependent. Moreover, the wavelength dependence in Eq. (2.1) is no longer necessarily well defined. Past attempts to characterize broad band extinction losses by means of separate extinction calibration measurements have mostly been limited to the characterization of mirror reflectivity by the use of O_4 in pure oxygen (25 times higher O_4 abundance over atmospheric conditions, O_4 measured at 446 nm and 532 nm bands) (Langridge et al., 2006; Ball et al., 2009; Ball and Jones, 2009b), NO_2 (using a known NO_2 mixture) (Langridge et al., 2006; Triki et al., 2008; Gherman et al., 2008; Vaughan et al., 2008) or CO_2 (Orphal and Ruth, 2008). Simultaneously to our work, a similar approach was developed to retrieve aerosol extinction in the red spectral range by (Varma et al., 2009) using the O_2 band at 685 nm in the SAPHIR chamber. Washenfelder et al.(2008) measured aerosol extinction in the blue spectral range using an absolute IBBCAS retrieval, representing the extinction with a polynomial. An inherent means to calibrate path length in the blue spectral range as a function of wavelength under atmospheric conditions in the presence of variable atmospheric turbulence, aerosols and/or cavity throughput

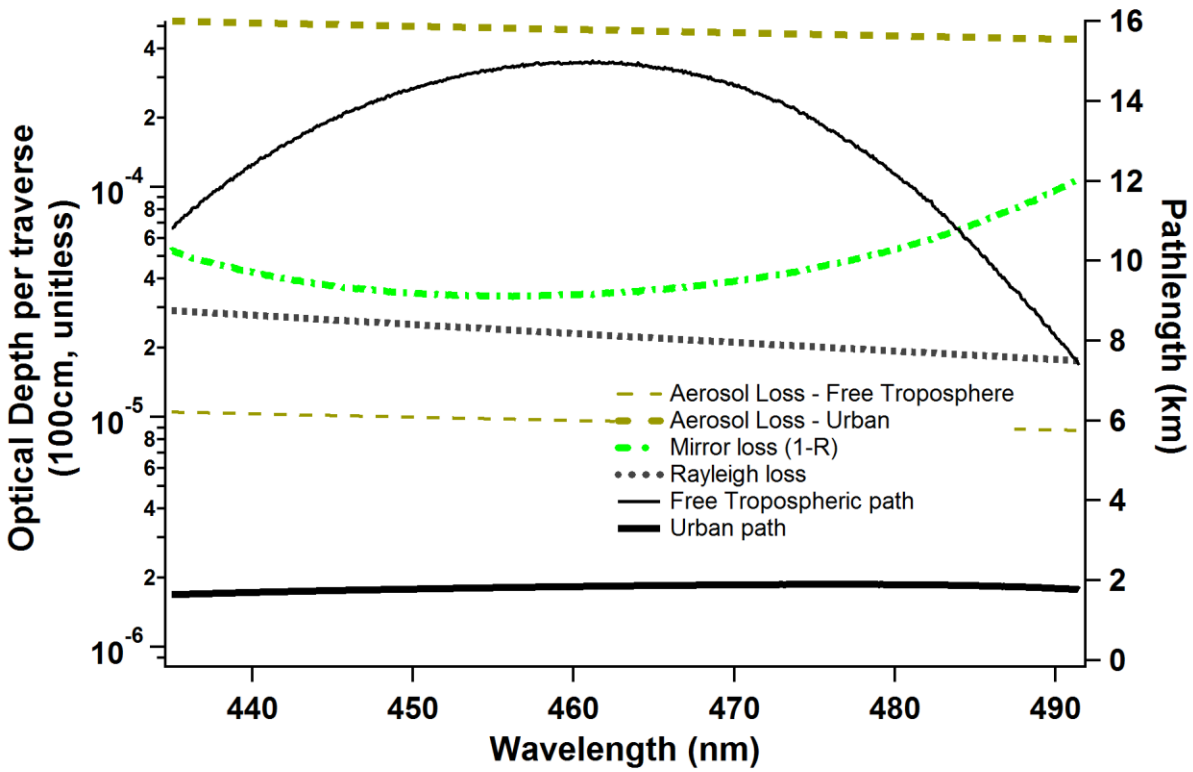

Figure 2.1: Aerosols can strongly affect the effective path length. The wavelength dependent extinction losses (dotted lines) are: mirror loss (1-R) of our cavity (green dashed - dotted line), Rayleigh scattering loss of air at 1 atm (gray dotted line), and aerosol losses for two scenarios: free tropospheric conditions (AOD = 1 x 10^{-7} cm^{-1} at 450 nm, thin dashed line); and polluted urban conditions (2.5 x 10^{-6} cm^{-1} at 450 nm, thick dashed line). The wavelength dependence of aerosol extinction was approximated as λ^{-3}. The corresponding effective path length for both scenarios is shown by the respective solid lines.

is desirable, and is currently missing.

The blue spectral range holds great potential to detect multiple interesting molecules directly in the atmosphere. Glyoxal is the smallest alpha-dicarbonyl and a novel indicator species for fast photochemistry of volatile organic compounds (VOCs) on local (Volkamer et al., 2005b; Sinreich et al., 2007) and global scales (Kurosu et al., 2005; Wittrock et al., 2006; Vrekoussis et al., 2009). The global CHOCHO source from land ranges between 50 and 108 Tg yr^{-1}, with a single VOC precursor, isoprene, contributing ca. 30% to the currently known sources (Fu et al., 2008; Myriokefalitakis et al., 2008; Stavrakou et al., 2009), but about half of the terrestrial source is currently unaccounted for (Stavrakou et al., 2009). Recent measurements demonstrate the uncertainties in the amount of glyoxal formed from isoprene. Current isoprene oxidation schemes consider glyoxal to be only a second and higher generation oxidation product (Bloss et al., 2005; Taraborrelli et al., 2009), but recent measurements (Volkamer et al., 2005a) confirm theoretical predictions (Dibble, 2004a; Dibble, 2004b), and demonstrate that it is also formed as a first generation product with a yield of up to 3% (Volkamer et al., 2005a). This corresponds to about an additional 10 Tg/yr of a glyoxal source on global scales that is currently not reflected in atmospheric models. While significant, it does not explain all of the missing glyoxal in biogenic areas. Further, there is also consistent evidence that CHOCHO is a building block for secondary organic aerosol (SOA) formation (Jang et al., 2002; Hastings et al., 2005; Liggio et al., 2005; Volkamer et al., 2007; Galloway et al., 2009; Tan et al., 2009; Volkamer et al., 2009b; Ervens and Volkamer, 2010). SOA is a concern for public health (Villalobos-Pietrini et al., 2007) and elevated SOA is linked to increased mortality rates (Pope and Dockery, 2006).

Experimental techniques that are sensitive enough to measure CHOCHO under atmospheric conditions either rely on derivatization (Yu et al., 1997), or employ long path

lengths to directly measure CHOCHO in the open atmosphere (Volkamer et al., 2005b). Sensitive in-situ techniques with good time resolution are only recently becoming available (Washenfelder et al., 2008; Huisman et al., 2008), and hold great potential to advance our scientific understanding of hydrocarbon and SOA sources on local and global scales. The blue spectral range is particularly attractive, as multiple gases with potential climate relevance are accessible here, e.g., IO and CHOCHO (Volkamer et al., 2010). A typical light source for these instruments is the Xe-arc lamp; however, the use of Xe-arc lamps creates complications in CEAS retrievals, see Fig. 2.2 in Washenfelder et al. (2008), because Xe-gas emission lines overlap here with the spectral structures of glyoxal and other gases. The spectral intensity and shape of these lines depends on temperature and pressure of the Xe gas, which fluctuate over time. The resulting temporal variability of the Xe-gas emission lines complicates DOAS applications of Xe-arc lamps in this spectral range. As the number of commercially available high-powered LEDs has increased, LEDs are starting to provide an interesting alternative light source to Xe-arc lamps that is particularly attractive to make the blue spectral range more accessible. Here we present an innovative prototype instrument that actively addresses these challenges, and enables the first inherently calibrated CEAS measurement of trace gases and aerosol extinction in the blue spectral range by a single measurement in open cavity mode under atmospheric conditions.

2.2 Experimental

2.2.1 Description of LED-CE-DOAS Instrument

Figure 2.2 depicts the set up of the LED-CE-DOAS instrument along with the gas delivery and aerosol generation and sizing instrumentation, i.e., an atomizer, differential mobility analyzer (DMA), condensation particle counter (CPC). Light from the LED is collimated and directed into

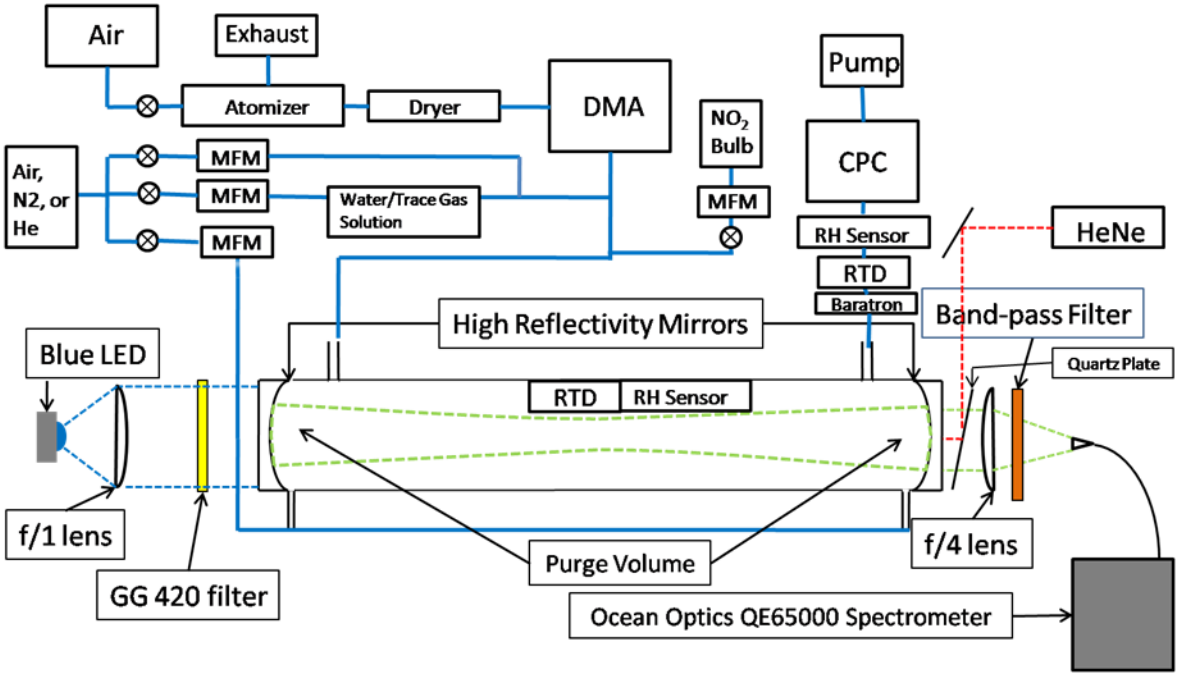

Figure 2.2: Schematic of cavity set up and block diagram of flow handling system for aerosol delivery.

the optical cavity where it makes many passes through the sample volume and is then focused onto the optical fiber and detected by the spectrometer/detector system attached.

2.2.1.1 Characterization of LED light sources

The criteria for a suitable blue LED for LED-CE-DOAS are: (1) lack of a Fabry-Pérot etalon; (2) match well with the expected reflectivity of the mirrors (Fig. 2.3a); (3) high light output, and (4) reasonably small chip size (< 1 mm^2). Variations of etalon structures, which are periodic emission features arising from the difference in the refractive indices of the coating layers on the LED chip, are caused by fluctuations in either the current (amperage) or the temperature of the LED chip, and can complicate the elimination of spectral features from the LED emission spectrum thus introducing residual structures that limit the sensitivity of the DOAS approach. A good match of LED and R consists in suitable optical power output of the LED, limited out of band light from single pass transmission through the cavity, with the overall effect that the intensity past the cavity is reasonably constant (balanced) over the dynamic range of the detector (Ball et al., 2004; Ball and Jones, 2009b). While the presence of etalon structures does not present a fundamental limitation (it can be eliminated by temperature stabilizing the LED, in combination with an extra stable power supply, and/or viewing the LED at an angle) (Kern et al., 2006; Sihler et al., 2009), the absence of etalon structures is desirable.

A variety of blue LEDs were tested. The LED emission spectrum and its spectral stability were characterized both as a function of electrical power and of time. The optical power output was measured using an optical power meter (Thorlabs, PM210) (Table 2.2). The Seoul and LEDengin blue LEDs matched best with the mirror reflectivity, did not show etalon structure, and had optimal emission spectra for the application. In absolute intensity the LEDengin LED was found to be the most powerful LED. Due to the combination of advantages, we chose the

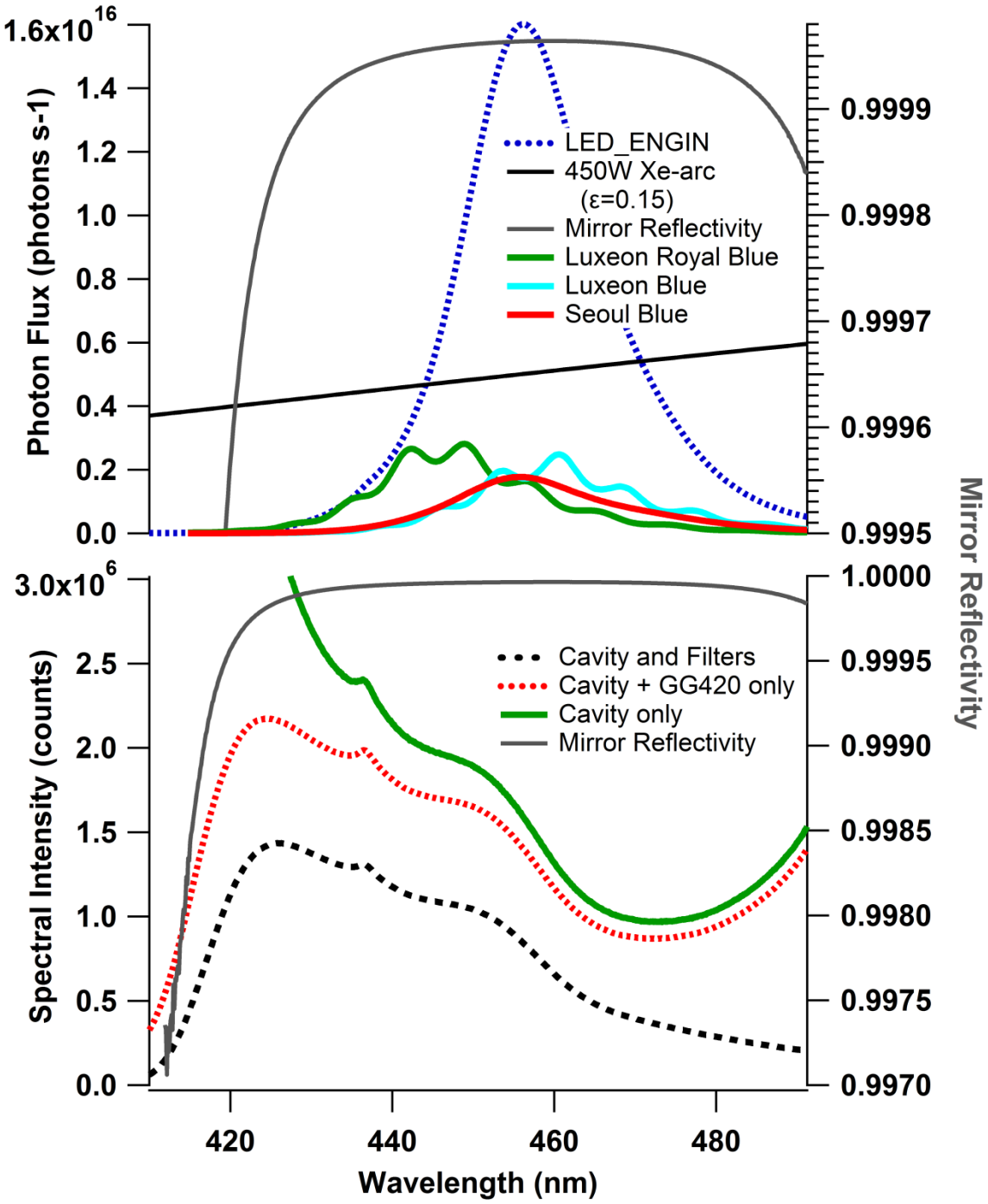

Figure 2.3: A. Emission spectra of several LEDs and a Xe arc lamp compared to mirror reflectivity. B. Sample measurement to illustrate the effect of each optical filter element (cavity mirrors, GG420 cut-off filter, band-pass filter) on spectral intensity.

Table 2.2: LED Characteristics

Company	Color	Model #	Peak λ (nm)	Etalon (Y/N)	Electrical Power (W)	Optical Power (W)	Chip Size (μm × μm)
Phillips-Luxeon	Blue	LXK2-PB14-P00	470	Y	3	0.216	992 × 992
Phillips-Luxeon	Royal Blue	LXK2-PR14-P00	455	Y	3	0.273	992 × 992
Seoul Semiconductor	Blue	B11190	465	N	1	0.180	755 × 755
LedEngin	Blue	LZ1-00B205	465	N	5	1.3	1000 × 1000

LEDengin for our LED-CE-DOAS light source. The LED was mounted to a temperature controlled cooling stage, which was PID stabilized at 10 ± 0.1°C, to control variability in the LED output and structure (peak width and dominant wavelength) that vary with the current and temperature. Such stabilization is standard in our laboratory, and not necessarily needed for CE-DOAS applications.

2.2.1.2 Characterization of the optical cavity and mirror reflectivity

The optical cavity (Fig. 2.2) consists of two 1 inch diameter mirrors with a one meter radius of curvature and a measured reflectivity of 99.9964% at 455 nm (Advanced Thin Films- Boulder, CO), which are mounted 99.0 cm apart. Out of band light was removed using a colored glass filter (Schott GG420) before the cavity and a band-pass filter (Newport 10BPF70-450, λ = 450nm, FWHM = 70nm) before the fiber. The effect of the cavity and the optical filters is demonstrated in Fig. 2.3b. The GG420 is used to avoid saturating the detector while maximizing the use of the detector in the region of interest. The band-pass filter was used to suppress the out of band light at longer wavelengths. If the spectrometer system has any issues with out of band light projection this can introduce stray light into the measurement spectra because the out of band light is orders of magnitude more intense than the measurement light in the region of interest. Light from the LED was collimated into the cavity by a 2 inch diameter f/1 lens and focused onto the fiber after the cavity by a 1 inch diameter f/4 lens (Thorlabs). The cavity and mirror mounts are designed so that the cavity can be enclosed using a 1 inch diameter stainless steel or Teflon tube.

After alignment the mirror reflectivity was determined using Rayleigh scattering as described in Washenfelder et al. (2008) by flowing helium in the cavity for a reference spectrum followed by air or nitrogen:

$$R(\lambda) = 1 - d_0 \frac{\left(\frac{I_{N_2}(\lambda)}{I_{He}(\lambda)}\varepsilon_{Ray}^{N_2}(\lambda)\right) - \left(\varepsilon_{Ray}^{He}(\lambda)\right)}{1 - \left(\frac{I_{N_2}(\lambda)}{I_{He}(\lambda)}\right)}, \quad (1.2)$$

where d_0 is the cavity length and ε_{Ray} is the extinction due to Rayleigh scattering and I_{N2} and I_{He} are the intensities of the helium and nitrogen spectra respectively.

2.2.1.3 **The spectrometer and detector systems**

The light exiting the cavity was focused onto an optical fiber. Two different sets of transfer optics and detector systems were used: (1) light was coupled via a 1 inch f/4 lens onto a 1mm diameter, f/4 glass optical fiber (Ocean Optics) which was coupled to an Ocean Optics QE65000 compact f/4 symmetrical-crossed Czerny-Turner spectrometer. This spectrometer has a 100 cm focal length and a 100 μm slit, and spectra were recorded using a 1.4 mm high Hamamatsu S7031-1006 (1024 × 58 pixels) CCD detector. The CCD chip was thermo electrically cooled to –10.0 ± 0.1°C in order to reduce dark current of the detector. The spectrometer was heated to 31.0 ± 0.003°C (above ambient) to remove temperature drifts in the wavelength pixel mapping of the spectrometer; (2) light was focused via the same lens onto a 1.5mm diameter multi-mode single core optical fiber (Ceramoptic) coupled to 27 individual fibers that were distributed vertically in front of the slit of an Acton 2300i spectrometer, which was coupled with a PIXIS400 CCD Camera (Roper Scientific). In the Acton 2300i a f/3.9 Czerny-Turner 300mm focal length spectrometer was used with a 1200 grooves/mm grating blazed at 450 nm. The PIXIS400 camera used a 8mm high 26.8 mm wide back illuminated CCD chip (e2v®, 1340 × 400 pixels),

that was thermoelectrically cooled to -75.0 ± 0.1°C in order to reduce dark current. The spectrometer was heated to 35 ± 0.1°C. Both spectrometer/detector systems are fully integrated and controlled by the ATMOSpecLab data acquisition LabVIEW code. The code also reads up to eight temperatures, and contains four PID loops used to control and stabilize temperature (Volkamer et al., 2009a; Coburn et al., 2011).

2.2.1.4 Signal to noise comparison

The signal to noise of the two spectrometer/detector systems was evaluated using the root mean square (RMS) fit residual of the DOAS trace gas fit. The theoretical noise level was calculated using combination of the noise levels of the reference and the sample spectra taken in quadrature where the theoretical noise is: $\Delta N = \sqrt{N}/N$ (N being the maximum number of counts in the spectra). The integration time used to record the reference spectrum was two minutes for the QE65000, while the Acton/PIXIS reference was 3.5 minutes. Consecutive spectra were recorded with an integration time of 30 seconds and co-added to increase the photon counting statistics. Figure 2.4 compares the signal to noise ratio of the QE65000 and the Acton/PIXIS spectrometers. The Acton/PIXIS achieves a 2-3 times lower RMS noise for comparable integration times reflecting a 4-9 times higher light throughput. The higher light throughput is primarily due to the high photon collection efficiency of a larger detector with high quantum efficiency, which is systematically exploited by the custom fiber assembly. The spectrometer/detector assembly is described in detail in Coburn et al., (2011).

2.2.2 Aerosol generation and measurement

To characterize the performance of LED-CE-DOAS in the presence of aerosols, mono-disperse aerosols of known size and refractive index were produced using the experimental setup shown

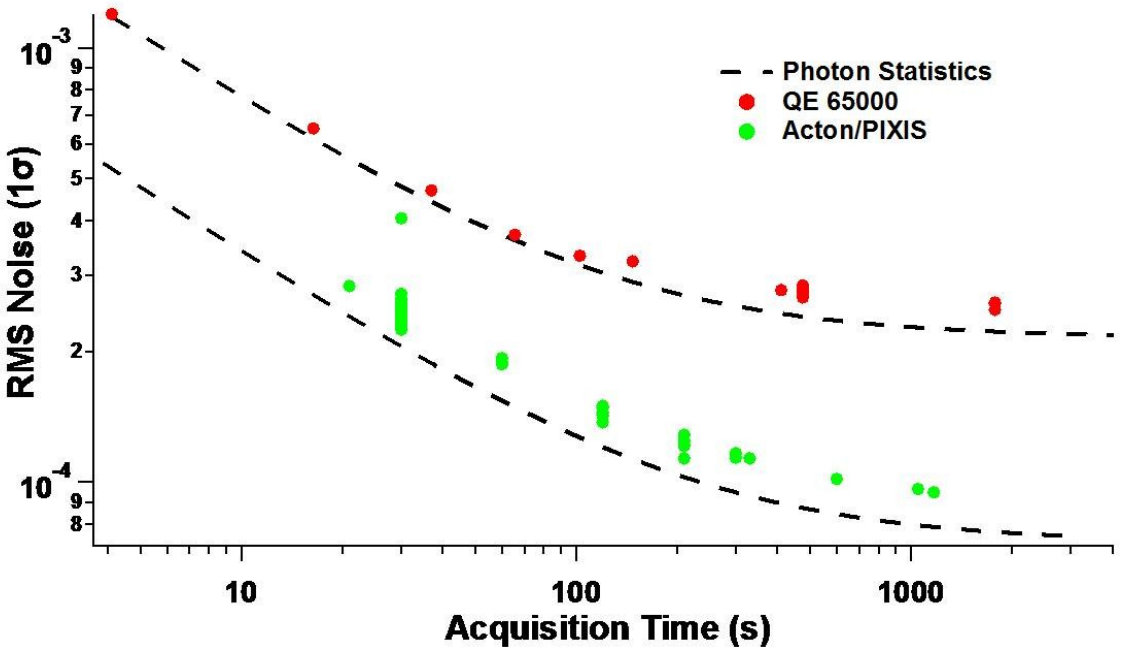

Figure 2.4: RMS Photon noise as a function of acquisition time as measured by the two spectrometer/detector systems used in this study. The theoretical limit of the noise reduction is shown by the dashed lines.

in Fig. 2.2. Polystyrene latex spheres were used as the spherical size-selected aerosol test case. An aqueous solution of polystyrene latex (PSL) spheres (Thermo Scientific, 350 nm ± 7 nm) was prepared by suspending ten drops of standard in approximately 200 mL of de-ionized water. The solution was then volatilized using an atomizer. The airstream was subsequently dried using silica beads, and passed through a Scanning Mobility Particle Sizer (SMPS) which consists of a Differential Mobility Analyzer (DMA) (TSI model 3081) and a Condensation Particle Counter (CPC) (TSI 3022A, in high flow mode) used to size select and count particles. The SMPS was set to 5 liters per minute (lpm) sheath flow and the sample flow through the DMA was 500 standard cubic centimeters per minute (sccm). The size of the aerosols selected by the DMA is known to a 3% uncertainty (Biskos et al., 2006). Particles were counted by the CPC before and after passing through the cavity, and numbers were found identical to within less than 1% indicating negligible particle losses inside the cavity. The mirrors were kept clean using a dry air purge at the ends of the cavity and the sample (aerosols and/or trace gases) was supplied in the middle of the enclosed cavity volume (Fig. 2.2).

2.2.3 Trace gas generation

Water was introduced in the flow volume after the aerosols had been selected by passing a dilution flow through a flask of de-ionized water (Fig. 2.2) and passed through a PFA Teflon® filter in a PFA Teflon® filter holder to remove any water droplets. Relative humidity (Honeywell, 4000-003, ±3.5%RH) and temperature (Omega RTD, ±0.01°C) were measured at the center of the cavity, while pressure (MKS Baratron 629, ±0.12% of reading) was measured as the airstream exited the cavity. For closed cavity measurements, glyoxal, methyl glyoxal and NO_2 were generated, and supplied to the cavity as shown in Fig. 2.2. Air was bubbled through a solution of glyoxal and methyl glyoxal and then diluted before the cavity to provide both trace

gases and water to the cavity. NO_2 was supplied from a standard bulb filled to a starting pressure of 830 Torr and a mixing ratio of $4x10^{-7}$ and then a small flow was leaked from the bulb, measured by a mass flow meter (Sierra Instruments) and diluted by the larger airstream. The NO_2 flow changed slowly over time as the pressure in the bulb reduced. The methyl glyoxal and glyoxal concentrations varied over time as a result of the difference in their respective Henry's Law coefficients (Betterton and Hoffmann, 1988; Ip et al., 2009).

Iodine monoxide measurements were made in closed-cavity mode. IO was generated via the reaction of ozone with iodine atoms as described by the mechanism outlined in Gomez-Martin et al. (2007)(2007). A 20 sccm flow of air was passed first through a flask that contained iodine crystals (Fisher Scientific) cooled in an ice bath and flowed into another flask equipped with an atomic Hg line emission lamp and a Xe line emission lamp (UVP). The Hg lamp was switched on briefly to produce ozone in the flask. The Xe lamp was on continuously, and produced iodine atoms by the photolysis of I_2, which then reacted with the ozone to make IO. The flow was diluted into a 1000 sccm total flow into the instrument. After exiting the cavity an ozone monitor (ThermoFisher Scientific, 49i) measured the amount of ozone in the sample flow.

For open cavity measurements the tube enclosing the cavity was removed and a curtain flow was maintained on the mirrors, allowing both mirrors to face the open room air. NO_2 and water were present in the room air in sufficiently high concentrations that no further supply was needed. Glyoxal and methyl glyoxal were introduced to the light path by placing a row of Petri dishes containing solutions of glyoxal and methyl glyoxal directly under the light path so that the solutions evaporated into the light path.

2.3 Results

2.3.1 LED Light Source

The LEDengin LED used here is 5 times more powerful than the Luxeon and is more powerful than the calculated output of the Xe arc (Fig. 2.3a). The LED also overcomes the limitation created by the highly unstable Xe emission lines that fall in the middle of the CHOCHO evaluation range (see e.g., (Washenfelder et al. (2008)). Because the LED emits less light at wavelengths where the mirror reflectivity drops (out of band light) than a Xe-arc lamp less filtering is needed to remove out of band light. Out of band light is orders of magnitude more intense than the sample light because of the drop in mirror reflectivity (more light allowed through the cavity). The reduced need for filtration allows for a wider useable wavelength range (420-490 nm) compared to arc lamp IBBCEAS setups (see Table 2.1), and helps increase light throughput by reducing optical surfaces.

Another advantage of the light source that has been exploited in our LED-CE-DOAS instrument is that the center wavelength of the LED can be chosen to match the wavelength of maximum mirror-reflectivity. This enables us to use the mirror in order to balance the light intensity across the detector. The effect of the mirror is illustrated in Fig. 2.3b, and enables us to measure a particularly broad spectral range that is 70 nm wide. This is wider than previous CEAS instruments, see Table 2.1. Our motivation in systematically widening the spectral range is innovative, because in contrast to previous work it is chosen to include measurement of the O_4 absorption band at 477 nm, together with the other gases. The O_4 absorption cross section is >10 times stronger at 477nm than at 446 nm. That strong O_4 band, and the water bands at 443 nm provide us with independent means to measure under atmospheric conditions even small variations in the effective extinction length of photons from the cavity at two wavelengths, as

part of each individual spectrum. Such variations could be caused by atmospheric turbulence or variable aerosol optical depth. By measuring the decrease in the O_4 and H_2O SCDs compared to clean (aerosol free) air, CE-DOAS in principle allows for the differential measurement of aerosol optical depth.

2.3.2 DOAS retrieval and absorption cross section weighting

A data analysis routine has been developed using the WinDOAS spectral fitting program (Fayt and Van Roosendael, 2001). The algorithm uses as input the high-resolution molecular absorption cross-section spectra of glyoxal (296K) (Volkamer et al., 2005c), methyl glyoxal (296K) (Meller et al., 1991), O_4 (Hermans et al., 1999; Hermans, 2010), H_2O (833mbar, 296K) (Rothman et al., 2006), NO_2 (294K) (Vandaele et al., 2002) and IO (Hönninger, 1999). These spectra are convoluted with the slit function of the spectrometer and interpolated onto the wavelength dispersion of the spectrometer. Two fit ranges were used, one for the trace gases (435-465 nm) and one for O_4 (455-487nm) each of these used a 4^{th} order polynomial for the high pass filter. The cross-sections are then fitted to the measured optical density to retrieve the slant column density (SCD, integrated concentration along a given path length). Other degrees of freedom of the non-linear least-square fitting routine are kept to a minimum in our retrieval, i.e., no spectral shift and intensity offset are allowed. The slant columns are converted to concentrations using the path length calibration.

DOAS uses Lambert Beer's Law:

$$\ln\left(\frac{I_0}{I}\right) = \sigma(\lambda)cl(\lambda) \qquad (1.3)$$

in a modified form that separates extinction processes as broadband and narrow-band (differential) processes:

$$\ln\left(\frac{I_0}{I}\right) = \left[\sum \sigma'(\lambda)c + \sum \sigma_b(\lambda)c + \varepsilon_{Ray} + \varepsilon_{Mie} + T(\lambda)\right]l = \left[\sum \sigma'(\lambda)c + polynomial\right]l \quad (1.4)$$

where I_0 and I are the reference and measurement intensities respectively and σ, *c* and *l* are the absorption cross-section, concentration and absorption path length, respectively; σ' is the differential (narrow band) portion of the absorption cross-section, σ_b is the broadband component, ε_{Ray} is the extinction from Rayleigh scattering, ε_{Mie} is the extinction from aerosols due to Mie scattering, and T is the instrument transfer function. A polynomial (or other form of a high pass filter) is used to represent all broadband processes (σ_b, both Rayleigh and Mie scattering and T), while the trace gases of interest are identified by their characteristic differential absorption structure. This application of Beer's law assumes that path length is constant within the wavelength interval used for the DOAS fit. However, in CEAS applications the effective path length, L_{eff}, varies strongly with wavelength, as given by Eq. (1), and illustrated in Fig. 2.1. The resulting wavelength dependence of path length creates residual structures if spectra are linearly scaled in the respective fit windows. The effect is illustrated in Figure 2.5 for a DOAS retrieval of glyoxal. For weak absorbers in a Rayleigh atmosphere (no aerosols), the cavity enhancement factor in BB-CEAS retrievals accounts for the wavelength dependence in path length and converts the optical density into extinction units (Fiedler et al., 2003; Washenfelder et al., 2008). For strong absorbers, the trace gas can further become self-limiting to path length at the center of an absorption band. This effect is discussed at a single wavelength by Platt et al. (2009). In this work all trace gas absorbers are optically thin (differential optical density < 4%), and the effect to self-limit path length is negligible. However, as illustrated in Fig. 2.1, aerosols can strongly modify the wavelength dependence of path length. Spectral distortions in DOAS applications are observed for various reasons (Platt et al., 2009), and our solution is to adopt a variation of the interpolation approach between

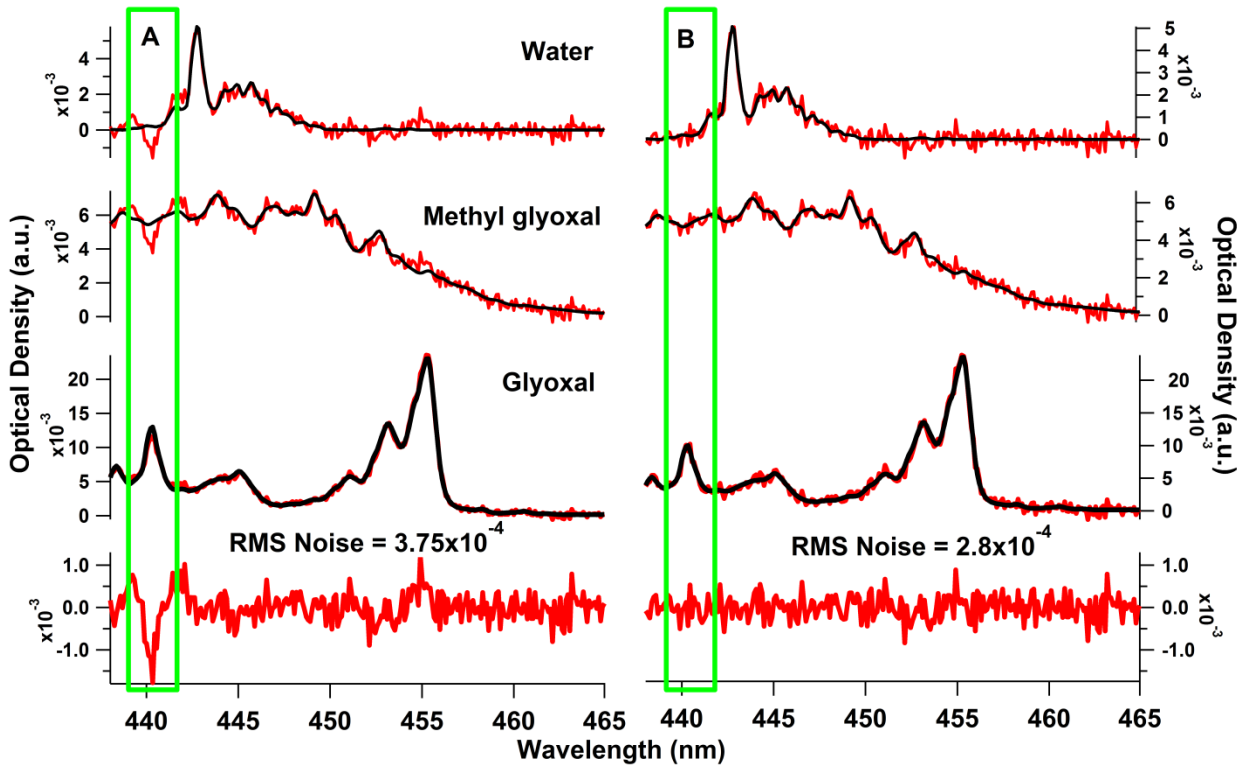

Figure 2.5: Effects of wavelength dependent path length on the fit residual. A. An unscaled glyoxal cross-section is fitted to the spectra. B. Scaled glyoxal cross-section fit (Eqs. (5) and (6), Rayleigh case in N_2). Cross-section scaling is able to reduce the RMS by eliminating systematic residual structures. The experimental conditions are: [glyoxal] = 1.45 ppbv, [methylglyoxal] = 2.05 ppbv, [H_2O] = 0.59%.

(Volkamer et al., 1998) two extreme cases: (1) the Rayleigh case and (2) an upper limit aerosol extinction (here $\varepsilon_{Mie} = 8\text{x}10^{-7}$ cm^{-1}). For each gas, two effective cross sections are included in Eq. (4), and the scaling factors derived from the non-linear fit are summed. We create the effective cross-sections, $\bar{\sigma}_{eff}(\lambda)$ as follows:

$$\bar{\sigma}_{eff}(\lambda) = \sigma(\lambda)F(\lambda) \tag{2.5}$$

where the weighing factor, F(λ), accounts for the relative variation of the wavelength dependence of path length; F is calculated as follows:

$$F(\lambda) = \frac{L_{eff}(\lambda)}{L_{eff}(peak\ \lambda\ of\ absorption)} \tag{2.6}$$

where L_{eff} is calculated according to Eq. (2.1), and normalization of F is most useful with respect to a wavelength where the path length is well known. At that wavelength F takes the value of unity (no scaling); F varied from $0.7 < F < 1.2$ for the spectral windows fitted, see Fig. A2.2 in the Appendix. This notation decouples the relative variation of path length over a fitting window (F) from the absolute value of L_{eff} at the wavelength of normalization. At any point in time L_{eff} is well defined at two wavelengths in our system, i.e., at 477nm from measurements of O_4:

$$\overline{L_{eff}}(477nm) = \frac{SCD_{O4,477nm}}{N_{O2}^2} = \frac{d_0}{1-R(477nm)+\varepsilon_{Ray}(477nm)d_0+\varepsilon_{Mie}(477nm)d_0+\sum\sigma_i c_i d_0} \tag{2.7a}$$

and at 443nm from measurements of water:

$$\overline{L_{eff}}(443nm) = \frac{SCD_{H2O,443nm}}{N_{H2O}} = \frac{d_0}{1-R(443nm)+\varepsilon_{Ray}(443nm)d_0+\varepsilon_{Mie}(443nm)d_0+\sum\sigma_i c_i d_0} \tag{2.7b}$$

where SCD_{O4} has units of molec^2 cm^{-5}, and N_{O2} is the number density of oxygen in units of molec cm^{-3}, and SCD_{H2O} has units of molec cm^{-2}, and N_{H2O} is the number density of water in units of molec cm^{-3}, else see Eq. (1). Only in situations where the wavelength dependence of F is

highly variable an interpolation between two extreme cases needs to be fitted simultaneously in order to avoid spectral distortions as shown in Fig. 2.5a. In most situations it is sufficient to derive a single appropriately scaled F that is applied to all cross sections; this is preferred, as minimizing the degrees of freedom in a respective fit window makes fitting more stable. This approach accounts for spectral distortions due to mirror- (Fiedler et al., 2007), Rayleigh- (Washenfelder et al., 2008) and/or self-limited path length (Platt et al., 2009), and extends beyond these effects by providing a generalized view on wavelength dependent extinction. We demonstrate a practical solution to experimentally constrain the wavelength dependence of aerosol extinction from observing pairs of trace gases, i.e., O_4 and NO_2 or O_4 and H_2O (see Sect. 3.8). Measurements of O_4 and water in the blue spectral range at ambient conditions require high reflectivity mirrors and low photon shot-noise (strong light sources) as pre-requisites; inherent path length calibration thus should be considered as an option when choosing mirror reflectivity; other factors are discussed by (Fiedler et al., 2007; Platt et al., 2009).

2.3.3 Determination of sample path, d_s

As depicted in Fig. 2.2, the aerosol and trace gas samples do not occupy the entire length of the cavity; the length of the volume (d_s) must be determined by a separate set of experiments. This is done by flowing a known amount of an absorber through the sample portion of the cavity. In each run of the experiment before aerosols were introduced, humidified air was flowed through the cavity and the water vapor concentration was measured by the combination of relative humidity sensor, RTD and the pressure sensor. The ratio d_s/d_0 is then calculated as the ratio of the retrieved light path for the water (H_2O SCD divided by concentration calculated from the RH) and the theoretical path, Eq. (2.1), at the wavelength of the water band. The sample path is then calculated by multiplying this ratio by d_0. This can also be done using O_4 by flowing

nitrogen in the purge volumes, and compressed air at known pressure in the cavity. Use of synthetic air requires characterization of the oxygen mixing ratio separately. In this experiment $d_0 = 99. \pm 0.1$ cm and $d_s = 83 \pm 1$ cm.

2.3.4 Accounting of broadband extinction by Polynomial order

In DOAS retrievals, fitting a polynomial is one means of numerical high pass filtering of spectra to represent broadband extinction, see Eq. (2.4). The wavelength dependence of the mirror reflectivity is a primary factor that imposes a broadband shape to the collected spectra in Rayleigh atmospheres. This variation in the number of times that R imposes its wavelength dependence is systematically exploited in Washenfelder et al. (2008) for the case of gases with different Rayleigh scattering cross sections to calculate mirror reflectivity over a wide wavelength range, Eq. (2.2). However, the imposition of R is also relevant to other cases of variable extinction (e.g., aerosols), and needs to be captured accurately in DOAS retrievals. When the cavity is sequentially filled with gases of different Rayleigh cross-sections, for example helium compared to nitrogen, or with air and aerosol compared to nitrogen only, the difference in the number of passes, Δn, is significant, and the mirror imposes its wavelength dependence according to a power law, i.e., $R^{\Delta n}$. The interpolation approach described in Sect. 2.3.2 can account for such variable wavelength dependence of extinction. An alternative means is to account for the variability in wavelength dependence of extinction by a suitable polynomial. A set of sensitivity studies were carried out that compared He and air spectra, and/or the Rayleigh case with an aerosol laden cavity, to test this. The results are shown in Fig. 2.6. It is found that a higher order polynomial (>3rd) is capable to account for the wavelength dependent intensity change between the reference and the measurement spectra. Notably, if the wavelength dependence of extinction is not adequately accounted for, this can cause spectral cross-

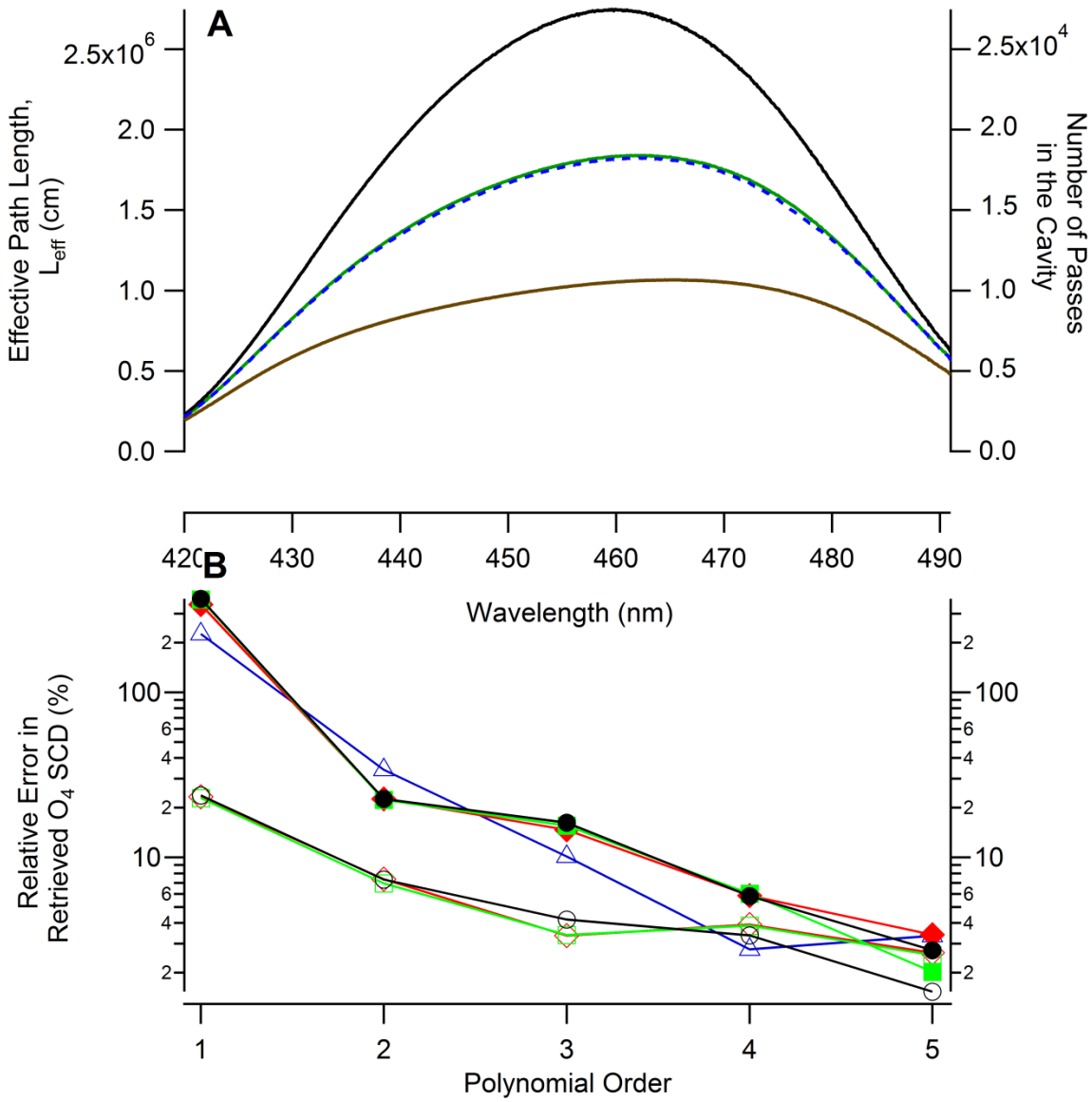

Figure 2.6: Effect of mirror reflectivity and high pass filter on the O_4 retrieval. Panel A: Effective path length and number of traverses in the cavity in helium (black), nitrogen (green), air (blue) and air with aerosol (brown, $\alpha_{aer} = 3 \times 10^{-7}$ cm^{-1}) calculated from theory using known Rayleigh cross-sections and the aerosol extinction cross-section from Mie theory(Bodhaine et al., 1999; Sneep and Ubachs, 2005); Panel B: The relative error in the retrieved O_4 slant column retrieved compared to the calculated O_4 slant column as a function of polynomial order of the high pass filter. If a spectrum in air fit against a nitrogen reference (open red squares), a helium reference (open blue triangles) and a nitrogen reference with an O_4 cross-section scaled to the aerosol case (open diamonds); O_4 slant column error for a spectrum of air + aerosol fit using a nitrogen reference (red squares) and a nitrogen reference with the O_4 cross-section scaled to the aerosol case (black diamonds).

correlations, as illustrated in Fig. 2.6b for the retrieved O_4 SCD. The error in the retrieved O_4 SCD is 10% for a 3rd degree polynomial, and higher for lower order polynomials. Higher order polynomials significantly reduce this error. For the case of comparing a He and air spectrum, Fig. 2.6b demonstrates that the observed O_4 matches to within better than 1% of the O_4 SCD inferred from knowledge of R and the Rayleigh cross section for a polynomial order of 4 and higher. Shifting the wavelength dependence of extinction into the polynomial order thus presents a viable option; this approach reduces the number of effective cross sections to be fitted simultaneously. In this example only a single O_4 effective cross section, scaled for the Rayleigh case in N_2, has been fitted in the presence and absence of aerosols. Notably, a key advantage of the DOAS optimized retrieval is that the residual RMS alerts of an incorrectly captured wavelength dependence of extinction and/or self-limitation in path length, as both effects can cause residual RMS that contain systematic structures (see Fig. 2.5a). In absence of such 'alerting' structures (i.e., purely statistical RMS), a single set of pre-calculated effective cross sections (one per gas) is sufficient also if the overall cavity extinction, and its wavelength dependence are variable.

2.3.5 Methyl glyoxal measurement

In addition to glyoxal and NO_2, methyl glyoxal was detected with the LED-CE-DOAS instrument. The spectral proof is shown for an example retrieval in Figure 2.5. The detection sensitivity of methyl glyoxal is approximately ten times less than that of glyoxal due to the smaller absorption cross-section. This lower sensitivity combined with the lower concentrations of methyl glyoxal make an atmospheric detection unlikely with our instrument. However, the sensitivity is high enough to be useful for the detection of methyl glyoxal in atmospheric simulation chambers where methyl glyoxal concentrations are higher. Detection limits for

glyoxal, methyl glyoxal, IO, NO_2, water and O_4 were calculated conservatively by taking two times the RMS noise of the fit residual and dividing by the peak differential cross-section and the path length; in Table 2.3 typical values for the detection limit are given for the free troposphere (aerosol free) and an urban environment (aerosol extinction = 5 x 10^{-6} cm^{-1}).

2.3.6 IO and I_2 measurement

IO was measured by the instrument in the presence of I_2 and ozone. Both the ozone absorption in the Huggins band, and the molecular iodine absorption provide broadband extinctions in the cavity. Because the measured ozone concentration (< 20 ppbv, an extinction of $2x10^{-10}$ cm^{-1} at 477 nm) was not high enough to change the path length in the cavity; absorption by iodine was then the only broadband extinction process within the DOAS analysis windows. While IO can nucleate particles, such nano-particles are inefficient in their interaction with light at our wavelengths: the extinction cross section of a 10 nm diameter particle (n=1.50) is on the order of 10^{-18} cm^2 $particle^{-1}$ at 450 nm, which corresponds to an extinction of $1x10^{-11}$ for $1x10^5$ particles cm^{-3}. The absence of other broadband extinction processes was further verified by a BBCEAS analysis of the spectra. This allowed the I_2 concentration to be retrieved in a similar manner to the aerosol extinction by the measurement of O_4, Eq. (2.8). The I_2 concentration was then used in combination with the wavelength dependence of the I_2 spectrum, and the mirror reflectivity curve to calculate the absorption path length for IO. Sample spectra are shown in Fig. 2.7a. A 1.5 pptv minimum detection limit for IO for a 2 minute integration time using the QE65000 spectrometer was calculated (Fig. 2.7b). The somewhat poorer detection sensitivity towards IO in this experiment compared to that listed in Table 2.3 is due to the greatly reduced path length and higher RMS caused by the I_2 absorption for a concentration that is orders of magnitude higher than that found in the marine background. Notably, in a reasonably moist atmosphere (see

Table 2.3) the path length at the blue end of our spectral range is constrained more directly from observing water.

2.3.7 Aerosol extinction measurements

For measurements in the ambient atmosphere, aerosols are likely the largest contributor to extinction and thus reduce the path length in the cavity (see Fig. 2.1). Aerosol extinction can be inferred from the change in the measured path in the presence of aerosols, compared to the path in the empty cavity (determined by separate measurements of R, Sect. 2.1.2, and knowledge of the Rayleigh scattering cross section of air, and air pressure). The aerosol extinction was calculated using a modified version of Eq. (2.1), with the substitution of d_s (the sample length) for d_0 (the cavity length) for aerosols and trace gases:

$$\varepsilon_{aer}(\lambda) = \frac{\left(\frac{d_0}{\overline{L_{aer}}(\lambda)}\right) - 1 + R(\lambda) - \varepsilon_{Ray}(\lambda) d_0}{d_s} . \quad (2.8)$$

This can be simplified if the sample path for the aerosols and the reference absorber are the same:

$$\varepsilon_{aer(\lambda)} = \frac{d_0}{d_s}\left(\frac{1}{\overline{L_{aer}}(\lambda)} - \frac{1}{\overline{L_0}(\lambda)}\right) = \frac{d_0}{d_s} O_{2\,vmr}{}^2 \frac{1}{\frac{O_4 SCD_{aer}}{N_{d,aer}{}^2}} - \frac{1}{\frac{O_4 SCD}{N_d{}^2}}. \quad (2.9)$$

where L_{aer} is the path in the presence of aerosols and L_0 is the path for the Rayleigh case in a clean cavity filled with air (see Eq. (2.1)), d_0 and d_S are defined in Sect. 3.3, N_d is the density of air (N_d = 2.09 x 10^{19} molecules cm^{-3} (at a pressure of 830 mbar and a temperature of 298K), $O_{2,vmr}$ is the oxygen volume mixing ratio of air, the O_4 SCD is the column density of the oxygen dimer in pure air, ε_{Ray} is the extinction due to Rayleigh scattering and O_4 SCD_{aer} is measured. Two different approaches were used to retrieve the aerosol extinction. The first approach used

Table 2.3 Detection Limits (2σ) for species in an aerosol free and an urban environment (ε_{aer} = 5 x 10^{-6} cm^{-1} at 450 nm).

Species Detected in 1 minute	Aerosol Free (L=15km)	Urban Environment (L=1.8 km)
CHOCHO	19 pptv	190 pptv
CH_3COCHO	170 pptv	1.5 ppbv
NO_2	30 pptv	290 pptv
IO	0.5 pptv	4.3 pptv
Water	280 ppm	0.3%
O_4	0.1% mixing ratio O_2	0.8%

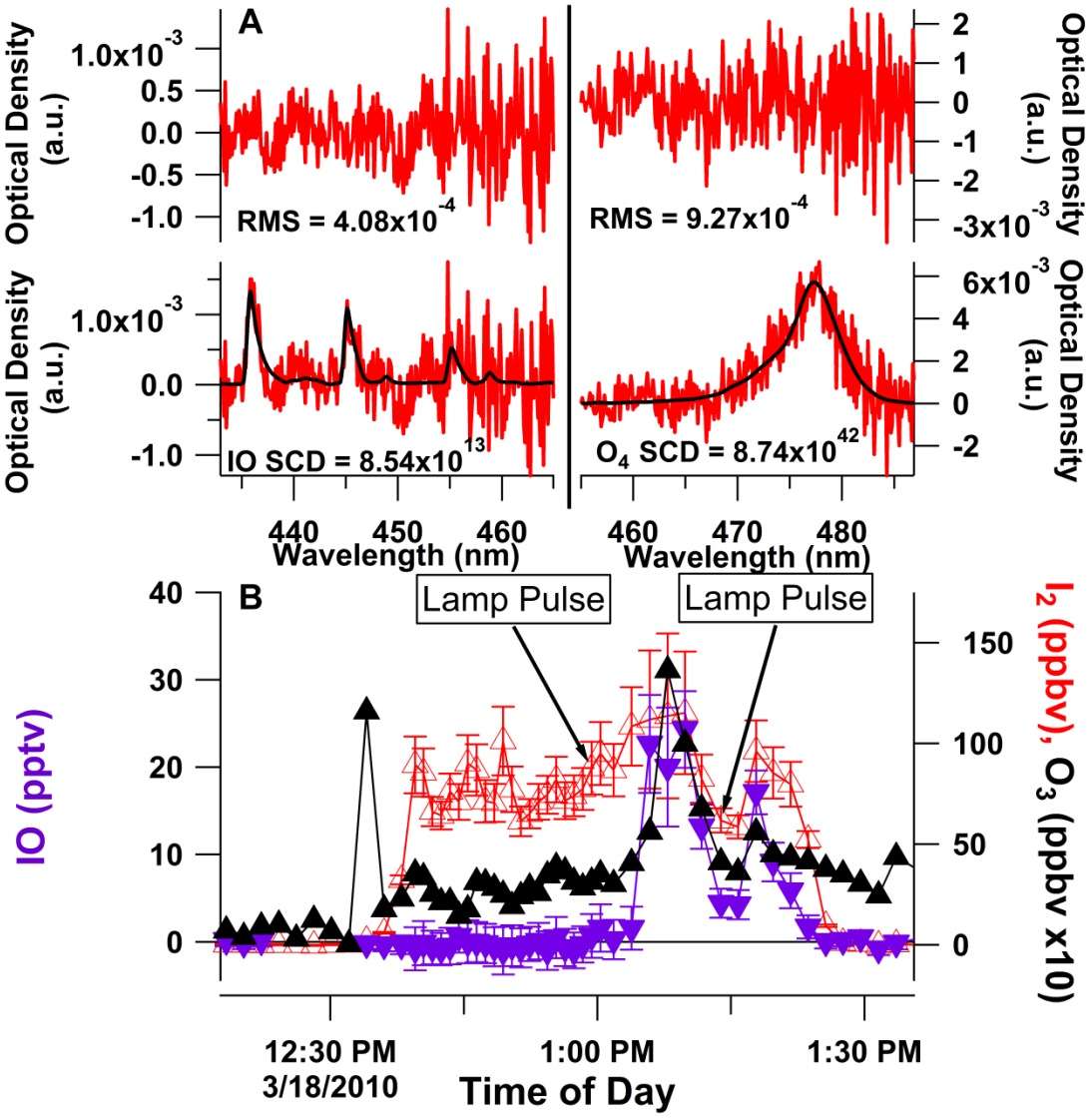

Figure 2.7: A. Example spectrum for the IO detection (4.4 pptv IO, 62 ppbv I_2) (left panel) with the corresponding O_4 fit shown in the right panel. B. Time trace showing the variations in IO, O_3 and I_2, as inferred from the reduction in O_4 path length. The detection limits for IO (dashed line) and I_2 (dotted line) increase towards longer wavelengths because of extinction losses due to I_2 (as seen in part A).

the change in the retrieved SCD of O_4 at 477 nm combined with the independent measurement of pressure and temperature and the knowledge of the oxygen mixing as given in Eq. (2.9). The second used a modified version of Eq. (9), using the SCD of water measured at 443 nm in a similar fashion to O_4, and relative humidity, pressure and temperature were measured separately to calculate the number density of water molecules in cm^3 of air. The detection limit for aerosol extinction is 1.6 x 10^{-8} cm^{-1} at 477 nm and 1 x 10^{-7} cm^{-1} at 443 nm.

2.3.8 Comparison to Mie theory

The aerosol extinctions as retrieved from the reduction of the path length in the cavity were compared to Mie theory. The wavelength dependence of the refractive index of the mono-disperse PSLs was calculated based on the Cauchy expression terms given in the PSL sphere datasheet (ThermoFisher Scientific Technical Note TN007.03). The aerosol scattering cross-section was then calculated using Mie theory. The scattering cross-section for a 350 ±15 nm PSL (σ_{443nm}= 3.54x10^{-9} cm^2, σ_{477nm}= 2.84x10^{-9} cm^2) was multiplied by the measured aerosol concentration to calculate the aerosol extinction in the cavity. There was no need to apply a correction for doubly charged particles (Wiedensohler, 1988) because only one size of particle was supplied to the DMA. The DMA was used to remove bead aggregates and surfactant particles that were also produced by the atomizer (Miles et al., 2010). A conservative uncertainty of ±4% (±15 nm) in the size-selected particle diameter is assumed based on the reported sensitivity of the SMPS (Biskos et al., 2006) and the size distribution in the PSL standard. As can be seen in Fig. 2.8 for aerosol with NO_2, and in Fig. 2.9 for aerosol with glyoxal and methyl glyoxal, the aerosol extinction retrieved from the change in the O_4 SCD by Eq. (2.9) agreed within error bars with the Mie theory calculations at 477nm (Fig. 2.8b, 2.9b) and 443nm (Fig. 2.8c). The measurement of the aerosol extinction at two wavelengths allows us to interpolate the

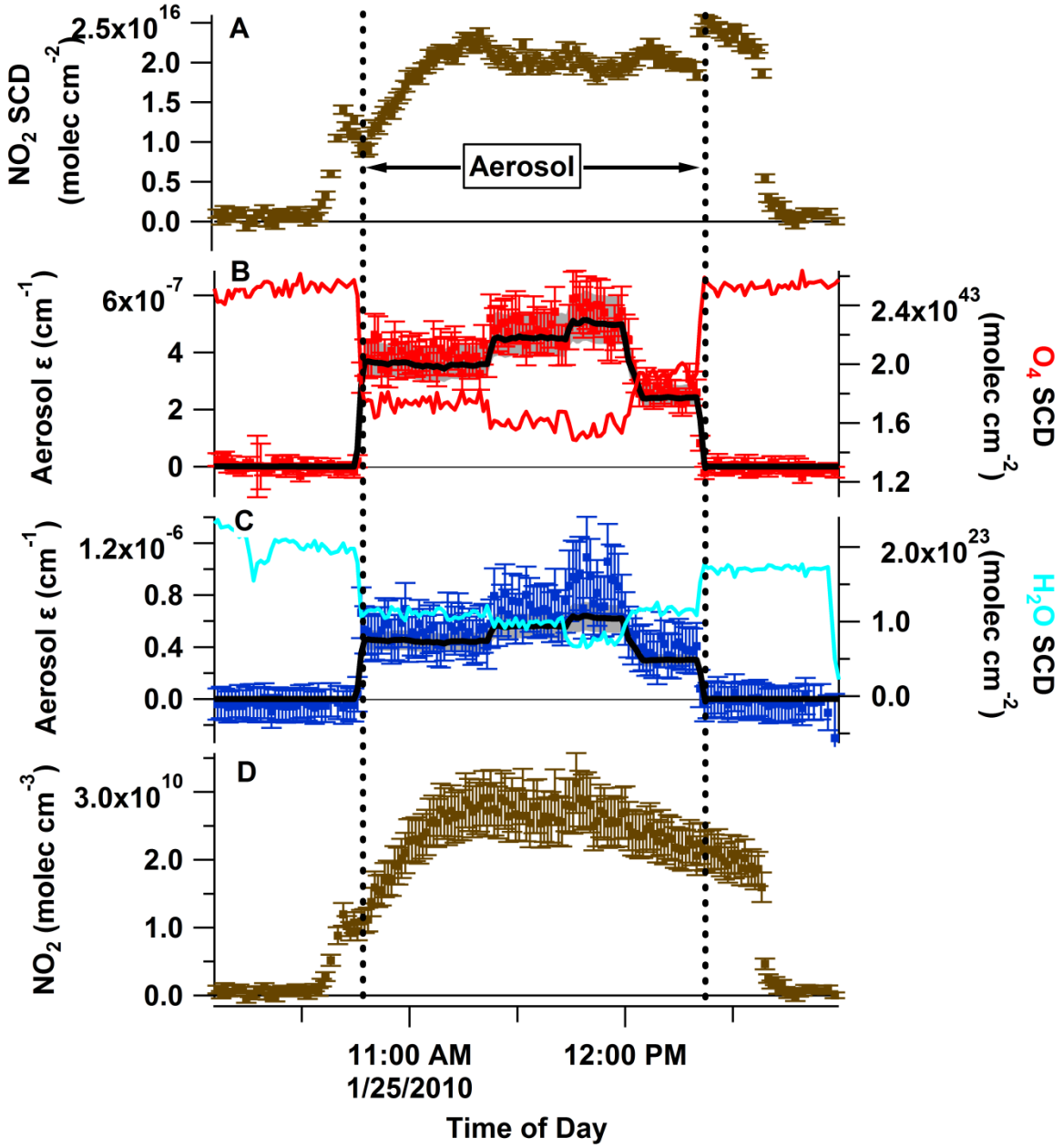

Figure 2.8: Simultaneous retrieval of NO_2 and aerosol extinction at two wavelengths in closed cavity mode. A. Retrieved NO_2 slant column density; B. O_4 SCD (Red Line) and aerosol extinction retrieved from O_4 absorption at 477 nm (red dots) compared to Mie theory (black line, gray area represents uncertainty in size of 350 nm PSLs); C. H_2O SCD and aerosol extinction retrieved from water absorption at 442.8 nm (blue dots) compared to theory (black line); D. NO_2 concentration corrected for the change in path length measured using O_4.

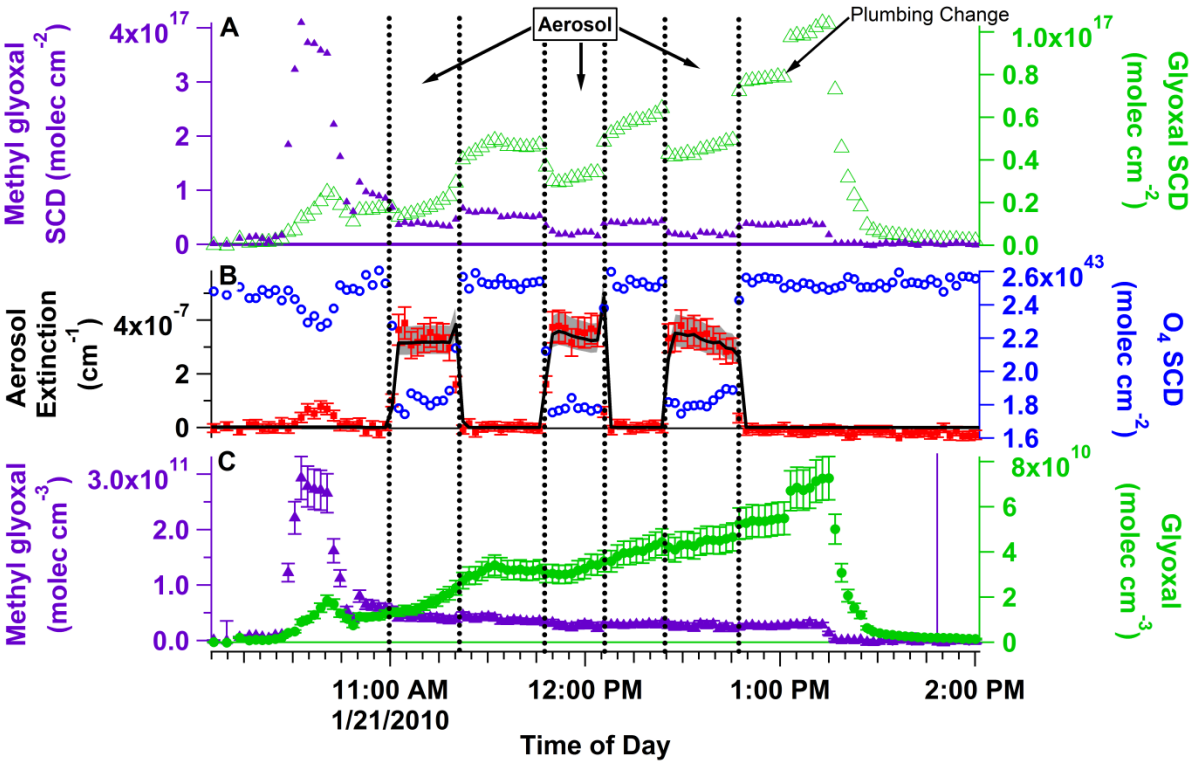

Figure 2.9: Simultaneous retrieval of glyoxal, methyl glyoxal and aerosol extinction at one wavelength in closed cavity mode. A: Slant column densities (SCD) of glyoxal (green open triangles) and methyl glyoxal (purple triangles); B: O_4 SCD (blue circles), retrieved aerosol extinction from the change in the O_4 SCD (red squares) and the calculated aerosol extinction from Mie theory (solid line, gray area represents the uncertainty in aerosol sizing; peaks at the end of the first two aerosol periods are due to artifacts in the CPC counting); C: Retrieved concentrations of glyoxal (green dots) and methyl glyoxal (purple triangles) corrected for path length by the retrieved aerosol extinction.

wavelength dependence of the aerosol extinction for the NO_2 experiment. The dynamic range over which aerosol extinction was varied is limited by the atomizer output, and needs to be regarded in relation to the aerosol free cavity loss. Indeed the lower value of aerosol extinction exceeds the extinction due to Rayleigh scattering in our cavity. The upper end value of aerosol extinction is the dominating over the combined Rayleigh and mirror loss. Our experiments vary the overall extinction loss by a significant factor of 2.2, as illustrated in Figure. A2.1 in the Appendix.

For the glyoxal and methyl glyoxal experiment the known wavelength dependence of the aerosol extinction was used with the mirror reflectivity to retrieve the path length for the glyoxal and methyl glyoxal. The retrieved λ^{-n} dependence ($\lambda^{-3.8\pm2.1}$) of the extinction matches well with the dependence calculated from Mie theory (λ^{-3}). The variability is still large due to the measurement of the aerosol extinction at the water wavelength that is currently limited by the accuracy in the RH measurement and the accuracy with which the water absorption cross sections are known. Alternative means to infer the wavelength dependence of aerosol extinction are provided by measuring a gas which absorbs over a broad wavelength range, e.g., NO_2, at 477nm (the O_4 wavelength), and use the known wavelength dependence of that gas to derive the wavelength dependence of aerosol extinction. While NO_2 cannot always be relied on to be present in detectable amounts, oxygen and water are among the most abundant molecules in the lower atmosphere, and provide sufficient means to calibrate the wavelength dependence of aerosol extinction, and thus derive L_{eff} as a function of wavelength.

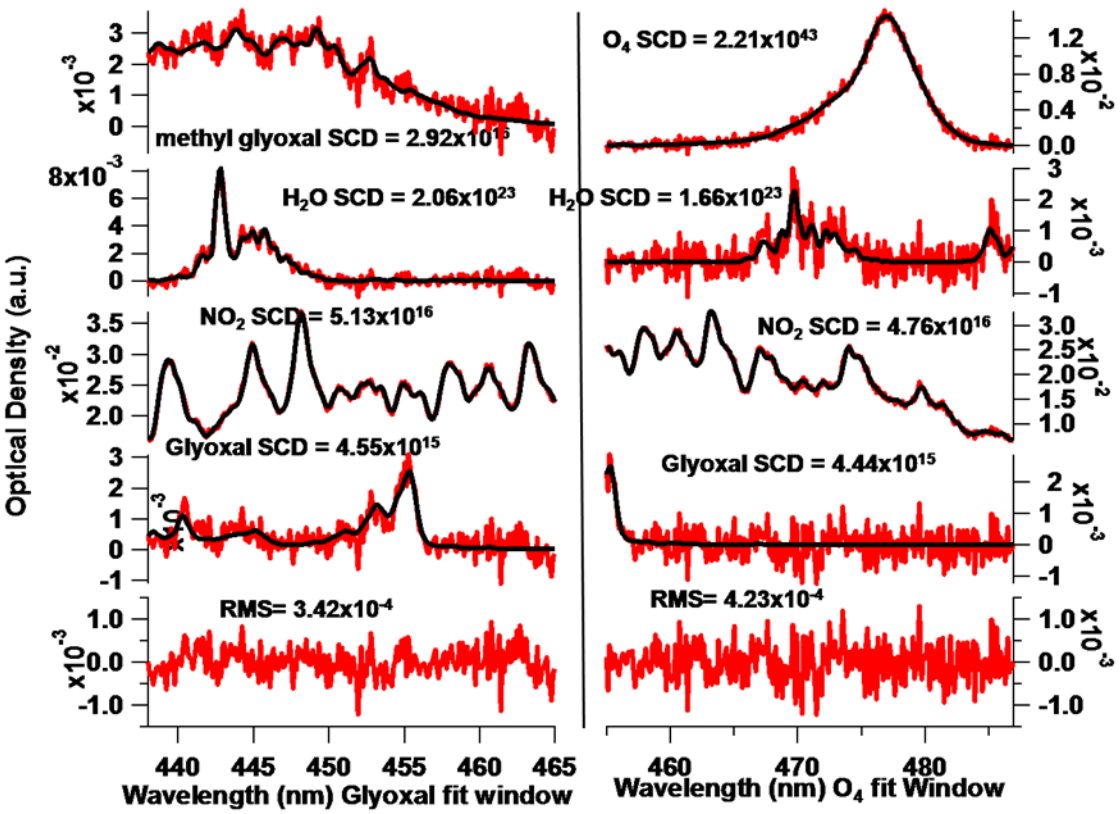

Figure 2.10: Example retrievals using LED-CE-DOAS in open cavity mode: glyoxal (274 ± 14 pptv), NO_2 (2.47 ± 0.07 ppbv), methyl glyoxal (1.2 ± 0.2ppbv), water and O_4.

2.3.9 Open Cavity Detection of NO_2, glyoxal and methyl glyoxal

The inherent O_4 path length calibration of our LED-CE-DOAS instrument enables its use in open cavity mode. The concentrations of NO_2, glyoxal and methyl glyoxal were measured simultaneously in laboratory air with the cavity operating in open cavity mode. Figure 2.10 shows the retrievals of these trace gases from spectra that were recorded in open cavity mode. The path length for glyoxal and methyl glyoxal were retrieved by using the O_4 path to measure the NO_2 concentration and then using the NO_2 concentration and SCD in the glyoxal fit window to retrieve the path length for the desired trace gases as described above. Using the inherent path length calibration, the lab air between the mirrors was characterized to be composed of: NO_2, methyl glyoxal and glyoxal of 2.47 ± 0.07 ppbv, 1.2 ± 0.2 pbbv, and 274 ± 14 pptv respectively and an aerosol extinction measured from O_4 of $4 \pm 3 \times 10^{-8}$ cm^{-1}. This is to our knowledge the first inherently calibrated blue CEAS measurement in open air.

2.4 Discussion

2.4.1 Normalization of blue CEAS instrument sensitivities

Table 2.4 compares the instruments listed in Table 2.1 in terms of their sensitivities for a common integration time of 1 minute. Normalization is needed to account for different units, and also to compare the 'detection sensitivity' of different instruments at a common confidence level. Values of RMS residuum noise in units of cm^{-1} (typical of previous CEAS literature at blue wavelengths) were converted into the equivalent RMS noise (arbitrary units) by multiplying with L_{eff}, see Table 2.4; RMS equivalent noise in such 'optical density' units is listed at the 2-sigma confidence level. The normalized 'detection sensitivity' (units of molec cm^{-3}) was then calculated by dividing this 2-sigma RMS noise by the product of σ (absolute retrievals; σ' for relative retrievals; units of cm^2 $molec^{-1}$) and L_{eff} (units of cm), see footnotes to Table 2.4 for

Table 2.4. Normalization and comparison of detection limits for trace gases measured with blue CEAS instruments

Trace Gas	L_{eff} (km[a])	1-σ RMS (reported units)	2-σ RMS (x 10^{-3} a.u.)	Normalized 2-σ Detection Limit (pptv)[b] in 1 min	Reference
NO_2	4.5	$2.9x10^{-9}$ cm^{-1}	2.6	326	(Langridge et al., 2006)
	17.9	20 pptv[c]	~4[d]	100[d]	(Washenfelder et al., 2008)
	4.5	$3.75x10^{-9}$ cm^{-1}	3.3	422	(Ball and Jones, 2009b)
	0.3	$1.26x10^{-8}$ cm^{-1}	1.0	2500	(Wu et al., 2009)
	13	$2 x 10^{-4}$	0.4	30	This work
CHOCHO	17.9	29 pptv[c]	~4[d]	150[d]	(Washenfelder et al., 2008)
	13	$4x10^{-4}$	0.4	19	This work
CH_3COCHO	13	$4x10^{-4}$	0.4	170	This work
IO	0.68	$7.9x10^{-8}$ cm-1	10.7	315	(Vaughan et al., 2008)
	3.2	$6.4x10^{-7}$ cm^{-1}	83	520	(Vaughan et al., 2008)
	11	$2x10^{-4}$	0.4	0.7	This work
H_2O	15	0.84 ppthv[c]	~4[d]	0.3%[d]	(Washenfelder et al., 2008)
	13	$2x10^{-4}$	0.4	0.028%	This work
O4	4.5	$2.9x10^{-9}$ cm^{-1}	2.6	43%[e]	(Langridge et al., 2006)
	0.3	$1.72x10^{-8}$ cm^{-1}	1.0	35%[e]	(Wu et al., 2009)
	14	$3.5x10^{-4}$	0.7	3.5%[e]	This work

[a] Calculated from Eq. (2.1) for Rayleigh case in air, density of 2.5 x 10^{19} molec cm^{-3}

[b], Normalized to reflect the 2-σ RMS confidence level in 'optical density' equivalent units; calculated by dividing 2-σ RMS by the path length, and the cross section; for NO2 the absolute cross-section is used for BB-CEAS retrievals (σ_{NO2} = $7x10^{-19}$ cm^2), and σ'_{NO2} = $4x10^{-19}$ cm^2 is used for DOAS retrievals (and 4 x 10-19 cm2 molec-1 for Wu et al., 2009), this gives a favourable estimate for BBCEAS (see Section 2.4.1); other gases are converted based on the following values: σ'_{IO} = 2 x 10^{-17} cm^2 $molec^{-1}$, σ'_{O4} (477 nm) = 6.5 x 10^{-46} cm^5 $molec^{-2}$, , σ'_{O4} (446 nm) = 5 x 10^{-47} cm^5 $molec^{-2}$, σ'_{CHOCHO}= 6.5 x 10^{-19} cm^2 $molec^{-1}$, σ'_{H2O} = 4.3 x 10^{-26} cm^2 $molec^{-1}$.

[c] Reported 1-σ fit error interpreted as equivalent to measurement precision (see sect. 2.41.), ppthv = permille volume mixing ratio

[d] No statistical residuals are reported in this paper; the detection limits are estimated from the distribution around zero in Fig. 8 of Washenfelder et al. (2008), see text for details.

[e] Calculated as quivalent O_2 partial pressure in air at STP.

values used for individual gases. Notably, this measure of instrument noise differs from that of the 'fit error' that is often treated as equivalent to 'detection sensitivity' in the BB-CEAS literature. For example, the 1-sigma RMS residual noise of 3.75×10^{-9} cm^{-1} reported by Ball and Jones (2009) corresponds to a 1-sigma fit error of 59 ppt NO_2; this same NO_2 concentration corresponds to an optical density of 4.6×10^{-4}, or ca. 0.3-sigma on the RMS noise scale (compare Table 2.4). Likewise, glyoxal concentrations observed in Fig. 8 of Washenfelder et al. (2008) are negative to 5-sigma 'fit error'; negative concentrations are non-physical, and are taken here to be marginally equivalent to 'zero' within the 2-sigma RMS noise equivalent detection sensitivity in Table 2.4. Our scaling is generally consistent with Stutz and Platt (1996), who found that the true error can be underestimated by up to a factor of 6 if equated to the standard least-squares fit error. Notably, Table 2.4 normalizes 'detection sensitivity' to a common and conservative confidence level for the simple means of comparison between instruments; a similar calculation could equally be performed at another confidence level. Our choice of 'normalized detection sensitivity' allows for reasonable 'white noise' residuals to verify 'by eye' the 'spectral proof' of detection.

2.4.2 LED and inherent path length calibration

Ball et al. (2004) pioneered the use of LEDs with CEAS applications (see Sect. 2.1.1). At blue wavelengths, the 3W Luxeon Royal blue used to be the strongest available LED; it had approximately half the intensity of a 450W Xe-arc lamp (Kern et al., 2006). The optical output measured in Sect. 2.1.2 from the 5W LEDengin LED, see Table 2.1, is about three times higher peak spectral intensity compared to that calculated for a 450W Xe-arc lamp (ε=0.15), and about 5-6 times higher than the 3W Luxeon LEDs, see Fig. 2.3a.

Notably, the inherent path length calibration requires high R mirrors and low photon shot-noise (strong light sources). The high R mirrors reject valuable photons in a situation where the instrument noise is photon shot noise limited. The high intensity LEDengin makes up for some of these losses, and enables us to widen the wavelength window by avoiding the use of filters to suppress out of band light (detection of O_4 at 477nm). The particular challenge with realizing inherent path length calibration at blue wavelengths is illustrated in Table 2.4, and consists in the need for accurate measurements of O_4 and or water at ambient O_2 partial pressures. Table 2.4 compares the normalized O_4 detection sensitivity of different instruments (expressed as equivalent O_2 partial pressure). Previous instruments detect O_4 only in an oxygen enriched atmosphere, leveraging that O_4 abundance scales with the square of the O_2 partial pressure (collision induced absorption of two O_2 molecules). Our O_4 signal-to-noise ratio is ~110 times higher than Wu et al. (2009) (using the same O_4 band) and ~150 times that in Langdridge et al. (2006). Such detection sensitivity is sufficient to detect a 1% change in the O_4 SCD under STP conditions in air, or 0.1% change in the ambient O_2 partial pressure, see Table 2.3. The combination of three factors enables this accuracy: (1) high R mirrors (longer L_{eff}), (2) low RMS noise, and (3) use of the stronger O_4 band near 477nm. The instrument sensitivity is improved also for other gases, i.e., by at least a factor of 3.3 (NO_2), 7 (CHOCHO), 630 (IO), and 10 (water), see Table 2.4.

Other LED advantages help to make the blue spectral range more accessible for DOAS applications, but are not unique to the LEDengin. These consist in an unstructured LED emission spectrum that is rather constant in time, the use of standard laboratory power supplies, reduction in instrument size, increased instrument reliability, longer lifetime and better cost and power effectiveness of the light source (compared to Xe-arc lamps).

2.4.3 Benefits of DOAS retrievals

DOAS retrievals are inherently insensitive to lamp drift. Once the retrieval method is established, such relative retrievals provide a software solution to the problem of lamp drift. Since CE-DOAS only relies on a relative intensity distribution of the lamp spectrum, the frequency at which the lamp needs to be characterized is greatly reduced. For example, we can run our instrument over several days with a single lamp spectrum, without the need to reduce the duty cycle to characterize the lamp intensity and/or cavity transmission. The strong LED, coupled with the reduced need for calibrations makes time and photons available to reduce photon shot noise, improve the signal-to-noise ratio, and achieve lower detection limits without sacrificing the ability to demonstrate 'control' over cavity transmission. While the measurement of O_4 and water are not proprietary of relative retrievals, the ability to detect these gases relies exclusively on the concept of 'differential' absorption for which DOAS retrievals are optimized.

Notably, for comparable 1-min integration time the RMS noise in our DOAS retrieval is about 2.5 to 10 times lower than previous CEAS applications at blue wavelengths, more in instances (see Table 2.4). We characterized the light intensity drift in our instrument at about $4x10^{-10}$ cm^{-1} over the course of several hours. With L_{eff} equal $1.3x10^{6}$ cm this corresponds to ~ $5x10^{-4}$ optical density. Notably, our RMS residual noise from relative retrievals is below this threshold already at 1-min integration time, and decreases further with no apparent deviation from photon-noise statistics for longer averaging times, compare Fig. 2.4. This presents a direct demonstration that the benefit of lower RMS can at least partly be attributed to DOAS retrievals. Previous CEAS applications listed in Table 2.4 used absolute retrievals (Ball et al., 2004, Fiedler et al., 2003; O'Keefe et al., 1998) that require knowledge of I_0, the light intensity in absence of absorbers. From Table 2.4 it appears that absolute retrievals are limited at RMS ~10^{-3}, higher in

instances. The higher RMS values tend to correspond to instruments that use Xe-arc lamps; instruments that employ LEDs tend to give better RMS. The study of Wu et al. (2009) employed very low R mirrors (two orders of magnitude lower than this work) and despite abundant light their noise level is about 2.5 times the RMS derived in this work; the stability of their LED did not allow for RMS to improve beyond ~50 to 100s averaging time. State-of-the-art CEAS applications currently dedicate separate hardware to measuring fluctuations in I_0 by observing 'single-traverse' out-of-band light (Washenfelder et al., 2008; Chen and Venables, 2010). The need to characterize and correct for drift in I_0 adds to the hardware cost, increases shot-noise in the measurement of interest by using a portion of the available photons to characterize I_0, and adds an uncertainty that can limit the minimal extinction which can be quantified; the uncertainty of the separate I_0 measurement needs to be propagated into the final error of absolute retrievals. DOAS retrievals eliminate such hardware needs and potential for error.

DOAS retrievals do not have any particular benefit over absolute retrievals to separate further between broad band extinction from aerosols, changes in R or cavity alignment, or atmospheric turbulence; in either retrieval the decoupling of aerosol extinction relies on engineering solutions of the cavity and air supply. Notably, in an unknown mixture of gases any retrieval techniques relies exclusively on differential absorption features to distinguish between the individual gases that contribute to the total extinction from the cavity. CEAS 'selectivity', or the ability to give spectral proof for unambiguous detection of a specific gas, relies on comparing the differential 'signal' (relative retrievals: arbitrary units typical of 'optical density'; absolute retrievals: units of cm^{-1}) in relation to the RMS noise; the broad band extinction from σ_b (Eq. (2.4)) is convoluted with aerosol extinction, changes in R or cavity alignment, and/or atmospheric turbulence, and – in the case of BB-CEAS retrievals also drift in I_0. Conversely the

benefit of σ_b towards the 'sensitivity', or ability to quantify the concentration, becomes ill defined. For gases like glyoxal and IO, where σ and σ' are near identical, there is no benefit in absolute retrievals.

Finally, the fit residual carries valuable information to 'alert' of the potential for systematic bias (Stutz and Platt, 2008): limitations in hardware, and/or the incomplete accounting of absorbers can create systematic residual structure and impose a limit on the attainable 'detection limit' due to spectral cross-correlations with overlapping features between the residual and other absorbers. DOAS retrievals maintain 'units' that facilitate a straightforward comparison with theoretical RMS noise (i.e., photon-shot-noise, see Fig. 2.4, Sect. 2.1.4). The attainable RMS of other DOAS applications continues to decrease as our understanding of hardware limitations that cause deviations from photon-shot noise statistics at very low noise levels continues to improve (Volkamer et al., 2009c; Coburn et al., 2011): 1-sigma RMS ~ $6x10^{-6}$ has been realized in laboratory applications, and ~$1x10^{-4}$ can now routinely be achieved (see Fig. 4, and also Table 1 in Coburn et al. (2011)). Such DOAS hardware is transferrable to LED-CE-DOAS applications. Future improvements in RMS will also depend on the availability of improved laboratory cross-section data.

2.5 Conclusions

We demonstrate inherently calibrated CEAS measurements at blue wavelengths, and measured glyoxal, methyl glyoxal, NO_2, water and aerosol extinction at 443nm and 477nm in open cavity mode. The open cavity mode eliminates the need for sampling lines, and is particularly useful for measurements of reactive gases and iodine oxide radicals that can get lost in sampling lines.

1. A strong LED coupled with high R mirrors and DOAS retrievals enables low detections limits, while maintaining the ability to demonstrate on-line 'control' over cavity

transmission. The method is based on excellent signal to noise measurements of O_4 at atmospheric conditions as part of each spectrum. The path length calculation only requires a pressure reading as input. Similarly, measurements of the H_2O in combination with relative humidity and temperature are used.

2. To our knowledge ours is the first retrieval of aerosol extinction by a CEAS instrument that has been verified quantitatively using Mie theory. Two methods are presented to characterize the wavelength dependence of aerosol extinction as pre-requisite for path length calculations in open cavity mode.
3. Such control over cavity transmission enables the use of CEAS cavities as direct alternative to traditional multi-reflection cells, for which the number of reflections is geometrically defined, and constant. The maximum number of passes in our cavity (~ $1.3x10^4$) compares favorably to White-cells (16 to 144), Herriott-cells (~100), and astigmatic-type multi-reflection cells (up to 182). The increased photon path length leads to an accordingly better sensitivity.
4. DOAS retrievals provide a software solution to the problem of lamp drift, and lowers the attainable RMS noise from CEAS measurements. The sensitivity of our LED-CE-DOAS is suitable for atmospheric measurements of glyoxal, iodine oxide, nitrogen dioxide and aerosol extinction in polluted and pristine air, and sufficient to detect methyl glyoxal directly under simulated atmospheric conditions.

Chapter III

3 Temperature dependent absorption cross-sections of O_2-O_2 collision pairs from 340-630 nm.

This chapter submitted to Physical Chemistry Chemical Physics as Thalman, R. and Volkamer, R., Temperature Dependent Absorption Cross-Sections of O_2-O_2 collision pairs between 340 and 630 nm at atmospherically relevant pressure, June 2013.

The collisions between two oxygen molecules give rise to O_4 absorption in the Earth atmosphere. O_4 absorption is relevant to atmospheric transmission and Earth's radiation budget. O_4 is further used as a reference gas by Differential Optical Absorption Spectroscopy (DOAS) applications to infer properties about clouds and aerosols. The O_4 absorption cross section spectrum of bands centered at 343, 360, 380, 446, 477, 532, 577 and 630 nm is investigated in dry air and oxygen as a function of temperature (203-295K), and at 820 mbar pressure. We characterize the temperature dependent O_4 line shape and provide high precision O_4 absorption cross section reference spectra that are suitable for atmospheric O_4 measurements. The peak absorption cross-section is found to increase at lower temperatures due to a corresponding narrowing of the spectral band width, while the integral cross-section remains constant (within < 3%, the uncertainty of our measurements). The enthalpy of formation is determined as $\Delta H^{250} = -0.12 \pm 0.12$ kJ/mole, which is essentially zero, and supports previous assignments of O_4 as collision induced absorption (CIA). At 203K, van der Waals complexes ($O_{2\text{-dimer}}$) contribute less than

0.14% to the O_4 absorption in air. We conclude that bound $O_{2\text{-dimer}}$ is not observable in the Earth atmosphere, and as a consequence, O_4 distribution can be predicted in the atmosphere with an accuracy of better than 10^{-3} from knowledge of the oxygen concentration profile.

3.1 Introduction

The collision of two O_2 molecules gives rise to the formation of several absorption bands throughout the ultra-violet, visible and near infrared regions of the electromagnetic spectrum. At very low temperatures –such as those typical of molecular beams- the formation of a weakly bound Van der Waals complex (binding energy, D_e = - 17.0 meV = -1.64 kJ/mole = ΔH^0; ΔH^0 is the enthalpy of formation at a temperature of 0K for the lowest energy state) (Aquilanti et al., 1999a) gives rise to $O_{4\text{-dimer}}$ absorption (Long and Ewing, 1973; Campargue et al., 1998; Biennier et al., 2000). The molecular structure of this open-shell complex has been studied by rotationally resolved measurements and theory (Biennier et al., 2000). At higher temperatures, collision induced absorption (CIA) results in additional $O_{4\text{-CIA}}$ absorption from O_2-O_2 collision pairs that overlap that of $O_{2\text{-dimer}}$. With CIA, the selection rules of molecular O_2 transitions are relaxed as a result of interactions between the electron shells of 2 O_2 molecules (Blake and McCoy, 1987; Greenblatt et al., 1990) during collisions that are fully reversible, i.e., do not involve a bound state. Despite many decades of research (Salow and Steiner, 1936; Long and Ewing, 1973; Wagner et al., 2002) discussions about O_4 absorption (sum of $O_{4\text{-CIA}}$ and $O_{2\text{-dimer}}$) in the atmosphere do not remain free of contradictions. For example, measurements in the atmosphere found a weak temperature dependence in the observed O_4 absorption, which –unless accounted for- can lead to errors on the order of 22 % (for a ΔT = 100 K) with the calculation of solar heating rates, inferred photon path lengths, and cloud height inferences from atmospheric O_4 observations (Pfeilsticker et al., 2001). On the other hand, laboratory evidence (Greenblatt et al.,

1990; Sneep et al., 2006) could in principle explain these observations by apparent changes in the spectral band-shape. However, knowledge about band shapes remains limited for measurements at atmospheric pressure. The question, whether $O_{2\text{-dimer}}$ contributes to atmospheric O_4 absorptions is of fundamental importance for the vertical distributions of O_4 in the atmosphere.

O_4 is a greenhouse gas that absorbs incoming solar radiation, and integrated over all O_4 bands- is responsible for 2.03-2.31 W/m^2 atmospheric forcing (1.06 W/m^2 only counting bands in the visible spectral range) (Pfeilsticker et al., 1997; Solomon et al., 1998). The vertical O_4 column density ~ $1.33x10^{43}$ $molec^2/cm^5$ (U.S.Standard Atmosphere, 1976) gives rise to weak absorptions (e.g., ~0.0007 optical density at 446 nm and ~0.015 at 577 nm for overhead sun, base e). This is due to the rather small absorption cross sections of O_4, σ_{O4}, that pose challenges to their accurate determination. Measurements of σ_{O4} require it to employ either (1) very long absorption light paths (several km), or (2) high O_2 pressure (several 10 bars) to derive a measurable signal. At higher than ambient pressures, pressure broadening could alter the band shapes found in the atmosphere and has not been systematically quantified. Further, the changes of band shape with temperature are currently not well known. Further, the changes of band shape with temperature are currently not well known. Only selected bands have been measured at lower than ambient temperatures, i.e., at 196K;(Greenblatt et al., 1990; Sneep et al., 2006) at 76K (Blickensderfer and Ewing, 1969; Tabisz et al., 1969; McKellar et al., 1972; Long and Ewing, 1973; Campargue et al., 1998); and at ~ 10K (Campargue et al., 1998; Biennier et al., 2000) More recent applications of high-finesse optical cavities to O_4 measurements (Naus and Ubachs, 1999; Tiedje et al., 2001; Morville et al., 2002; Sneep and Ubachs, 2003; Sneep et al., 2006) provide first measurements that benefit from (1) close to atmospheric conditions, and (2)

compact experimental design for straightforward temperature control, but employed monochromatic light sources. Here we present the first use of a high-finesse optical cavity coupled with (3) polychromatic light sources to determine O_4 absorption band shapes over extended wavelength ranges that are wide enough to include one or several absorption bands simultaneously (multiplex advantage).

The O_4 bands are used by Differential Optical Absorption Spectroscopy (DOAS) (Platt and Stutz, 2008) instruments to infer information about aerosols and clouds, i.e., satellite DOAS (Bogumil et al., 2003; Platt and Stutz, 2008), multi-axis DOAS (MAX-DOAS) (Platt and Stutz, 2008; Coburn et al., 2011), and airborne MAX-DOAS (Bruns et al., 2004; Volkamer et al., 2009c; Baidar et al., 2012), and further provide an internal reference gas for in-situ CE-DOAS (Thalman and Volkamer, 2010). DOAS measurements require high quality reference spectra of O_4, and are particularly sensitive to changes in the O_4 band shape. There is a need for high signal-to-noise O_4 spectra under atmospheric pressure, and over the range of temperatures found in the atmosphere.

3.2 Experimental

The absorption cross-sections of O_2-O_2 collision pairs were measured using Cavity Enhanced Differential Optical Absorption Spectroscopy (CE-DOAS) (Platt et al., 2009; Thalman and Volkamer, 2010). We utilized a broad-band light source to measure all wavelengths of a single band simultaneously rather than step-scanning a laser as with ring-down apparatus (Naus and Ubachs, 1999; Tiedje et al., 2001; Morville et al., 2002; Sneep et al., 2006).

The absorption cross-section of O_4 absorption, $\sigma_{O4,}$ is usually expressed in units of $cm^5/molec^2$, owing to the fact that the equilibrium constant K_{eq} (Johnston et al., 1984) is not well known:

$$2\ O_2 \leftrightarrow O_4;\ K_{eq} = [O_4]/[O_2]^2 \tag{3.1}$$

The values of σ_{O4} are instead conveniently calculated using the following equation:

$$Absorbance\ (optical\ depth) = OD = \ ln\left(\frac{I_0}{I}\right); \tag{3.2}$$

where the observed optical depth (OD) is found from Beer's Law and solved for the binary absorption coefficient (hereafter referred to as the cross-section):

$$\sigma_{O_4} = \frac{OD}{O_{2mr}{}^2 N_d^2 l}; \tag{3.3}$$

where O_{2mr} is the oxygen mixing ratio (here: 20.95%$_{v/v}$), N_d is the number density and l is the absorption length.

3.2.1 Experimental Set up

3.2.1.1 Temperature Controlled Cavity

Measurements were carried out using a custom built temperature controlled high finesse optical cavity as shown in Figure 3.1. A key feature of this cavity is that the high reflectivity mirrors (see Appendix Table A3.1) are placed inside the cold region to minimize temperature gradients along the light path between the mirrors. The cold cavity was constructed of aluminum, and consists of an 86 cm long, 3.81 cm diameter tube. The tube is joined at the ends to a 2.54 cm long 10.2 cm diameter tube that houses the mirror mounts inside a cooled region sealed by quartz windows to the ambient air. In the final assembly, the mirrors are placed 87.0 (±0.1) cm apart. The tube is encased in a temperature jacketed cell, while the end regions are surrounded by copper tubing soldered to the aluminum and connected to the cooling fluid. Methanol was used as the cooling fluid in an ultra-low temperature bath (NESLAB Endocal ULT-80), and is supplied near one end of the cavity assembly to lower temperatures homogeneously over the full

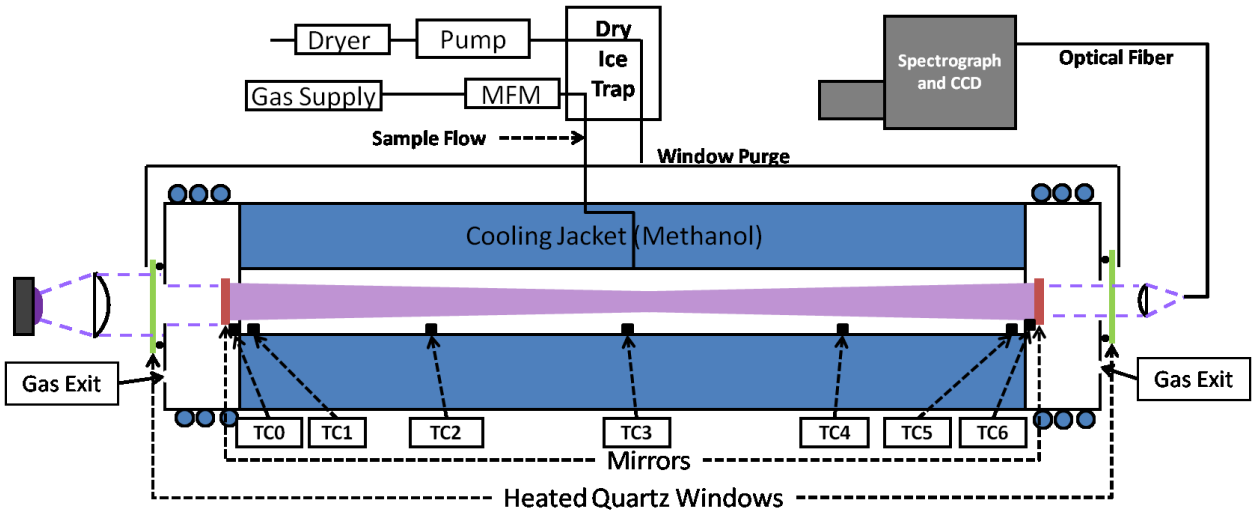

Figure 3.1: Sketch of the experimental setup. TC0 to TC6 indicate temperature probes placed along the inside wall of the temperature controlled cavity enclosure. Gas flow is from the center of the cavity, exiting on the back side of both mirrors.

cavity length from room temperature (295K) down to 203K. Seven thermocouples (Type K, Omega Engineering, CASS-116E-24) were permanently installed in the cavity in the center, mid-way between the center and at the end of the cavity, and just on the inside and outside of the mirror region and signals were recorded using a National Instruments data acquisition module (USB-DAQ). Pressure was measured at the exit of the cell using a Honeywell (model PPT0015) pressure transducer. During the design of the apparatus, attention was paid to place the mirrors as close as possible to the exit of the cavity to minimize temperature gradients. Heated quartz windows (held at 293K) close off the mirror mount region to outside air and the outside of the windows was flushed continuously with ~10 liters per minute of dried room air. Sample gas flow was measured with a mass flow meter (Sierra Instruments) and dried in a dry-ice (CO_2) trap to remove residual water vapor before adding it through the jacket of the cell. Nitrogen (Airgas, 99.998%), air (AIRGAS breathing quality air, O_2 mixing ratio of 20.95%), argon (Airgas, 0.99998%), oxygen (Airgas, industrial grade > 99.9% purity) and helium (Airgas, 0.99998%) were supplied to the cavity in sequence during the measurements

3.2.1.2 Experimental Conditions

For each wavelength range, measurements were taken starting at room temperature with the following cycle of gases: He then N_2 to measure the mirror reflectivity curve (Washenfelder et al., 2008; Thalman and Volkamer, 2010); followed by addition of either air or pure oxygen to measure the collision pair absorbance (see Appendix Table A3.1). This was followed by the addition of either N_2 or Ar as a reference. N_2 is used as the I_0 for measurements in air while Ar was used for measurements in pure O_2 due to the more similar Rayleigh scattering cross-section of O_2 and Ar. A typical cycle of gases at one temperature was as follows: 15 minutes each of He, N_2, Air, and N_2 (for stronger bands at 477, 577 and 630 nm) or 15 minutes each of He, N_2, O_2,

and Ar (for weaker bands at 446 and 532 nm, or lower reflectivity mirrors at UV wavelengths). The cavity was cooled to take individual measurements at set points of 293, 273, 253, 233, 213 and 200 K. The actual temperature in the cavity at the lower temperatures was higher than the desired set point of the chiller bath, but was held constant at each level for the measurements. The individual temperature sensors showed deviations from each other that were smaller than 4K at 203K. The path length weighted temperature uncertainty across the entire length of the cavity was than smaller 0.3K (see Figure 3.2). Each temperature and wavelength range was sampled independently at least two times for reproducibility.

3.2.1.3 Mirror and LED combinations

Five different pairs of high reflectivity mirrors were used to cover the ultra-violet and visible range from 330-660 nm (360, 455, 532, 580 and 630 nm) centering on each of the oxygen collision pair absorption bands. Light emitting diodes (LEDEngin, for specific model information see details in Appendix Table A3.1) centered at each mirror wavelength were used as the light sources for the visible wavelengths. The LEDs were mounted on a single stage Peltier cooling stage, equipped with a PID temperature control to stabilize temperature at 20±0.01°C. In the ultraviolet spectral range, a Xe-arc lamp (Hamamatsu L2273, 150W, 2 mm arc) was used. A full description of light sources and cavity mirrors is provided as part of the Supplemental information (Table S1). The control of the temperature of the LED cooling led to a peak to peak variability in the flux of <0.02% over one hour. The Xe arc was much less stable. Attempts to adjust the spectra for power fluctuations based on scaling by scaling to out of band light levels (Washenfelder et al., 2008) were found to increase the overall error and abandoned. It was decided to minimize measurement time between different gases, and intensity drifts were accounted for by the background/offset correction as described in Section 3.2.2.

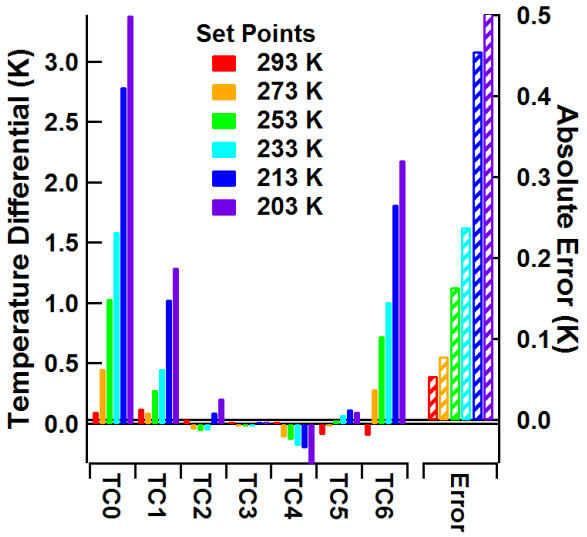

Figure 3.2: Temperature variation across the cavity. The ‘error’ denotes the integral temperature variation over length, and is given as the average error over the full cavity length in units of Kelvin. TC0 to TC6 refer to Figure 3.1.

3.2.1.4 Spectrometer and detector

The light from the LED or Xe-arc was collimated using a 50.8 mm f/1 lens into the cavity. The measurement light was passed through a set of optical filters placed before and after the cavity to remove out of band light. Light exiting the cavity was focused onto a 1.35 mm diameter optical fiber (Ceramoptic) using a 25.4 mm f/4 lens. The light from the mono-fiber was transferred to a fiber bundle (36x145μm) which was arranged vertically on the slit of the Acton SP2300i spectrometer equipped with a 1200 g/mm grating (500 nm blaze wavelength), and coupled to a PIXIS400b (Roper Scientific) CCD camera (Thalman and Volkamer, 2010; Coburn et al., 2011). Custom LabView data acquisition software was used to collect spectra and control the temperature of the spectrometer (spectrometer housing temperature, 34±0.02°C; Spectrometer and electronics rack, 26.0±0.8°C) as well as the LED temperature. The resolution of the measurements ranged from 0.32-0.45 nm full width at half maximum (FWHM) resolution as determined by atomic emission lines, and depending on the wavelength range of interest (UV to red). Instrument line functions were measured using Hg, Xe, Kr or Ne atomic emission lines for each wavelength range. The line functions were slightly asymmetric with the tail towards the shorter wavelengths, but do not limit the apparent band shape of O_4 bands (which were typically about 10 times wider). The change in the resolution across the detector is exemplified as the change in the FWHM of Xe atomic line emissions for the blue cavity (455 nm centered) [0.368 nm FWHM, 450.22 nm, pixel 257; 0.360 nm FWHM, 473.54 nm, pixel 748; 0.355 nm FWHM, 484.47 nm, pixel 952]. For measurements near 630 nm, we used a 600 g/mm grating (300 nm blaze wavelength) giving a resolution of 0.68 nm FWHM. This was necessary to better capture the entire absorption band at 630 nm, which is significantly wider than other bands (for specifics on wavelength range and resolution of each cavity see Table A3.1). The wavelength pixel mapping was determined by recording solar stray-light spectra from connecting the optical fiber

at the exit of the cavity to a small telescope, and pointing it out of the window. The Fraunhofer lines were compared to the Kurucz spectrum (Kurucz et al., 1984), using the WinDOAS software (Fayt and Van Roosendael, 2001). From these comparisons we determine the reported wavelength stamp to be accurate within 0.01 nm.

3.2.1.5 Data Analysis

The mirror reflectivity curve of each cavity at each temperature was measured with respect to wavelength as in Washenfelder et al. (2008) and Thalman and Volkamer (2010) from the difference in the Rayleigh scattering of He and N_2 according to the following equation:

$$R(\lambda) = 1 - d\frac{\left(\frac{I_{N_2}(\lambda)}{I_{He}(\lambda)}\right)\alpha_{Ray}^{N_2}(\lambda) - \alpha_{Ray}^{He}(\lambda)}{1 - \frac{I_{N_2}(\lambda)}{I_{He}(\lambda)}} \quad (3.4)$$

where R is the mirror reflectivity, *d* is the cavity length; *I* is the intensity spectra for each gas and α is the extinction due to N_2 or He gas respectively (cm^{-1}) all with respect to wavelength. Ten to fifteen minutes of spectra were accumulated for each gas and averaged to decrease the photon shot noise in the averaged spectra. Measurement spectra were analyzed in two ways: (1) comparing absolute intensities as done in BBCEAS (Fiedler et al., 2003; Washenfelder et al., 2008; Ball and Jones, 2009a) was employed for the weaker O_4 absorptions in air, or (2) using the Beer-Lambert law as defined in equation (3.3).

With the first approach, BBCEAS fitting based on the following equation derives the extinction in the cavity:

$$\alpha(\lambda) = \left(\left(\frac{1 - R(\lambda)}{d}\right) + \alpha_{Ray}^{Air}(\lambda)\right)\left(\frac{I_0(\lambda) - I(\lambda)}{I(\lambda)}\right). \quad (3.5)$$

The extinction was then divided by the square of the oxygen concentration to calculate the absorption cross-section (cm^5 $molecules^{-2}$). Because the Rayleigh scattering cross section of the

measurement gas differs from that of the sample gas (e.g. N_2 vs. air, or Ar vs. O_2), and to correct for small lamp drifts over time, a baseline correction was calculated. This baseline correction was done by fitting the baseline regions of the spectrum (regions free of O_4 absorption) (Hermans et al., 1999; Hermans, 2010) to a polynomial (2-4th order depending on the wavelength range); the latter was then subtracted from the spectrum.

With the second analysis approach, equations (3.2) and (3.3) are employed as in traditional absorption spectroscopy. Corrections are needed as (a) the path length varies strongly as a function of wavelength, and (b) O_4 absorption may become self-limiting to path length if the O_4 absorptions exceed a few percent optical density. Both corrections were applied simultaneously by means of the following equation from Platt et al.(2009):

$$L(\lambda) = \frac{d}{1 - R(\lambda) + d\, N_d\, \sigma_{Ray}(\lambda) + d\, O_{2mr}{}^2\, N_d{}^2\, \sigma_{O_4}(\lambda)}. \qquad (3.6)$$

The correction for self-limitation becomes significant in our data whenever the O_4 absorption term (last term in denominator to equation (3.6)) contributed more than ~3% to the path-length as determined. Under these conditions we employed Eq. (3.6) iteratively to calculate a path length correction to the optical density and derive the absorption cross-section. The calculated cross-section from the first iteration is used to re-calculate the path length equation and the cross-section is retrieved accounting for the reduction in the light path (Eq. 3). This cycle typically converges to relative changes between iterations of less than 1% within 3 iterations.

Molecular oxygen overtone bands overlap with O_4 bands near 579 and 630 nm. They were accounted to retrieve the collision pair absorption cross-section by convolving the HITRAN (Rothman et al., 2006) database output for the 628.8 nm γ overtone band of the O_2 [$b^1\Sigma_g^+(\upsilon'=2) \leftarrow X^3\Sigma_g^-(\upsilon''=0)$] using the instrument line function. We performed high resolution

cross section modeling in intensity space for the appropriate slant column density of O_2 to represent distortions of the apparent band shape of O_2 at the limited instrument resolution prior to convoluting the spectra to obtain the best possible match with our measurements (Volkamer et al., 1998). Separate cross section spectra were calculated at each temperature at the appropriate oxygen slant column densities. For lack of data for the 2nd overtone of O_2 (δ, 579.7 nm, $[b^1\Sigma_g^+(\upsilon'=3) \leftarrow X^3\Sigma_g^-(\upsilon''=0)]$) in HITRAN, room temperature spectra were fitted using the Hermans band shape and the residual used as the cross-section for the O_2 band. This correction worked well for the much weaker 2nd overtone band. However, it was found that residuals remained visible for the much stronger 1st overtone; necessitating the further smoothing of O_4 spectra near the blue shoulders of the 630 nm O_4 band. We accomplished this by fitting a high order (6+) polynomial to the peak and replacing a limited region near the peak with the polynomial.

Rayleigh scattering cross-sections for N_2 and Ar were taken from expressions in Table 1 in Sneep and Ubachs(2005) (also see Table 1 in Naus and Ubachs(2000)) and equations 1 and 2 in Bodhaine et al.(1999), while the Rayleigh scattering cross-section of He gas was from the expression given in Washenfelder et al.(2013) The Rayleigh scattering cross-section of O_2 was calculated from the fitted data of Shardanand and Rao(1977), combined with the reported data of Sneep and Ubachs(2005) to give an expression of $\sigma_{O2,\,Rayleigh} = 3.1572 \times 10^{-16}\,\lambda(nm)^{-3.98146}$.

The overall error in the measurements of peak and integral σ_{O4} is the sum of contributions resulting from measurements of temperature and pressure, geometry, and corrections to spectra and are detailed in Table 1. The statistical error was either limited by (a) the spectra to spectra variability of the peak and integral σ_{O4} within a single sequence of gas fillings (usually accumulations of 30 seconds worth of scans) and is generally <1%; it was mostly found to be

limiting when using the Xe-arc lamp, and represents the precision in the method of background correction for light source drift as described earlier in this section, or (b) the variation in the peak and integrated σ_{O4} values between separate gas fillings during repeat runs; it represents the variability in temperature set points and the reproducibility of the cavity and is generally <3%, and was typically found to be limiting with the LED light sources (2-4%). The 3σ variability of peak and integral σ_{O4} within a single run is comparable to the variability between repeat measurements. For the reporting of data the 1σ variability (for n>2) or the range (n=2) for repeat runs are reported as the uncertainty.

3.3 Results

3.3.1 Absorption cross section spectra of O_4

The absorption cross-section spectrum of O_4 is shown in Figure 3.3, and compared to the literature cross-sections of Hermans (1999; 2010) and Greenblatt et al.(1990) Notably, the Hermans spectrum is recorded at much higher resolution (~0.02 nm FWHM), and should be directly comparable to our data. The spectrum by Greenblatt was recorded at 0.6 nm FWHM resolution, which is about five to 20 times better resolution than the line width of O_4 bands (see Table 2). Both spectra are compared here with no further treatment of the data. In this work bands at 340, 360, 380, 446, 477, 532, 577 and 630 were observed with signal to noise for most bands of >100. Our measurements show small differences when compared to Hermans, but much larger differences due to variations in the band shape with respect to Greenblatt that are illustrated in the top panel. Generally, we reproduce the spectral shape for Hermans within better than 5% for the stronger bands. Larger relative differences are found for the weaker O_4 bands near 446, as is shown in the inset of Figure 3.3. The residual wiggles that appear as differences to our spectrum are about 15 times larger than the 1-σ RMS noise in our data, and thus are highly

Table 3.1: Characterization of error sources

Error Description	Maximum Correction (%)	Relative error [a] (%)
Temperature inhomogeneity		0.3
Temperature measurement		0.75-2.0
Pressure measurement		0.1
Rayleigh Scattering Cross-sections		2
Oxygen mixing ratio (Air/O_2)		0.05/0.01
Cavity Length		0.6
Mirror Reflectivity Uncertainty		2.3
Self Limitation correction		
344 nm	<2	-
360 nm	<20	1-2.5
380 nm	<8	-
446 nm	<10	-
532 nm	<30	-
O_2 band subtraction		
580 nm	<0.1	-
630 nm	20	2.3
Baseline drift (offset correction)	1(630)-20(UV-343 nm)	1-3
Overall Error		2.7-4

[a]relative error is calculated after correction

significant. However, the larger differences are observed to the spectrum of Greenblatt et al. (1990), which shows clear indications for line broadening when comparing the bands at 360 nm, 380 nm, 477 nm, 580 nm and 630 nm. More broad (unstructured) differences are observed for the weaker bands at 344 nm, 446 nm and 532 nm.

The temperature dependence in the absorption cross-sections is illustrated for selected temperatures (200, 253 and 295K) in Figure 3.4. The differences between cross sections are plotted in the top panel (calculated as σ_{O4} (T) - σ_{O4} (295K)). The changes in band shape are observed for all bands at all temperatures studied. The peak cross section, band width and integrated cross section are tabulated for the individual bands and temperature studied in Table 3.2. As can be seen in Figure 3.4, the peak σ_{O4} increases with decreasing temperature for all bands and the changes in the peak σ_{O4} vary between 10 and 20% over the temperature range studied, for all bands. The two difference spectra in the top panel compare a change over 42K (253K, light blue line) with that over 50K (203K, dark blue line). While the first range is only ~25% larger, the σ_{O4} changes are 2 to 5 times larger at colder temperatures. Thus, changes in spectral band shapes of σ_{O4} are relatively minor at typical ambient temperatures, and down to temperatures below 253K.

The widths of the σ_{O4} bands are generally poorly described by fitting mathematical functions to represent the spectra (see discussion in Sneep et al. (2006)). As such we are listing the width in Table 3.2 as the FWHM, taking the half height on either side of the absorption band to determine the width. This width is observed to decrease with temperature for all bands. Similar findings had been reported for the 360, 477, 532, 577 and 630 nm bands in the literature (Greenblatt et al., 1990; Newnham and Ballard, 1998; Sneep and Ubachs, 2003; Sneep et al., 2006) while this is the first reported decrease in the width for the 380 and 446 nm bands.

Table 3.2 Results

Band	Temp (K)	Peak (nm)	Peak σ ($x10^{-46}$ cm^5 $molec^{-2}$)	Width (nm/cm^{-1})	Range (nm)	Integral σ ($x10^{-43}$ cm^4 $molec^{-2}$)
344 $^1\Sigma_g^+ + {}^1\Sigma_g^+$(v=2)	295	343.9	0.95(4)	3.21/272.2	339.8-	0.276
	273	343.85	0.95(4)	4.0/339.5	347.2	0.252
	253	344.0	0.98(4)	3.04/257.7		0.2.69
	233	343.95	1.07(4)	3.07/260.3		0.293
	213	344.0	1.13(4)	3.02/256.2		0.316
	203	344.0	1.20(4)	2.94/247.5		0.316
360 $^1\Sigma_g^+ + {}^1\Sigma_g^+$(v=1)	295	360.97	4.29(6)	4.3/332	349.5-	1.70(4)
	273		4.42(7)	4.07(3)/314(3)	368.0	1.64(5)
	253		4.58(7)	3.85(13)/296(14)		1.66(4)
	233		4.86(4)	3.75/289		1.65(4)
	213		5.12(20)	3.63(1)/280(1)		1.69(5)
	203		5.32(20)	3.63/280		1.76(10)
380 $^1\Sigma_g^+ + {}^1\Sigma_g^+$	295	380.32	2.43(3)	4.04(7)/279(5)	370.0-	7.5(2)
	273		2.56(8)	3.88(6)/268(4)	386.1	7.6(3)
	253		2.68(8)	3.71(3)/257(2)		7.5(3)
	233		3.1(2)	3.61(4)/249(3)		8.7(6)
	213		3.3(2)	3.42(2)/237(2)		8.7(5)
	203		3.5(3)	3.32(2)/229(1)		9.1(10)
446 $^1\Sigma_g^+ + {}^1\Delta_g$ (v=1)	293	446.52	0.520(20)	4.496/225.6	433.5-	0.14(1)
	273	446.43	0.552(5)	4.35/218.3	453.8	0.1532(2)
	253	446.53	0.53(2)	3.88/194.4		0.136(10)
	233	446.48	0.587(14)	3.93/196.8		0.151(1)
	213	446.43	0.618(23)	3.61/181.1		0.150(20)
	203	446.43	0.639(15)	3.6/180.6		0.150(30)
477 $^1\Sigma_g^+ + {}^1\Delta_g$ (v=0)	293	477.02	6.598(97)	5.39/236.68	459.4-	1.98(7)
	273	476.88	6.75(3)	5.37/235.86	487.6	2.02(4)
	253	476.88	6.91(4)	5.08/223.34		1.91(9)
	233	476.98	7.01(6)	4.66/204.73		1.89(3)
	213	476.83	7.36(3)	4.52/198.56		1.91(2)
	203	476.84	7.67(20)	4.04/177.62		1.92(1)
532 $^1\Delta_g + {}^1\Delta_g$ (v=2)	293	532.7(1)	1.09(6)	8.89/315.1	511.5-	0.378(1)
	273	532.7(1)	1.11(6)	8.58/303.8	544.3	0.385(40)
	253	532.9(1)	1.10(6)	8.26/292.5		0.364(50)
	233	532.7(3)	1.27(7)	7.97/282.1		0.398(20)
	213	532.8(1)	1.36(7)	7.48/264.6		0.400(33)
	203	532.8(3)	1.37(6)	7.31/258.6		0.408(23)
577 $^1\Delta_g + {}^1\Delta_g$ (v=1)	293	577.6	11.2(1)	11.2(2)/338(5)	552.0-	4.35(6)
	273	577.5	11.3(6)	10.82(3)/326.3(9)	595.0	4.25(1)
	253	577.7	11.5(1)	10.51(3)/316.8(10)		4.17(5)
	233	577.7	12.3(1)	9.99(3)/301.1(9)		4.26(5)
	213	577.7	13.2(1)	9.56(3)/288(1)		4.43(2)
	203	577.7	13.8(1)	9.25(5)/278.9(15)		3.51(2)

630 $^1\Delta_g + {}^1\Delta_g$ (v=0)	293	630.2*	7.11(2)	13.75/346.8*	600.0- 654.0	2.80(8)
	273	630.1	7.27(7)	13.25/334.0		2.79(8)
	253	630.0	7.44(30)	12.76/315.7		2.8(2)
	233	630.1	7.69(30)	12.48/314.7		2.74(10)
	213	630.1	8.1(3)	12.24/308.73		2.85(8)
	203	630.1	8.43(20)	12.00/302.5		2.94(5)

*Locations and widths for the 630 band are approximate due to oxygen subtraction.

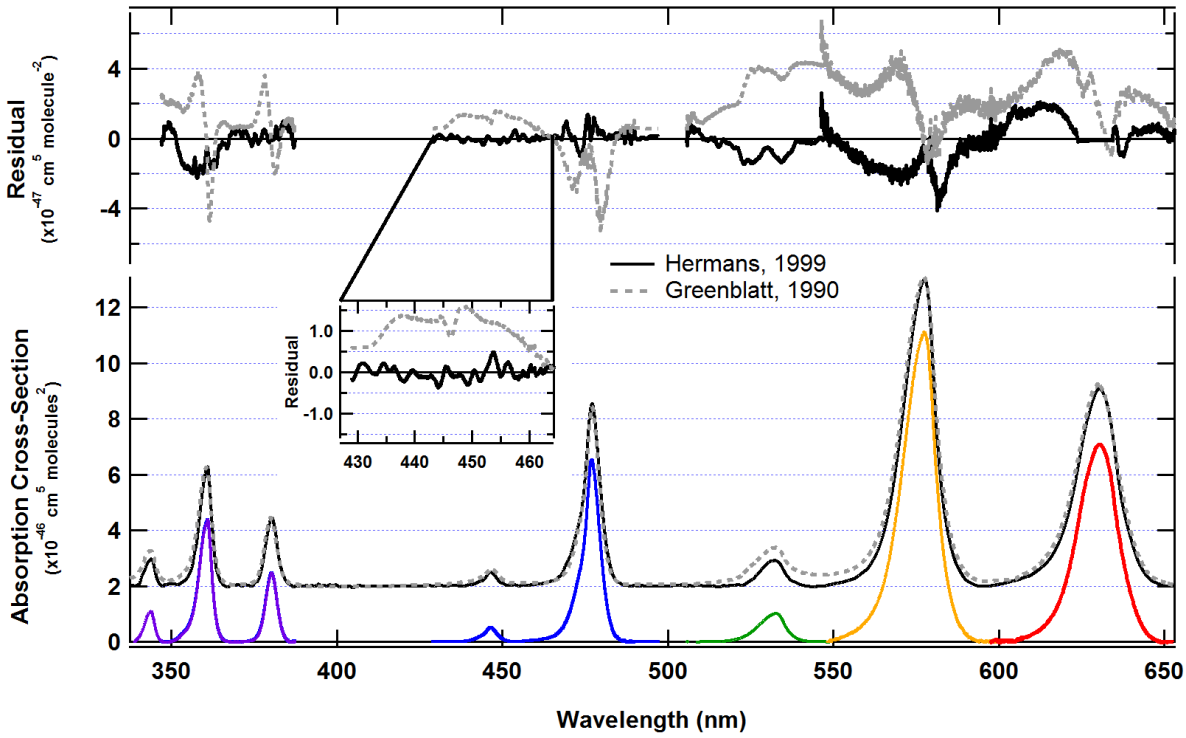

Figure 3.3: Comparison of O_4 absorption cross-sections to literature spectra at room temperature. For improved display the Hermans and Greenblatt cross-sections are offset.

Figure 3.5 illustrates the different behavior for the peak σ_{O4} and for the integrated σ_{O4} over any individual band for the 4 most prominent wavelengths relevant to DOAS measurements, and compares our data with literature values. A similar behavior is observed for all other bands that were studied. While the integral σ_{O4} scatters for all bands around a slope of zero (Figure 3.5, lower trace in all four panels), i.e., do not show any significant change with respect to temperature, the peak σ_{O4} increases with decreasing temperature as described above. Detailed values for each temperature are reported in Table 2. The lack of any significant temperature dependence in the integral σ_{O4} suggests that $O_{4\text{-dimer}}$ absorption does not contribute to the observed O_4 absorption over the range of temperatures investigated.

To corroborate this further, we have segregated our data for measurements in air and O_2. The similarity of data in air and O_2 is illustrated in Figure 3.6, where data from Table 3.2 have been renormalized and pooled for all wavelengths. First, for any given wavelength, the integral cross sections have been normalized to the average across all temperatures for this wavelength (grey symbols). The relative difference to this global average integral cross section was then plotted over temperature (grey symbols). Second, the normalized data from different wavelengths have been pooled at any given temperature according to (1) spectra recorded in air (dark blue), (2) O_2 (light blue), and (3) all data (black); measurements of 343, 380, 446 and 532 nm bands were in O_2, the 477, 577 and 630 nm bands in air, and the 360 nm band in both O_2 and air. The regression line equations for these data pools are (1) slope: -0.028±0.025; R^2 = 0.25 (2) -0.047±0.03; R^2=0.38, and (3) -0.023±0.02; R^2=0.24, respectively. In particular, no significant difference between air and O_2 is observed in the slopes, and slopes are further found compatible with zero (within 2-σ). More importantly, at the coldest temperature, the integral sigma difference in air is actually higher than that in pure O_2. We conclude that over the full range of

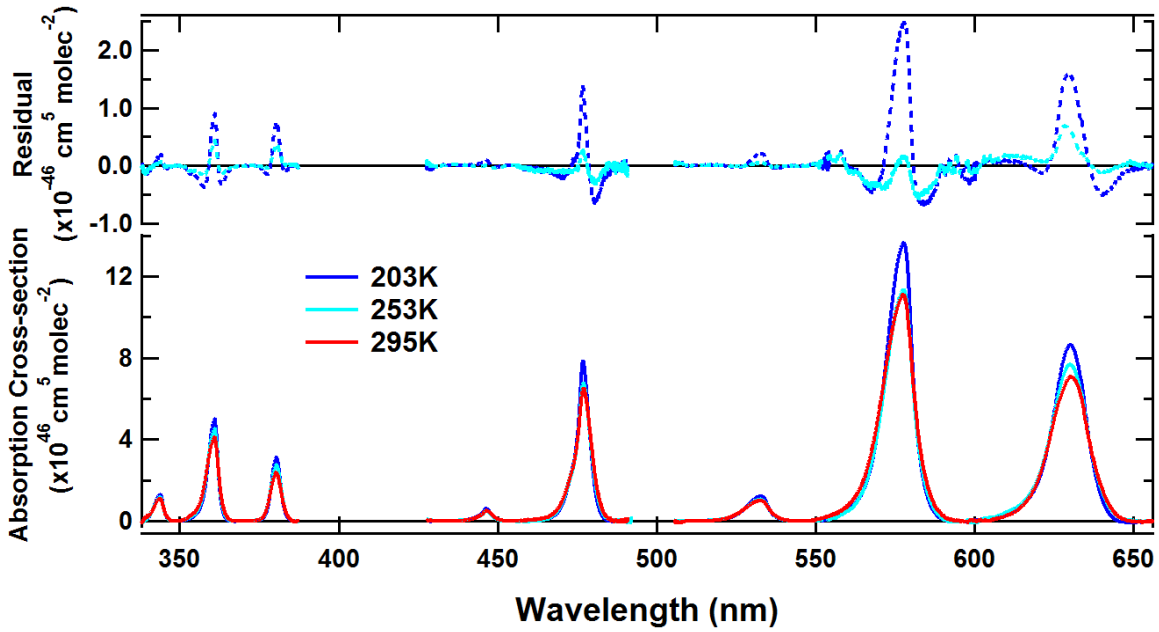

Figure 3.4: Temperature dependence of the band shapes at 295K, 253K and 203K. The 'difference' (top panel) is calculated as: $\sigma(T) - \sigma(295K)$.

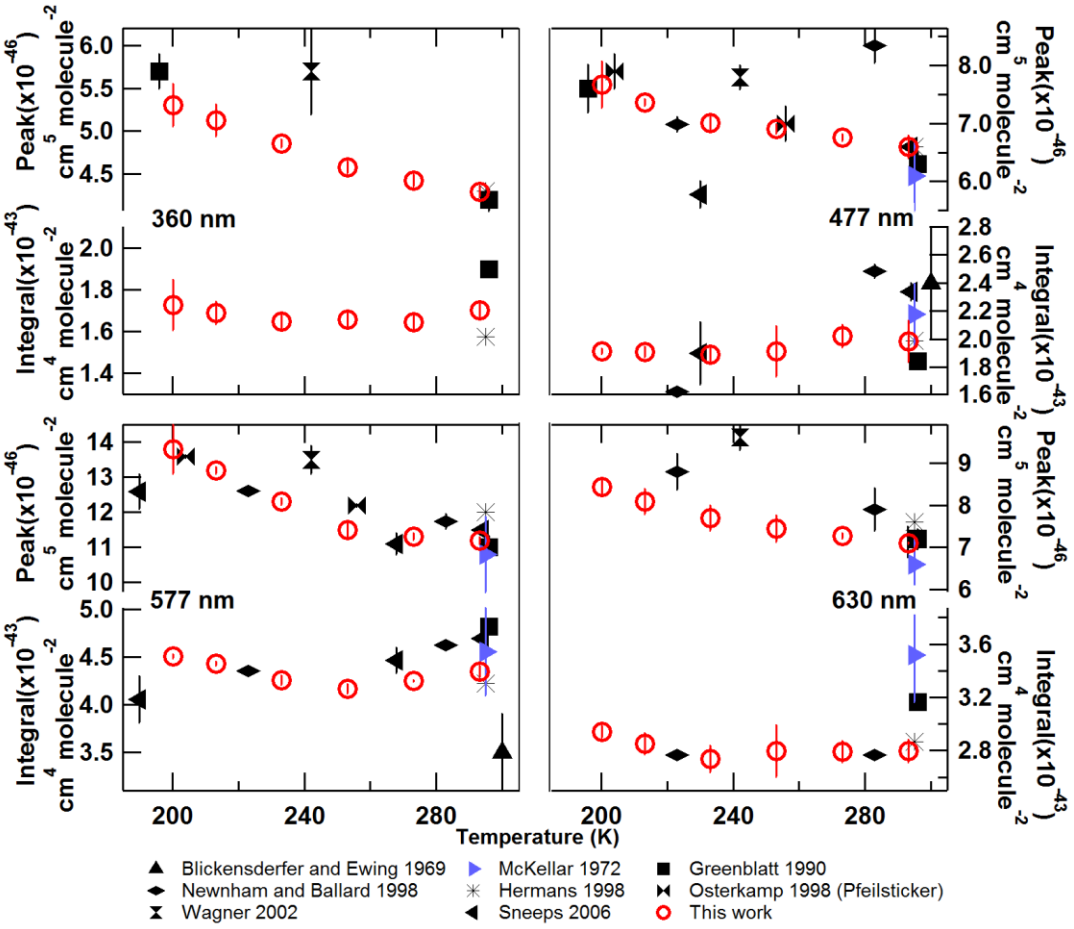

Figure 3.5: Comparison of peak and integral cross-sections to available literature values at four wavelengths.

temperatures, the maximum contribution of $O_{2\text{-dimer}}$ to the O_4 absorption is smaller 3% in both air and O_2. This lack of an apparent difference between data recorded in air and O_2 allows us to refine our conclusions about the relative importance of $O_{2\text{-dimer}}$ vs $O_{4\text{-CIA}}$ as contributors to O_4 absorption in the atmosphere (see Section 3.4.3). By solving the equation for the equilibrium, substituting the pooled and averaged integrated cross-sections for the equilibrium constant:

$$ln\left(K_{eq}(T)\right) = -\frac{<\Delta H>}{R}\frac{1}{T} + \frac{\Delta S}{R}, \quad (3.8)$$

The thermally averaged enthalpy of formation can be found from the slope of ln(σ) vs. 1/T. The results of this analysis yields a $\Delta H^{250} = -0.1_2 \pm 0.1_2$ kJ/mole.

3.4 Discussion

3.4.1 Comparison to Literature spectra

The reported values for our peak and integral σ_{O4} values compare within 5% of those reported by Hermans (2010) as well as Greenblatt et al. (1990) at room temperature. A selection of available literature values for peak and integral σ_{O4} at 360, 477, 577 and 630 nm are shown in Figure 3.5 (a complete listing of prior literature peak, integral σ_{O4} values as well as the widths of the bands is provided in Table A3.2 in Appendix A) (Salow and Steiner, 1936; Herman, 1939; Dianov-Klokov, 1964; Blickensderfer and Ewing, 1969; Tabisz et al., 1969; McKellar et al., 1972; Long and Ewing, 1973; Perner and Platt, 1980; Greenblatt et al., 1990; Volkamer, 1996; Pfeilsticker et al., 1997; Newnham and Ballard, 1998; Hermans et al., 1999; Naus and Ubachs, 1999; Tiedje et al., 2001; Wagner et al., 2002; Morville et al., 2002; Sneep and Ubachs, 2003; Sneep et al., 2006; Hermans, 2010). Prior studies in the atmospheric temperature range of 180-320K have observed the overall increase of peak σ_{O4} values with respect to temperature (Greenblatt et al., 1990; Pfeilsticker et al., 1997; Newnham and Ballard, 1998; Wagner et al., 2002; Morville et al., 2002; Sneep et al., 2006). Our work is consistent with this finding (Figure 3.5). It further reproduces

the change in peak σ_{O4} with respect to temperature within 5% for all bands investigated by Pfeilsticker et al, (1997) from atmospheric spectra (a digitized version of their Figure 3 is overlaid with the peak values of this work as Figure A3.1 in Appendix A). Notably, at the good temperature resolution of our measurements it becomes apparent that the band shape is increasingly distorted as temperature decreases. This change is more pronounced at lower temperatures than near room temperature, and corresponds to an increase in the peak σ_{O4} as is visible in Figure 3.6. The integrated σ_{O4} remains constant. See also the related discussion in Section 3.3, and Figure 3.4.

For a discussion of the comparison with room temperature spectra by Hermans and Greenblatt et al., see Section 3.3. Observations of the integrated σ_{O4} over this temperature range are less common (Greenblatt et al., 1990; Newnham and Ballard, 1998; Sneep et al., 2006). These previous studies for 477, 532, 577 and 630 nm show either no increase (Greenblatt et al., 1990; Newnham and Ballard, 1998) or a slight decrease (Sneep et al., 2006) in the integral band strength (Figure 3.5). Early studies at very low temperatures (87-113K) (Blickensderfer and Ewing, 1969; Tabisz et al., 1969; McKellar et al., 1972; Long and Ewing, 1973) observed a very large increase in both peak and integral σ_{O4} as well as extreme skewing of the band shape (especially the 477 nm band(McKellar et al., 1972)).

3.4.2 Van der Waals dimer vs. Collision induced absorption (CIA)

Previous studies (Long and Ewing, 1973; Johnston et al., 1984; Horowitz et al., 1989; Orlando et al., 1991; Biennier et al., 2000; Pfeilsticker et al., 2001) have used a variety of approaches to quantify ΔH^T of $O_{2\text{-dimer}}$, and estimate the equilibrium constant (Johnston et al., 1984). Aquilanti et al. conducted molecular beam experiments and observed the angular dependence of molecular scattering of oxygen at cold rotation temperature (~12 K) and a value of -1.64±0.1 kJ/mole for

the bond energy of lowest energy configuration and -1.14 ± 0.08 kJ/mole for the average of all configurations (Aquilanti et al., 1999a; Aquilanti et al., 1999b). Long and Ewing (Long and Ewing, 1971; 1973) were first to report a value of ΔH^0 = -2.2±0.3 kJ/mole from the increase in the integral of rotational absorptions on top of the collision induced oxygen bands at 6.2μm. Significant $O_{2\text{-dimer}}$ absorption was only observed at temperatures below 100 K (Orlando et al., 1991). A similar study by Orlando et al. (1991) yielded a value of ΔH^{290} = -4.6±2 kJ/mole for temperatures between 225 – 356 K. Horowitz et al. (1989) observed the decrease in ozone formation from oxygen photolysis at 214 nm, and determined a value of ΔH^{342} = -0.8 ± 1.6kJ/mole. Pfeilsticker et al. (2001) reported observations of the change in the peak absorption of O_4 bands (360 nm to 630 nm) in the atmosphere by balloon-borne DOAS measurements over the temperature range of 200 – 295 K (average temperature = 248 K). The authors inferred ΔH^{248} = -1.20 ± 0.08kJ/mole which 'should be understood as representative of the atmospheric conditions rather than as a characteristic of the truly bonded dimer' (Pfeilsticker et al., 2001). Notably, the authors observed no change in the spectral band-shape of O_4 with temperature (see Section 3.4.3). Observations of non-zero values of ΔH^T at temperatures above 200K(Orlando et al., 1991; Pfeilsticker et al., 2001) are currently taken as evidence for a weak temperature dependence of O_4 in the atmosphere. Our value of $\Delta H^{250} = -0.1_2 \pm 0.1_2$ kJ/mole is zero within measurement uncertainty, and consistent with previous studies that found negligible ΔH^T at temperatures above 100K,(Horowitz et al., 1989) and confirm previous observations that suggest no dimer is formed at temperatures above 100K (Long and Ewing, 1971; Long and Ewing, 1973; Greenblatt et al., 1990; Aquilanti et al., 1999a; Aquilanti et al., 1999b; Aquilanti et al., 2002).

Greenblatt et al. (1990) noted that their observed change in the integrated σ_{O4} due to $O_{2\text{-dimer}}$ was smaller than expected based on the ΔH^0 reported by Long and Ewing (1973); indeed

they observed no change in the integrated σ_{O4} with ±15% uncertainty (360, 380 and 477 nm bands). Our data confirm these findings with lower error. The integrated σ_{O4} does not increase by more than 3% in neither air, nor O_2 (see Section 3.3.1, and Figure 3.6) despite $O_{2\text{-dimer}}$ formation should be ~22.78 times more pronounced in O_2 over air. From this we conclude that $O_{2\text{-dimer}}$ contributes less than 0.13% to the O_4 absorption at 203K in air.

Our data confirms the previous conclusions reached by Greenblatt et al. (1990) and Sneep et al. (2006), that in O_2 and at moderately warm temperatures the UV-visible absorption bands of O_4 are not significantly influenced by $O_{2\text{-dimer}}$, and support their assignments of O_4 bands as CIA (Ellis and Kneser, 1933). We conclude that $O_{2\text{-dimer}}$ is not observable in the atmosphere. As a consequence, atmospheric predictions of the O_4 vertical profile only depend on air density, and can be predicted with very small uncertainty ~10^{-3}. Knowledge about how O_4 is distributed in the atmosphere is hence primariliy limited by the accuracy at which air temperature, pressure and humidity (as it affects the oxygen partial pressure) are known.

3.4.3 DOAS reference spectra

The weak temperature dependence of spectral band shapes near the upper range of temperatures that we have probed suggests that our room temperature spectrum is representative of the atmospheric O_4 absorption also at temperatures well above those found in the atmosphere. Only a limited volume of the atmosphere actually experiences colder temperatures than we have probed. Notably, the tropical free troposphere or the polar atmospheres during winter can experience slightly lower temperatures than those that were probed here.

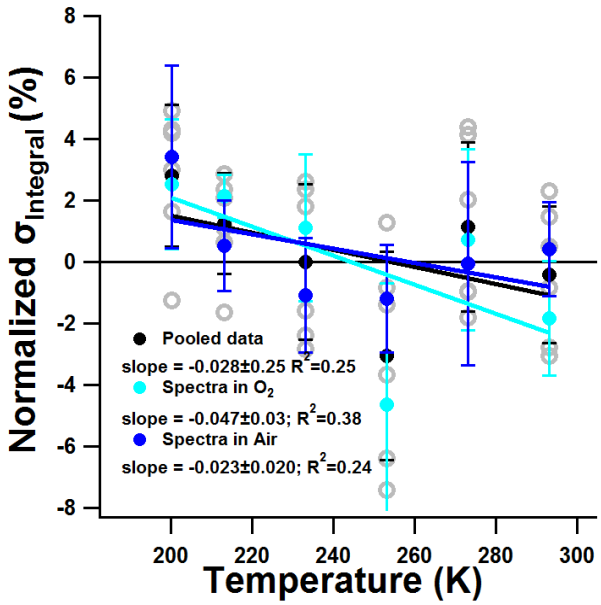

Figure 3.6: The normalized integral cross section is independent of temperature in O_2 and air. Grey symbols reflect normalized data from Table 2 that is pooled for (1) spectra recorded in air (dark blue; 360, 477, 577 and 630 nm bands), (2) O_2 (light blue; 343, 360, 380, 446 and 532 nm bands), and (3) all data (black). Regression lines show no significant difference between air and O_2, and slopes are compatible with zero (within 2σ).

The band shape change is particularly relevant at colder temperatures typical of airborne DOAS applications, or in polar atmospheres. Assuming a constant band shape leads to errors in measured O_4 slant column densities as high as 20% at the lowest possible atmospheric temperatures (Pfeilsticker et al., 2001). Accounting for temperature effects of spectral band shape now allows eliminating this uncertainty. We recommend including two O_4 cross section spectra of different temperatures for simultaneous fitting as part of the DOAS least-squares analysis. The respective temperatures of the two O_4 reference spectra should be chosen to bracket the range of atmospheric temperature extremes, and be fitted simultaneously to represent the actual temperature as a linear combination of both temperature extremes. In this way, systematic residual structures can be minimized, and accurate O_4 SCD measurements be made with errors of few percent under most conditions.

The optical resolution of our O_4 spectra is generally about 10-30 times better than the width of the observed spectral features (compare Table A3.1 with Table 3.2). As such we believe that our spectra can be considered as 'fully resolved', i.e., provide reference spectra that can easily be adopted to any DOAS instrument by convolution with the respective instrument line function, and over the full range of atmospherically relevant temperatures.

3.5 Conclusions

Absorption cross-section spectra of O_2-O_2 collision pairs (O_4) have been measured for 8 O_4 bands in air and O_2, at six temperatures (i.e., 203, 213, 233, 253, 273, and 293K), and at ambient pressure. The accuracy of the line strength is better 3% for most bands, and limited in part by our knowledge of the Rayleigh cross sections of N_2 (and He) that limit knowledge of our mirror curve. Our measurements combine (i) high signal-to-noise O_4 spectra ($60<S/N<1000$), (ii) small temperature variations through the optical cavity ($\Delta T<0.3K$ for all temperatures), and (iii)

temperature controlled polychromatic light sources (Light Emitting Diodes for most bands) to assess effects of temperature on the spectral band shape. The accuracy in our wavelength stamp is ±0.01 nm.

We conclude:

1. Changes in the spectral band shapes are observed for all bands, and visible for all pairs of temperatures investigated. For the same temperature increment, these changes become disproportionately larger in spectra recorded at temperatures below 253K. However, the integrated absorption cross section is independent from temperature to within 3% over the full range of temperatures investigated. Even at 203K no indications are found for additional absorption from bound Van der Waals complexes ($O_{2\text{-dimer}}$).
2. Near room temperature, the absorption cross section and band shape of Hermans (1999) was reproduced within 5% for the stronger O_4 bands. At σ_{O4} below $6x10^{-47}$ $cm^5/molec^2$ we observe larger differences (up to 20% for the weaker band at 446 nm).
3. Our measurements confirm previous findings (Greenblatt et al., 1990; Newnham and Ballard, 1998; Sneep et al., 2006) that the integrated σ_{O4} is independent of temperature with ~ 5 to 10 times higher accuracy. We provide first measurements of the lack of a temperature dependence for the O_4 bands at 446 and 630 nm that had not previously been reported.
4. O2-dimer is not observable in the Earth atmosphere. Our determination of $\Delta H^{T>200K}$ being essentially zero with very little error implies that $O_{2\text{-dimer}}$ is not observable at atmospheric temperatures. We estimate that the O_4 vertical profile scales with an error better 10^{-3} with air density in the atmosphere.

Future theoretical studies might benefit from the changes we have observed in spectral band shapes, which seem to indicate that long-range collision interactions between two O_2 molecules extend well beyond 1 nm (distance between O_2 molecules). The optical resolution employed in our work (~0.3 nm FWHM) -while sufficient to resolve the studied O_4 bands- is insufficient to provide a good correction of O_2 bands near 628 nm [$b^1\Sigma_g^+(\upsilon'=2) \leftarrow X^3\Sigma_g^-(\upsilon''=0)$]. The representation of these bands in the HITRAN database (Rothman et al., 2006) was found to insufficiently remove the observed O_2 absorption, and limits our analysis of the spectral band shape for O_4 at 630 nm. Future studies of these weak O_2 bands at higher optical resolution seem feasible under atmospheric conditions by means of optical cavities, and will be beneficial to improve the HITRAN database, and confirm the approximate band shape reported for this O_4 band.

Chapter IV

4 Investigation of Rayleigh Scattering Cross-section for use by Optical Cavity Methods

4.1 Introduction

As discussed briefly in the chapters 2 and 3, Rayleigh scattering by gases, is an important part of the total attenuation of incoming solar radiation. The theory and measurements of the scattering of gases has been studied for well over a century (Strutt, 1899) and explains the blue color of the sky. The interaction of light (electromagnetic fields) with a wavelength much larger than the size of a molecule gives rise to the scattering of light. The combined effect is known as Rayleigh scattering and accounts for scattering, local field effects (Lorentz-Lorenz (Strutt, 1920)) as well as depolarization from the non-sphericity of particles (King correction factor (Strutt, 1918; King, 1923)).

The cross-section for Rayleigh scattering can be calculated based on the refractive index of the gas as follows:

$$\sigma(\nu) = \frac{24\pi^3\nu^4}{N^2}\left(\frac{n_\nu^2-1}{n_\nu^2+2}\right)^2 F_k(\nu), \tag{4.1}$$

where ν is the wavenumber of light (cm^{-1}), N is the density (molecules cm^{-3}) and n_ν is the wavenumber dependent refractive index and F_k is the King correction factor which accounts for the depolarization. Detailed derivation and explanation of the different influences on the scattering can be found elsewhere in the literature (Bates, 1984; Bodhaine et al., 1999; Naus and Ubachs, 2000; Sneep and Ubachs, 2005; Eberhard, 2010).

While measurements of the different components of scattering (correction factors, refractive index) have been performed for the better part of a century (Strutt, 1920; Cuthbertson and Cuthbertson, 1932; Abjean et al., 1970a; Abjean et al., 1970b; Leonard, 1974) laboratory measurements of the scattering cross-section are limited (Shardanand and Rao, 1977; Naus and Ubachs, 2000; Sneep and Ubachs, 2005).

Rayleigh scattering cross-section measurements in the literature have been carried out in two ways: (1) direct measurement of scattering using a nephelometer based technique and integrating the scattering signal over all wavelengths (Shardanand and Rao, 1977) and (2) cavity-ring down spectroscopy (CRDS) measurements of the change in extinction by the decay of pulsed light in a high-finesse optical cavity due to scattering with change in pressure (Naus and Ubachs, 2000; Sneep and Ubachs, 2005). The work from Shardanand and Rao is the only work of its kind and set a baseline for calculations of Rayleigh scattering cross-sections from theory. Unfortunately, the reported values towards the ultra-violet show significant deviation from theory and have a high uncertainty (±11%). CRDS measurements leverage the sensitivity of high finesse cavities to retrieve the scattering cross-section at pressures of 1-100% of ambient pressure. The CRD measurements agreed very well with refractive index based theoretical calculations (within 1%) over the range investigated (479-650 nm).

In more recent years the Rayleigh scattering of pure gases is important to the calibration of cavity-enhanced methods as they rely on the absolute scattering cross-sections to understand the mirror reflectivity, in particular helium and nitrogen and then secondly in the calculation of extinction (Eq. 3.5). Recent work by Washenfelder et al. (2013) used exponential expressions to represent the scattering cross-section by fitting to the experimental data. With the limited number of data available in the literature, interpolation of the cross-section between points in the range of 350-480 nm can lead to systematic bias and large uncertainty.

In this chapter we establish the use of broad-band cavity enhanced spectroscopy for the measurement of *relative* Rayleigh scattering cross-sections with wavelength coverage from 350-700 nm as well as use cavity ring-down spectroscopy at 532 and 405 nm to extend the available *absolute* Rayleigh scattering cross-sections towards shorter wavelengths.

4.2 Experimental

4.2.1 Calculations of refractive index based Rayleigh scattering

4.2.1.1 Helium

The scattering cross-sections of the gases investigated (He, N_2, O_2, Ar and Air) were calculated with Eq. (4.1) based on the data for refractive index available in the literature. For He data from (Cuthbertson and Cuthbertson, 1932; Abjean et al., 1970a; Leonard, 1974) is fitted to the expression ($\nu(cm^{-1})$):

$$(n-1)\times 10^8 = 2283 + \left(\frac{1.8102\times 10^{13}}{1.5342\times 10^{10} - \nu^2}\right) \quad (4.2)$$

over the range of $33333 > \nu > 14285$ cm^{-1}, with a King correction factor equal to 1 for a monatomic gas.

4.2.1.2 Nitrogen

The refractive index of N_2 was calculated from Eq. (4.1) and the expression given in (Bates, 1984) and converted from microns to wavenumbers by Sneep et al. (2005) for the range of 21360 < ν < 39370 cm^{-1}:

$$(n-1)\times 10^8 = 5677.465 + \left(\frac{318.81874\times 10^{12}}{14.4\times 10^9 - \nu^2}\right) \quad (4.3)$$

and 4860 < ν < 21360 cm^{-1}:

$$(n-1)\times 10^8 = 6498.2 + \left(\frac{307.4335\times 10^{13}}{14.4\times 10^9 - \nu^2}\right) \quad (4.4)$$

With a depolarization King correction factor of (Bates, 1984; Sneep and Ubachs, 2005):

$$F_k(\nu) = 1.034 + 3.17\times 10^{-12}\nu. \quad (4.5)$$

4.2.1.3 Oxygen

The Rayleigh scattering cross-section of O_2 was calculated from Eq. (4.1) and the expressions for refractive index and the King correction factor given in Bates (1984) (wavenumbers, ν(cm^{-1})):

$$(n(\nu)-1)\times 10^8 = 20564.8 + \left(\frac{2.480899\times 10^{13}}{4.09\times 10^9 - \nu^2}\right) \quad (4.6)$$

$$F_k(\nu) = 1.096 + 1.385\times 10^{-11}\nu^2 + 1.448\times 10^{-20}\nu^4. \quad (4.7)$$

For oxygen a density at 273 K and 1013 mbar should be used to calculate the scattering cross-section, which varies from that used for the other gases (288 K, 1013 mbar).

4.2.1.4 Argon

The Rayleigh scattering cross-section of Ar was calculated from Eq (4.1) and the expression for the refractive index given by Bates (1984) in the form given by Naus and Ubachs (2000) and King correction factor of 1 (for frequency in wavenumbers):

$$(n-1)\times 10^8 = 6432.135 + \left(\frac{286.06021\times 10^{12}}{14.4\times 10^9 - \nu^2}\right). \quad (4.8)$$

4.2.1.5 Air

The Rayleigh scattering cross-section of air was calculated from the expressions given in Bodhaine et al. (1999) from the refractive index and mixing ratio weighted King correction factors for N_2, O_2, Ar and CO_2.

4.2.2 Measurements of N_2 Rayleigh scattering by CRDS

The Rayleigh scattering cross-section of N_2 was measured by CRDS using a similar technique as described in the work of Naus and Ubachs (2000) and Sneep and Ubachs (2005), though the measurement was made at discreet wavelengths of 405.8 nm and 532.2 nm where CRDS cells were already in use (mirrors- Advanced Thin Films). The density in the cells was controlled by placing a pump and restriction downstream of the cavities and changing the restriction to adjust the pressure to fixed levels between 80 and 100 percent of ambient pressure (Boulder , CO; 630 Torr). The fitted slope of the loss rate (1/(τc)) in cm^{-1} vs. the density (molecules cm^{-3}) is the Rayliegh scattering cross-section (in cm^{-2}). The error is taken as the distribution of retrieved cross-sections between all runs.

4.2.3 Measurements of Ar, O_2 and Air Rayleigh scattering by BBCEES

The Rayleigh scattering cross-sections of Ar, O_2 and air were measured by Broad-Band Cavity Enhanced Extinction Spectroscopy (BBCEES) by first measuring the mirror reflectivity as a function of wavelength:

$$R(\lambda) = 1 - d_0 \frac{\left(\frac{I_{N_2}(\lambda)}{I_{He}(\lambda)}\alpha_{Ray}^{N_2}(\lambda)\right) - \left(\alpha_{Ray}^{He}(\lambda)\right)}{1 - \left(\frac{I_{N_2}(\lambda)}{I_{He}(\lambda)}\right)} \quad (4.9)$$

and using the following equation written for the measurement of the O_2 Rayleigh scattering cross-section:

$$\alpha_{Ray}^{O_2} = \left(\left(\frac{1-R(\lambda)}{d_0}\right)\left(1-\frac{I_{O_2}}{I_{N2}}\right)+\alpha_{Ray}^{N2}\right)\left(\frac{I_{N2}}{I_{O_2}}\right) \quad (4.10)$$

where $\alpha_{Ray}^{O_2}$ is the extinction due to Rayleigh scattering by O_2 (or N_2), R(λ) is the mirror reflectivity with respect to wavelength, *I* is the intensity of the spectrum in each gas, and d_0 is the cavity length. Dividing this quantity ($\alpha_{Ray}^{O_2}$, the extinction) by the density of the gas yields the Rayliegh scattering cross-section. This measurement is done relative to the known value of the N_2 Rayleigh scattering cross-section and the mirror curve (*R*, measured based on the scattering of He and N_2, Eq. 4.9). It is not an independent measurement of the absolute Rayleigh scattering cross-section as it is measured with CRD. The advantage of this approach is the ability to measure at many wavelengths simultaneously and with good wavelength coverage.

Measurements were performed using cavities with centers and reflectivities of 365 (0.99985), 405 (0.99995), 455 (0.999972), 532 (0.99998), 580 (0.999978) and 630 nm (0.99993) (See Table A3.1). O_2 and air scattering was retrieved at wavelengths in between the O_4 absorption bands (see Chapter 3). Spectra were recorded with an Acton 2300i spectrometer using a PIXIS 400b CCD detector (see Chapter 2 for details of the spectrometer system).

4.3 Results

4.3.1 Helium

Comparison of the one set of literature values (Shardanand and Rao, 1977) for He are compared to the theory in Figure 4.1 along with the empirical exponential fit to the data (Washenfelder et al., 2013) and the deviation from the theory of both the data as well as the fit to the data

[(experimental-theory)/theory]. The fit to the available data does a good (<5% variation) job of representing the theory as the measured data scatters around the theory line.

4.3.2 Nitrogen

The results of the CRDS measurements of the N_2 Rayleigh scattering cross-section are shown along with the relevant literature data and n-based theory calculations in Figure 4.2. The agreement of the measurement at 405 nm is within 1% of the theory. Shown in the figure are the available data from the literature (Shardanand and Rao, 1977; Naus and Ubachs, 2000; Sneep and Ubachs, 2005) as well as the deviation of the exponential fits of Naus and Ubachs (2000). This fit is representative over the range it was fit (500-700 nm) but begins to diverge from the theory at shorter wavelengths. The fit by Washenfelder et al. (2013) to the data of Bodhaine et al. (1999) deviates widely from the refractive index based calculation.

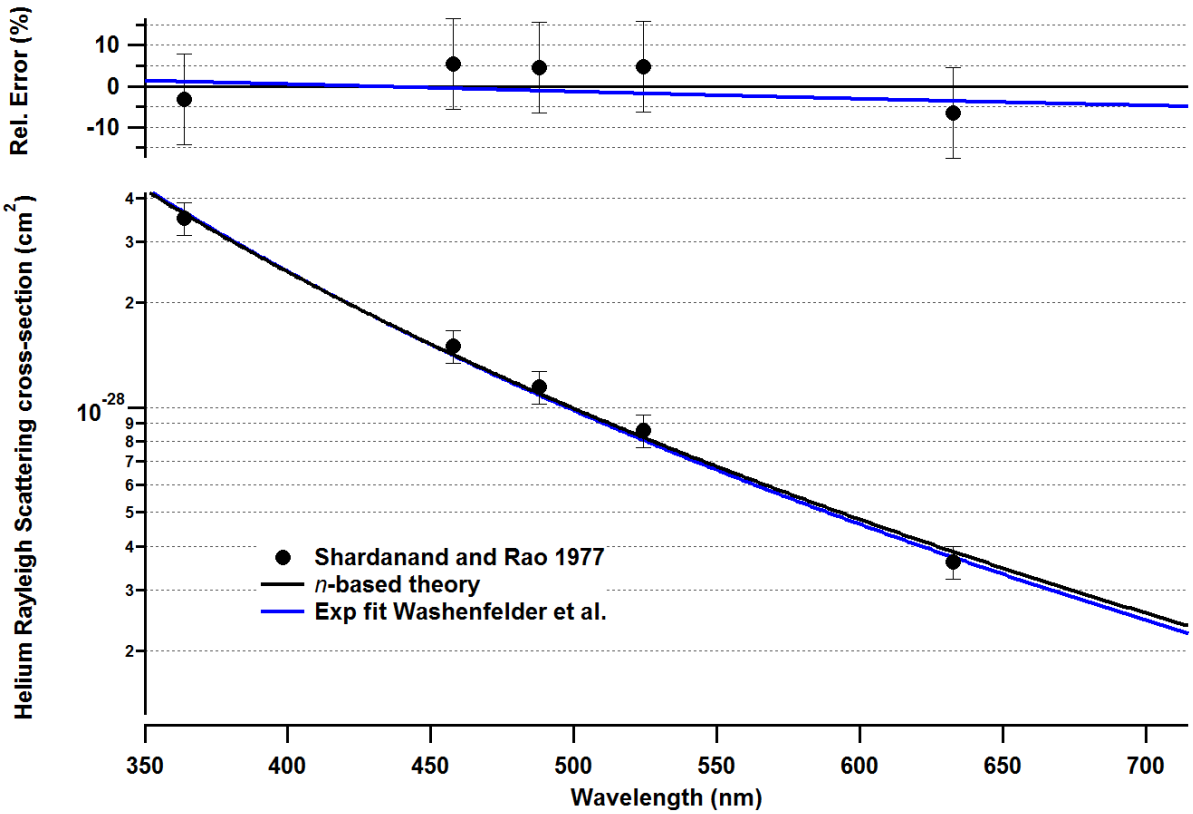

Figure 4.1: Rayleigh scattering cross-section of He. Top panel shows the deviation of the measurements and fitted expressions to that of the *n*-based theory.

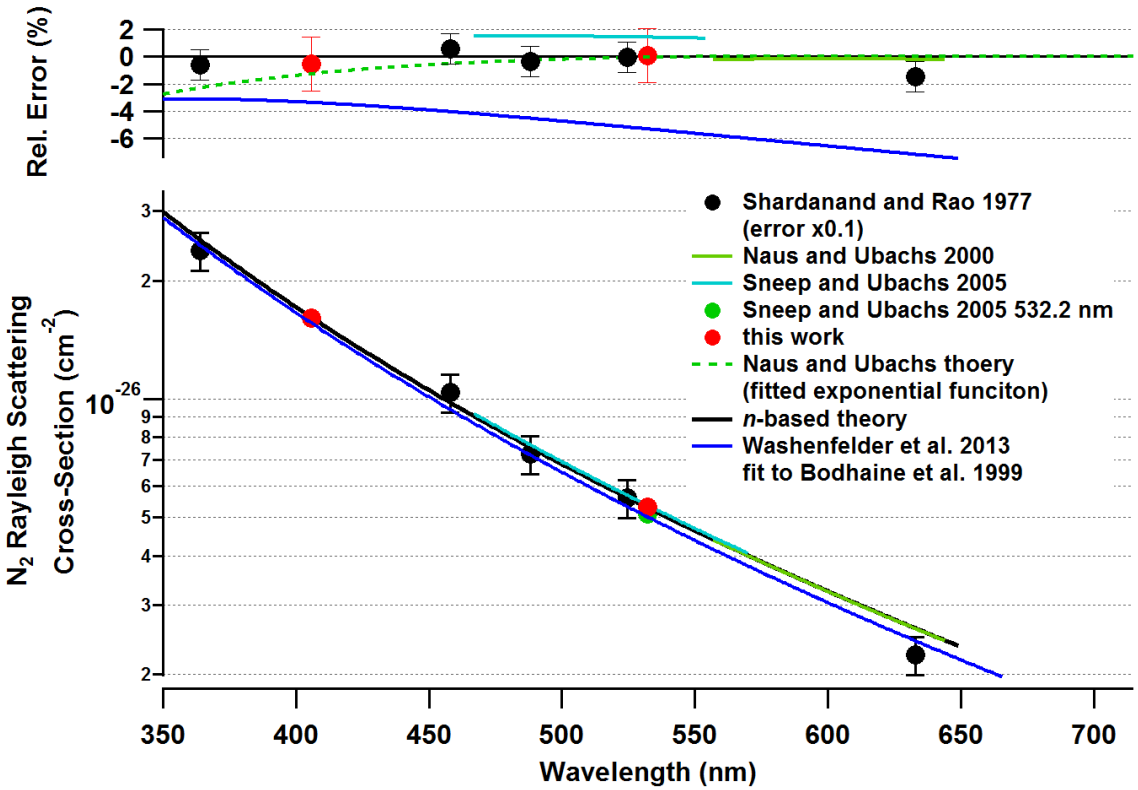

Figure 4.2: Rayleigh scattering cross-section of N_2 from 350 to 700 nm measured by CRDS compared with theory and literature values.

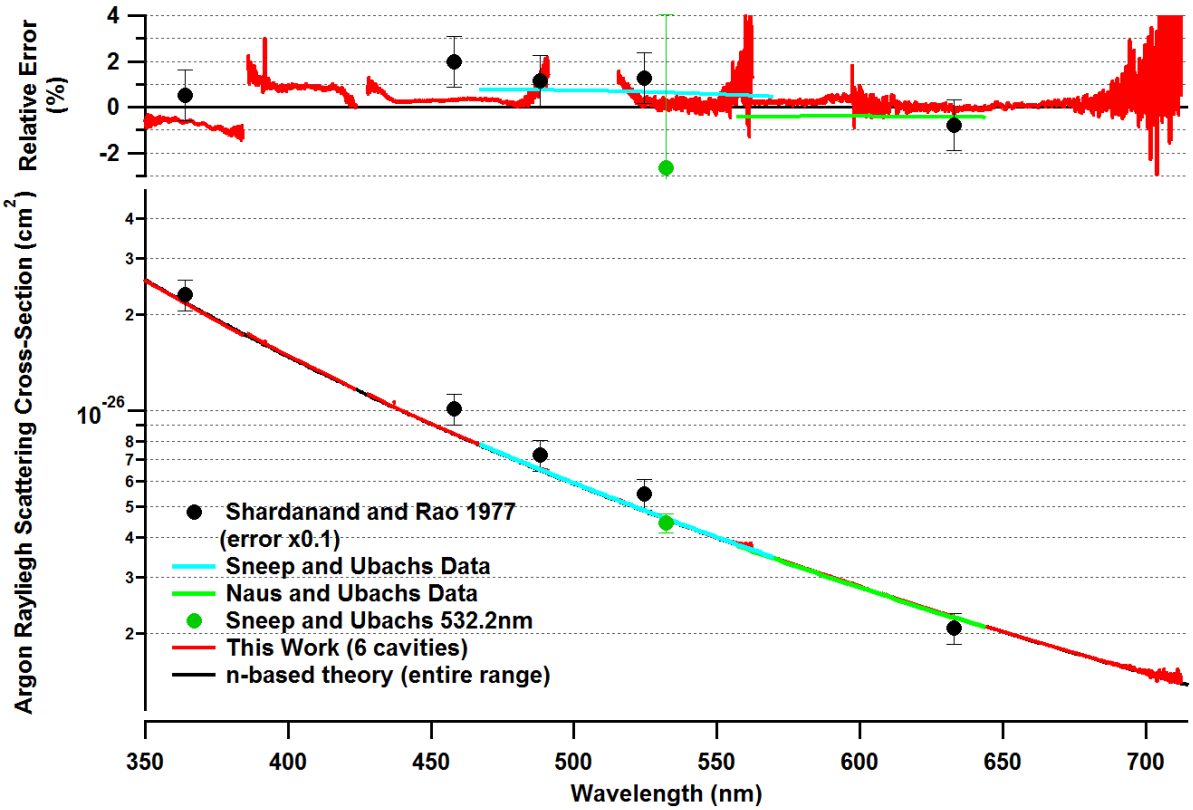

Figure 4.3: Rayleigh scattering of Ar from 350 to 700 nm measured by BBCEES compared with theory and previous literature values.

4.3.3 Argon

The results of the BBCEES measurements of the Ar Rayleigh scattering cross-section are shown along with the literature data and n-based theory from 350-700 nm in Figure 4.3. The BBCEES measurements are within 1% of the theory for all but the shortest wavelengths and cover nearly the entire wavelength range. The variability near the edges of the mirrors (and light sources) can be observed for each set of mirrors.

4.3.4 Oxygen

Measurements of the O_2 Rayleigh scattering cross-section are displayed in Figure 4.4 along with the literature data and theory calculation. Data is only used between the O_4 absorption bands from 370 – 660 nm. The *n*-based theory is consistent with the measurements as well as the reported theory value in Sneep and Ubachs (2005).

4.3.5 Air

Measurements of the air Rayleigh scattering cross-section are displayed in Figure 4.5 along with the theory calculations as given by Penndorf (1957) and Bodhaine et al. (1999). Reported data is from the windows in between the O_4 absorption bands.

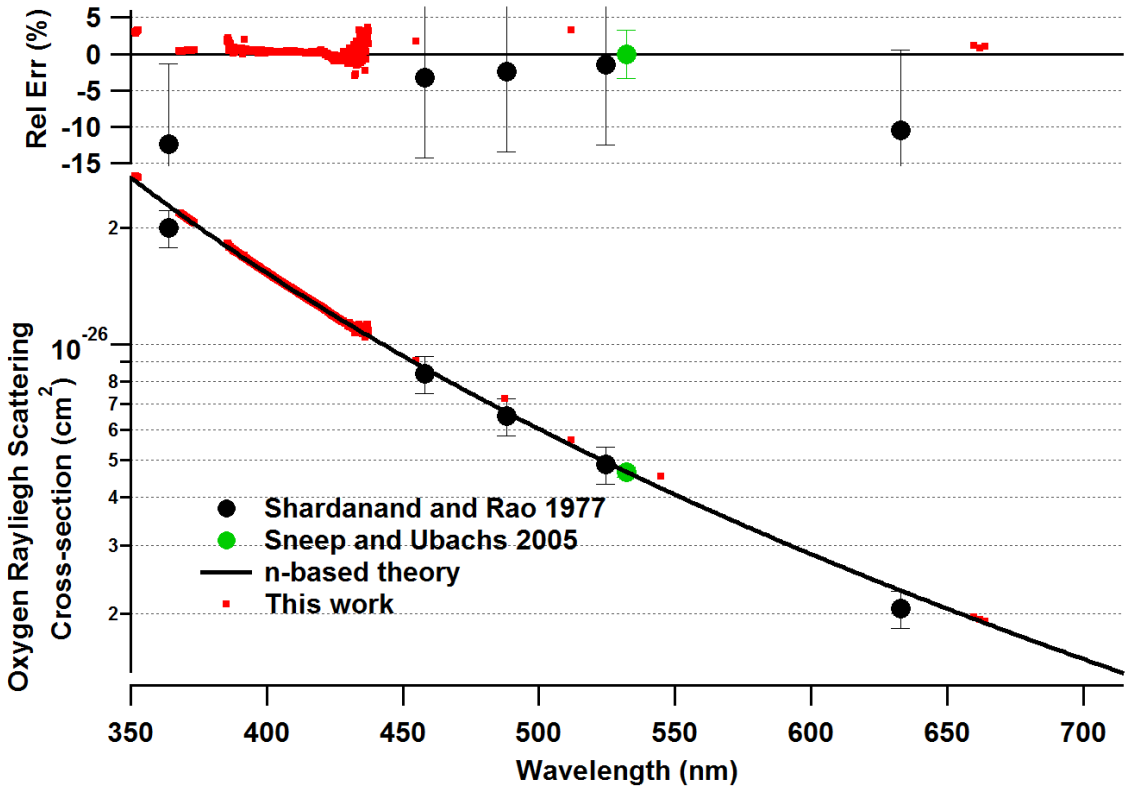

Figure 4.4: O_2 Rayleigh scattering cross-section measured by BBCEES compared to previous measurements in the literature and the theory.

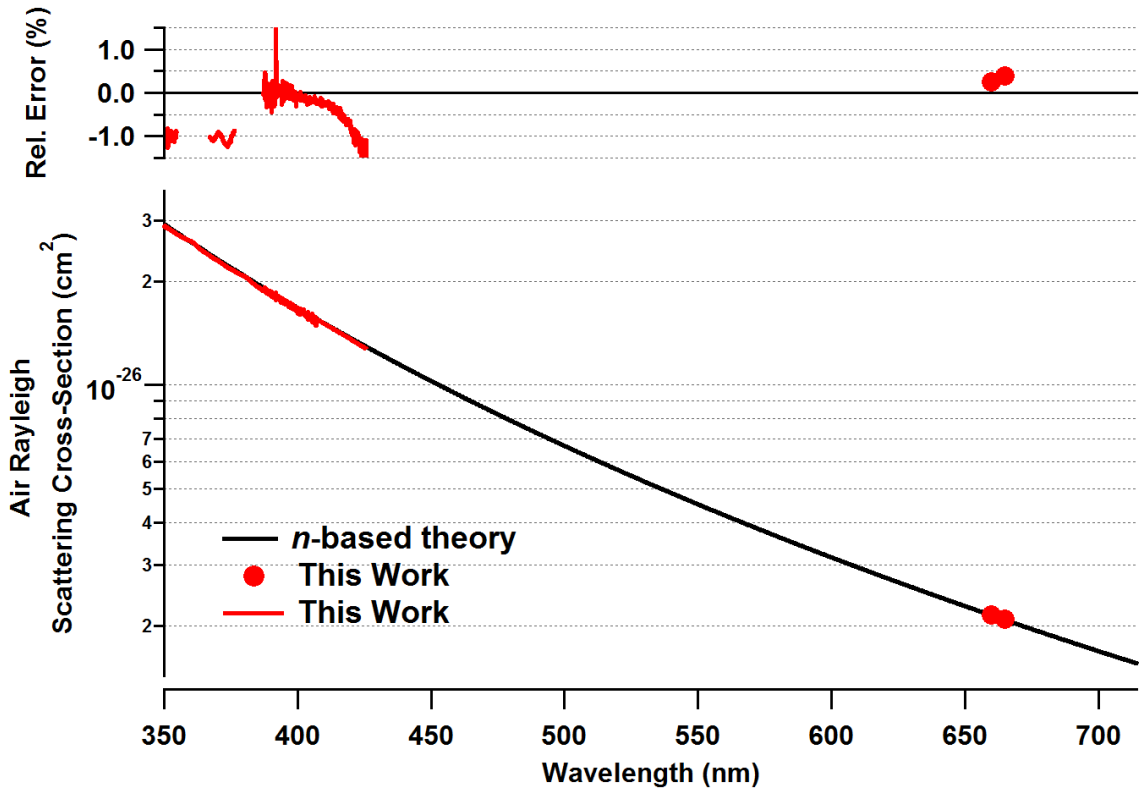

Figure 4.5: Air Rayleigh scattering cross-section measured by BBCEES compared to theory.

4.4 Discussion and Conclusion

The measurements of Rayleigh scattering cross-sections by Broad-Band Cavity Enhanced Extinction Spectroscopy (BBCEES) were able to retrieve the values for Ar, O_2 and air relative to N_2 within 1-4% of refractive index based theory calculations. The previous measurements for He compare favorably to theory but are not represented well by exponential fits to the available experimental data. Although the uncertainty in the He Rayleigh scattering cross-section contributes only a small portion of the error since the extinction due to He is subtracted in the mirror reflectivity equation (Eq. 4.9). Further measurements of the Rayleigh scattering cross-section of He by CRD at wavelengths from 355 to 532 would be a valuable addition to the available literature. A 1% bias in the Rayleigh scattering cross-section translates directly to 1% bias in the mirror reflectivity and in the path length.

The measurements of the N_2 Rayleigh scattering cross-section by cavity-ring down spectroscopy (CRDS) agree within 2% with n-based theory and extends the validation of the theory down to 405 nm in the range where Rayleigh scattering represents a dominant attenuation of solar radiation (the range where ozone absorption is at a minimum). Measurements of the Ar and air Rayleigh scattering cross-sections referenced to the *n*-based theory values show some variability from theory below 450 nm, but still within 1-4% and mostly less than 1%. Measurements of the O_2 Rayleigh Scattering cross-section agree well with theory and are consistent with the refractive index based values. The refractive index calculations match those reported in Shardanand and Rao (1977). Measurements in the UV had lower sensitivity (lower R mirrors, see Table A3.1) and are subject to more interference from lamp intensity drifts and structure variability.

Cavity enhanced measurements rely on the knowledge of the Rayleigh scattering cross-sections of the various gases as their primary calibration and are the largest contributing errors in the calibration of the mirror reflectivity. As such it is important to use the correct and most accurate values for the scattering as possible or the instrument will be subject to measurement bias from its calibration. These updated measurements:

1. Give confidence in the theory to replicate the measured values and allow for the calculation of the scattering to calibration these cavity enhanced techniques.
2. Show the use of BBCEES can provide wavelength resolved data of Rayleigh scattering in a single measurement at a single density relative to a reference gas. The relative retrieval of Ar also serves as a verification of the mirror reflectivity calculation.
3. Highlight the importance of using correct values for Rayleigh scattering for the calibration of cavity enhanced spectroscopy techniques.
4. Extend the range of agreement with theory for the Rayleigh scattering of Ar, air and O_2 into the UV range with very good uncertainty, where only one set of measurements has been done previously.

Chapter V

5 Instrument Inter-comparisons at Chambers

5.1 Introduction

The performance of LED-CE-DOAS was tested against a variety of other instruments as part of two inter-comparison experiments. The first took place as part of a series of experiments at the National Center for Atmospheric Research (NCAR) environmental chamber investigating isoprene oxidation chemistry during the springs of 2011 and 2012. The second was a European Union Eurochamp funded formal inter-comparison for the measurement of alpha-dicarbonyls (glyoxal and methyl glyoxal) that took place in Valencia, Spain at the EUropean PHotoREactor (EUPHORE) chamber in June and July 2011.

The purpose of an inter-comparison is to compare the response, linearity, accuracy and precision of instruments that measure similar compounds using a variety of techniques (optical absorption spectroscopy, fluorescence, phosphorescence, mass spectrometry, or chromatography) with common samples. These exercises provide the opportunity to compare techniques from different research groups and around the globe and to discuss and form a common language for discussing limits of detection, accuracy and precision.

5.2 NCAR Chamber Experiments

5.2.1 Experiment Description

Experiments were carried out in the National Center for Atmospheric Chemistry (NCAR) atmospheric simulation chamber. The chamber consists of a stainless steel cylinder (~47L) connected to a Fourier transform infrared spectrometer. This set up has been previously described in the literature (Shetter et al., 1987; Orlando and Tyndall, 2002) (Figure 4.1). The chamber was chilled by circulating ethanol to cool the chamber to 260K or heated (320K) by circulating water. Small yield products of the oxidation mechanisms were probed by proton transfer mass spectrometry (PTR-MS, both quadrapole and time of flight instruments) (Jordan et al., 2009), Gas Chromatography (Hasson et al., 2012) and Light Emitting Diode Cavity Enhanced Differential Optical Absorption Spectroscopy (LED-CE-DOAS) (Thalman and Volkamer, 2010) instruments provided by groups at NCAR and the University of Colorado. For each experiment the chamber was over-pressurized and sample was leaked from the chamber through a valve and divided to each instrument (experiments with GC detection were performed separately). The flow (5 sccm for CE-DOAS and 25 sccm for the PTRs) out of the chamber was controlled by mass flow controllers (MKS) or stationary Teflon valves. These small flows were then diluted and delivered to each instrument. The sample flow and dilution varied for each specific experiment (2.5-25 sccm from the chamber into 500 sccm). For hot and cold temperature experiments the temperature of the chamber was allowed to equilibrate after the gases were added and before the reactions were initiated.

The sample delivery to the PTRs and CE-DOAS were validated through a series of instrument comparison experiments where compounds were measured simultaneously by FT-IR and the PTR and CE-DOAS. Glyoxal was added by oxidation of acetylene in the chamber by

either Cl (formed by the photolysis of Cl_2) or OH in the presence of NO (formed from the photolysis of isopropyl nitrite ($CH_3CH(ONO)CH_3$) by a filtered Xe arc lamp). Methyl glyoxal was produced by the oxidation of hydroxyacetone with Cl radicals and measured by FT-IR, CE-DOAS and PTR. The experiments served as an additional comparison for the measurement of hydroxyacetone by FT-IR and PTR. Calibration for glycolaldehyde was accomplished by the oxidation of 2-methyl-3-buten-2-ol (MBO) in the presence of NO_x. Comparison of the PTR and FT-IR for isoprene was done during regular experiments. The response of the GC was calibrated directly using the FT-IR.

5.2.2 Results

Comparison of the LED-CE-DOAS and PTR-MS instruments to the FT-IR standards was carried out with experiments at each temperature to check sampling losses for glyoxal and methyl glyoxal. Any instrument offsets have been subtracted (residual from sample lines or mass flow controllers) to compare the slope of the instrument response. The instruments compared very well at room and higher temperatures as shown by the correlation plots in Figure 5.2).

5.2.3 NCAR Summary

The CU-LED-CE-DOAS instrument performed excellent in comparison to the NCAR FT-IR and the PTR-MS. In particular the ability to quantitatively transfer the compounds of interest between the chamber and the instrument were validated even when sampling dry air containing glyoxal and methyl glyoxal through a mass-flow controller. In addition good agreement (±5%) was seen between instruments using absorption cross-sections in different wavelength ranges (UV-vis and infrared).

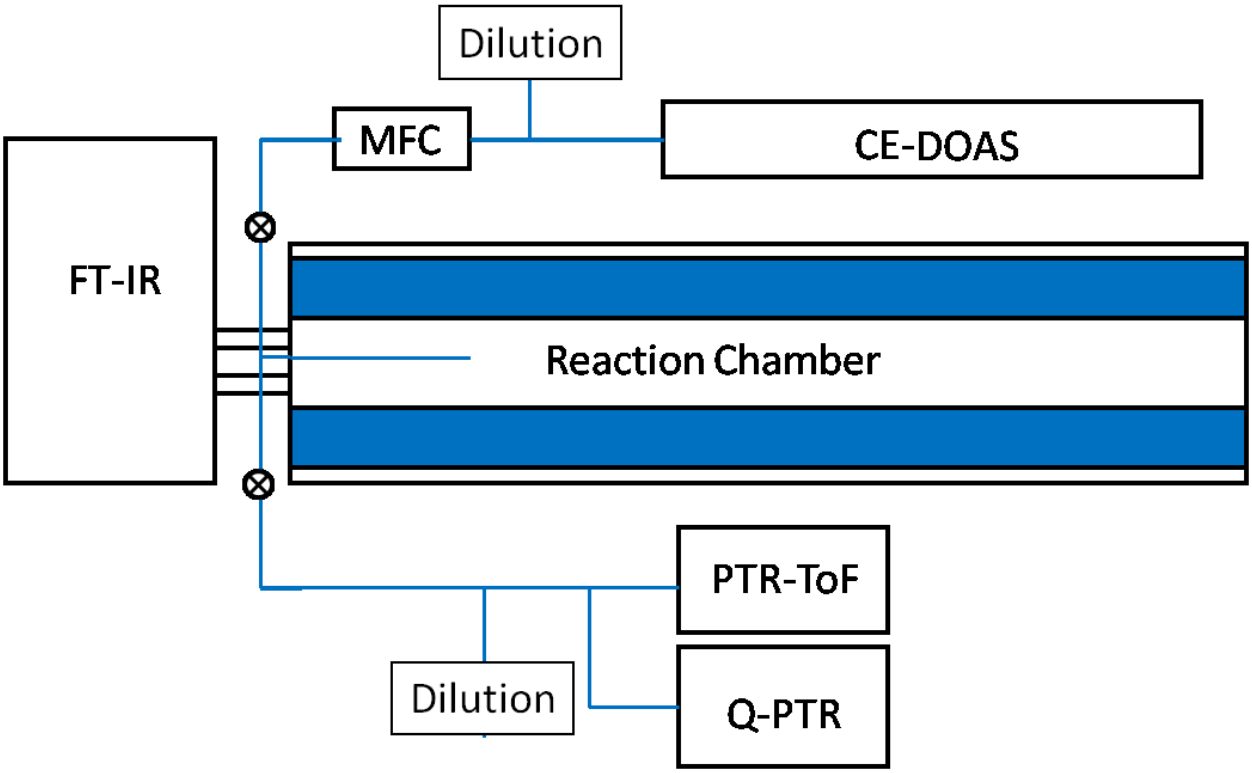

Figure 5.1: Scheme of chamber and instruments set up for NCAR intercomparison. The FT-IR light path passes through the reaction chamber while both CE-DOAS and PTR instruments sample flows from the chamber after dilution.

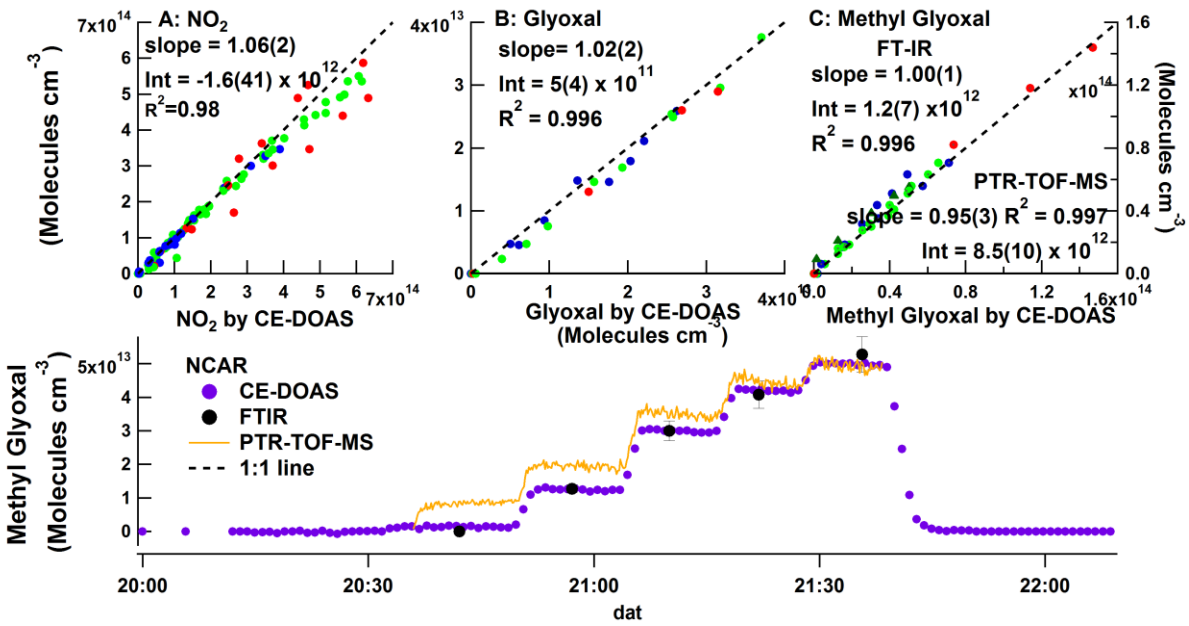

Figure 5.2: Correlation plots for NCAR inter-comparison for all species of interest in isoprene oxidation experiments.

5.3 EUPHORE

Recent developments in techniques for the detection of glyoxal and methyl glyoxal prompted an instrument inter-comparison at the EUPHORE chamber at the Centro de Estudios Ambientales del Mediterraneo (CEAM) in Valencia, Spain sponsored by the EUROCHAMP-2 program. The project entitled AlDiIn (Alpha-Dicarbonyl Inter-comparison) involved groups from England (University of Leeds- Aerosol Time of Flight Mass Spectrometer; University of Leicester- BBCEAS (Langridge et al., 2008a) and PTR-MS), the University of Wisconsin- Madison (Laser-Induced Phosphoresence (Mad-LIP) (Huisman et al., 2008)) and the University of Colorado (LED-CE-DOAS (Thalman and Volkamer, 2010)) along with the host institution (FT-IR, White-cell UV-Vis DOAS (W-DOAS) and solid-phase micro-extraction (SPME)). Detailed descriptions of the instruments can be found in Table 5.2. A variety of experiments were conducted to test the range, stability and interferences of the various techniques. Data from the various groups was worked up separately and then analyzed to compare between the respective instruments. Experiments also explored the interferences of NO_2 or O_3 in spectral retrievals as well as the possible production/loss of compounds in sample lines.

5.3.1 Experiment Description

The EUPHORE facility consists of a pair of 200 m^3 hemispherical Teflon enclosures with retractable roofs to allow for ambient illumination of the chambers for radical production. Figure 5.3 shows the layout of the chamber including the locations of the various instrument sampling ports, gas injection and circulation. The experiments consisted of 2 day of glyoxal injection and dilution into the chamber, a day of methyl glyoxal injection and one day using the oxidation of o-xylene to produce glyoxal, methyl glyoxal as well as biacetyl (Butane-2,3-dione, $CH_3C(O)C(O)CH_3$) in the presence of NO_x along with ambient sampling. Detailed descriptions of all EUPHORE experiments can be found in Table 5.3.

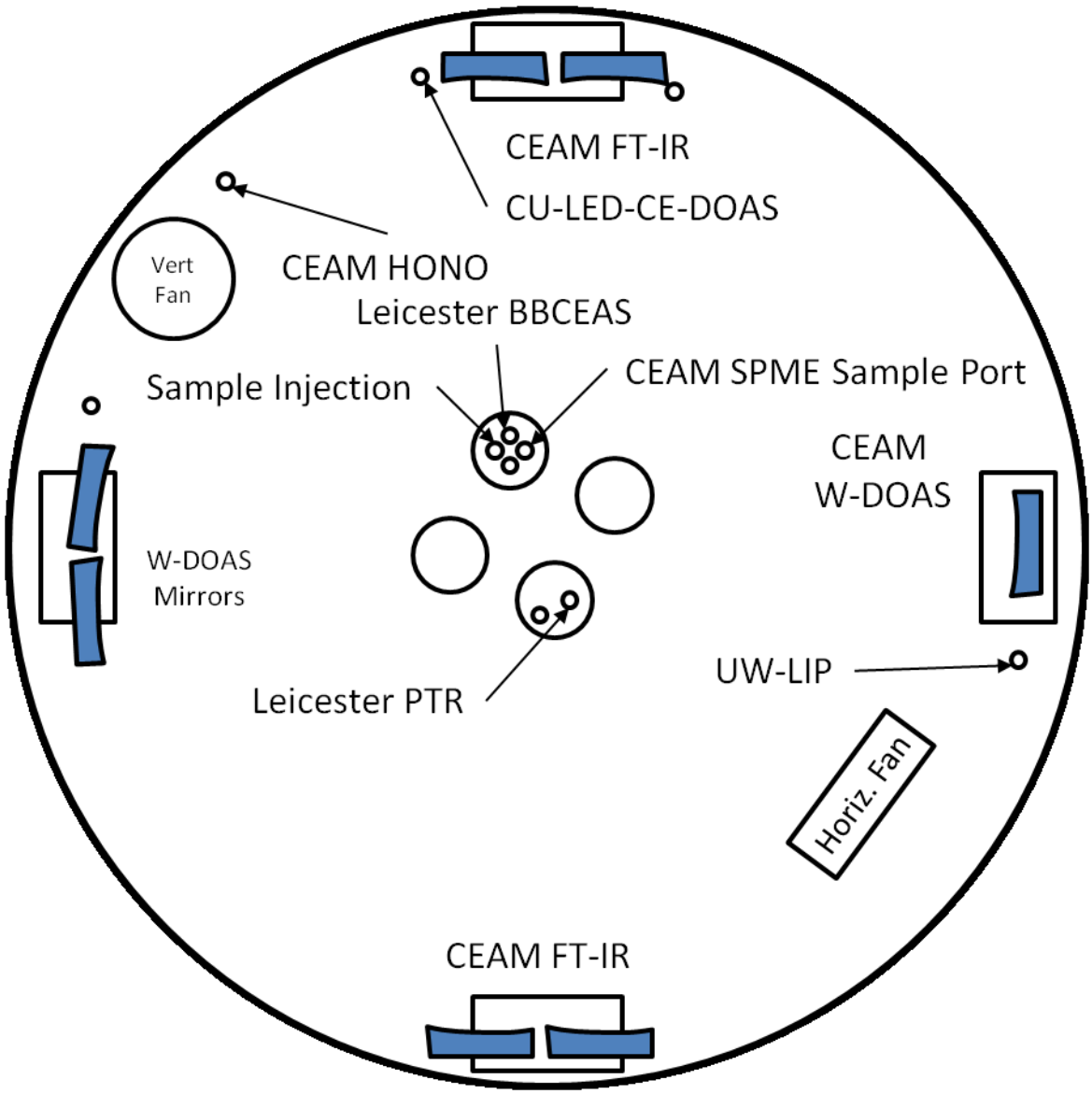

Figure 5.3: Layout of instruments at EUPHORE. Small circles are sampling ports while the FT-IR and White-cell DOAS light paths cross the entire chamber.

Table 5.1 Instrumentation and parameters at NCAR and EUPHORE

Instrument [a]	Participant	Location	Measured Species [b]	LODs [c]	LODs [d]	Measured quantity	Sample location	Time resolution (min.)
CE-DOAS	University of Colorado Boulder, USA	NCAR/ EUPHORE	G ,M , N	0.015/ 0.15	0.004/ 0.09	[e]	Outside Edge	1
FTIR	NCAR, USA	NCAR	G ,M , N	-	-	[e]	-	4
ToF-PTR-MS	NCAR, USA	NCAR	M	-	-	[m]	-	0.3
Q-PTR-MS	NCAR, USA	NCAR	M	-	-	[m]	-	0.3
BBCEAS	University of Leicester, UK	EUPHORE	G, M, N	0.025/ 0.35	0.015/ 0.21	[e]	Center of Chamber	1
PTR-ToF-MS	University of Leicester, UK	EUPHORE	M	-/0.53	-	[m]	Outside Edge	1
Mad-LIP	University of Wisconsin - Madison, USA	EUPHORE	G, M	0.044/ 0.43	0.013/ 0.29	[e]	Outside Edge	1
White-cell DOAS	CEAM, Spain	EUPHORE	G, M, N	0.4/ 6.0	0.10/ --	[e]	Inside	1.5
FTIR	CEAM, Spain	EUPHORE	G, M	2.5/ 2.7	0.37/ --	[e]	Inside	10
SPME with GC-FID detection	CEAM, Spain	EUPHORE	G, M	0.1/ 0.15	-	[m]	Outside Edge	10

[a] Abbreviations given in the text; [b] G - glyoxal, M - methyl glyoxal, N – NO_2; [c] Reported Detection Limits (ppbv, Glyoxal/Methyl Glyoxal); [d] Experimentally Determined (ppbv Glyoxal/Methyl Glyoxal); [e] Concentration (molecule cm^{-3}); [m] Volume mixing ratio referenced to temperature and pressure of the chamber as measured in the chamber.

Table 5.2: Description of EUPHORE AlDiIN Inter-comparison Experiments

Exp #	Date	Experiment Name	Description
1	24 Jun 11	Glyoxal Inter-comparison	Injection of 40 pbbv of glyoxal followed by dilution to 10's pptv
2	27 Jun 11	Methyl Glyoxal Inter-comparison	Injection of 20 ppbv of methyl glyoxal followed by dilution to 100 pptv
3	28 Jun 11	O_3 + o-xylene	Chamber (Teflon) plus ozone and line residence times; followed by generation of products from the oxidation of o-xylene.
4	29 Jun 11	Isoprene, High NO_x	In-situ generation of products of isoprene oxidation under high-NOx conditions
5	30 Jun 11	O_3 + C_2H_2	In-situ generation of glyoxal from the reaction of OH+ acetylene in the presence of ozone
6	1 Jul 11	Ambient Air	Ambient Air filling the chamber followed by addition of glyoxal/methyl glyoxal
7	4 Jul 11	Isoprene, NO_x Control	Repeat of Exp 4 with NOx control and lower initial isoprene to keep at lower NOx levels
8	5 Jul 11	Glyoxal Inter-comparison	Repeat of Exp 1
9	6 Jul 11	Glyoxal Inter-comparison	Addition of 10-200 ppbv of NO_2 on top of ~300 pptv glyoxal
10	6 Jul 11	Methyl Glyoxal Inter-comparison	Repeat of Exp 9 with the addition of 10-200 ppbv of NO_2 on top of ~5 ppbv methyl glyoxal

[a] experiments with injection of glyoxal or methyl glyoxal
[b] Experiments with in-situ production of glyoxal/methyl glyoxal

All visiting (non-CEAM) instruments sampled from the chamber via sampling ports and some variability in measured concentrations around the injection of compounds could be expected. All optical instruments (CE-DOAS, BBCEAS, FT-IR, Mad-LIP and W-DOAS) were calibrated based on the absorption cross-sections for glyoxal (Volkamer et al., 2005c), methyl glyoxal (Meller et al., 1991), and NO_2 (Vandaele et al., 2002). The Mad-LIP instrument phosphorescence signal was calibrated using a cavity-ring down cell and standards for glyoxal and methyl glyoxal. The FT-IR is calibrated by scaling the measured signal to the concentration measured by the W-DOAS instrument. The SPME-fiber (extracted and measured with GC-FID) was calibrated with the CEAM FT-IR and is thus an indirect measurement in this comparison.

5.3.1.1 CE-DOAS Analysis

Analysis of CE-DOAS spectra was performed for the retrieval of glyoxal, methyl glyoxal, NO_2 and O_4 as described in Chapter 2 except in the case of Exps. 1, 9 and 10. In Exp. 1 very high (~40ppbv) glyoxal causes path-length self limitation for glyoxal (see chapter 2 section 2.3.2) concentrations of glyoxal were retrieved in two ways: (1) interpolation of cross-sections bounding the absorption range or (2) fitting of the weak absorption structures in the wavelength range 458.5-475nm (where the normal glyoxal fit window is 435-465 nm). For Experiments 9 and 10 an NO_2 residual is fitted to account for systematic structures arising from extremely high NO_2 concentrations leading to a more stable retrieval of the glyoxal or methyl glyoxal concentration.

5.3.2 Results

5.3.2.1 Glyoxal, Methyl Glyoxal and o-Xylene Experiments

The data from all instruments was analyzed by the individual groups and then correlations were calculated with respect to CE-DOAS between each pair of measurements for the EUPHORE experiments. Individual data points were averaged to the longest time interval of any given pair (see Table 5.1) and data points from injection periods were filtered out. Correlations were calculated in IGOR Pro (Wavemetrics) using the optimal distance regression (ODR) and optimizing for both uncertainty in X and Y data.

Results from the experiments 1,2,3, 9 and 10 (24, 27 and 28 of June and 6 of July 2011) were compared for all instruments for NO_2 (W-DOAS, BBCEAS and CE-DOAS), glyoxal (FT-IR, SPME, W-DOAS, Mad-LIP, BBCCEAS and CE-DOAS) and methyl glyoxal (FT-IR, SPME, W-DOAS, Mad-LIP, BBCCEAS and CE-DOAS). The various instruments are also compared with respect to interferences from the first three experiments as well as experiments 9 and 10. Summaries of CE-DOAS data for all experiments as well as chamber parameters (temperature, pressure and RH) as found in Figures A5.1-A5.22 in the Appendix.

The experiments conducted on 24 June and 5 July, 2011 (Experiments 1 and 8) consisted of the injection of glyoxal into the chamber and dilution to several levels of glyoxal in the chamber. Correlation plots of the high and low concentration data are shown in Figure 5.4 (Figure A5.23 in the appendix shows an additional timeseries plot for Experiment 1). The data for the two experiments has been pooled and is shown in Table 5.4 (the correlation data for each day can be found in Tables A5.1 and A5.2 in the Appendix). Experiment 9, carried out on July 6, 2011 highlighted the possible interference of large amount of NO_2 with detection of glyoxal for instruments using visible (430-490 nm) light spectroscopy. In this experiment the Mad-LIP was

used as the standard or unaffected instrument against which the CE-DOAS and BBCEAS were evaluated. Figure 5.5 shows the time series of glyoxal and NO_2 concentrations in the chamber for the various instruments as well as the instrument uncertainty which increases with NO_2 concentration for most of the instruments. The bias created by the NO_2 is quantified in Table 5.4.

Experiment 2, conducted on 27 June 2011 was used for the comparison of all instruments for the measurement of methyl glyoxal. Up to 25 ppbv of methyl glyoxal was injected into the chamber and diluted in 6 discreet steps and then finally down to less than 1 ppbv. Figure 5.6 shows the high and low concentration correlation plots (Timeseries plots are shown in Figure A5.24 in the Appendix). Table 5.6 contains the results of the cross-correlation calculations. Experiment 10 conducted on 6 July 2011 tested the interference of NO_2 on methyl glyoxal detection by increasing NO_2 levels in the chamber up to 200 ppbv on top of several ppbv of methyl glyoxal. Figure 5.7 shows the time series of the methyl glyoxal and NO_2 data. In this experiment the FTIR is used as the baseline "unaffected" instrument and the calculated interference is recorded in Table 5.4 for CE-DOAS and BBCEAS.

Data from Experiment 3, the oxidation of o-xylene by OH in the presence of NO, is shown in Figure 5.8 (Additional time-series plots can be found in Figure A5.25 in the Appendix). The experiment progression is shown in the bottom set of panels for products and reactants measured by the FT-IR and for the products measured by the other instruments. Correlation plots for NO_2 (plotted relative to W-DOAS), glyoxal (relative to CE-DOAS) and methyl glyoxal (relative to CE-DOAS). Some variability is shown for NO_2 between the three visible absorption measurements which is likely attributable to gradients in the formation/loss of NO_2 within the chamber and the proximity of some instruments to the edge of the chamber (CE-DOAS) while the roof was open.

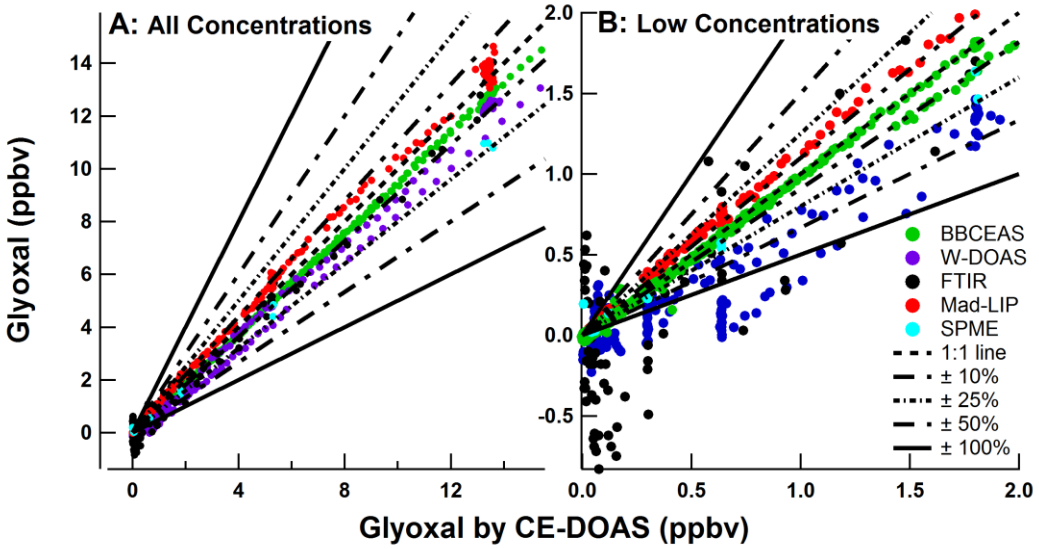

Figure 5.4: Glyoxal correlation of individual instruments versus CE-DOAS for the experiment conducted at EUPHORE on 5 July 2011. Panel A shows the full range of measured concentrations while Panel B shows only those measured concentrations below 2 ppbv.

Table 5.3: Correlation data for glyoxal pooled from 24 June and 5 July 2011 [a]

Y↓ X→	CE-DOAS	BBCEAS	Mad-LIP [d]	FT-IR [b]	W-DOAS	SPME
CE-DOAS						
Slope	-	1.035(2)	1.1(2)	1.01(1)	1.090(4)	1.13(8)
Int[c]		0.006(1)	-0.04(2)	0.17(8)	0.07(1)	0.003(10)
R^2		0.9997	-	0.997	0.9996	0.991
BBCEAS						
Slope	0.966(2)	-	1.1(2)	0.965(9)	1.046 (1)	1.09(8)
Int	-0.006(1)		-0.02(1)	0.07(10)	0.022(8)	-0.01(1)
R^2	0.9997		-	0.998	0.9996	0.99
Mad-LIP [d]						
Slope	0.9(2)	0.9(2)	-	0.9(1)	0.9(1)	0.9(3)
Int	0.04(2)	0.02(1)		0.1(1)	0.01(6)	0.02(1)
R^2	-	-		-	-	-
FT-IR [b]						
Slope	0.99(1)	1.04(1)	1.1(2)	-	1.074(9)	1.17(11)
Int	-0.17(8)	-0.07(10)	-0.1(2)		0.00(7)	-0.1(3)
R^2	0.997	0.998	-		0.999	0.98
W-DOAS						
Slope	0.917(3)	0.956(1)	1.07(13)	0.930(8)	-	0.98(8)
Int	-0.066(9)	-0.021(8)	-0.01(6)	0.00(7)		-0.10(3)
R^2	0.9996	0.9996	-	0.999		0.99
SPME						
Slope	0.89(7)	0.92(7)	1.05(30)	0.85(8)	1.01(8)	-
Int	-0.002(9)	0.01(1)	-0.02(2)	0.1(2)	0.10(3)	
R^2	0.991	0.99	-	0.98	0.99	

[a] Number in parenthesis is the 1-σ fit error of the last displayed digit
[b] Correlations for high concentration data only
[c] Units of the intercept are ppbv
[d] Mad-LIP comparisons listed are the average of the two experiments with the error being the variability between experiments.

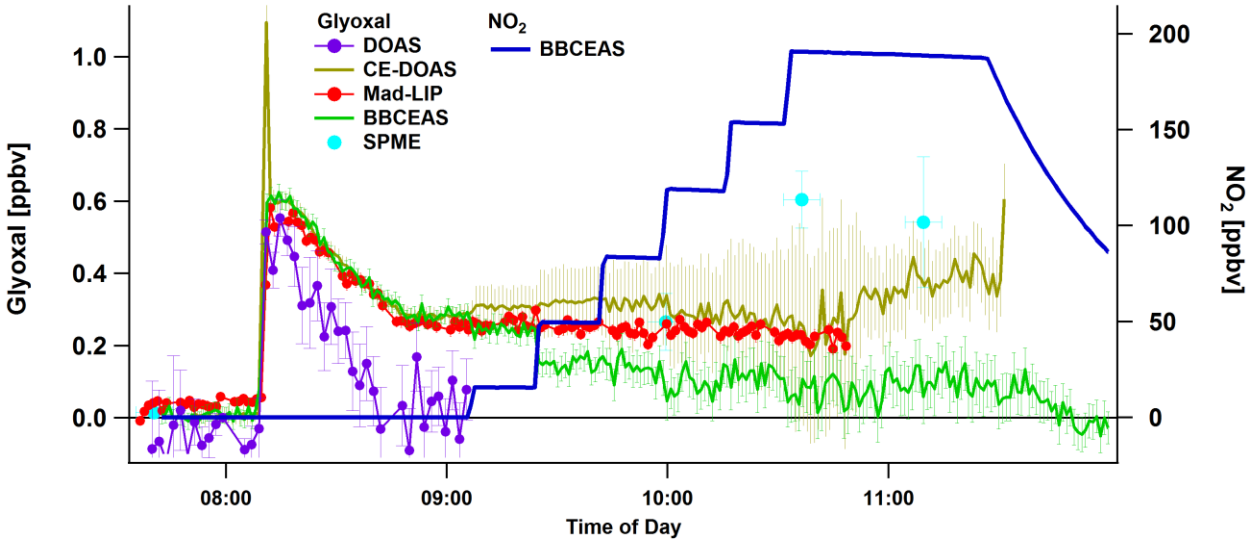

Figure 5.5: Sensitivity of glyoxal detection by UV-vis absorption techniques to high levels of NO_2 from 6 July 2011.

Table 5.4: Sensitivity of UV-Vis absorption measurements to NO_2 (6 July 2011)

Instrument	Glyoxal [a, b]	Methyl Glyoxal [c]
CE-DOAS	0.05±0.04	1±1
BBCEAS	-0.78±0.02	0.4±1.2

[a] units of pptv deviation per ppbv of NO_2; [b] Deviation with respect to Mad-LIP; [c] Deviation with respect to FTIR

Table 5.5 Correlation Matrix for Methyl Glyoxal from 27 June 2011

Y↓ X→	CE-DOAS	BBCEAS	Mad-LIP	FTIR	PTR-MS
CE-DOAS					
Slope [a]	-	0.990(3)	0.714(3)	0.852(9)	0.813(3)
Int		-0.35(2)	0.02(2)	-0.55(12)	0.86(2)
R^2		0.9987	0.997	0.996	0.96
BBCEAS					
Slope	1.010(3)	-	0.720(3)	0.854(9)	0.820(4)
Int	0.36(2)		0.38(3)	-0.02(10)	1.25(3)
R^2	0.9987		0.996	0.994	0.96
Mad-LIP					
Slope	1.400(6)	1.388(6)	-	1.16 ± 0.02	1.093(7)
Int	-0.03(3)	-0.53(4)		-0.6 ± 0.1	1.22(3)
R^2	0.997	0.996		0.995	0.96
FTIR					
Slope	1.174(13)	1.17(1)	0.86(1)	-	1.04(3)
Int	0.65(13)	0.02(12)	0.5(1)		0.3(2)
R^2	0.996	0.994	0.995		0.97
PTR-MS[1]					
Slope	1.231(5)	1.220(6)	0.915(6)	0.96(3)	-
Int	-1.05(2)	-1.53(4)	-1.12(3)	-0.3(2)	
R^2	0.96	0.96	0.96	0.97	

[a] Number in () is the 1 sigma standard deviation for the last reported digit [1] PTR-MS data filtered for ramp up and odd section that bumps higher than the trend in all of the other instruments and assumes a 5% uncertainty in the 1 minute PTR data.

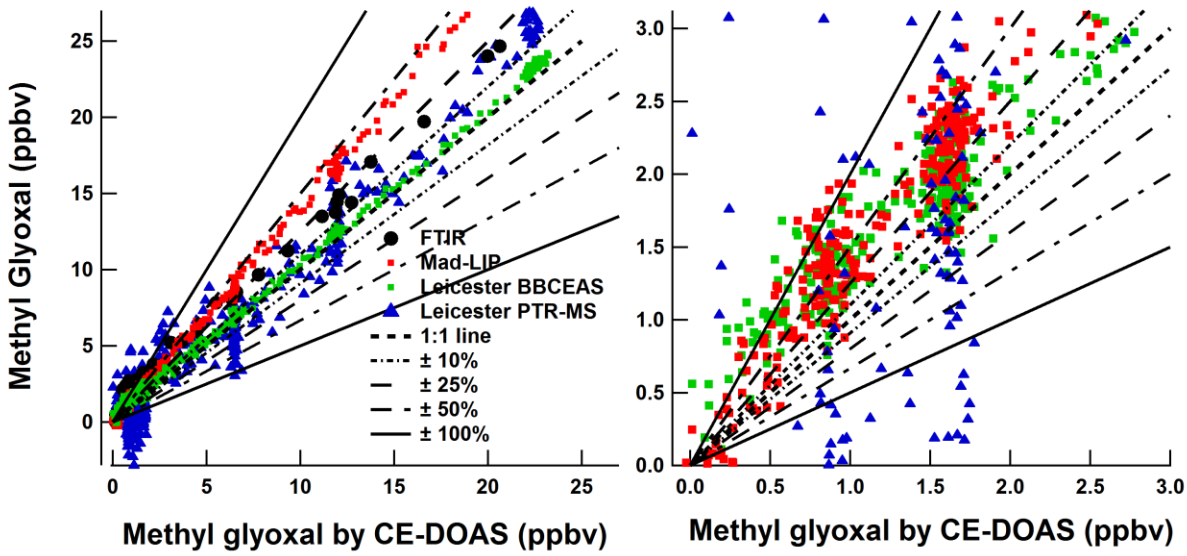

Figure 5.6: Correlation plots for methyl glyoxal plotted versus CE-DOAS from 27 June 2011.

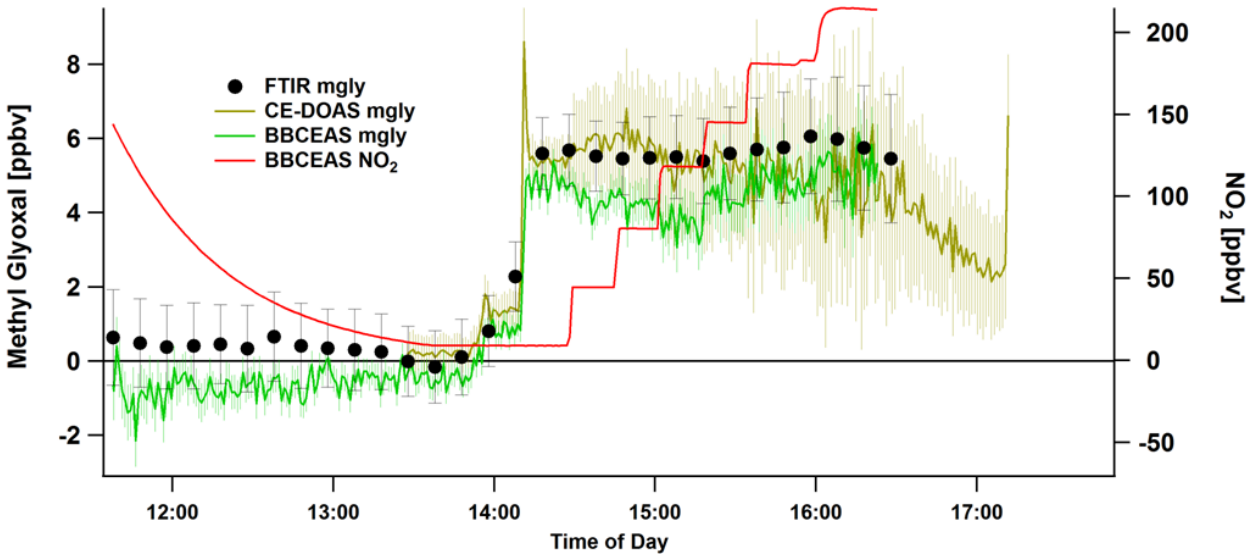

Figure 5.7: Sensitivity of methyl glyoxal detection by UV-vis absorption techniques to high levels of NO_2.

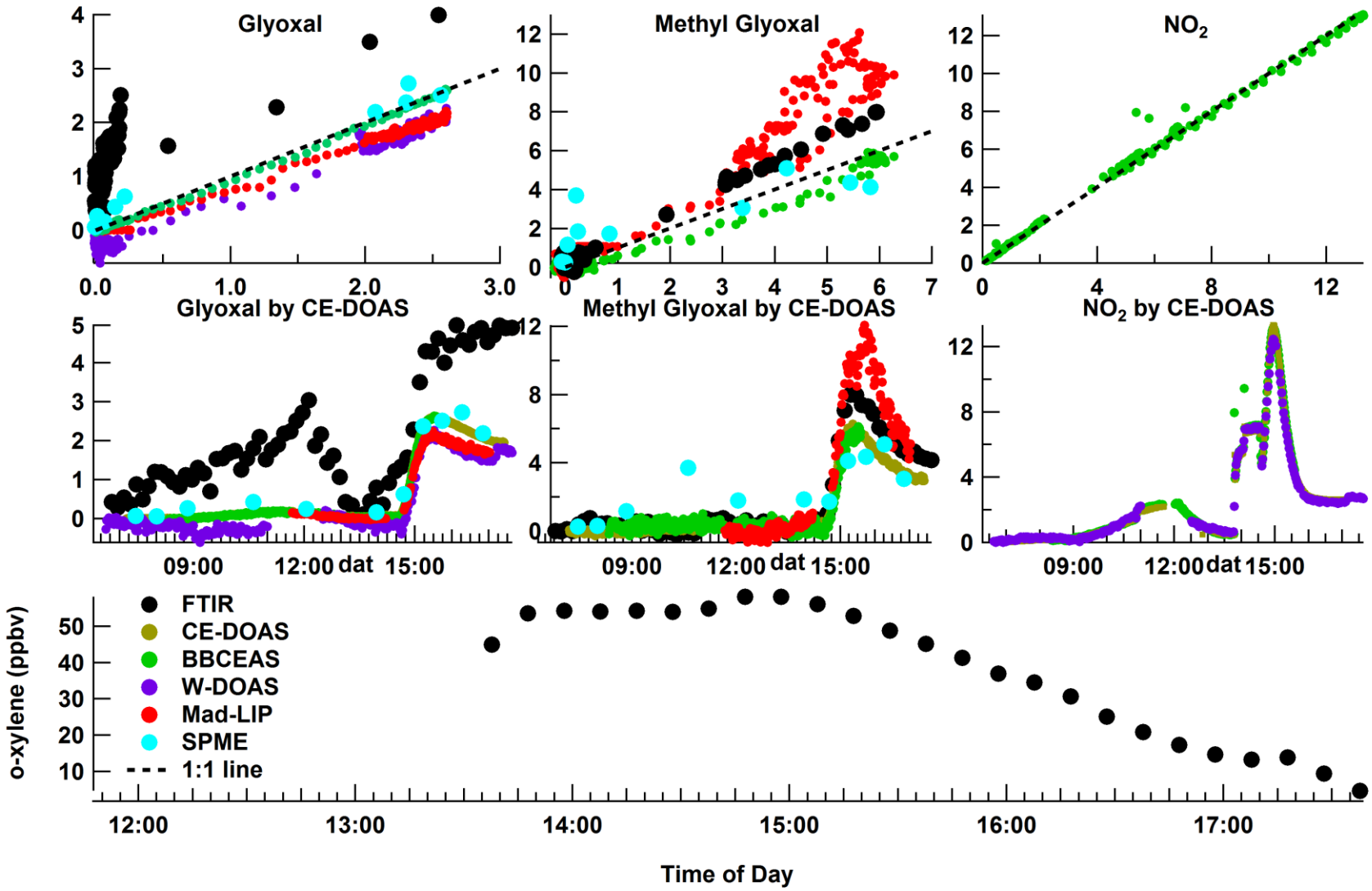

Figure 5.8: Oxidation of o-xylene under high NOx conditions to produce glyoxal and methyl glyoxal, as well as biacetyl. All displayed concentrations are in ppbv. Correlation plots on the top level panels are plotted versus measurements by CE-DOAS.

5.3.2.2 Instrument Precision

Following Experiment 8 on 5 July 2011 a large quantity of glyoxal was injected into the chamber and the chamber was then set to flush overnight with all of the instruments measuring continuously in their normal operating set up until the next morning. This allowed for the acquisition of several hours of data in a clean chamber. From this baseline data histograms were calculated for each of the instruments with available data. A Gaussian function was fitted to the histograms except in the case of the FTIR, where the spread of data did not form a fit-able distribution and a simple average and standard deviation were calculated. From the Gaussian distribution the standard deviation and mean were calculated for each instrument (see Figure 5.9 for glyoxal and Figure 5.10 for methyl glyoxal).

5.3.3 EUPHORE Discussion

5.3.3.1 Glyoxal

The detection of glyoxal by the various instruments performed to the specifications of each instrument. Comparisons to the FT-IR at high concentrations yielded slopes of ±5% of unity for most instruments. The Mad-LIP experienced difficulties at high concentrations for the first experiment but performed better in the second experiment after changing the flow rates (See Tables A5.1 and A5.2). The BBCEAS and CE-DOAS which differ primarily in the reflectivity of the mirrors used (0.9998 to 0.99997) and the analysis procedure, exhibited variability up to 5% which is in general within the uncertainty of the propagated errors. Systematic biases can exist between the two instruments, especially in the value used for the sample path length (relative volume occupied by the sample, not including the purges; see Chapter 2). While the glyoxal and methyl glyoxal varied the measurements of NO_2 were is very close agreement for experiment 3. For the CE-DOAS measurements at very high glyoxal it was possible to get more accurate values by selectively fitting weaker absorption bands.

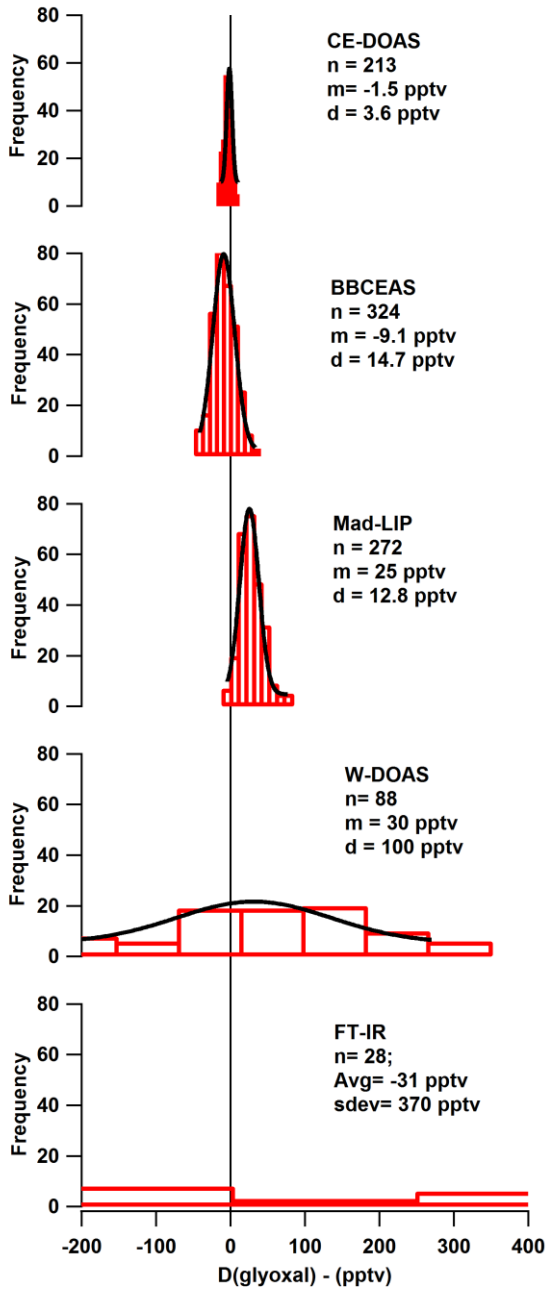

Figure 5.9: Histograms of glyoxal baseline variability on July 5, 2011. The instruments sampled from a clean chamber. The number of points in the distribution (n), the mean (m) and 1 standard deviation (d) are listed on each graph. Histogram distributions are used to calculate experimentally determined limits of detection.

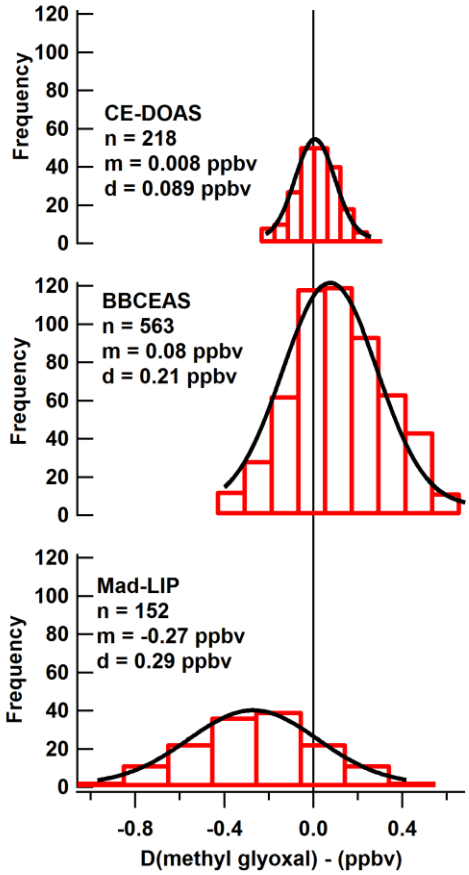

Figure 5.10: Histograms of methyl glyoxal baseline variability on July 5, 2011. The number of points in the distribution (n), the mean (m) and 1 standard deviation (d) are listed on each graph. Histogram distributions are used to calculate experimentally determined limits of detection.

5.3.3.2 Methyl Glyoxal

The detection of methyl glyoxal for all available spectroscopic instruments compared well during Exp. 2 and less optimally during Exp. 3 (See Table 5.4). For all experiments the Mad-LIP exhibited consistent calibration non-linearity at high concentrations even though the instrument is calibrated against a CRDS measurement of standards of both glyoxal and methyl glyoxal, the source of this non-linearity in the calibration is still uncertain (section 5.3.3.1). The two cavity based techniques compared within ±1% of each other in the presence of no other interfering species and less well in the presence of interfering species.

5.3.3.3 UV-Vis vs. IR absorption cross-sections

Because all of the instruments measuring glyoxal involved in the EUPHORE experiments were tied to the UV-Vis cross-section either directly (fitting of the literature cross-sections- W-DOAS, CE-DOAS and BBCEAS) or indirectly through calibration (FTIR cross-section calibrated to the W-DOAS, SPME calibrated to the FTIR and the Mad-LIP calibrated to a ring-down cell) it was useful to compare the performance of the CE-DOAS against the IR cross-sections in the NCAR experiments where the two sets of cross-sections are used independently. In this case the cross-sections compare favourably as well with methyl glyoxal.

5.3.3.4 Limits of Detection

Among the instruments tested the CE-DOAS demonstrated the lowest attainable detection limits for glyoxal and methyl glyoxal in the clean chamber. As seen in Figures 8 and 9, the distributions are Gaussian (except the FTIR) and yielded 1-sigma detection limits lower than their reported values.

5.3.3.5 Limitations and interferences

All instruments have limitations, from the influence of sampling lines to cross interference from similar absorption cross-section (i.e. methyl glyoxal and biacetyl or NO_2 -see Figure A5.26 in the

Appendix for a comparison of the various absorption cross-sections at a typical instrument resolution). Experiment 5 tested the effects of O_3 in combination with Teflon tubing. It had been suggested in the past that O_3 reacted with Teflon tubing to create glyoxal. The only effect observed in Experiment 5 was the conversion of some of the NO trapped in the Teflon into NO_2 that varied with the length of the inlet line, no other effect was observed due to O_3.

Very high levels of NO_2 did appear to affect the cavity-based instruments (CE-DOAS and BBCEAS) because high extinction in the optical cavity (in this case from the NO_2) limits the effective absorption path in the instrument, limiting the sensitivity. For the CE-DOAS (R=0.999972) 200 ppbv of NO_2 changes the sample path length from 15 km to 3.5 km equating to a factor of 4 decrease in sensitivity in addition to the highly structured absorption path which makes detection of lower concentration compounds difficult (For BBCEAS this would be a reduction from 5 to 2.3 km, or a factor of 2). The Mad-LIP appeared to be unaffected by large amounts of NO_2 while the FTIR even showed an increase in the methyl glyoxal measured when it should have stayed the same or decreased (due to dilution).

We were unable to access the interference of biacetyl for any of the instruments as the Mad-LIP was not working consistently during the period of the o-xylene experiment. Though, it might be a reason why the methyl glyoxal and not the glyoxal was affected for that experiment as the glyoxal has a faster phosphorescence decay than methyl glyoxal and biacetyl may be expected to have a similar response as methyl glyoxal. The BBCEAS and CE-DOAS are insensitive to interference from biacetyl due to its relatively unstructured absorption cross-section and the fact that the retrievals are built to be sensitive to the differential structures (DOAS-type retrievals).

5.4 Summary

The CU LED-CE-DOAS instrument compared favorably with other instruments measuring NO_2, glyoxal and methyl glyoxal during two separate inter-comparison campaigns. CE-DOAS was shown to have a robust spectral retrieval in the presence of interfering species and the lowest overall detection limits for the measurement of the three species investigated. The instrument showed the lowest variability in data among all instruments. With respect to other cavity-based technique (BBCEAS) the CE-DOAS compared within the uncertainty of both instruments and the correlation of the two instruments with respect to each other varied depending on the species measured and the experiment (compound measured on its own or with interferences). Between the two sets of data it was shown that the infrared and visible cross-sections of glyoxal and methyl glyoxal compared very well as verified by the correlation between the different instruments.

Chapter VI

6 Temperature dependent first generation product yields of minor mono and di-substituted carbonyls from the OH-radical initiated oxidation of isoprene under high and near-zero NOx conditions

This chapter prepared with Eleanor Waxman and Rainer Volkamer from the University of Colorado, Geoff Tyndall, Jon Orlando, Thomas Karl, Seawung Kim and Roger Seco from the National Center for Atmospheric Research and Luping Su and John Mak from the State University of New York, Stony Brook.

6.1 Introduction

Isoprene emitted by the biosphere is the largest single volatile organic compound (VOC) of biogenic origin in the global budget of VOCs, contributing an estimated 400-500 Tg annually, and comprising half of all biogenic emissions (Guenther et al., 2012). Isoprene is emitted by plants and is dependent on sunlight, heat stress and atmospheric CO_2 concentrations (Guenther et al., 2000; Pegoraro et al., 2004; Heald et al., 2009). The fate of isoprene in the atmosphere is dominated by reaction with hydroxyl radical (OH). Isoprene is also a major sink for OH in biogenic regions (Karl et al., 2009), and in some urban areas (Washenfelder et al., 2011). The oxidation of VOCs in the atmosphere contributes to the creation of ozone and secondary organic aerosol (SOA) (Carlton et al., 2009). Ozone is linked to asthma while aerosols are known to contribute to an increase in overall mortality and are known mutagens (Pope and Dockery, 2006; Villalobos-Pietrini et al., 2007).

Reaction of isoprene with OH forms formaldehyde (HCHO), methacrolein (MACR), and methyl vinyl ketone (MVK) as major first generation products (Tuazon and Atkinson, 1990).

While the mono- and di-subsituted carbonyl compounds hydroxyacetone (HACET), glycolaldehyde (GLYC), glyoxal (GLYOX) and methyl glyoxal (MGLYOX) do not make up a large part of the prompt reaction products, they do form a significant portion of the second and third generation products. These compounds are thought to contribute significantly to the formation and growth of SOA (Kroll et al., 2005; Liggio et al., 2005; Galloway et al., 2009; Carlton et al., 2009; Volkamer et al., 2009b). Isoprene accounts for ~46% and ~78% of the global production of glyoxal and methyl glyoxal respectively (Fu et al., 2008). Taking this into account, changes in the yields of these small molar yield products can make a very large difference to their global budgets. Previous field studies have sought to quantify the losses of glyoxal to determine the possible contribution to SOA mass in places such as Mexico City (Volkamer et al., 2007)or Los Angeles (Washenfelder et al., 2011). In Mexico City, where the glyoxal sources are dominated by aromatic compounds (toluene and the xylenes) the sources are well understood and the sinks of glyoxal can be investigated by comparing measurements of glyoxal to the photochemical models. But, in Los Angeles where glyoxal production is dominated by isoprene it becomes more important to understand the sources of glyoxal as the mechanisms of glyoxal formation are less well known (See Figure A6.1 in the Appendix).

Isoprene oxidation has been revisited many times in the past more than two decades (Tuazon and Atkinson, 1989; Yu et al., 1997; Sprengnether et al., 2002; Paulot et al., 2009; Galloway et al., 2011; Navarro et al., 2011; Berndt, 2012). While the measured yields of some products are consistent (MACR), other products either were not measured (glyoxal, methyl glyoxal, hydroxyacetone, glycolaldehyde), show high variability (MVK), or inconsistent detection (3-methyl furan). Until recently glyoxal and methyl glyoxal were only thought to be produced upon further oxidation of 1st generation products (C-5 hydroxy carbonyls, MACR or

MVK). Recent field work has shown that chemical models are unable to explain high OH levels in isoprene dominated areas and have attributed this to the recycling of HO_x (HO_2 + OH) radicals in the isoprene oxidation mechanism. Dibble (2004a; 2004b) predicted a route of production of glyoxal and methyl glyoxal as well as co-products glycolaldehyde and hydroxyacetone through a series of isomerization and 1,5 hydrogen shift steps involving multiple oxygen additions and peroxy (RO_2) to oxy (RO) radical conversions while also regenerating HO_2 (Peeters et al., 2009). First generation production of glyoxal was first observed by Volkamer et al. (2005a) at the EUropean PHoto-REactor (EUPHORE) in relation to the production of methacrolein molar yield and was 1-3%. Paulot et al. (2009) measured hydroxyacetone and glycolaldehyde and inferred the production of the co-products of glyoxal and methyl glyoxal according to the Dibble mechanism with yields of 3.8 and 4.2% for glyoxal and methyl glyoxal respectively from the yields of the co-products. Galloway et al. (2011) measured the 1st generation yield of glyoxal to be 2.1% using a laser induced phosphorescence technique at the Caltech chamber and further updated the yields of other products. Peeters and Nguyen (2012) proposed an updated pathway to production of alpha-dicarbonyls from the Dibble mechanism, involving fewer peroxy to oxy radical conversions via a faster isomerization step of the RO_2 radicals. As the evidence for minor, but yet still important, channels has grown, the fate of RO_2 radicals has become increasingly important. Recent work on the oxidation of methacrolein (Crounse et al., 2012) has shown that the fate of peroxy radicals differs based on the lifetime of the radical. As the pathway transitions from reactions with NO to reactions with HO_2, other RO_2s or by isomerization when the NO_x regime changes. We present here the first temperature dependant measurements of first generation glyoxal and methyl glyoxal as well as their co-products and other first generation products of isoprene oxidation by hydroxyl radical under high and near zero NO_x conditions. In

contrast to previous experiments the fate of RO_2 radicals in our near zero NO_x experiments is dominated by RO_2 self-reactions. Previous studies had mostly been dominated by $RO_2 + HO_2$ reactions. In addition we investigate the oxidation chemistry of another di-alkene, 1,3-butadiene as an analogous compound to isoprene to verify the rapid formation of glyoxal.

6.2 Experimental

6.3 Chamber operation

Experiments were carried out in the National Center for Atmospheric Chemistry (NCAR) atmospheric simulation chamber. The chamber consists of a stainless steel cylinder (~47L) connected to a Fourier transform infrared spectrometer. This set up has been previously described in the literature (Shetter et al., 1987; Orlando and Tyndall, 2002) (for further description see Figure 5.1). The chamber was chilled by circulating ethanol to cool the chamber to 260K or heated (320K) by circulating water. Reaction chemistry was initiated by photolysis of an appropriate precursor using a filtered Xe arc lamp or by injection of O_3 to react with an appropriate alkene. Reactant gases for the various experiments were injected from a calibrated bulb into the chamber via a gas line as described previously in the literature (Orlando and Tyndall, 2002). Small yield products of the oxidation mechanisms were probed by proton transfer mass spectrometry (PTR-MS, both quadrapole and time of flight instruments) (Jordan et al., 2009), Gas Chromatography (Hasson et al., 2012) and Light Emitting Diode Cavity Enhanced Differential Optical Absorption Spectroscopy (LED-CE-DOAS) (Thalman and Volkamer, 2010) instruments provided by groups at NCAR and the University of Colorado. For each experiment the chamber was over-pressurized and sample was leaked from the chamber through a valve and divided to each instrument (experiments with GC detection were performed separately). The flow (5 sccm for CE-DOAS and 25 sccm for the PTRs) out of the chamber was

controlled by mass flow controllers (MKS) or stationary Teflon valves. These small flows were then diluted and delivered to each instrument. The sample flow and dilution varied for each specific experiment. For hot and cold temperature experiments the temperature of the chamber was allowed to equilibrate after the gases were added and before the reactions were initiated.

6.3.1 Calibration Experiments for minor carbonyl products

Sample delivery and instrument response for compounds of interest were calibrated as shown in Chapter 5. Additional calibrations were run for hydroxyacetone, glycolaldehyde and isoprene. These compounds generally agreed within 10% for the FT-IR and PTR-MS (plots of the calibration experiments can be found in Figure A6.2 the Appendix.

6.3.2 High NO_x Experiments

For high NO_x conditions $7.0 \pm 0.1 \times 10^{14}$ molecules cm^{-3} of the reactant (isoprene or 1,3-butadiene) were mixed with $2.3 \pm 0.1 \times 10^{14}$ molecules cm^{-3} of NO and $1.4 \pm 0.1 \times 10^{15}$ molecules cm^{-3} of isopropyl nitrite (molecular formula $CH_3CH(CH_3)ONO$) and the chamber brought to a pressure of ~800 Torr with the bulk of the mixture as oxygen and nitrogen. OH radicals were produced in small bursts by photolysis (30-60 seconds) of isopropyl nitrite (high NO_x experiments outlined in Table A6.1). For some experiments additional NO was added to the chamber part way through the experiment to ensure that the NO still propagated the reaction chain. Because of the high levels of NO_2 that accumulate in the chamber there was some chain initiation for isoprene oxidation from the reaction of isoprene with NO_2 (Atkinson et al., 1984).

6.3.3 NO_x free experiments

Isoprene reaction chemistry was also probed under NO_x free conditions. In these experiments 2,3 dimethyl 2-butene (tetra-methyl ethylene, or TME) or trans-2-butene (T2B) was reacted with O_3 to make OH in the absence of NO_x. The ozonolysis of these alkenes also makes methyl glyoxal and hydroxyacetone (TME) and glyoxal and glycolaldehyde (T2B) which requires each reaction

to be run twice, once to measure the glyoxal and glycolaldehyde and a second time to measure the methyl glyoxal and hydroxyacetone produced from isoprene (This was simpler for TME experiments as the ratios of rate constants with isoprene were more favorable to maximize OH + isoprene reactions). Control experiments for O_3 + alkene were run for isoprene, TME and T2B at each temperature to check for possible product interferences. For these experiments the concentration of OH source and isoprene were varied to optimize reaction of isoprene with OH and minimize the reaction of the isoprene with O_3. After reactants were injected and the chamber brought to pressure, an aliquot of O_3 was injected into the chamber along with additional N_2. Additional amounts of O_3 were injected as needed to further oxidize the species of interest. Low NO_x experiments were carried out in the dark eliminating any wall sources for NO. The NO_2 measured by CE-DOAS was less than 1 ppbv (not significantly above the background of the mass-flow controller). High O_3 (4-5 x 10^{13}) would have further suppressed any NO that could have been present in the chamber, leaving RO_2 radicals to react with HO_2 or other RO_2s. The loss of isoprene with respect to OH was found by modeling the relative contributions of OH and O_3 using a simplified model run in Kintecus (Ianni, 2003) or the Master Chemical Mechanism (MCM) version 3.2 (Jenkin et al., 2012) using the Atchem online web portal (https://atchem.leeds.ac.uk/). A complete list of experiments under all conditions is given in the Appendix, Table A6.1.

6.4 Instrumentation

6.4.1 FT-IR

The BOMEM DA3.01 FT-IR was operated as described in the literature (Shetter et al., 1987; Orlando and Tyndall, 2002). The modified white cell optics give a path length of 32 m and detection sensitivity for isoprene, MACR, MVK and HCHO of 2 x 10^{12}, 5 x 10^{12}, 5 x 10^{12}, 2 x 10^{12} respectively. Absorption cross-section standards were calibrated from known partial

pressures of standards in the chamber measured by the same instrument at the same instrument resolution of 1 cm^{-1}.

6.4.2 CU LED-CE-DOAS

CE-DOAS measured NO_2 (Vandaele et al., 2002), glyoxal (Volkamer et al., 2005c), methyl glyoxal (Meller et al., 1991) and O_4 (Hermans et al., 1999) using differential optical absorption (Thalman and Volkamer, 2010). This CE-DOAS instrument incorporated a 92 cm optical cavity with a sample length of 79 cm and a peak mirror reflectivity at 455 nm of 0.999975. LED light was collimated into the cavity and the exiting light was directed to an OceanOptics QE65000 spectrometer via a 1mm optical fiber as described in Thalman and Volkamer (2010). Measured concentrations were scaled back to the concentration in the chamber by accounting for the dilution and pressure difference (Flow for the PTR ranged from 20-25 ccm and was 5 sccm for CE-DOAS). Extremely high NO_2 concentrations were present in the cavity (up to 100 ppbv) for all high NOx experiments. In order to account for this large amount of NO_2 in the cavity spectra (and inaccuracies in the convolution of the standard absorption cross-sections); known amounts of NO_2 in N_2 were supplied to the cavity to measure the residual due to large amounts of NO_2, which could then be fitted during the experiments allowing for the fitting of the weaker absorbers in the presence of large amounts of NO_2. The detection limits in the chamber as measured by CE-DOAS for glyoxal, methyl glyoxal and NO_2 were 1.0 x 10^{11}, 2.5 x 10^{11} and 1.5 x 10^{11} molecules cm^{-3} as respectively. NO_2 was retrieved using an IBBCEAS retrieval and the measured NO_2 was supplied to the path length equation with the CE-DOAS retrieval to retrieve concentrations of the lower concentration compounds.

6.4.3 Quad and Time of Flight Proton Transfer Mass Spectrometry

Concentrations of compounds measured by the PTR-MS were retrieved as described in Jordon et al. (2009) for runs done near the initial calibration of the instruments from standards and the

proton transfer reaction rates. Later (warm temperature) data was calibrated from comparison to the FT-IR.

6.4.4 Gas Chromatography

Isoprene, methacrolein, methyl vinyl ketone and possibly glycolaldehyde were measured by GC using a flame ionization detector by flowing continuously from the chamber and injecting a small sample loop onto the column. The column was operated at room temperature with a fast flow (6 cm/s) of the carrier gas. The detection sensitivity for each compound was better than 1 x 10^{12}, 1.6 x 10^{12}, 1.6 x 10^{12}, 5 x 10^{12} molecules cm^{-3} for isoprene, methacrolein, methyl vinyl ketone and glycolaldehyde respectively.

6.5 Results

6.5.1 Instrument Calibration Experiments

Comparison of the LED-CE-DOAS and PTR-MS instruments to the FT-IR standards was carried out with experiments at each temperature to check sampling losses for isoprene, glyoxal, methyl glyoxal, hydroxyacetone and glycolaldehyde. The glyoxal, methyl glyoxal, NO_2 concentrations measured between the three instruments compared very well (±5%) while the isoprene, hydroxyacetone and glycolaldehyde, while were comparable exhibited varying backgrounds in the PTR-MS instruments, while their slopes compared favorably to the FT-IR (usually within ±5% for room temperature and worse at lower temperatures). Detailed results of the calibration experiments are found in Chapter 5 and in Figure 6.2 in the Appendix.

6.5.2 High NOx Chemistry

First generation yields for the minor carbonyl compounds (GLYOX, MGLYOX, HACET and GLYC) were observed for isoprene oxidation at all temperatures investigated, and are reported in Table 6.1 and Figure 6.1 along with yields of the major products as well (yield plots are also shown in Figure A6.3 in Appendix A). First generation yields are determined with respect to the

isoprene reacted. Figure 6.1 shows the production of glyoxal, methyl glyoxal, glycolaldehyde and hydroxyacetone compared with model runs of isoprene oxidation carried out in MCM. Secondary production causes slopes to curve up for these minor products (except glyoxal). By adjusting the results of the MCM (which only contains secondary and tertiary production of these products) with a simple primary production we arrive at yields of 2.3% for glycolaldehyde and hydroxyacetone and 1.8% for methyl glyoxal. Photolysis in the chamber of reaction products is negligible. The highest uncertainty for the yields is the determination of the reacted amount of isoprene by FT-IR which has an uncertainty in Δisoprene of 10%. Example spectra and fits for glyoxal and NO_2 from CE-DOAS (Figure A6.5, A6.6) as well from the FT-IR for major reactants and products (Figure A6.7) are found in Appendix A. Explicit description of the isoprene mechanism can be found in Figures A6.11-A6.13 in the Appendix.

6.5.3 Low NOx Chemistry

First generation yields for minor and major products from isoprene oxidation were observed under Low-NOx conditions at all temperatures and are reported in Table 6.1, excepting formaldehyde which was also formed as a reaction product of the OH source. The isoprene turnover with respect to OH was retrieved by modeling the relative contributions of OH and O_3, with OH accounting for 85-90% of isoprene loss for TME + O_3 and ~90% for T2B + O_3.

Table 6.1 Primary yields (%) of isoprene reaction with OH (range between repeat exps)

Compound	High NO_x			Zero NO_x		
	260K	296K	320K	260K	296K	320K
Glyoxal	0.86(0.06)[1]	2.17(0.2)[1]	2.1(0.2)[1]	0.26 (0.11)[2]	0.27 (0.03)[1]	0.22 (0.12)[2]
Hydroxyacetone	0.48(0.03)[1]	2.3(0.3)[2]	2.3(2)[1]	0[#]-0.8[3]	0.9-1.8[3]	2.9[3]
Methyl glyoxal	0.7(0.4)[2]	1.8(0.4)[2]	1.8(0.2)[1]	0[#]-1.1[3]	0.2-0.9[3]	1.0[3]
Glycolaldehyde	0.41(0.06)[2]	2.3(0.4)[2]	2.3(0.2)[1]	-	-	3.6[3]
Methacrolein	24(3)[2]	25(2)[2]	24(3)[2]	16(3)[2]	24(1)[1]	14(2)[3]
Methyl Vinyl Ketone*	15(3)[2]	31(1)[2+] 27(1)*[2]	32(5)*[+2]	26(11)[*+2]	17(5)*[2]	4-67*[+3]
Formaldehyde	43(4)[1]	53(4)[1]	55(5)[2]	-	-	-
Sum of MVK + MACR	45	57	59	43	42	-

[1] ≥2 samples, <10% range;[2] ≥ 2samples, >10% range;[3] ≤2 samples, >50% range; *MVK = $[MVK/MACR]_{PTR}$ - $[MACR]_{FTIR}$; [+] FTIR and GC retrieved MVK; # Below detection limit

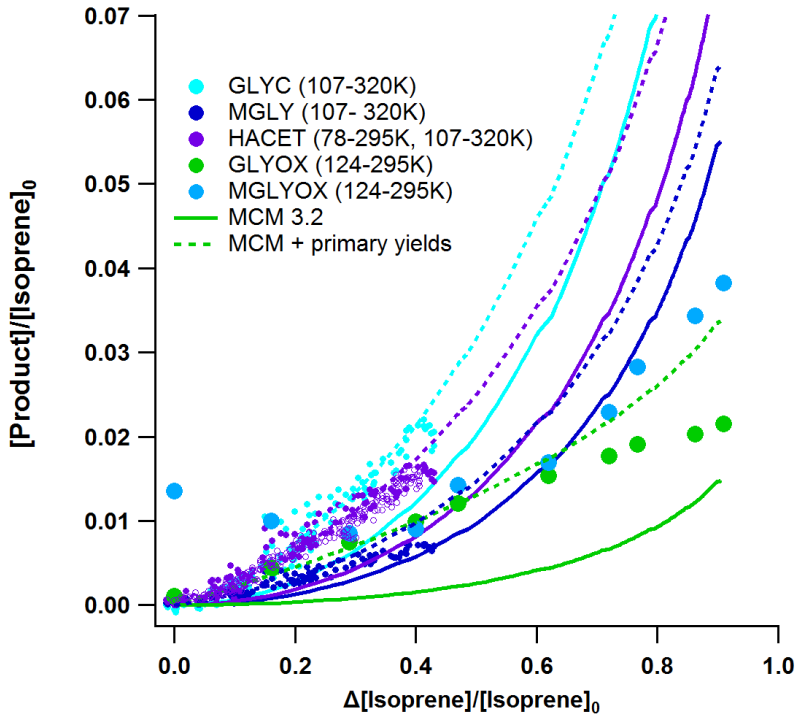

Figure 6.1: Product yields of minor carbonyl products with respect to fraction of isoprene consumed under high NO_x conditions. Secondary production (solid lines) is accounted for to retrieve primary yields of glycolaldehyde and hydroxyacetone (dashed lines- sum of primary and secondary). The measured data for all species appears linear over the range of isoprene reacted (except the methyl glyoxal (teal blue larger dots) from experiment 124, which is offset in the graph to account for the CE-DOAS's inability to measure the lower concentrations against the high NO_2 background) while the modeled data has some curvature at higher amounts of isoprene reacted.

6.5.4 Secondary Chemistry and 1,3-Butadiene

6.5.4.1 Isoprene Second Generation products

Product formation of major and minor reaction products were also measured for experiments with high isoprene turnover (~90%). In these experiments only the FT-IR and CE-DOAS were in operation. The results of these experiments (one at 47°C and two at room temperature) are plotted in Figure 6.2 with respect to the fraction of isoprene starting material consumed. Additional lines are added in each panel to represent the expected yields of glyoxal products as given by the MCM. A linear dependence for glyoxal is observed even at high isoprene turnover, indicating that the primary yield of glyoxal dominates from isoprene.

6.5.4.2 1,3-Butadiene chemistry

Reaction of 1,3-Butadiene was investigated and yields of acrolein, formaldehyde, glyoxal and C-4-hydroxy carbonyls were observed by FT-IR and CE-DOAS. A primary yield of 2.1% for glyoxal at room temperature and 47°C was observed for the first time. Acrolein and formaldehyde primary yields of 52/28, and 53/44% respectively were measured for 295/320K. Detailed results can be found in the Appendix Table A6.2 compared with the literature. Low NO_x yields of 0.38 and 30% were also measured for glyoxal and acrolein respectively at 295K. Secondary production of glyoxal from the oxidation of C4-hydroxy carbonyls was observed by reacting >80% of the starting 1,3-Butadiene as in Figure 6.2 in comparison to the isoprene data (Further comparison of the results of the 1,3-Butadiene oxidation compared with a modified version of MCM v 3.2 can be found in Figure A6.10 in the Appendix).

6.6 Discussion

6.6.1 High NO_x Isoprene Chemistry

6.6.1.1 Room Temperature

The observed primary yields of the major products of isoprene oxidation were observed to be consistent (within the errors) with those reported in the literature (See Table A6.3 in the Appendix). The measured yields were fitted from only the first 20% of isoprene reactions while up to 40% of the isoprene was reacted in some experiments. We observe for the first time the primary yield of methyl glyoxal (1.8%) and find that it is within the error bars of the reported glyoxal yield. By adjusting the observed glycolaldehyde and hydroxyacetone for secondary production (based on MCM) we find yields of 2.3±0.2% for each is slightly lower than the literature values but agrees well with the measured glyoxal and methyl glyoxal yields (see Figure 6.1). Measured yields at room temperature are compared to the literature in Table A6.3 in Appendix A.

6.6.1.2 Temperature Dependent High NO_x yields

For the first time we observe temperature dependence of isoprene oxidation product yields. For all products we see a reduction of yields at lower temperatures and little to no change as the reaction was taken to higher temperatures from room temperature (Table 6.1 and Figure A6.3). This could be due to the changing contribution of isomerization steps in the oxidation mechanism as well as a varying contribution of nitrate compounds (these would be more stable at lower temperatures). At higher temperatures yields remain constant. For the major products MVK appears to have a lower yield than MACR at low temperatures, while the yields of HACET and GLYC reduce in a different manner from GLYOX and MGLYOX. This could be caused by the influence of reaction channels that are minor or negligible at higher temperatures.

6.6.2 Low NO_x Isoprene Chemistry

For low NO_x chemistry an important consideration is the fate of the peroxy (RO_2) radicals as their reactions with other RO_2s, HO_2 and NO are in competition with isomerization. From simulations run in MCM, we estimate that RO_2 dominates HO_2 by a factor of 10 in these experiments. At these levels of [RO_2], RO_2-RO_2 interactions are the dominant fate of peroxy radicals (70% of all RO_2 radicals react with other RO_2s, see Figure A6.4 in Appendix A). We observe a decrease in the observed yields of the minor products of a factor of 2-8 compared to high NO_x experiments. For the major compounds MVK production appears to decrease while MACR remains the same. The largest uncertainty in the low NO_x experiments is the very small turnover of isoprene combined with the correction for O_3 reactions. The variation of temperature did not realize a single trend in yields and as such the interpretation of these data beyond the empirical result becomes impossible without further investigation. As isomerization as well as RO_2, HO_2 and NO reactions are in competition it is difficult to interpret further the mechanistic details of these low-NOx experiments.

6.6.3 Higher Generation High NO_x Isoprene Chemistry

Further oxidation of isoprene (up to 90% of isoprene consumed) allowed us to observe the trend of glyoxal production across multiple oxidation generations. As shown in Figures 6.1 and 6.2, glyoxal production remains linear with isoprene consumption all the way to greater than 90% consumption. As was observed by Galloway et al. (2011) there is no justification for secondary production of glyoxal from the oxidation of five carbon hydroxyl-carbonyls by OH as is included in the MCM. A similar trend for methyl glyoxal was not able to be observed as high NO_2 backgrounds in these experiments limited CE-DOAS sensitivity and the PTR-MS instruments were not in operation. Comparison of results to MCM v3.2 is shown in Appendix A as Figure A6.8.

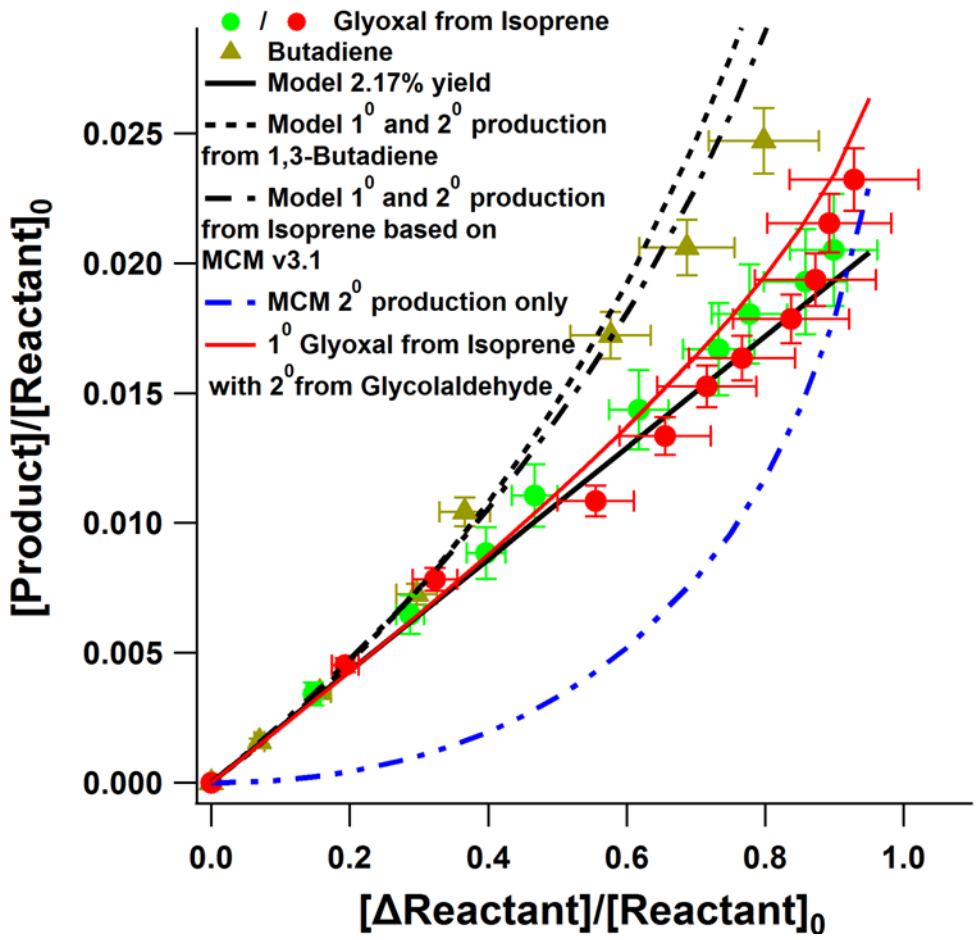

Figure 6.2: Production of glyoxal from isoprene compared to glyoxal formation from 1,3 butadiene. Primary and secondary production are shown separated for isoprene and combined for both isoprene and 1,3 butadiene, compared with the experimental results. Model results for secondary yields are taken from Berndt and Boge (2007) for 1,3-butadiene and from v3.2 of the MCM for isoprene while the primary yields are taken from the experimental values in this work.

6.6.4 1,3-Butadiene

The oxidation of 1,3-butadiene by OH under high and low NOx conditions was observed at 295 and 320 K. Under high NOx conditions, a first generation yield for glyoxal of 2.1% was observed for the first time (Table A6.2, Figure 6.2). The formation of glyoxal from 1,3-butadiene- another di-alkene- indicates that reaction pathways similar to those of isoprene are available to form less-likely products (due to isomerization and hydrogen shifts). The proposed mechanisms of formation are shown in Figure A6.9 in Appendix A. Not all of the pathways outlined in the mechanism will necessarily yield glyoxal, as they represent branching/competing reactions. It would be expected that the 1,6-H shifts would dominate over the NO reactions for the RO2 radicals that have competing reactions leaving only the one pathway to primary glyoxal formation. This pathway creates the same 3 carbon peroxy radical used as the test case for modeling of the 1,6-H shifts by Peeters and Nguyen (2012) for isoprene. As was observed with isoprene, low NOx chemistry greatly reduced the product yields for both glyoxal and acrolein. At higher temperatures glyoxal production remained constant while acrolein and formaldehyde were reduced. Previous studies (Tuazon et al., 1999; Sprengnether et al., 2002; Berndt and Böge, 2007) reported yields of acrolein have varied from 54-58% molar yield, while the total nitrate yield in these same studies varies inversely from 11-6%. Data on the yield of nitrates in our experiments are not known- but could explain the variation from the literature as experiments were carried out under very high NO_x conditions.

1,3-butadiene forms one four carbon hydroxy-carbonyl compound on reaction with OH (23% yield (Berndt and Böge, 2007)) which goes on to form glyoxal with a yield of 17%. Further oxidation of 1,3-butadiene (>80%) reflected this secondary production of glyoxal in

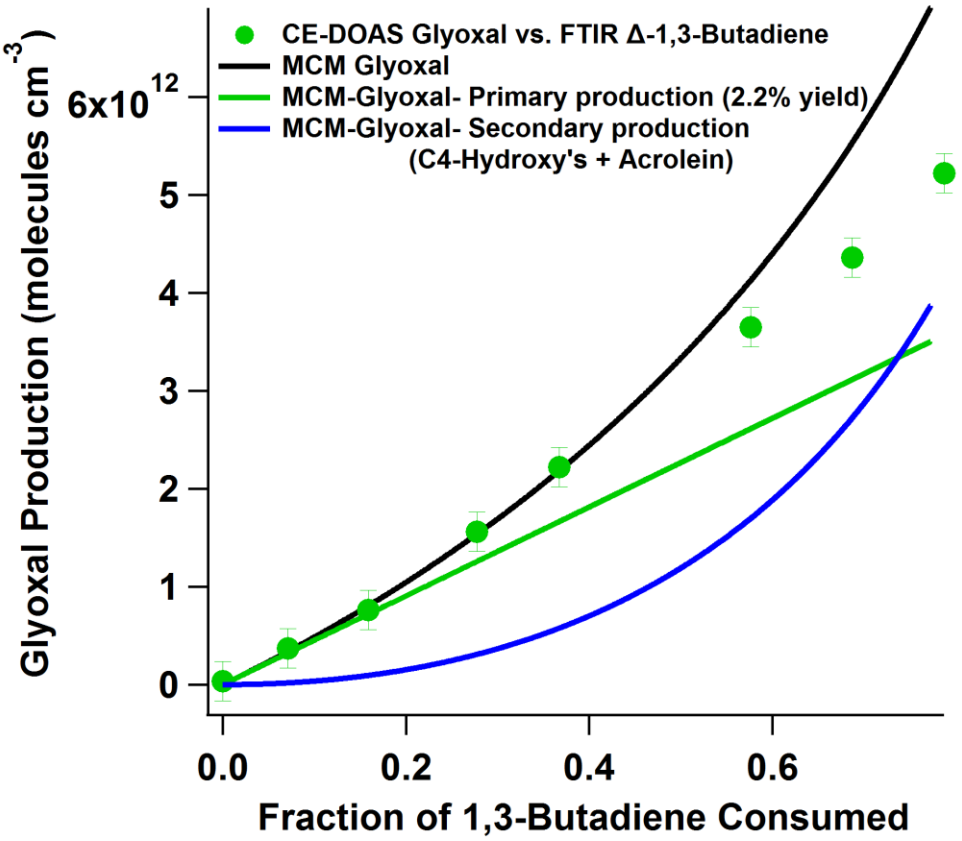

Figure 6.3: Glyoxal production from 1,3-butadiene with respect to fraction of reactant consumed. Measurements are compared to a version of the MCM mechanism modified to include a primary glyoxal source and reduction of MCM secondary glyoxal production from C4-Hydroxy carbonyls (to match yields measured by Berndt and Böge (2007)).

addition to the primary production (Figure 6.2 and Figure 6.3). The MCM v3.2 mechanism was modified to include the primary production of glyoxal as shown in Figure A6.9 in the Appendix and the secondary production from the oxidation of C4-Hydroxy carbonyls was reduced to match the yields of Berndt and Böge (2007). The MCM had the C4-Hyrdroxy compounds making equal amounts of glycolaldehyde and glyoxal which was not observed by Berndt and Böge (2007). The results of these modifications are compared with the measurements in Figure 6.3. The primary and secondary glyoxal production is plotted separately. At higher turnovers (>50%) of 1,3-butadiene the MCM and the measurements diverge, likely due to the difficulty in modeling the extra NO added to the reaction at the mid-point of the experiment. We observe the secondary production and estimate either the yield of glyoxal from the C4-hydroxy-carbonyl or the initial C4-hydroxy-carbonyl yield to be match than that measured by Berndt and Böge in these conditions.

6.7 Conclusions

In this work we report the temperature and NOx dependence of isoprene and 1,3-butadiene oxidation initiated by OH. In particular:

1. Instrument calibration and comparison to the FT-IR standard removes uncertainty with respect to transfer and line loss issues and validates detection of minor compounds by LED-CE-DOAS and PTR-MS.
2. Primary production of methyl glyoxal from isoprene is here observed for the first time.
3. Yields of the co-products, glyoxal/hydroxyacetone and methyl glyoxal/glycolaldehyde agree within the uncertainty of the measurements and support the mechanisms proposed in the literature.

4. Under low-NOx conditions observed minor product yields decrease indicating the shifting to more dominant pathways under the reaction conditions probed.
5. Low-NOx chemistry was investigated for the first time in a regime where RO_2-RO_2 reactions dominate the fate of RO_2 radicals. These results warrant further investigation by applying models such as the MCM and Leuven isoprene mechanism (LIM) (Peeters et al., 2009).
6. Primary production of glyoxal from 1,3-butadiene is observed for the first time and a mechanism based on the mechanism of isoprene is proposed to explain the prompt chemistry.

Chapter VII

7 Selected Field Deployments

7.1 CalNex 2010: California Nexus- Research at the Nexus of Air Quality and Climate Change

7.1.1 Campaign Overview

The CalNex 2010 field campaign (http://www.esrl.noaa.gov/csd/projects/calnex/) combined the efforts of a large number of institutions to understand the influence of urban pollution on air quality and climate in the Los Angeles basin of California. This involved measurements of gas and aerosol composition and properties at a ground site located at California Institute of Technology in Pasadena, CA as well as from several mobile platforms (NOAA P-3 aircraft, CIT CHIRPAS Twin-Otter, and NOAA Twin-Otter). Description of the measurements and platforms are given in detail in the campaign overview paper by Ryerson et al.(2013). LED-CE-DOAS measurements were taken from the top of the Millikan Library on the CalTech campus approx. 1km from the main ground site and at an elevation of ~30 m above the ground level. Pasadena, CA is approx. 18km down-wind of the Los Angeles business sector and the site is considered as "anthropogenically influenced" (Veres et al., 2011).

7.1.2 Instrument Set and Description

A prototype LED-CE-DOAS instrument was first deployed in the field during the CalNex field campaign from May15, 2010 to June 16, 2010. The instrument used a configuration similar to

that described in Chapter 2 with the optics and cavity mounted to a rail system (Thorlabs) and the optical head mounted to the structure of the roof. Electronics, pump, gases and flow controls were located inside the Library book elevator shaft control room. This room is temperature controlled as the stairwell flow vents into and through this room located on the roof of the Library. The spectrometer utilized secondary temperature control to keep the spectrometer stable at 31±0.001°C. During one portion of the campaign the co-located MAX-DOAS instrument was taken off-line and the spectrometer was used to take simultaneous data for a second open cavity set-up (Figures 7.1 and Figures A7.1 and A7.2 in the appendix). This system utilized the Acton-PIXIS spectrometer and detector as described in Chapters 2 and 3.

7.1.3 CE-DOAS Results and Summary

The measurements by CE-DOAS at CalNex show that glyoxal is produced from photolysis in Pasadena during the length of the campaign (Figures 7.2, 7.3 and 7.4). NO_2 does not show a strong diurnal profile at the surface as it is much more variable day to day. Open cavity measurements of aerosol optical extinction from the reduction of O_4 absorption (see Chapter 2 for derivation of the extinction retrieval) match the temporal evolution of the aerosol as measured by Cavity Attenuated Phase-Shift (Massoli et al., 2010). Further development of the open cavity technique, is needed to reduce the variability and accuracy of the technique to measure aerosols and trace gases without using an inlet: (1) understand better the sample path and (2) how atmospheric turbulence (non-laminar flow) effects total extinction. The CE-DOAS instrument and retrieval were able to realize sensitive, low-noise detection with less-frequent backgrounds over the course of the whole campaign.

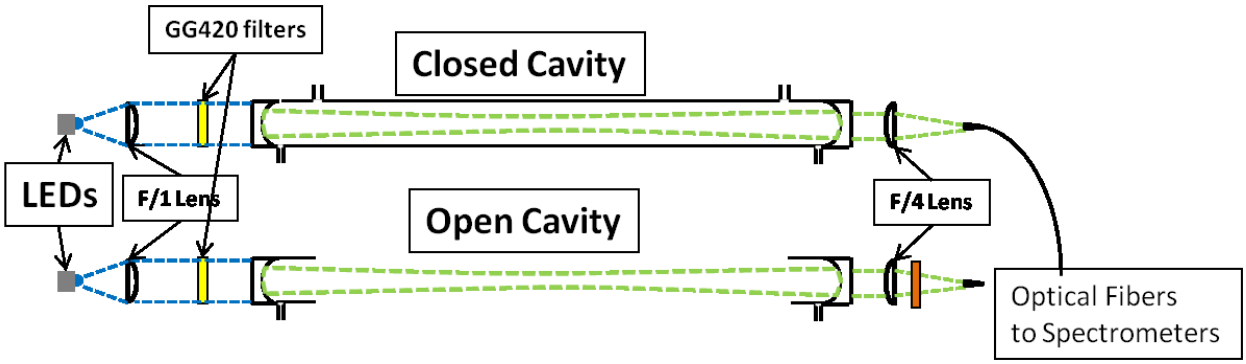

Figure 7.1: Configuration of Dual cavities located on the roof of the Millikan Library during CalNex.

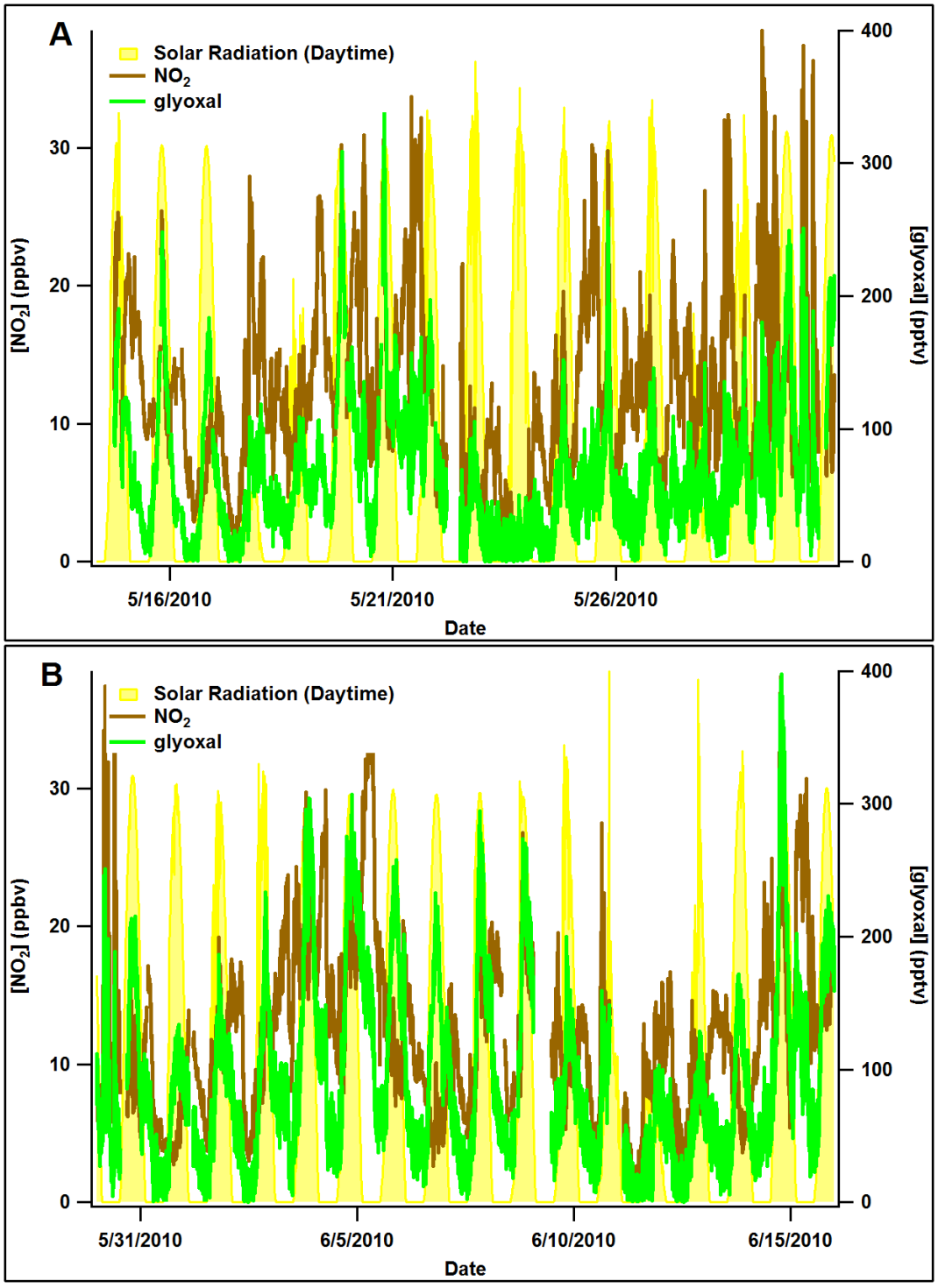

Figure 7.2: Measured NO_2 and glyoxal by CE-DOAS at CalNex 2010. Panel A shows the first half of the campaign while panel B shows the second half.

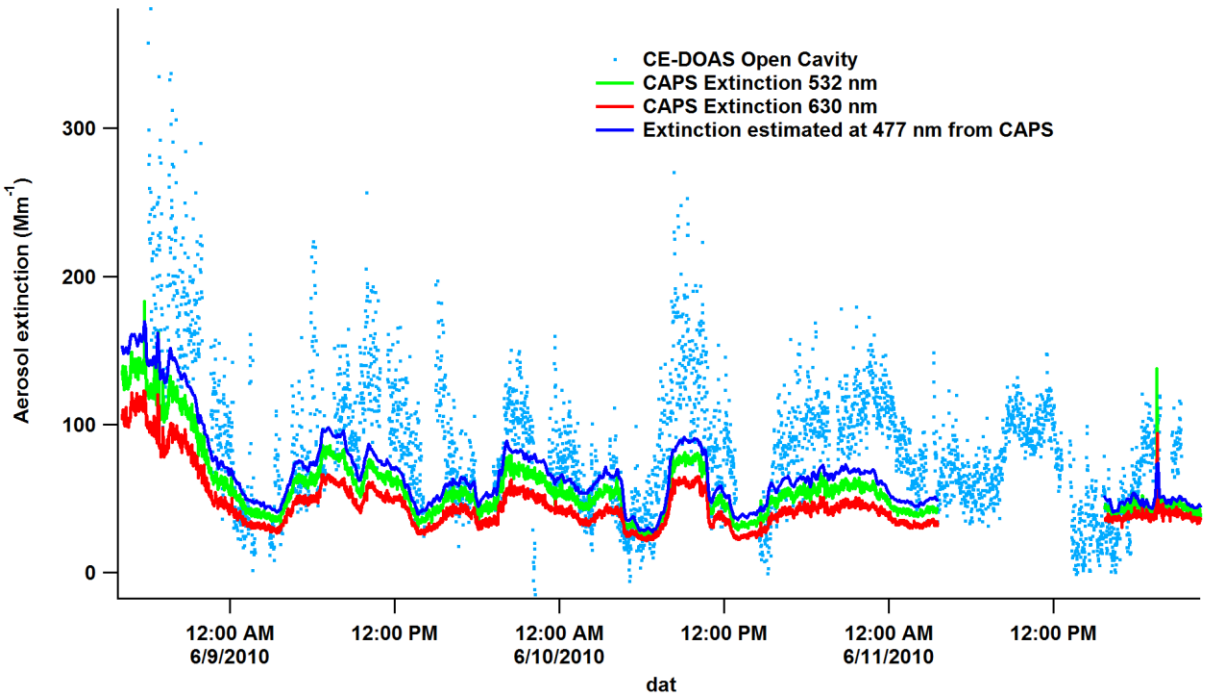

Figure 7.3: Aerosol extinction measured by open-cavity CE-DOAS at 477 nm compared to ground site measurements by the CAPS instrument.

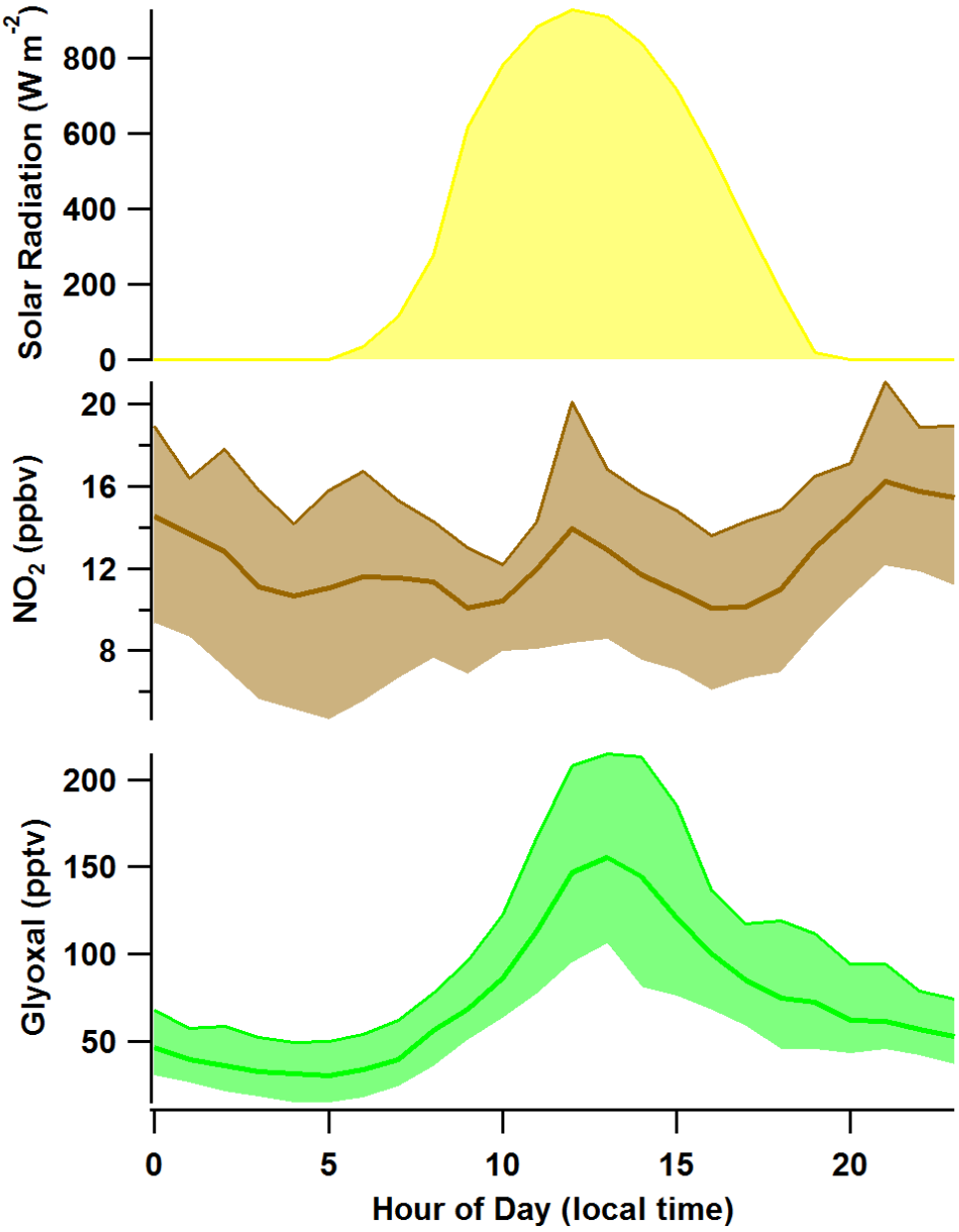

Figure 7.4: Diurnal averaged profiles of solar radiation, NO_2 and glyoxal during CalNex.

7.2 Four-Mile Fire Measurements

During September 2010 the open and closed cavity LED-CE-DOAS instrument was installed in the ATMOS Observatory on the roof of Folsom Field at the University of Colorado. During this period a forest fire in the local foothills impacted the local air quality. The Four-Mile Fire started burning at approximately 10:00 am on September 6, 2010 and burned until the 11th when it was finally considered contained after burning more than 6000 acres and more than 100 structures making it the most destructive fire in the history of the city of Boulder. The measurement site was east and south of the burn area but was highly impacted by the smoke plume as the winds changed, blowing smoke into and out of Boulder (see Figure A7.3 in the Appendix).

7.2.1 Results and Summary

The first day of the fire was sampled by the closed-cavity CE-DOAS instrument over the Labor Day holiday weekend and the data for the first day of the fire are shown in Figure 7.5. Elevated levels of glyoxal were first seen around 13:00 on the 6th coinciding with the sampling of the smoke plume from the fire (as shown in the reduced solar radiation of the weather station on the top of the Duane Physics building at the University of Colorado). Later that evening as the fire progressed the plume appears to have moved back over the sample site and now elevated levels of both glyoxal and methyl glyoxal are observed. The spectral proof for the detection of methyl glyoxal is shown in Figure 7.6. This represents the first optical detection of methyl glyoxal in ambient air of which I am aware. Interestingly, the relative levels of glyoxal and methyl glyoxal are very different for the two plume samples which may be due to changes in the burn intensity or of mixing time of the air sampled (smoke diluted and then subjected to photochemistry)

On the morning of September 7, the instrument was switched to measure in open-cavity mode and the aerosol extinction was retrieved and is shown in Figure 7.7. The aerosol is elevated

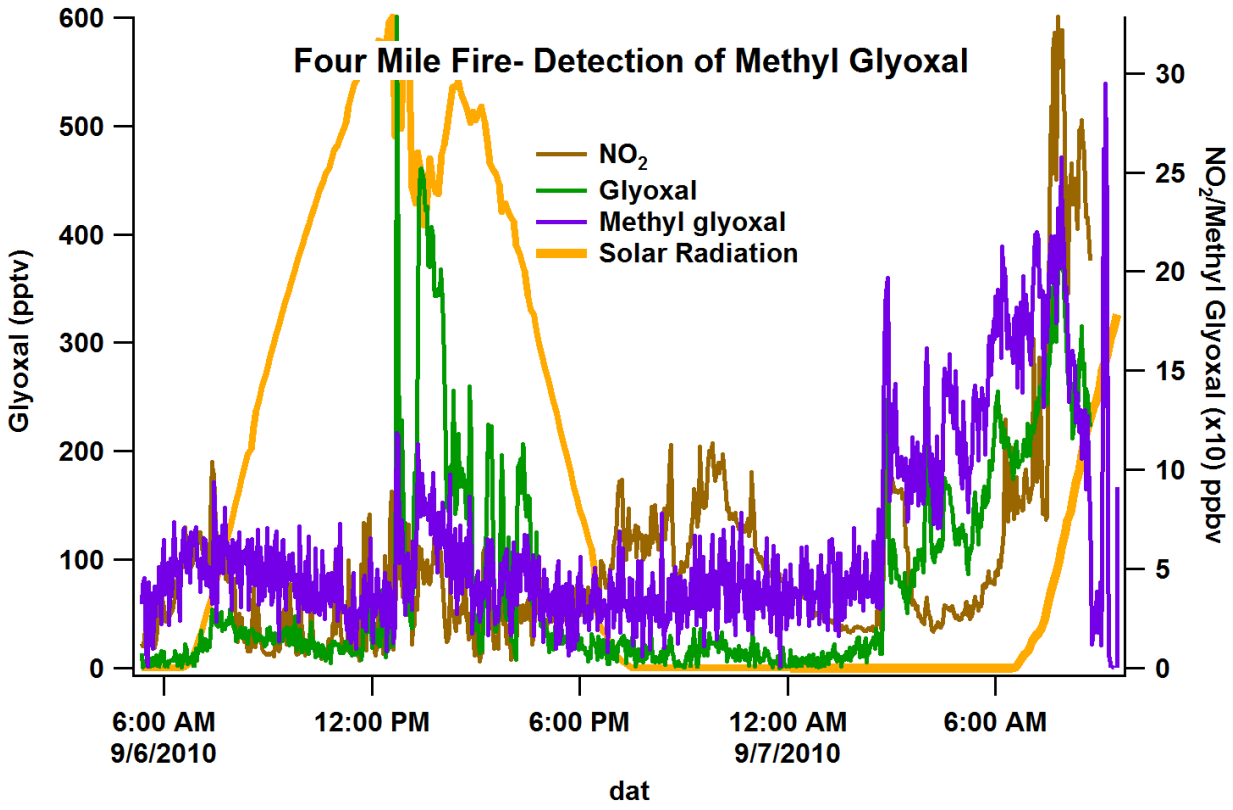

Figure 7.5: Detection of NO2, glyoxal and methyl glyoxal on September 6 and 7, 2010 during the Fourmile Canyon Fire. Levels of up to 2 ppbv of methyl glyoxal are detected in the early morning of September 7.

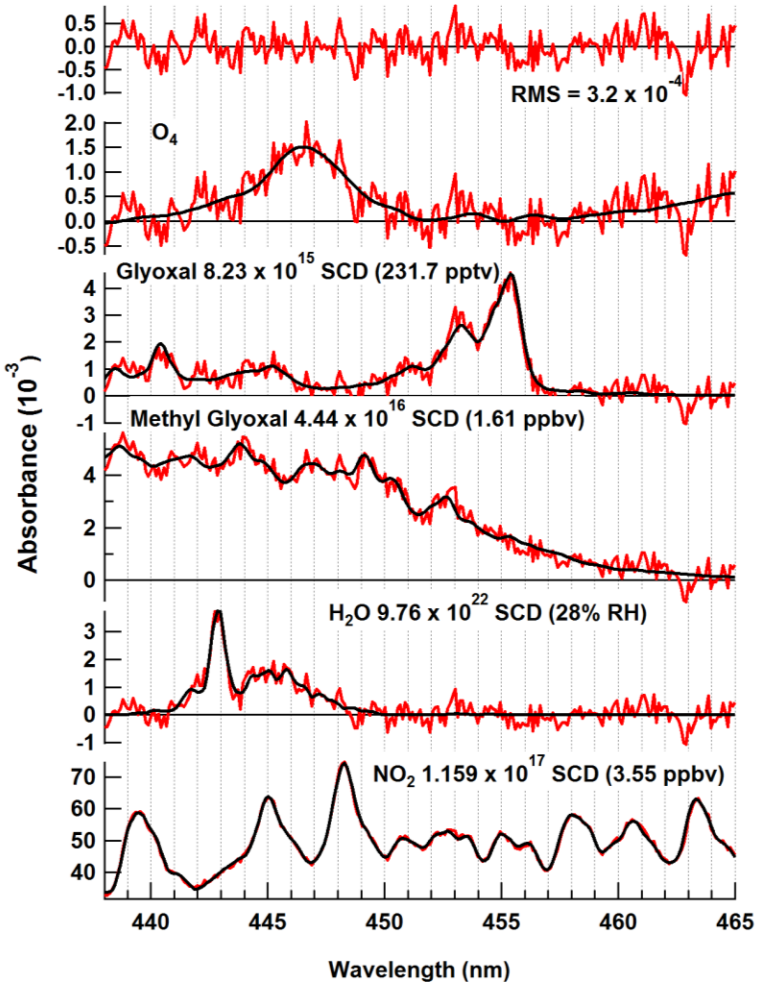

Figure 7.6: Fitted spectra from 4:00 AM on September 7, 2010.

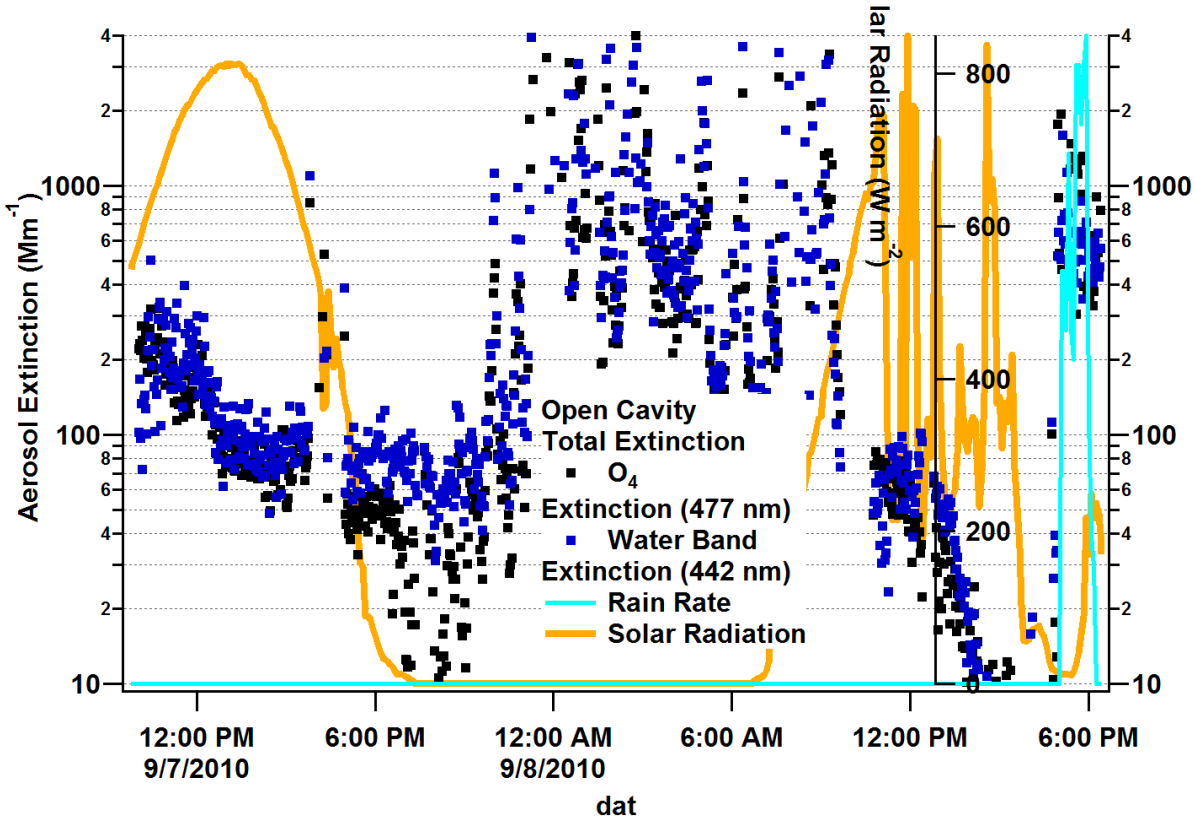

Figure 7.7: Aerosol extinction measured at 442 and 477 nm by LED-CE-DOAS during the Fourmile Canyon Fire.

to the point of no signal reaching the detector at various points in the time-series shown. Measurements ended when a thunderstorm deposited water onto the cavity mirrors in spite of the roof protecting the cavities as well as the mirror purges. High aerosol extinction is observed during the evening of September 7 while the daytime measurements were relatively clear (no direct sampling of the smoke plume appears to impact the measured solar radiation. On the evening of the 8th the rain appears to be raining out the aerosol as the extinction drops below 10 Mm^{-1}. The LED-CE-DOAS instrument here measured spectroscopically methyl glyoxal for the first time and was able to retrieve the aerosol extinction during times impacted by the Fourmile Canyon fire.

7.3 Future Developments and Deployments

The successful deployment of the LED-CE-DOAS instrument at CalNex and during the Fourmile Fire as well as at atmospheric chambers (Chapters 5 and 6) has lead to the deployment of the instrument for the measurement of glyoxal during several other past and projected field campaigns. Further development of the instrument has included the containment of the instrument in a weather proof box (gun case) and modification to run at a high sample rate (2 Hz) to measure the flux of glyoxal over the ocean. The initial tests at CalNex and chamber studies made possible these developments and exploration of the ruggedness of the instrument.

Chapter IIX

8 Summary

A Light Emitting Diode Cavity Enhanced Differential Optical Absorption Spectrometer (LED-CE-DOAS) instrument has been designed, assembled and applied to measure trace gases. The instrument has a very high sensitivity in a small instrument foot-print (Chapter 2) and is applied to measurements at atmospheric simulation chambers (Chapters 5 and 6) and field measurements (Chapter 7). The compact nature of the folded light path has further been used to investigate the physical and chemical properties of oxygen collision pairs and dimer molecules at a variety of temperatures (O_4, Chapter 3) and to measure Rayleigh Scattering cross-sections (Chapter 4). The findings of these studies demonstrate the unique potential that coupling of optical cavities with Differential Optical Absorption Spectroscopy has to advance the atmospheric sciences. The findings of this work are as follows:

1. A strong LED coupled with high reflectivity mirrors and DOAS retrievals enables low detections limits, while maintaining the ability to demonstrate on-line 'control' over cavity alignment. The method is based on excellent signal to noise measurements of O_4 at atmospheric conditions as part of each spectrum. The path length calculation only requires a pressure reading as input. Similarly, measurements of the H_2O in combination with relative humidity and temperature can also be used as a path length calibration (Chapter 2).

2. The use of DOAS retrievals makes the instrument independent to variation in the light-source that limits retrievals based on absolute intensity. Even though LEDs are more stable than other broad-band sources (e.g. Xe-arc lamps) they still exhibit variability (intensity and structure, see Section 2.2.1.1). The stability of the DOAS retrieval allows for the averaging of many spectra to reduce photon-shot noise and increase sensitivity.
3. For the first time, the O_4 (O_2-O_2 collision pair) absorption cross-sections are measured by means of a polychromatic light source in an optical cavity under atmospheric conditions. The measurements provide high quality reference spectra for DOAS retrievals (point 1) for CEAS applications as well as remote sensing techniques (Chapter 3).
4. Temperature dependant measurements of O_2-O_2 collision pair absorption show that at all temperatures and pressures in the atmosphere the O_4 absorption will be due to collisions, not a bound state and will scale with the square of the density. Previous findings attributing an increase in atmospheric absorption with respect to temperature to dimer formation are here identified as the effect of the changing band-shape with temperature, while the integral cross-section remains constant. The bond strength of the O_4 dimer is not large enough to expect dimer formation under conditions found in the atmosphere (500-760 Torr, 200-300K) (Chapter 3).
5. New measurements of Rayleigh scattering cross-sections for the N_2, Ar, O_2 and air are presented. They validate the mirror curve equations and constrain the possible errors (or bias) in using incorrect σ_{Ray} which can be large and compound when considering the mirror reflectivity and extinction in a BBCEES analysis (Chapter 4).
6. The CE-DOAS technique has been compared with the FT-IR and PTR-MS at NCAR as well as FT-IR, White-Cell DOAS, laser induced phosphorescence (LIP), and Broadband

Cavity Enhanced Absorption Spectroscopy (BBCEAS) at EUPHORE and has been shown to be an accurate and transferrable standard when compared to other cavity instruments as well as FT-IR. The limit of detection of CE-DOAS can be as low as 3 pptv in 1 minute which is comparable to LIP. The primary benefit of CE-DOAS consists in a direct calibration from the absorption cross-section spectra (accurate to ~3%), as well as the ability to measure small concentrations of species on top of large backgrounds of compounds that absorb in the same range (Chapter 5).

7. CE-DOAS is applied in atmospheric simulation chambers, and shown to sensitively and selectively probe reaction products of important VOCs such as isoprene. Understanding the production of minor products such as glyoxal and methyl glyoxal disproportionately affects our understanding of the global budget of these compounds because of the extremely large production of isoprene in the biosphere (Chapter 6).
8. CE-DOAS provides a stable, field deployable technique suitable for the measurement of atmospheric trace gases. DOAS retrievals allow for the robust retrieval of data independent of instrument instabilities that could be caused by lamp drift, mirror degradation, cavity de-alignment, or other environmental variables. Open-path measurements using CE-DOAS are shown to be possible without the loss of calibration, and allow for the retrieval of gas phase species without the use of an inlet and in the presence of particles using O_4 as a path length standard (Chapter 7).

References

U.S. Clean Air Act:http://www.epa.gov/air/caa/2008

Abjean, R., Mehu, A., and Johannin, A.: Interferometric Measurement of Refraction Indices of Helium and Neon in Ultra Violet, Comptes Rendus Hebdomadaires des Seances de l Academie des Sciences Serie B, 271, 835-&, 1970a.

Abjean, R., Mehu, A., and Johannin, A.: Interferometric Measurement of Refraction Indices of Nitrogen and Argon in Ultraviolet, Comptes Rendus Hebdomadaires des Seances de l Academie des Sciences Serie B, 271, 411-&, 1970b.

Aquilanti, V., Ascenzi, D., Bartolomei, M., Cappelletti, D., Cavalli, S., de Castro Vítores, M., and Pirani, F.: Molecular Beam Scattering of Aligned Oxygen Molecules. The Nature of the Bond in the O_2-O_2 Dimer, J.Am.Chem.Soc., 121, 10794-10802, 1999a.

Aquilanti, V., Ascenzi, D., Bartolomei, M., Cappelletti, D., Cavalli, S., de Castro Vítores, M., and Pirani, F.: Quantum Interference Scattering of Aligned Molecules: Bonding in O_4 and Role in Spin Coupling, Phys.Rev.Lett., 82, 69-72, 1999b.

Aquilanti, V., Carmona-Novillo, E., and Pirani, F.: Quantum mechanics of molecular oxygen clusters: rotovibrational dimer dynamics from realistic potential energy surfaces, Phys.Chem.Chem.Phys., 4, 4970-4978, 2002.

Atkinson, R. and Arey, J.: Atmospheric degradation of volatile organic compounds, Chem.Rev., 103, 4605-4638, 2003.

Atkinson, R., Aschmann, S. M., Winer, A. M., and Pitts, J. N.: Gas-Phase Reaction of NO2 with Alkenes and Dialkenes, International Journal of Chemical Kinetics, 16, 697-706, 1984.

Baidar, S., Oetjen, H., Coburn, S., Dix, B., Ortega, I., Sinreich, R., and Volkamer, R.: The CU Airborne MAX-DOAS instrument: ground based validation, and vertical profiling of aerosol extinction and trace gases, Atmos.Meas.Tech.Discuss., 5, 7243-7292, 2012.

Ball, S. M., Hollingsworth, A. M., Humbles, J., Leblanc, C., Potin, P., and McFiggans, G.: Spectroscopic studies of molecular iodine emitted into the gas phase by seaweed, Atmos.Chem.Phys.Discuss., 9, 26329-26376, 2009.

Ball, S. M. and Jones, R. L.:Broadband Cavity Ring-Down Spectroscopy, in: Cavity Ring-Down Spectroscopy: Techniques and Applications, Berden, G and Englen, R, John Wiley and Sons LTD,Chichester,89-111, 2009a.

Ball, S. M. and Jones, R. L.:Cavity Ring-Down Spectroscopy in Analytical Chemistry, in: Cavity Ring-Down Spectroscopy: Techniques and Applications, Berden, G and Englen, R, John Wiley and Sons LTD,Chichester,89-111, 2009b.

Ball, S. M., Langridge, J. M., and Jones, R. L.: Broadband cavity enhanced absorption spectroscopy using light emitting diodes, Chem.Phys.Lett., 398, 68-74, 2004.

Bates, D. R.: Rayleigh-Scattering by Air, Planetary and Space Science, 32, 785-790, 1984.

Berndt, T.: Formation of carbonyls and hydroperoxyenals (HPALDs) from the OH radical reaction of isoprene for low-NOx conditions: influence of temperature and water vapour content, Journal of Atmospheric Chemistry, 69, 253-272, 2012.

Berndt, T. and Böge, O.: Atmospheric reaction of OH radicals with 1,3-butadiene and 4-hydroxy-2-butenal, Journal of Physical Chemistry A, 111, 12099-12105, 2007.

Betterton, E. A. and Hoffmann, M. R.: Henry's law constants of some environmentally important aldehydes, Envir.Sci.Technol., 22, 1415-1418, 1988.

Biennier, L., Romanini, D., Kachanov, A., Campargue, A., Bussery-Honvault, B., and Bacis, R.: Structure and rovibrational analysis of the $[O_2(^1\Delta_g)_{v=0}]_2 \leftarrow [O_2(^3\Sigma_g^-)_{v=0}]_2$ transition of the O_2 dimer, J.Chem.Phys., 112, 6309-6321, 2000.

Biskos, G., Paulsen, D., Russell, L. M., Buseck, P. R., and Martin, S. T.: Prompt deliquescence and efflorescence of aerosol nanoparticles, Atmos.Chem.Phys., 6, 4633-4642, 2006.

Blake, A. J. and McCoy, D. G.: The pressure dependence of the Herzberg photoabsorption continuum of oxygen, J.Quant.Spectrosc.Radiat.Transfer, 38, 113-120, 1987.

Blickensderfer, R. P. and Ewing, G. E.: Collision-Induced Absorption Spectrum of Gaseous Oxygen at Low Temperatures and Pressures. II. The Simultaneous Transitions $^1\Delta_g + {}^1\Delta g \leftarrow {}^3\Sigma_g^- + {}^3\Sigma_g^-$ and $^1\Delta_g + {}^1\Sigma_g^+ \leftarrow 3\Sigma_g^- + 3\Sigma_g^-$, J.Chem.Phys., 51, 5284-5289, 1969.

Bloss, C., Wagner, V., Bonzanini, A., Jenkin, M. E., Wirtz, K., Martin-Reviejo, M., and Pilling, M. J.: Evaluation of detailed aromatic mechanisms (MCMv3 and MCMv3.1) against environmental chamber data, Atmos.Chem.Phys., 5, 623-639, 2005.

Bodhaine, B. A., Wood, N. B., Dutton, E. G., and Slusser, J. R.: On Rayleigh Optical Depth Calculations, J.Atmos.Oceanic Technol., 16, 1854-1861, 1999.

Bogumil, K., Orphal, J., Homann, T., Voigt, S., Spietz, P., Fleischmann, O. C., Vogel, A., Hartmann, M., Kromminga, H., Bovensmann, H., Frerick, J., and Burrows, J. P.: Measurements of molecular absorption spectra with the SCIAMACHY pre-flight model: instrument characterization and reference data for atmospheric remote-sensing in the 230–2380 nm region, J.Photochem.Photobio., A, 157, 167-184, 2003.

Brown, S. S.: Absorption spectroscopy in high-finesse cavities for atmospheric studies, Chem.Rev., 103, 5219-5238, 2003.

Bruns, M., Buehler, S. A., Burrows, J. P., Heue, K. P., Platt, U., Pundt, I., Richter, A., Rozanov, A., Wagner, T., and Wang, P.: Retrieval of Profile Information from Airborne Multiaxis UV-Visible Skylight Absorption Measurements, Appl.Opt., 43, 4415-4426, 2004.

Campargue, A., Biennier, L., Kachanov, A., Jost, R., Bussery-Honvault, B., Veyret, V., Churassy, S., and Bacis, R.: Rotationally resolved absorption spectrum of the O_2 dimer in the visible range, Chem.Phys.Lett., 288, 734-742, 1998.

Carlton, A., Wiedinmyer, C., and Kroll, J.: A review of Secondary Organic Aerosol (SOA) formation from isoprene, Atmos.Chem.Phys., 9, 4987-5005, 2009.

Chen, J. and Venables, D. S.: A broadband optical cavity spectrometer for measuring weak near-ultraviolet absorption spectra of gases, Atmos.Meas.Tech.Discuss., 3, 4571-4602, 2010.

Coburn, S., Dix, B., Sinreich, R., and Volkamer, R.: Development and Characterization of the CU Ground MAX-DOAS Instrument: lowering RMS noise and first measurements of BrO, IO, and CHOCHO near Pensacola, FL, Atmos.Meas.Tech., 4, 2421-2439, 2011.

Crounse, J. D., Knap, H. C., Ornso, K. B., Jorgensen, S., Paulot, F., Kjaergaard, H. G., and Wennberg, P. O.: Atmospheric Fate of Methacrolein. 1. Peroxy Radical Isomerization Following Addition of OH and O-2, Journal of Physical Chemistry A, 116, 5756-5762, 2012.

Cuthbertson, C. and Cuthbertson, M.: The Refraction and Dispersion of Neon and Helium, Proceedings of the Royal Society of London.Series A, Containing Papers of a Mathematical and Physical Character, 135, 40-47, 1932.

Dianov-Klokov, V. I.: Absorption spectrum of oxygen at pressures from 2 to 35 atm in the region from 12600 to 3600 A, Opt.Spectrosc., 16, 224-227, 1964.

Dibble, T. S.: Intramolecular Hydrogen Bonding and Double H-Atom Transfer in Peroxy and Alkoxy Radicals from Isoprene, J.Phys.Chem.A, 108, 2199-2207, 2004a.

Dibble, T. S.: Prompt Chemistry of Alkenoxy Radical Products of the Double H-Atom Transfer of Alkoxy Radicals from Isoprene, J.Phys.Chem.A, 108, 2208-2215, 2004b.

Dixneuf, S., Ruth, A. A., Vaughan, S., Varma, R. M., and Orphal, J.: The time dependence of molecular iodine emission from Laminaria digitata, Atmos.Chem.Phys., 9, 823-829, 2009.

Eberhard, W. L.: Correct equations and common approximations for calculating Rayleigh scatter in pure gases and mixtures and evaluation of differences, Appl.Opt., 49, 1116-1130, 2010.

Ellis, J. W. and Kneser, H. O.: Combination relationship in the absorption spectrum of the liquid oxygen, Zeitschrift für Physik, 86, 583-591, 1933.

Ervens, B. and Volkamer, R.: Glyoxal processing by aerosol multiphase chemistry: towards a kinetic modeling framework of secondary organic aerosol formation in aqueous particles, Atmos.Chem.Phys., 10, 8219-8244, 2010.

Fayt, C. and Van Roosendael, M.: WinDOAS User Manual, 2001.

Fiedler, S. E., Hese, A., and Ruth, A. A.: Incoherent broad-band cavity-enhanced absorption spectroscopy, Chem.Phys.Lett., 371, 284-294, 2003.

Fu, T. M., Jacob, D. J., Wittrock, F., Burrows, J. P., Vrekoussis, M., and Henze, D. K.: Global budgets of atmospheric glyoxal and methyl glyoxal, and implications for formation of secondary organic aerosols, J.Geophys.Res., 113, D15303, 2008.

Galloway, M. M., Chhabra, P. S., Chan, A. W. H., Surratt, J. D., Flagan, R. C., Seinfeld, J. H., and Keutsch, F. N.: Glyoxal uptake on ammonium sulphate seed aerosol: reaction products and reversibility of uptake under dark and irradiated conditions, Atmos.Chem.Phys., 9, 3331-3345, 2009.

Galloway, M. M., Huisman, A. J., Yee, L. D., Chan, A. W. H., Loza, C. L., Seinfeld, J. H., and Keutsch, F. N.: Yields of oxidized volatile organic compounds during the OH radical initiated oxidation of isoprene, methyl vinyl ketone, and methacrolein under high-NOx conditions, Atmos.Chem.Phys., 11, 10779-10790, 2011.

Gherman, T., Venables, D. S., Vaughan, S., Orphal, J., and Ruth, A. A.: Incoherent broadband cavity-enhanced absorption spectroscopy in the near-ultraviolet: Application to HONO and NO2, Envir.Sci.Technol., 42, 890-895, 2008.

Gomez-Martin, J. C., Spietz, P., and Burrows, J. P.: Kinetic and mechanistic studies of the I-2/O-3 photochemistry, J.Phys.Chem.A, 111, 306-320, 2007.

Greenblatt, G. D., Orlando, J. J., Burkholder, J. B., and Ravishankara, A. R.: Absorption measurements of oxygen between 330 and 1140 nm, J.Geophys.Res., 95, 18577-18582, 1990.

Guenther, A., Geron, C., Pierce, T., Lamb, B., Harley, P., and Fall, R.: Natural emissions of non-methane volatile organic compounds; carbon monoxide, and oxides of nitrogen from North America, Atmos.Environ., 34, 2205-2230, 2000.

Guenther, A. B., Jiang, X., Heald, C. L., Sakulyanontvittaya, T., Duhl, T., Emmons, L. K., and Wang, X.: The Model of Emissions of Gases and Aerosols from Nature version 2.1 (MEGAN2.1): an extended and updated framework for modeling biogenic emissions, Geoscientific Model Development, 5, 1471-1492, 2012.

Hasson, A. S., Tyndall, G. S., Orlando, J. J., Singh, S., Hernandez, S. Q., Campbell, S., and Ibarra, Y.: Branching Ratios for the Reaction of Selected Carbonyl-Containing Peroxy Radicals with Hydroperoxy Radicals, J.Phys.Chem.A, 116, 6264-6281, 2012.

Hastings, W. P., Koehler, C. A., Bailey, E. L., and De Haan, D. O.: Secondary organic aerosol formation by glyoxal hydration and oligomer formation: Humidity effects and equilibrium shifts during analysis, Envir.Sci.Technol., 39, 8728-8735, 2005.

Heald, C. L., Wilkinson, M. J., Monson, R. K., Alo, C. A., Wang, G., and Guenther, A.: Response of isoprene emission to ambient CO2 changes and implications for global budgets, Global Change Biology, 15, 1127-1140, 2009.

Herman, L.: Spectre d'absorption de l'oxygene, Ann.Phys.(Paris), 1, 548-611, 1939.

Hermans, C.,Measurement of absorption cross sections and spectroscopic molecular parameters: O_2 and its collisonal induced absorption:http://www.aeronomie.be/spectrolab/o2.htm4-9-20104-26-3010.

Hermans, C., Vandaele, A., Carleer, M., Fally, S., Colin, R., Jenouvrier, A., Coquart, B., and Mérienne, M. F.: Absorption cross-sections of atmospheric constituents: NO_2, O_2, and H_2O, Environ.Sci.& Pollut.Res., 6, 151-158, 1999.

Herriott, D. R. and Schulte, H. J.: Folded Optical Delay Lines, Appl.Opt., 4, 883-889, 1965.

Hildebrandt, L., Donahue, N. M., and Pandis, S. N.: High formation of secondary organic aerosol from the photo-oxidation of toluene, Atmos.Chem.Phys., 9, 2973-2986, 2009.

Hönninger, G.: Referenzspektren reaktiver Halogenverbindungen für DOAS-Messungen, Diploma-Arbeit, University of Heidelburg, 1999.

Horowitz, A., Schneider, W., and Moortgat, G. K.: The role of oxygen dimer in oxygen photolysis in the Herzberg continuum: a temperature dependence study, J.Phys.Chem., 93, 7859-7863, 1989.

Huisman, A. J., Hottle, J. R., Coens, K. L., DiGangi, J. P., Galloway, M. M., Kammrath, A., and Keutsch, F. N.: Laser-Induced Phosphorescence for the in Situ Detection of Glyoxal at Part per Trillion Mixing Ratios, Anal.Chem., 80, 5884-5891, 2008.

Ianni, J. C.:A Comparison of the Bader-Deuflhard and the Cash-Karp Runge-Kutta Integrators for the GRI-MECH 3.0 Model Based on the Chemical Kinetics Code Kintecus, in: Computational Fluid and Solid Mechanics, Bathe, K. J., Elsevier Science Ltd.,Oxford, UK.,1368-1372, 2003.

Ip, H. S. S., Huang, X. H. H., and Yu, J. Z.: Effective Henry's law constants of glyoxal, glyoxylic acid, and glycolic acid, Geophys.Res.Lett., 36, L01802, 2009.

Jang, M., Czoschke, N. M., Lee, S., and Kamens, R. M.: Heterogeneous Atmospheric Aerosol Production by Acid-Catalyzed Particle-Phase Reactions, Science, 298, 814-817, 2002.

Jenkin, M. E., Wyche, K. P., Evans, C. J., Carr, T., Monks, P. S., Alfarra, M. R., Barley, M. H., McFiggans, G. B., Young, J. C., and Rickard, A. R.: Development and chamber evaluation of the MCM v3.2 degradation scheme for beta-caryophyllene, Atmos.Chem.Phys., 12, 5275-5308, 2012.

Johnston, H. S., Paige, M., and Yao, F.: Oxygen absorption cross sections in the herzberg continuum and between 206 and 327 K, J.Geophys.Res., 89, 11661-11665, 1984.

Jordan, A., Haidacher, S., Hanel, G., Hartungen, E., Märk, L., Seehauser, H., Schottkowsky, R., Sulzer, P., and Märk, T. D.: A high resolution and high sensitivity proton-transfer-reaction time-of-flight mass spectrometer (PTR-TOF-MS), International Journal of Mass Spectrometry, 286, 122-128, 2009.

Karl, T., Guenther, A., Turnipseed, A., Tyndall, G., Artaxo, P., and Martin, S.: Rapid formation of isoprene photo-oxidation products observed in Amazonia, Atmos.Chem.Phys., 9, 7753-7767, 2009.

Kern, C., Trick, S., Rippel, B., and Platt, U.: Applicability of light-emitting diodes as light sources for active differential optical absorption spectroscopy measurements, Appl.Opt., 45, 2077-2088, 2006.

King, L. V.: On the Complex Anisotropic Molecule in Relation to the Dispersion and Scattering of Light, Proceedings of the Royal Society of London.Series A, 104, 333-357, 1923.

Kroll, J. H., Ng, N. L., Murphy, S. M., Varutbangkul, V., Flagan, R. C., and Seinfeld, J. H.: Chamber studies of secondary organic aerosol growth by reactive uptake of simple carbonyl compounds, J.Geophys.Res., 110, D23207, 2005.

Kurosu, T., Chance, K., and Volkamer, R.: Global measurements of OClO, BrO, HCHO, and CHO-CHO from the Ozone Monitoring Instruments on EOS Aura, EOS Trans.EGU, 86, Fall Meet. Suppl. Abstract A54B-01, 2005.

Kurucz, R. L., Furenlid, I., Brault, J., and Testerman, L.: Solar Atlas from 296 to 1300 nm,

Langridge, J. M., Ball, S. M., and Jones, R. L.: A compact broadband cavity enhanced absorption spectrometer for detection of atmospheric NO_2 using light emitting diodes, Analyst, 131, 916-922, 2006.

Langridge, J. M., Ball, S. M., Shillings, A. J. L., and Jones, R. L.: A broadband absorption spectrometer using light emitting diodes for ultrasensitive, in situ trace gas detection, Rev.Sci.Instrum., 79, 2008a.

Langridge, J. M., Laurila, T., Watt, R. S., Jones, R. L., Kaminski, C. F., and Hult, J.: Cavity enhanced absorption spectroscopy of multiple trace gas species using a supercontinuum radiation source, Opt.Express, 16, 10178-10188, 2008b.

Leonard, P. J.: Refractive indices, Verdet constants, and Polarizabilities of the inert gases, Atomic Data and Nuclear Data Tables, 14, 21-37, 1974.

Liggio, J., Li, S. M., and McLaren, R.: Reactive uptake of glyoxal by particulate matter, J.Geophys.Res., 110, D10304, 2005.

Long, C. A. and Ewing, G. E.: The infrared spectrum of bound state oxygen dimers in the gas phase, Chem.Phys.Lett., 9, 225-229, 1971.

Long, C. A. and Ewing, G. E.: Spectroscopic investigation of van der Waals molecules. I. The infrared and visible spectra of $(O_2)_2$, J.Chem.Phys., 58, 4824-4834, 1973.

Massoli, P., Kebabian, P. L., Onasch, T. B., Hills, F. B., and Freedman, A.: Aerosol Light Extinction Measurements by Cavity Attenuated Phase Shift (CAPS) Spectroscopy: Laboratory Validation and Field Deployment of a Compact Aerosol Particle Extinction Monitor, Aerosol Science and Technology, 44, 428-435, 2010.

McKellar, A. R. W., Rich, N. H., and Welsh, H. L.: Collision-Induced Vibrational and Electronic Spectra of Gaseous Oxygen at Low Temperatures, Can.J.Phys., 50, 1-9, 1972.

McManus, J. B., Kebabian, P. L., and Zahniser, M. S.: Astigmatic mirror multipass absorption cells for long-path-length spectroscopy, Appl.Opt., 34, 3336-3348, 1995.

Meinen, J., Thieser, J., Platt, U., and Leisner, T.: Using a high finesse optical resonator to provide a long light path for differential optical absorption spectroscopy: CE-DOAS, Atmos.Meas.Tech., 8, 10665-10695, 2008.

Meller, R., Raber, W., Crowley, J. N., Jenkin, M. E., and Moortgat, G. K.: The UV-visible absorption spectrum of methylglyoxal, J.Photochem.Photobio., A, 62, 163-171, 1991.

Miles, R. E. H., Rudic, S., Orr-Ewing, A. J., and Reid, J. P.: Measurements of the wavelength dependent extinction of aerosols by cavity ring down spectroscopy, Phys.Chem.Chem.Phys., 12, 3914-3920, 2010.

Morville, J., Romanini, D., Campargue, A., and Bacis, R.: OPO-pulsed CRDS of the visible collision induced absorption bands of oxygen at low temperature, Chem.Phys.Lett., 363, 498-504, 2002.

Myriokefalitakis, S., Vrekoussis, M., Tsigaridis, K., Wittrock, F., Richter, A., Brühl, C., Volkamer, R., Burrows, J. P., and Kanakidou, M.: The influence of natural and anthropogenic secondary sources on the glyoxal global distribution, Atmos.Chem.Phys., 8, 4965-4981, 2008.

Naus, H. and Ubachs, W.: Visible Absorption Bands of the (O2)2 Collision Complex at Pressures Below 760 Torr, Appl.Opt., 38, 3423-3428, 1999.

Naus, H. and Ubachs, W.: Experimental verification of Rayleigh scattering cross sections, Opt.Lett., 25, 347-349, 2000.

Navarro, M. A., Dusanter, S., Hites, R. A., and Stevens, P. S.: Radical Dependence of the Yields of Methacrolein and Methyl Vinyl Ketone from the OH-Initiated Oxidation of Isoprene under NOx-Free Conditions, Envir.Sci.Technol., 45, 923-929, 2011.

Newnham, D. A. and Ballard, J.: Visible absorption cross sections and integrated absorption intensities of molecular oxygen (O_2 and O_4), J.Geophys.Res., 103, 28801-28815, 1998.

O'Keefe, A. and Deacon, D. A. G.: Cavity Ring-Down Optical Spectrometer for Absorption-Measurements Using Pulsed Laser Sources, Rev.Sci.Instrum., 59, 2544-2551, 1988.

Orlando, J. J. and Tyndall, G. S.: Mechanisms for the reactions of OH with two unsaturated aldehydes: Crotonaldehyde and acrolein, Journal of Physical Chemistry A, 106, 12252-12259, 2002.

Orlando, J. J., Tyndall, G. S., Nickerson, K. E., and Calvert, J. G.: The temperature dependence of collision-induced absorption by oxygen near 6 μm, J.Geophys.Res., 96, 20755-20760, 1991.

Orphal, J. and Ruth, A. A.: High-resolution Fourier-transform cavity-enhanced absorption spectroscopy in the near-infrared using an incoherent broad-band light source, Opt.Express, 16, 19232-19243, 2008.

Paulot, F., Crounse, J. D., Kjaergaard, H. G., Kuerten, A., St Clair, J. M., Seinfeld, J. H., and Wennberg, P. O.: Unexpected Epoxide Formation in the Gas-Phase Photooxidation of Isoprene, Science, 325, 730-733, 2009.

Peeters, J., Nguyen, T., and Vereecken, L.: HOx radical regeneration in the oxidation of isoprene, Phys.Chem.Chem.Phys., 11, 5935-5939, 2009.

Peeters, J. and Nguyen, T. L.: Unusually Fast 1,6-H Shifts of Enolic Hydrogens in Peroxy Radicals: Formation of the First-Generation C-2 and C-3 Carbonyls in the Oxidation of Isoprene, Journal of Physical Chemistry A, 116, 6134-6141, 2012.

Pegoraro, E., Rey, A., Greenberg, J., Harley, P., Grace, J., Malhi, Y., and Guenther, A.: Effect of drought on isoprene emission rates from leaves of Quercus virginiana Mill, Atmos.Environ., 38, 6149-6156, 2004.

Penndorf, R.: Tables of the Refractive Index for Standard Air and the Rayleigh Scattering Coefficient for the Spectral Region Between 0.2 and 20.0-Mu and Their Application to Atmospheric Optics, J.Opt.Soc.Am., 47, 176-182, 1957.

Perner, D. and Platt, U.: Absorption of light in the atmosphere by collision pairs of oxygen $(O_2)_2$, Geophys.Res.Lett., 7, 1053-1056, 1980.

Pfeilsticker, K., Bösch, H., Camy-Peyret, C., Fitzenberger, R., Harder, H., and Osterkamp, H.: First atmospheric profile measurements of UV/visible O4 absorption band intensities: Implications for the spectroscopy, and the formation enthalpy of the O_2-O_2 dimer, Geophys.Res.Lett., 28, 4595-4598, 2001.

Pfeilsticker, K., Erle, F., and Platt, U.: Absorption of Solar Radiation by Atmospheric O_4, J.Atmos.Sci., 54, 933-939, 1997.

Platt, U., Meinen, J., Pöhler, D., and Leisner, T.: Broadband Cavity Enhanced Differential Optical Absorption Spectroscopy (CE-DOAS); applicability and corrections, Atmos.Meas.Tech., 2, 713-723, 2009.

Platt, U. and Stutz, J.: Differential optical absorption spectroscopy : principles and applications, 1, Springer Verlag, 2008, Berlin, 2008.

Pope, C. A. and Dockery, D. W.: Health effects of fine particulate air pollution: Lines that connect, J.Air Waste Manage.Assoc., 56, 709-742, 2006.

Rothman, L. S., Gordon, I. E., Barbe, A., Benner, D. C., Bernath, P. F., Birk, M., Boudon, V., Brown, L. R., Campargue, A., Champion, J. P., Chance, K., Coudert, L. H., Dana, V., Devi, V. M., Fally, S., Flaud, J. M., Gamache, R. R., Goldman, A., Jacquemart, D., Kleiner, I., Lacome, N., Lafferty, W. J., Mandin, J. Y., Massie, S. T., Mikhailenko, S. N., Miller, C. E., Moazzen-Ahmadi, N., Naumenko, O. V., Nikitin, A. V., Orphal, J., Perevalov, V. I., Perrin, A., Predoi-Cross, A., Rinsland, C. P., Rotger, M., Simeckovβ, M., Smith, M. A. H., Sung, K., Tashkun, S. A., Tennyson, J., Toth, R. A., Vandaele, A. C., and Vander Auwera, J.: The HITRAN 2008 molecular spectroscopic database, J.Quant.Spectrosc.Radiat.Transfer, 110, 533-572, 2006.

Ryerson, T. B., Andrews, A. E., Angevine, W. M., Bates, T. S., Brock, C. A., Cairns, B., Cohen, R. C., Cooper, O. R., de Gouw, J. A., Fehsenfeld, F. C., Ferrare, R. A., Fischer, M. L., Flagan, R. C., Goldstein, A. H., Hair, J. W., Hardesty, R. M., Hostetler, C. A., Jimenez, J. L., Langford, A. O., McCauley, E., McKeen, S. A., Molina, L. T., Nenes, A., Oltmans, S. J., Parrish, D. D., Pederson, J. R., Pierce, R. B., Prather, K., Quinn, P. K., Seinfeld, J. H., Senff, C. J., Sorooshian, A., Stutz, J., Surratt, J. D., Trainer, M., Volkamer, R., Williams, E. J., and Wofsy, S. C.: The 2010 California research at the Nexus of air quality and climate change (CalNex) field study, J.Geophys.Res., n/a, 2013.

Salow, H. and Steiner, W.: The forces caused by interaction of the oxygen absorption spectra, Zeitschrift fur Physik, 99, 137-158, 1936.

Schuster, G., Labazan, I., and Crowley, J. N.: A cavity ring down/cavity enhanced absorption device for measurement of ambient NO_3 and N_2O_5, Atmos.Meas.Tech., 2, 1867-1381, 2009.

Shardanand and Rao, A. D. P.: Absolute Rayleigh Scattering Cross Sections of Gases and Freons of Stratospheric Interest in the Visible and Ultraviolet Regions,

Shetter, R. E., Davidson, J. A., Cantrell, C. A., and Calvert, J. G.: Temperature Variable Long Path Cell for Absorption-Measurements, Rev.Sci.Instrum., 58, 1427-1428, 1987.

Sihler, H., Kern, C., Pohler, D., and Platt, U.: Applying light-emitting diodes with narrowband emission features in differential spectroscopy, Opt.Lett., 34, 3716-3718, 2009.

Sinreich, R., Volkamer, R., Filsinger, F., Frieß, U., Kern, C., Platt, U., Sebastian, O., and Wagner, T.: MAX-DOAS detection of glyoxal during ICARTT 2004, Atmos.Chem.Phys., 7, 1293-1303, 2007.

Sneep, M., Ityaksov, D., Aben, I., Linnartz, H., and Ubachs, W.: Temperature-dependent cross sections of collision-induced absorption resonances at 477 and 577 nm, J.Quant.Spectrosc.Radiat.Transfer, 98, 405-424, 2006.

Sneep, M. and Ubachs, W.: Cavity ring-down measurement of the O_2–O_2 collision-induced absorption resonance at 477 nm at sub-atmospheric pressures, J.Quant.Spectrosc.Radiat.Transfer, 78, 171-178, 2003.

Sneep, M. and Ubachs, W.: Direct measurement of the Rayleigh scattering cross section in various gases, J.Quant.Spectrosc.Radiat.Transfer, 92, 293-310, 2005.

Solomon, S., Portmann, R. W., Sanders, R. W., and Daniel, J. S.: Absorption of solar radiation by water vapor, oxygen, and related collision pairs in the Earth's atmosphere, J.Geophys.Res., 103, 3847-3858, 1998.

Sprengnether, M., Demerjian, K. L., Donahue, N. M., and Anderson, J. G.: Product analysis of the OH oxidation of isoprene and 1,3-butadiene in the presence of NO, Journal of Geophysical Research-Atmospheres, 107, 2002.

Stavrakou, T., Müller, J. F., De Smedt, I., Van Roozendael, M., Kanakidou, M., Vrekoussis, M., Wittrock, F., Richter, A., and Burrows, J. P.: The continental source of glyoxal estimated by the synergistic use of spaceborne measurements and inverse modelling, Atmos.Chem.Phys., 9, 8431-8446, 2009.

Strutt, J. W. L. R.: On the transmission of light through an atmosphere containing small particles in suspension, and on the origin of the blue of the sky, Philos.Mag., 47, 375-384, 1899.

Strutt, J. W. L. R.: A Re-Examination of the Light Scattered by Gases in Respect of Polarisation. I. Experiments on the Common Gases, Proceedings of the Royal Society of London.Series A, 97, 435-450, 1920.

Strutt, R. J.: The Light Scattered by Gases: Its Polarisation and Intensity, Proceedings of the Royal Society of London.Series A, 95, 155-176, 1918.

Stutz, J. and Platt, U.: Numerical analysis and estimation of the statistical error of differential optical absorption spectroscopy measurements with least-squares methods, Appl.Opt., 35, 6041-6053, 1996.

Tabisz, G. C., Allin, E. J., and Welsh, H. L.: Interpretation of the visible and near-infrared absorption spectra of compressed oxygen as collision-induced electronic transitions, Can.J.Phys., 47, 2859-2871, 1969.

Tan, Y., Perri, M. J., Seitzinger, S. P., and Turpin, B. J.: Effects of Precursor Concentration and Acidic Sulfate in Aqueous Glyoxal–OH Radical Oxidation and Implications for Secondary Organic Aerosol, Envir.Sci.Technol., 43, 8105-8112, 2009.

Taraborrelli, D., Lawrence, M. G., Butler, T. M., Sander, R., and Lelieveld, J.: Mainz Isoprene Mechanism 2 (MIM2): an isoprene oxidation mechanism for regional and global atmospheric modelling, Atmos.Chem.Phys., 9, 2751-2777, 2009.

Thalman, R. and Volkamer, R.: Inherent calibration of a blue LED-CE-DOAS instrument to measure iodine oxide, glyoxal, methyl glyoxal, nitrogen dioxide, water vapour and aerosol extinction in open cavity mode, Atmos.Meas.Tech., 3, 1797-1814, 2010.

Tiedje, H. F., DeMille, S., MacArthur, L., and Brooks, R. L.: Cavity ring-down spectroscopy of transient O_2-O_2 dimers, Can.J.Phys., 79, 773-781, 2001.

Triki, M., Cermak, P., Mejean, G., and Romanini, D.: Cavity-enhanced absorption spectroscopy with a red LED source for NO_x trace analysis, Appl.Phys.B, 91, 195-201, 2008.

Tuazon, E. C., Alvarado, A., Aschmann, S. M., Atkinson, R., and Arey, J.: Products of the gas-phase reactions of 1,3-butadiene with OH and NO3 radicals, Envir.Sci.Technol., 33, 3586-3595, 1999.

Tuazon, E. C. and Atkinson, R.: A Product Study of the Gas-Phase Reaction of Methyl Vinyl Ketone with the OH Radical in the Presence of NO_x, International Journal of Chemical Kinetics, 21, 1141-1152, 1989.

Tuazon, E. C. and Atkinson, R.: A Product Study of the Gas-Phase Reaction of Isoprene with the OH Radical in the Presence of NO_x, International Journal of Chemical Kinetics, 22, 1221-1236, 1990.

U.S.Standard Atmosphere, U.S. Standard Atmosphere: http://ntrs.nasa.gov/archive/nasa/casi.ntrs.nasa.gov/19770009539_1977009539.pdf 1976

Vandaele, A. C., Hermans, C., Fally, S., Carleer, M., Colin, R., Merienne, M. F., Jenouvrier, A., and Coquart, B.: High-resolution Fourier transform measurement of the NO_2 visible and near-infared absorption cross sections: Temperature and pressure effects, J.Geophys.Res., 107, 4348, 2002.

Varma, R. M., Venables, D. S., Ruth, A. A., Heitmann, U., Schlosser, E., and Dixneuf, S.: Long optical cavities for open-path monitoring of atmospheric trace gases and aerosol extinction, Appl.Opt., 48, B159-B171, 2009.

Vaughan, S., Gherman, T., Ruth, A. A., and Orphal, J.: Incoherent broad-band cavity-enhanced absorption spectroscopy of the marine boundary layer species I_2, IO and OIO, Phys.Chem.Chem.Phys., 10, 4471-4477, 2008.

Venables, D. S., Gherman, T., Orphal, J., Wenger, J. C., and Ruth, A. A.: High sensitivity in situ monitoring of NO_3 in an atmospheric simulation chamber using incoherent broadband cavity-enhanced absorption spectroscopy, Envir.Sci.Technol., 40, 6758-6763, 2006.

Veres, P. R., Roberts, J. M., Cochran, A. K., Gilman, J. B., Kuster, W. C., Holloway, J. S., Graus, M., Flynn, J., Lefer, B., Warneke, C., and de Gouw, J.: Evidence of rapid production of organic acids in an urban air mass, Geophys.Res.Lett., 38, L17807, 2011.

Villalobos-Pietrini, R., Hernandez-Mena, L., Amador-Munoz, O., Munive-Colin, Z., Bravo-Cabrera, J. L., Gomez-Arroyo, S., Frias-Villegas, A., Waliszewski, S., Ramirez-Pulido, J., and Ortiz-Muniz, R.: Biodirected mutagenic chemical assay of PM_{10} extractable organic matter in Southwest Mexico City, Mutat.Res./Gen.Toxicol.Environ.Mutag., 634, 192-204, 2007.

Volkamer, R., Barnes, I., Platt, U., Molina, L. T., and Molina, M. J.: Remote Sensing of Glyoxal by Differential Optical Absorption Spectroscopy (DOAS): Advancements in Simulation Chamber and Field Experiments, 2005a.

Volkamer, R., Coburn, S., Dix, B., and Sinreich, R.: MAX-DOAS observations from ground, ship, and research aircraft: maximizing signal-to-noise to measure 'weak' absorbers, 2009a.

Volkamer, R., Coburn, S., Dix, B., and Sinreich, R.: The Eastern Pacific Ocean is a source for short lived trace gases: Glyoxal and Iodine Oxide, April 2010, 2010.

Volkamer, R., Etzkorn, T., Geyer, A., and Platt, U.: Correction of the oxygen interference with UV spectroscopic (DOAS) measurements of monocyclic aromatic hydrocarbons in the atmosphere, Atmos.Environ., 32, 3731-3747, 1998.

Volkamer, R., Ziemann, P. J., and Molina, M. J.: Secondary Organic Aerosol Formation from Acetylene (C_2H_2): seed effect on SOA yields due to organic photochemistry in the aerosol aqueous phase, Atmos.Chem.Phys., 9, 1907-1928, 2009b.

Volkamer, R., Coburn, S., Dix, B., and Sinreich, R.: MAX-DOAS observations from ground, ship, and research aircraft: maximizing signal-to-noise to measure 'weak' absorbers, 746203-746209, 2009c.

Volkamer, R., Molina, L. T., Molina, M. J., Shirley, T., and Brune, W. H.: DOAS measurement of glyoxal as an indicator for fast VOC chemistry in urban air, Geophys.Res.Lett., 32, L08806, 2005b.

Volkamer, R., San Martini, F., Molina, L. T., Salcedo, D., Jimenez, J. L., and Molina, M. J.: A missing sink for gas-phase glyoxal in Mexico City: Formation of secondary organic aerosol, Geophys.Res.Lett., 34, L19807, 2007.

Volkamer, R., Spietz, P., Burrows, J., and Platt, U.: High-resolution absorption cross-section of glyoxal in the UV-vis and IR spectral ranges, J.Photochem.Photobio., A, 172, 35-46, 2005c.

Volkamer, R. M.: Absorption von Sauerstoff im Herzberg I System und Anwendung auf Aromatenmessungen am EUropean PHOto REactor (EUPHORE)., Diploma thesis D-491, 1996.

Vrekoussis, M., Wittrock, F., Richter, A., and Burrows, J. P.: Temporal and spatial variability of glyoxal as observed from space, Atmos.Chem.Phys., 9, 4485-4504, 2009.

Wagner, T., von Friedeburg, C., Wenig, M., Otten, C., and Platt, U.: UV-visible observations of atmospheric O4 absorptions using direct moonlight and zenith-scattered sunlight for clear-sky and cloudy sky conditions, J.Geophys.Res., 107, AAC, 2002.

Washenfelder, R. A., Flores, J. M., Brock, C. A., Brown, S. S., and Rudich, Y.: Broadband measurements of aerosol extinction in the ultraviolet spectral region, Atmos.Meas.Tech.Discuss., 6, 113-157, 2013.

Washenfelder, R. A., Langford, A. O., Fuchs, H., and Brown, S. S.: Measurement of glyoxal using an incoherent broadband cavity enhanced absorption spectrometer, Atmos.Chem.Phys., 8, 7779-7793, 2008.

Washenfelder, R. A., Young, C. J., Brown, S. S., Angevine, W. M., Atlas, E. L., Blake, D. R., Bon, D. M., Cubison, M. J., de Gouw, J. A., Dusanter, S., Flynn, J., Gilman, J. B., Graus, M., Griffith, S., Grossberg, N., Hayes, P. L., Jimenez, J. L., Kuster, W. C., Lefer, B. L., Pollack, I. B., Ryerson, T. B., Stark, H., Stevens, P. S., and Trainer, M. K.: The glyoxal budget and its contribution to organic aerosol for Los Angeles, California, during CalNex 2010, J.Geophys.Res., 116, D00V02, 2011.

White, J. U.: Long Optical Paths of Large Aperture, J.Opt.Soc.Am., 32, 285-288, 1942.

Wiedensohler, A.: An approximation of the bipolar charge distribution for particles in the submicron size range, J.Aerosol Sci., 19, 387-389, 1988.

Wittrock, F., Richter, A., Oetjen, H., Burrows, J. P., Kanakidou, M., Myriokefalitakis, S., Volkamer, R., Beirle, S., Platt, U., and Wagner, T.: Simultaneous global observations of glyoxal and formaldehyde from space, Geophys.Res.Lett., 33, L16804, 2006.

Wu, T., Zhao, W., Chen, W., Zhang, W., and Gao, X.: Incoherent broadband cavity enhanced absorption spectroscopy for in situ measurements of NO_2 with a blue light emitting diode, Appl.Phys.B, 94, 85-94, 2009.

Yu, J., Jeffries, H. E., and Sexton, K. G.: Atmospheric photooxidation of alkylbenzenes--I. Carbonyl product analyses, Atmos.Environ., 31, 2261-2280, 1997.

Appendix A Supplemental Figures and Tables for Chapters 1-7

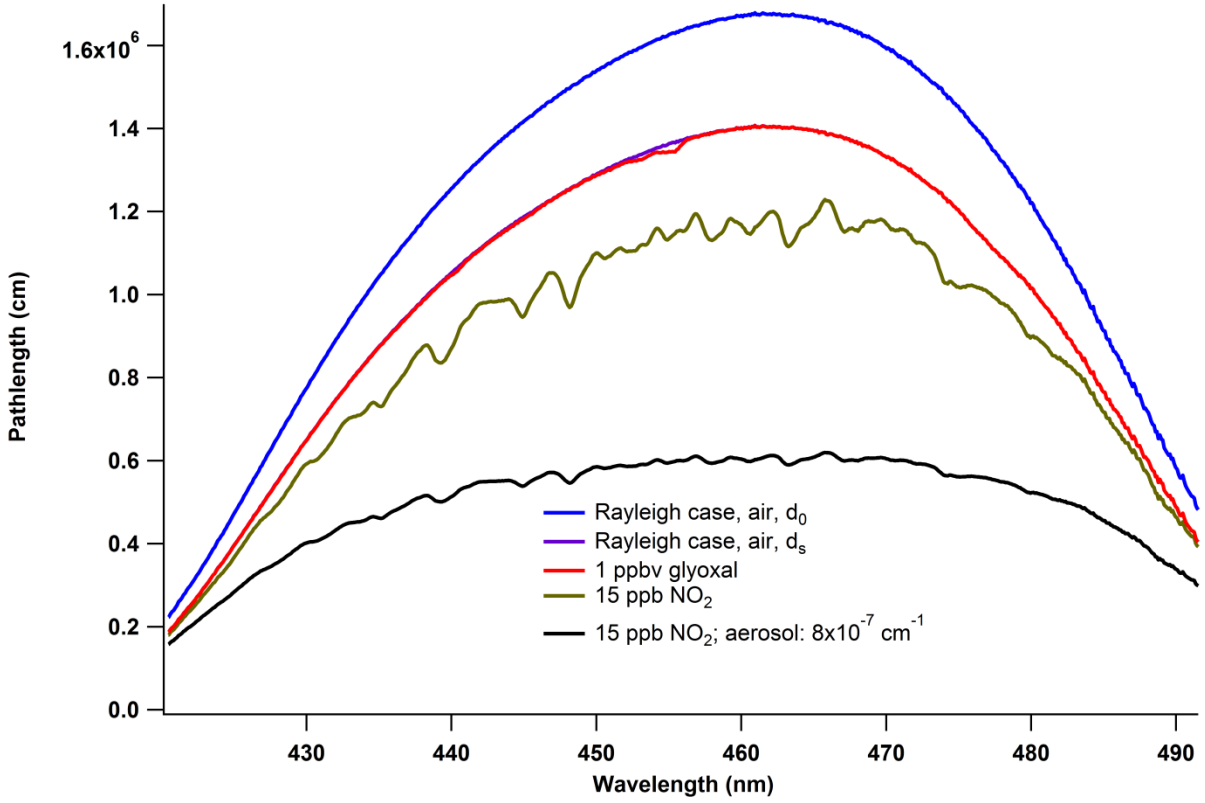

Figure A2.1: Effective path lengths in the cavity with given amounts of aerosol or trace gases, calculated using equation (2.1).

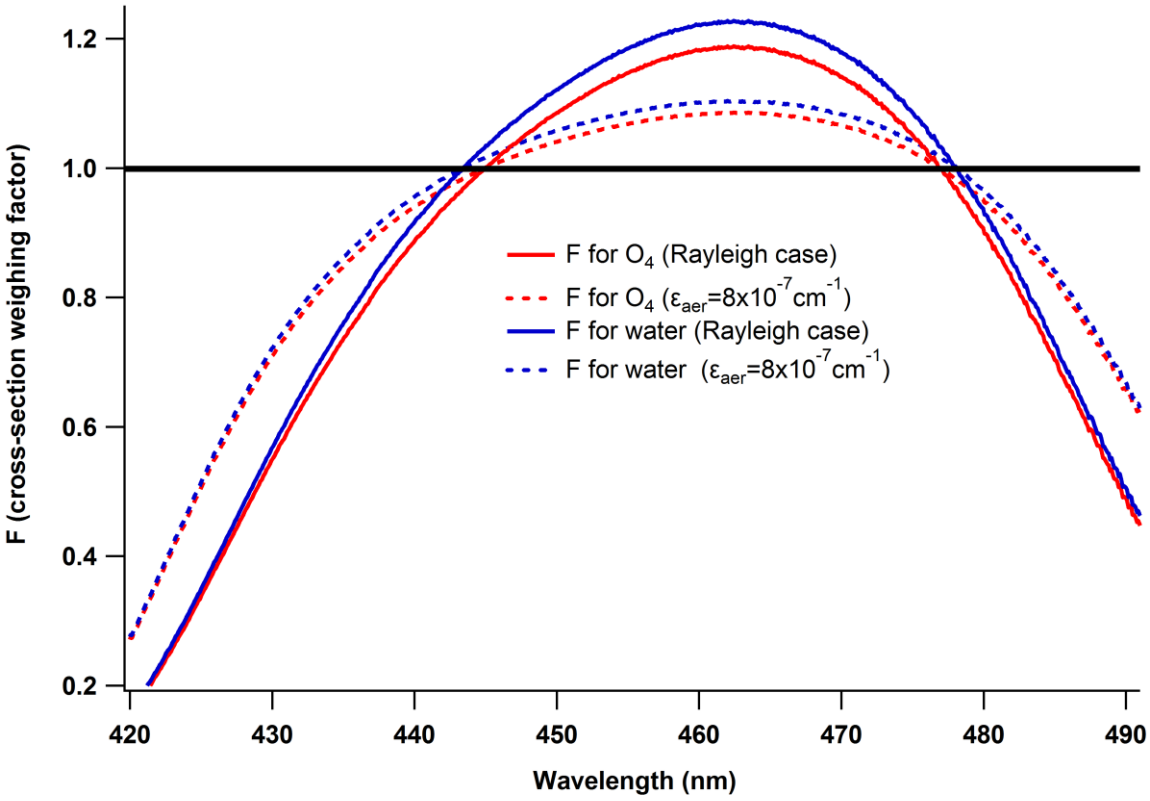

Figure A2.2: Absorption cross-section spectra weighting factors, F, calculated from equation (6) for the Rayleigh (solid lines) and aerosol cases (dotted lines) normalized at the O_4 wavelength (477nm, red) and the water wavelength (443nm, blue). The differences between the solid and the two dashed lines reflect the uncertainty in our RH measurement.

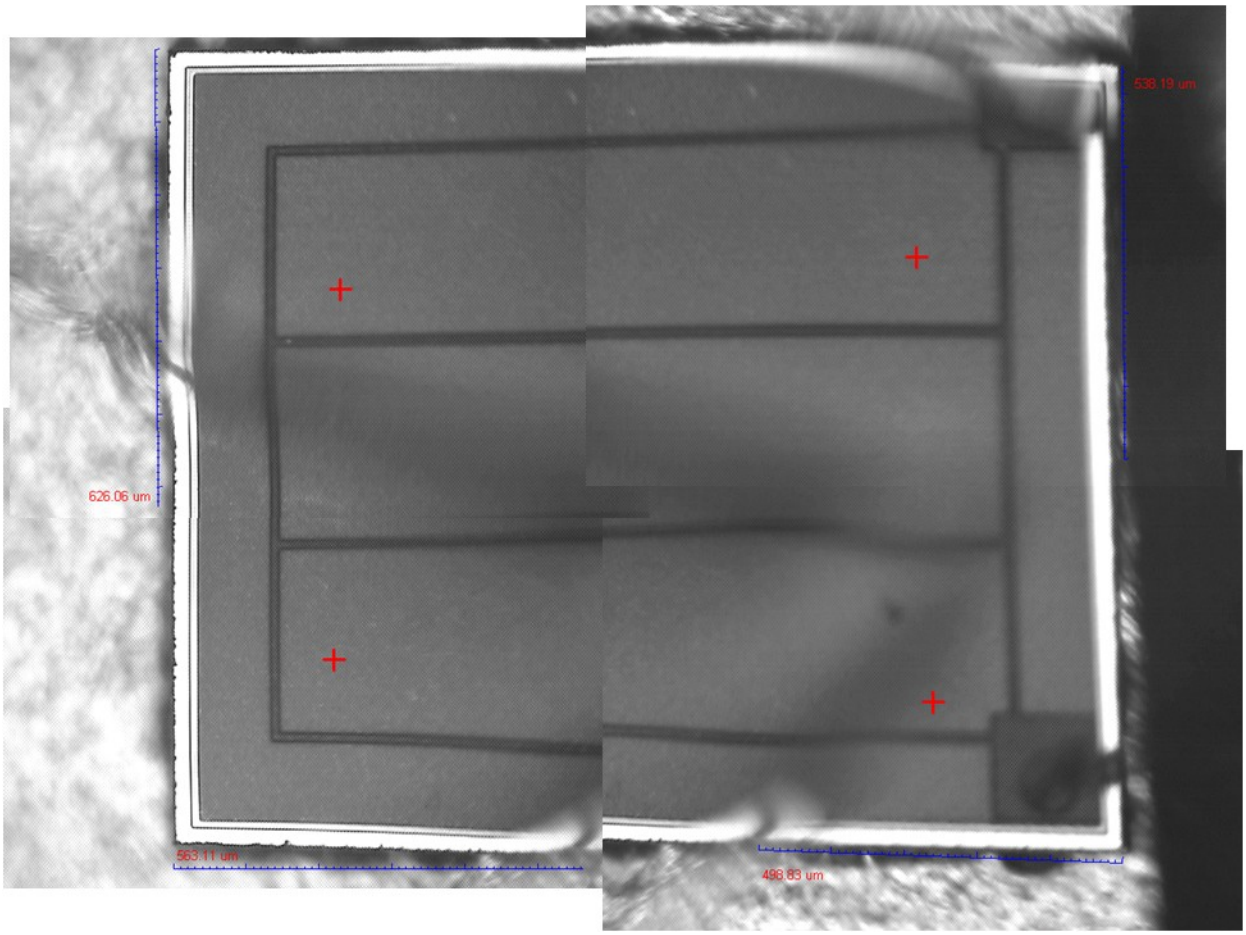

Figure A2.3: Image of LEDEngin LED chip. The chip is 1mm x 1mm in size.

Table A3.1: Description of Cavities for O_4 cross-section measurements

Cavity	O_4 Bands	Mirror Center λ	Reflectivity (Peak)	Range (nm)	Filters	Resolution FWHM (nm)	Grating (g/mm)	Light Source
UV	344[a], 360[a,b], 380[a]	355 (ATF)	0.99983	335-387	Pyrex plate, 325 LPF (CVI), UG11 (Schott)	0.32	1200	Xe-arc
Blue	446[a] 477[b]	455 (ATF)	0.99997	420-495	GG435(Schott), 500SWP (Thorlabs), 450 BPF (Thorlabs)	0.36	1200	LED LZ1-10B205
Green	532[a]	532 (ATF)	0.99998	510-555	OG515 (Schott), 550SWP (Newport)	0.38	1200	Green LED LZ1-10G105
Amber	577[b]	580 (crd-optics)	0.999978	550-596	550 LWP (Thorlabs), 600SWP (Thorlabs)	0.38	1200	Warm White LED LZ1-10WW00
Red	630[b]	630 (Los-Gatos)	0.99993	550-680	600 LWP (Thorlabs)	0.4 and 0.68	600	Red LED LZ1-10R205

[a]Measurement/Reference gas: O_2/Ar; [b]Measurement/Reference gas: Air/N_2;

Table A3.2: Comparison of Literature Data for O_4 absorption cross-sections

Study	Year	Temp	Wavelength (nm)	Peak ($x10^{-46}$ cm^5 $molecule^{-2}$)	Integral ($x10^{-43}$$cm^4$ $molecule^{-2}$)	Width (nm/cm^{-1})
Salow and Steiner #	1936	-	343.6	0.99	-	-
			360.7	3.6		
			380.3	2.1		
			446.4	0.3		
			477.0	5.3		
			532.3	0.4		
			577.3	7.7		
			629.9	5.3		
Hermans #	1939	-	477.3	8.0	-	-
			577.2	13		
			630.0	6.2		
Dianov-Klokov #	1964	-	360.5	4.4	-	-
			380.2	2.2		
			446.7	0.70		
			477.3	5.5		
			532.2	1.5		
			577.2	9.8		
			630.0	6.9		
			1065.2	12		
Blickensderfer and Ewing (data in Naus and Ubachs 1-σ?)	1969	78	477	-	2.5(4)	-
			577		6.1(4)	
			630		5.4(6)*	
		300	477		2.4(4)	
			577		3.5(4)	
			630		1.5(6)*	
Tabniz et al.	1969	577	-	-	4.63(7)	-
		630			3.47(7)	
McKellar et al.*	1972	90	477	17.4	2.47	-
			577	29.2	6.48	
			630	22	5.03	
		113	477	11.3	2.03	
			577	20.4	5.52	
			630	14.1	4.18	
		295	477	6.1	2.18	
			577	10.8	4.56	
			630	6.6	3.52	
Long and Ewing*	1973	87	577	35.8		7.3/220
Perner and Platt	1980	279	343.9	0.70(24)	-	1.6
			360.5	5.4(1.5)		4.9
			380.2	<1.4		~6
			444.0	1.0(12)		7.4
			476.9	5.9(1.8)		5.8
			575.0	16(6)		9.5

Greenblatt et al. (3-σ)	1990	296	343.4	1.2(1)	-	4.2
			360.5	4.1(4)		4.8
			380.2	2.4(2)		4.4
			446.7	0.57(6)		5.6
			477.3	6.3(6)		6.2
			532.2	1.0(1)		10.2
			577.2	11(1)		11.6
			630.0	7.2(7)		13.8
		196	360.8	5.7(6)		4.2
			380.2	3.7(4)		3.7
			477.3	7.6(13)		4.7
Volkamer (? Sigma)	1996	296	342.7	1.18(9)	-	5.8(5)
			360.8	5.42(7)		4.3(1)
			380.2	2.4(2)		3.6(2)
			477.1	6.1(3)		5.2(8)
			531.7	1.3(3)		13(8)
			576.9	10.3(3)		11.2(1)
			630.6	5.5-6.9(6)		14.(1)
Newnham and Ballard (3 Sigma, doesn't say in the paper, but reports the 3-σ values of Greenblatt)	1998	223	477	6.99(35)	1.629(21)	339(15)
			532	1.31(20)	0.404(11)	369(6)
			577	12.61(11)	4.3585(76)	
			630	8.8(13)	2.766(72)	
			630*	8.34(83)	2.9227(76)	
		283	477	1.23(38)	2.483(48)	
			532	11.75(20)	0.431(17)	
			577	7.9(15)	4.625(14)	
			630		2.769(99)	
			630*		3.025(17)	
Osterkamp et al. (data from Wagner 2002)	1998	204	477	7.9(3)		
			532	1.4(2)		
			577	12.2(4)		
		256	477	7.0(3)		
			532	1.2(2)		
			577	13.6(4)		
Hermans et al. (extracted from data from webpage)	1998	RT	343.96	0.983	0.307	3.65/309.5
			360.89	4.291	1.578	4.15/319.6
			380.25	2.467	0.771	4.06/280.6
			446.39	0.502	0.124	3.97/199.1
			477.10	6.553	1.99	5.36/235.3
			532.36	0.907	0.29	8.25/292.2
			577.5	11.01	4.23	11.0/331.8
			630.3	7.076	2.87	13.77/347.4
Naus and Ubachs (1σ)	1999	294	577	11.41(15)	4.66(9)	340(3)
			630	7.55(15)	3.19(9)	367(3
Tiedje et al. (1σ)	2001	-	577	12.07(30)	4.93(20)	/337(3)
			630	7.71(20)	3.26(14)	/360(3)
Wagner et al.	2002	241	360.5	5.70(50)		
			380.2	2.44(40)		
			477.3	7.80(20)		

			532.2	1.74(50)		
			577.2	13.50(40)		
			630.0	9.61(30)		
Morville et al. (1-sig)	2002	296	576.3	11.22(25)	-	345(2)
			629.3	7.2(3)	-	323(15)
		192.5	577.3	12.8(4)	-	292(2)
			629.3	8.7(3)	-	281(15)
		132	575.3	17.5(16)	-	276(2)
			629.3	11.6(1)	-	173(15)
Sneeps et al.	2006	294	477.79(6)	6.60(6)	2.34(6)	5.64(16)/247.1(68)
(294K 577 data from Naus			577.17*	11.5(1)	4.70(6)	11.5(1)/346.5(30)
and Ubachs)		268	577.3(1)	11.1(3)	4.47(13)	11.3(2)/342.3(71)
(1 sigma)		230	477.47(26)	5.78(23)	1.90(22)	5.2(6)/228(26)
		190	577.6(2)	12.6(5)	4.06(24)	9.6(3)/290(10)
		184	477.25(14)	7.33(20)	2.07(16)	4.5(3)/239(14)
Chen and Venables	2009	296	360.1	4.0	-	-

#Data reproduced from MPI Mainz database (http://www.atmosphere.mpg.de/enid/5db486bc26e00f61354f2fbe841be944,0/Spectra/Introduction_1rr.html)
*Data retrieved from graphs

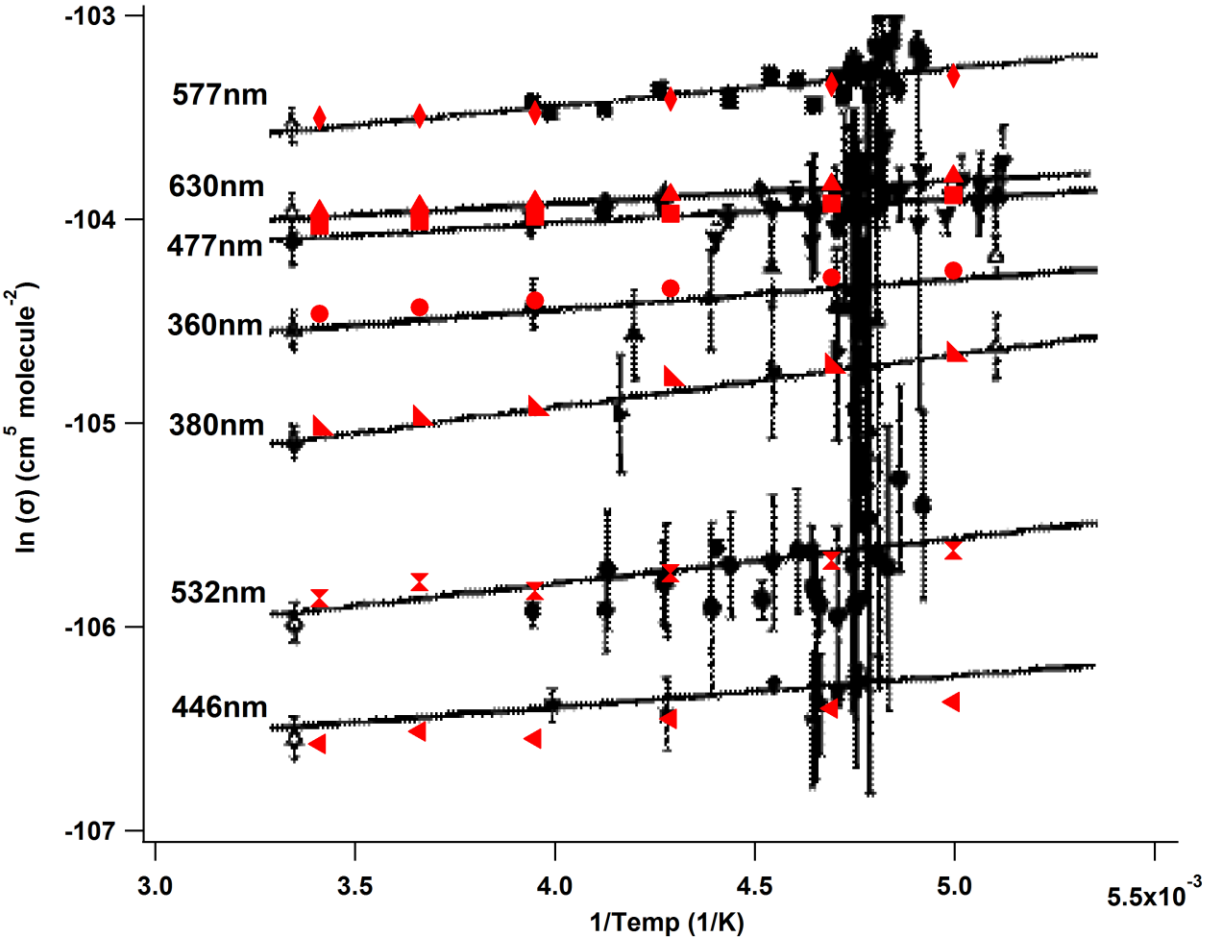

Figure A3.1: Comparison of Peak $\sigma_{O4\text{-}CIA}$ of this work to Figure 3 of Pfeilsticker et al. 2001.

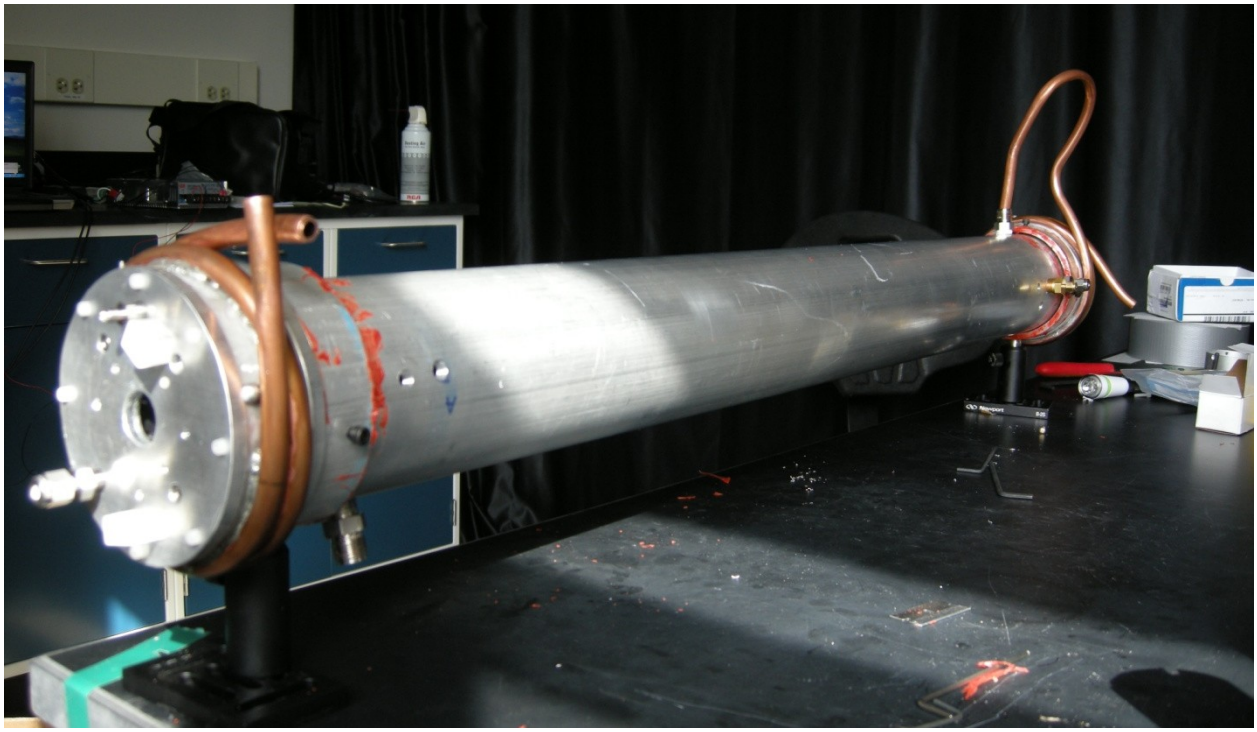

Figure A3.2: Assembled Temperature controlled cavity without insulating foam. Copper tubing is soldered to the end regions that hold the mirror mounts.

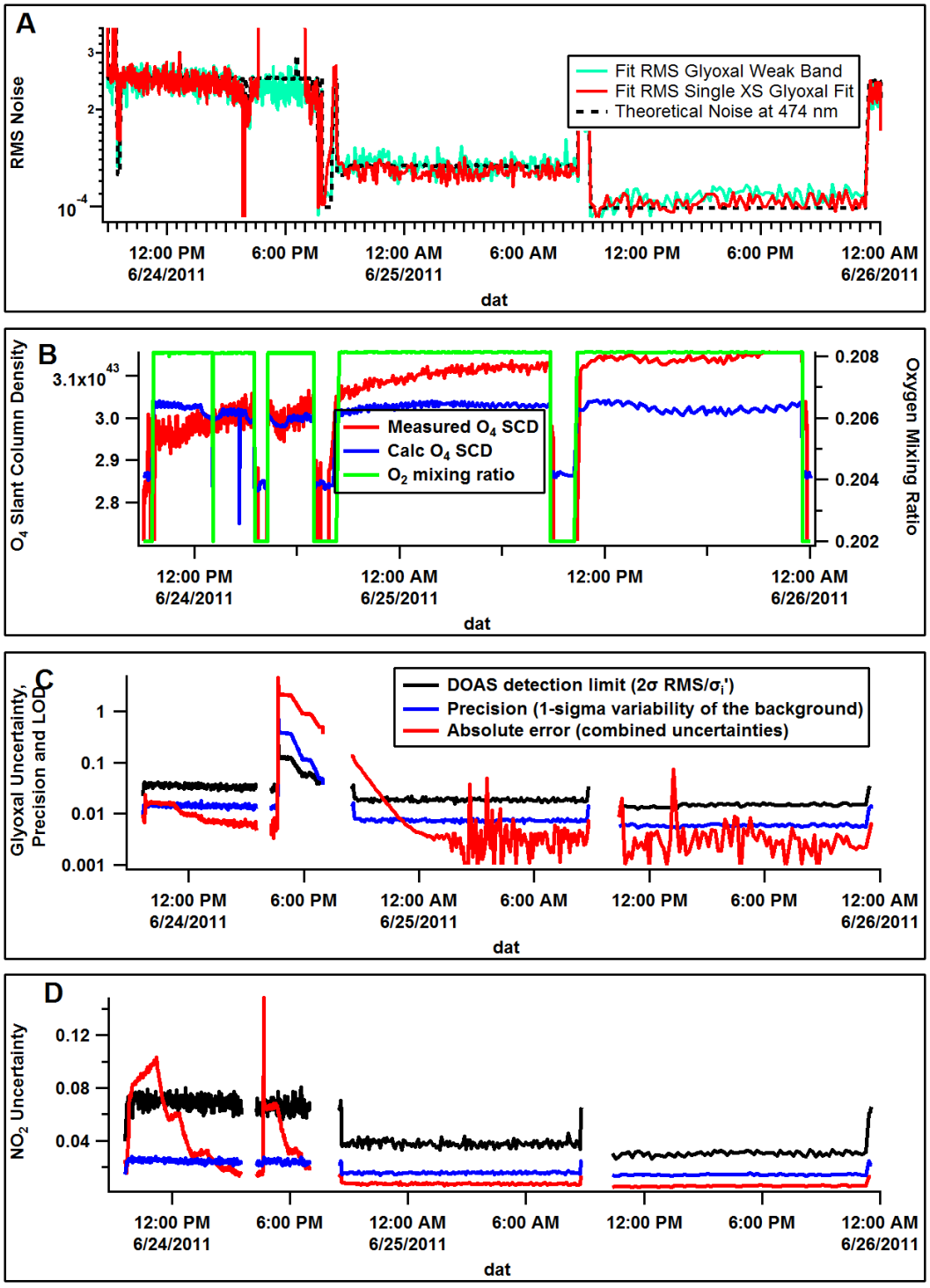

Figure A5.1: Theoretical noise comparison (A), O4 slant column density comparison (measured/calculated), and glyoxal (C) and NO_2 (D) uncertainty contributions from 24 June 2011 at EUPHORE during AlDiIn.

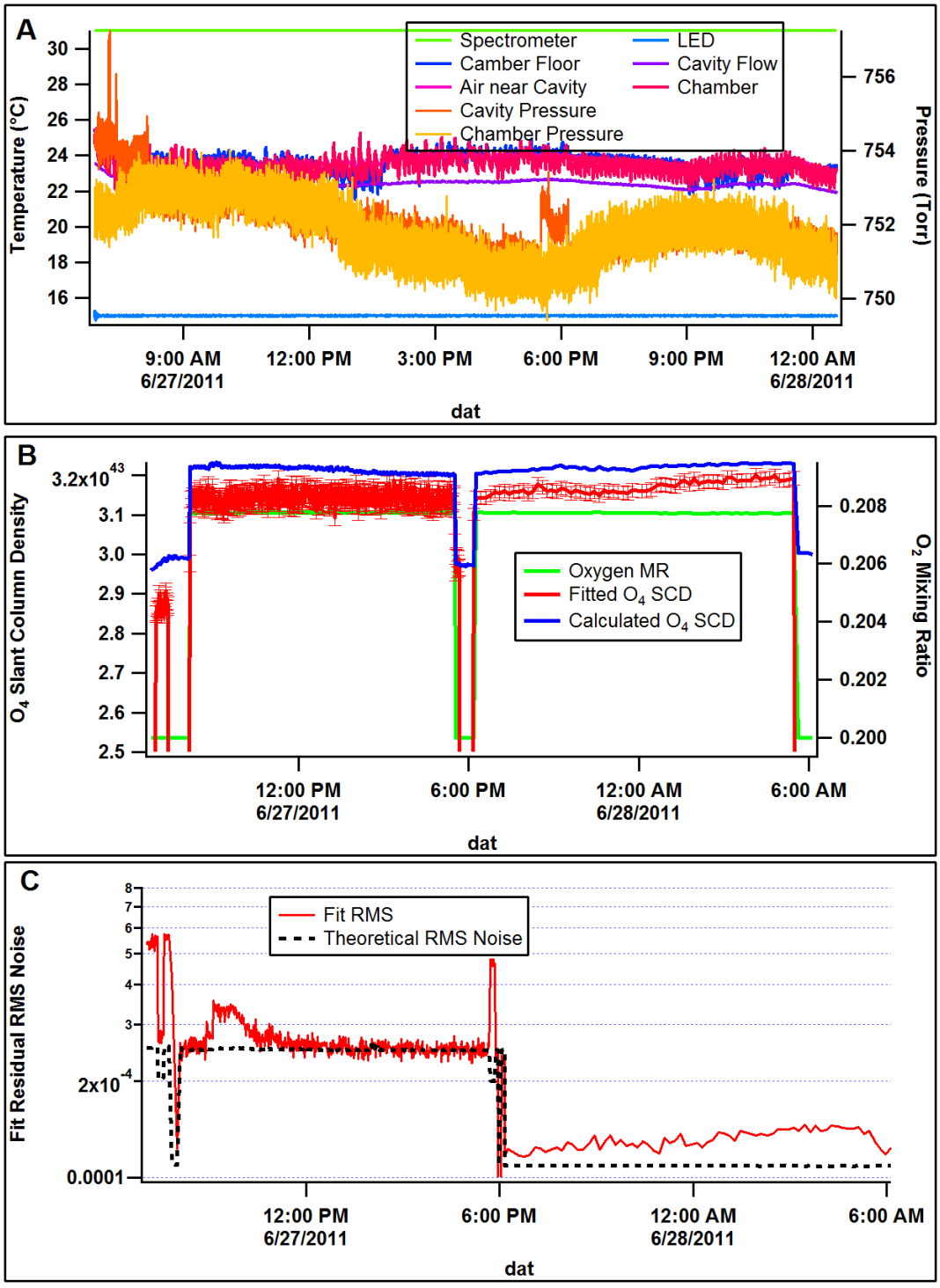

Figure A5.2: Environmental parameters (A), O4 slant column comparison (B) and theoretical noise comparison (C) from 27 June 2011 at EUPHORE during AlDiIn.

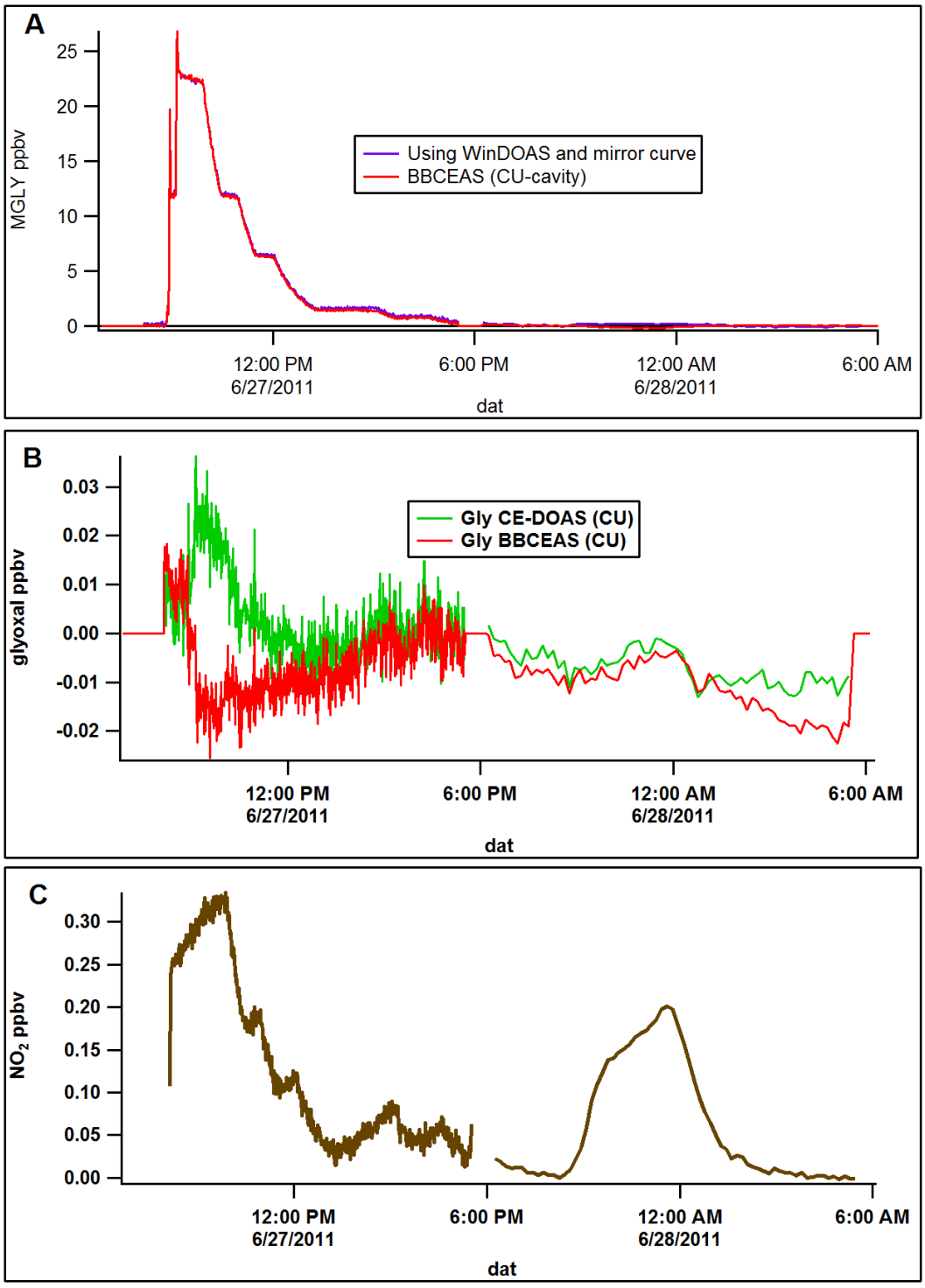

Figure A5.3: Measured concentrations of methyl glyoxal (A), glyoxal (B- comparison of CE-DOAS and BBCEAS retrievals) and NO_2 (C) from 27 June 2011 during AlDiIn experiments at EUPHORE.

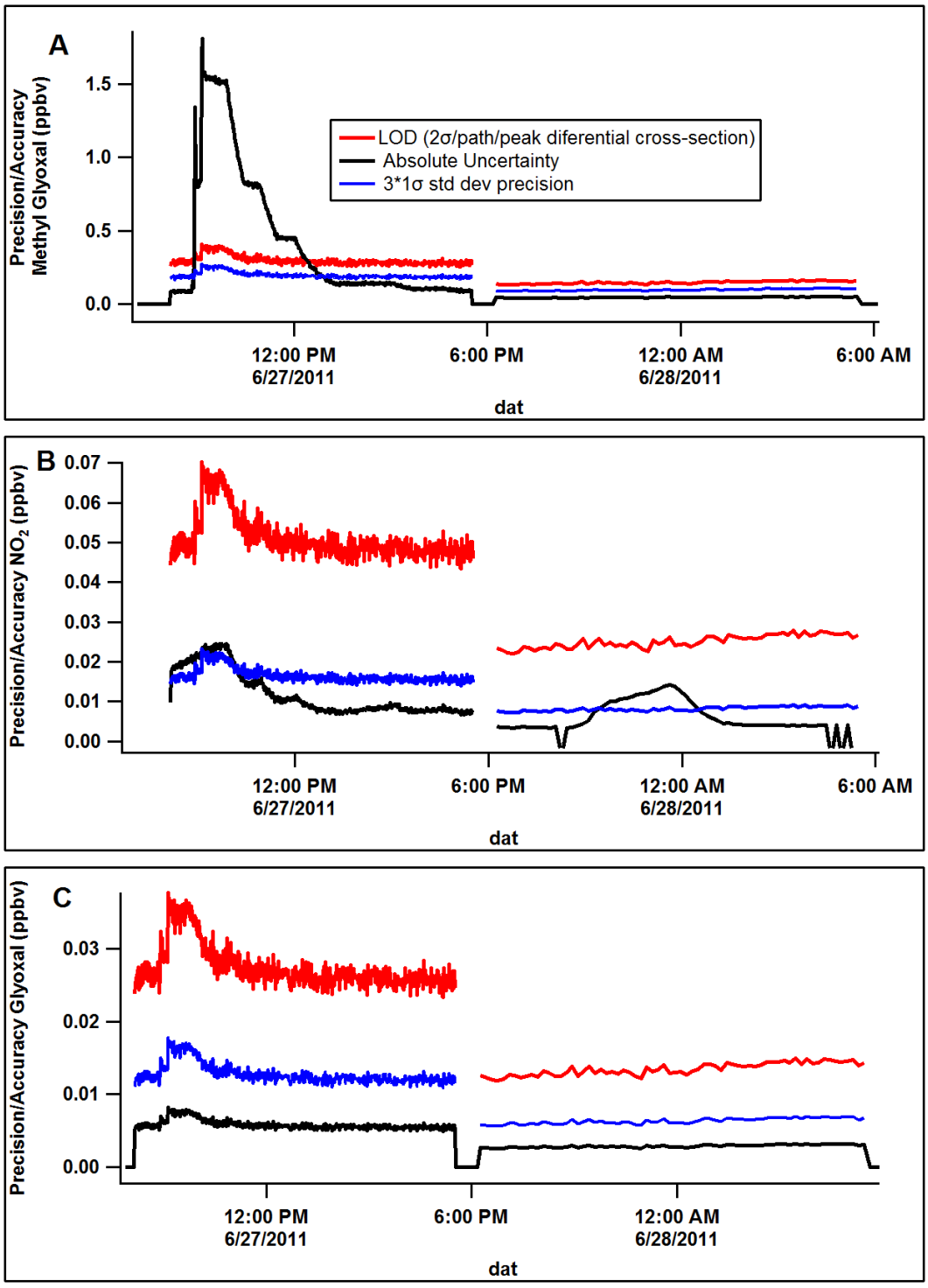

Figure A5.4: Contributing uncertainties for 27 June 2011 for methyl glyoxal (A), NO_2 (B) and glyoxal (C) during AlDiIn experiments at EUPHORE.

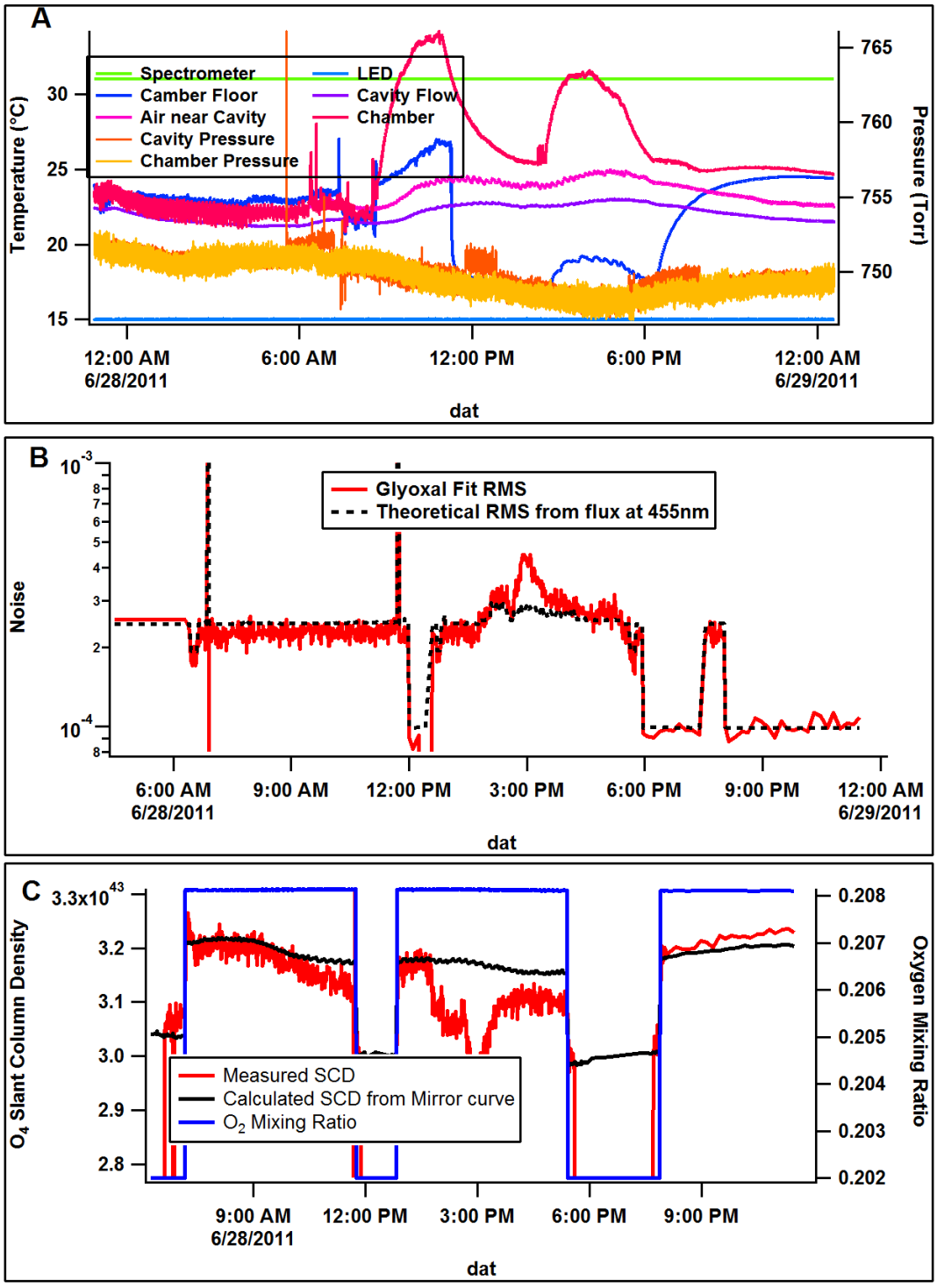

Figure A5.5: Environmental parameters (A), theoretical noise comparison (B) and O_4 slant column density comparison (C) for 28 June 2011 during AlDiIn experiments at EUPHORE.

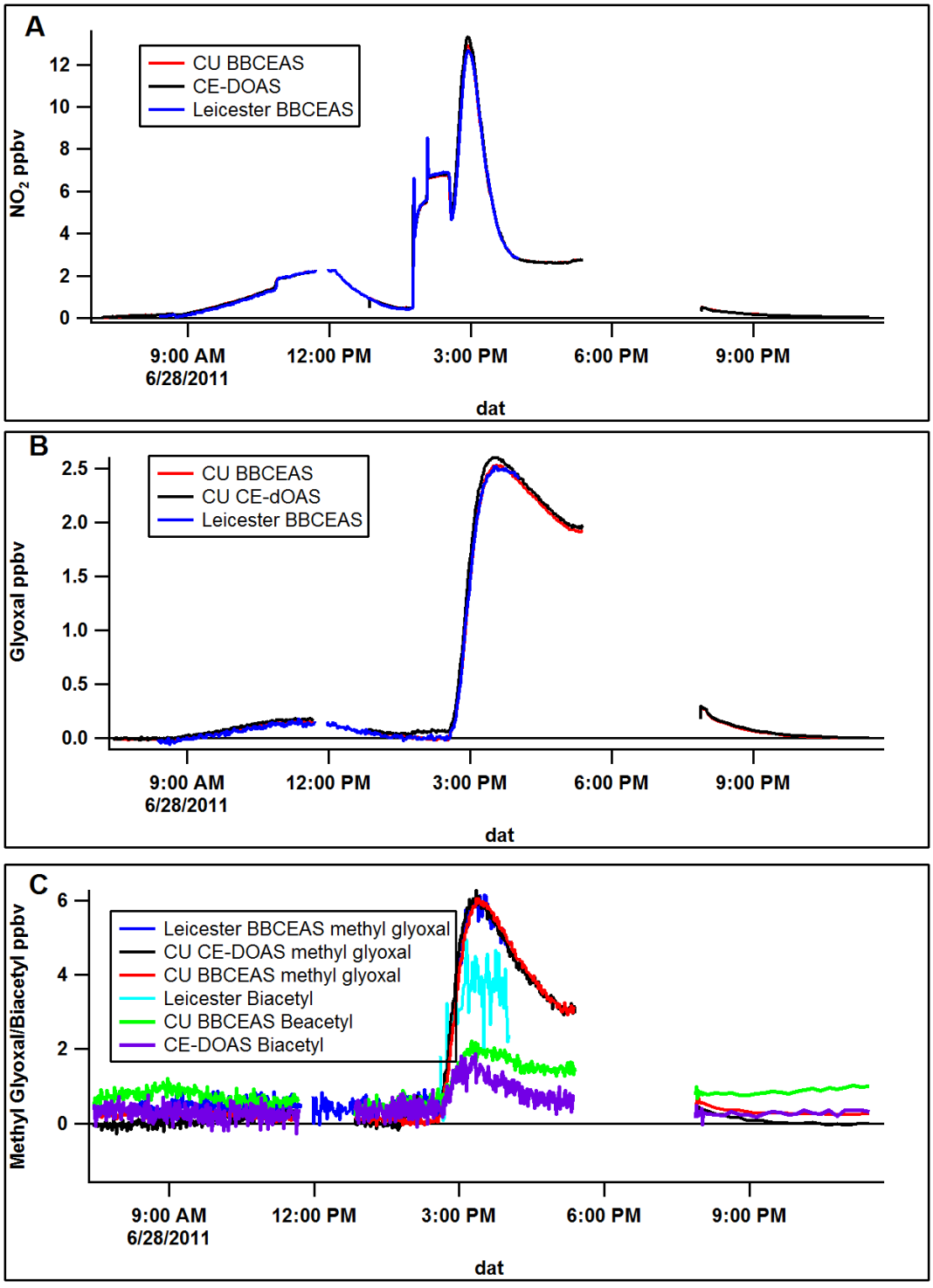

Figure A5.6: Measured concentrations from CE-DOAS and Leicester BBCEAS for NO_2 (A), glyoxal (B), methyl glyoxal (C) and biacetyl (C) for o-xyene oxidation experiment on June 28, 2011 at EUPHORE.

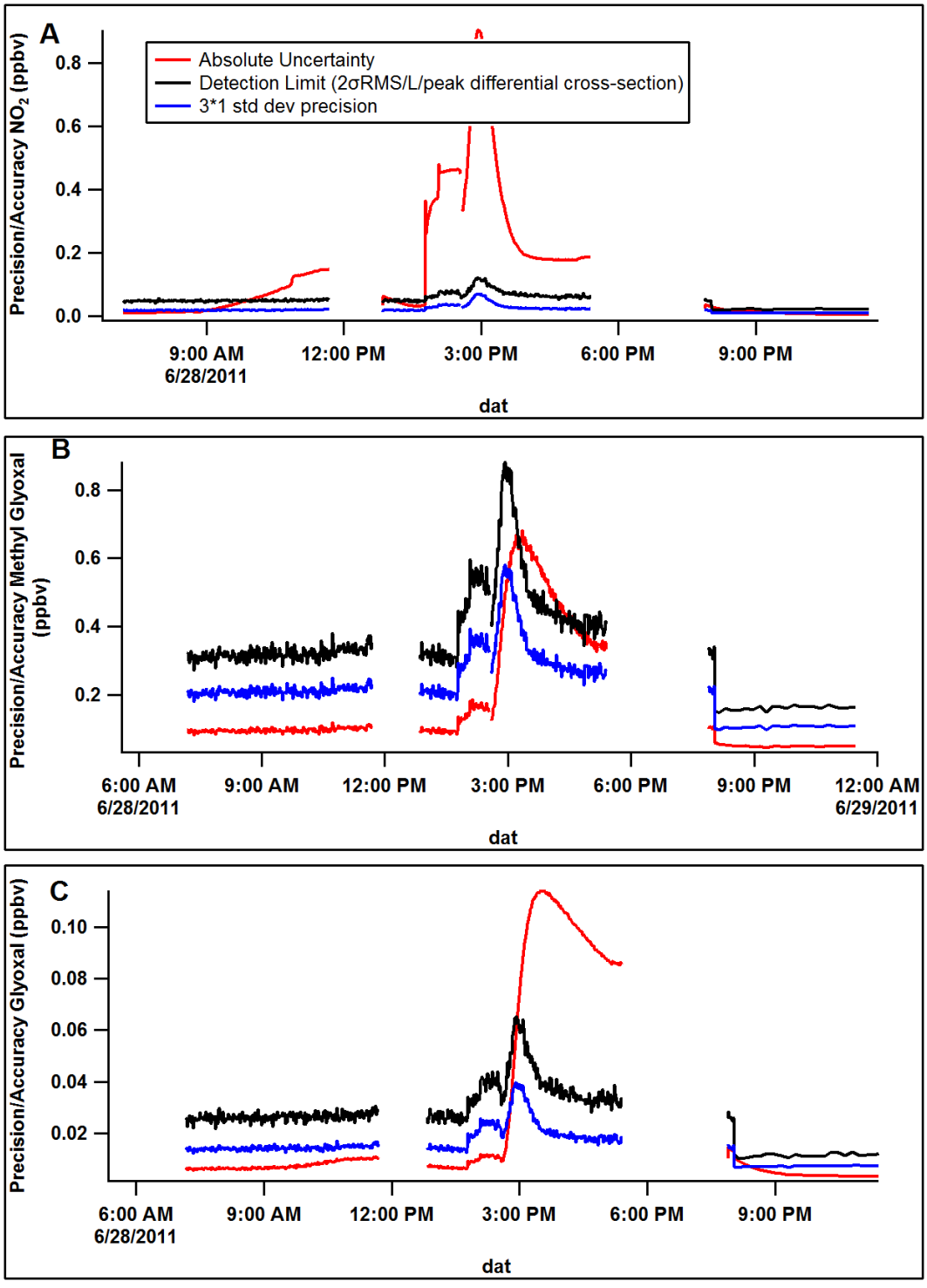

Figure A5.7: Uncertainties for CE-DOAS measured species NO_2 (A), glyoxal (B) and methyl glyoxal (C) for 28 June 2011 at EUPHORE.

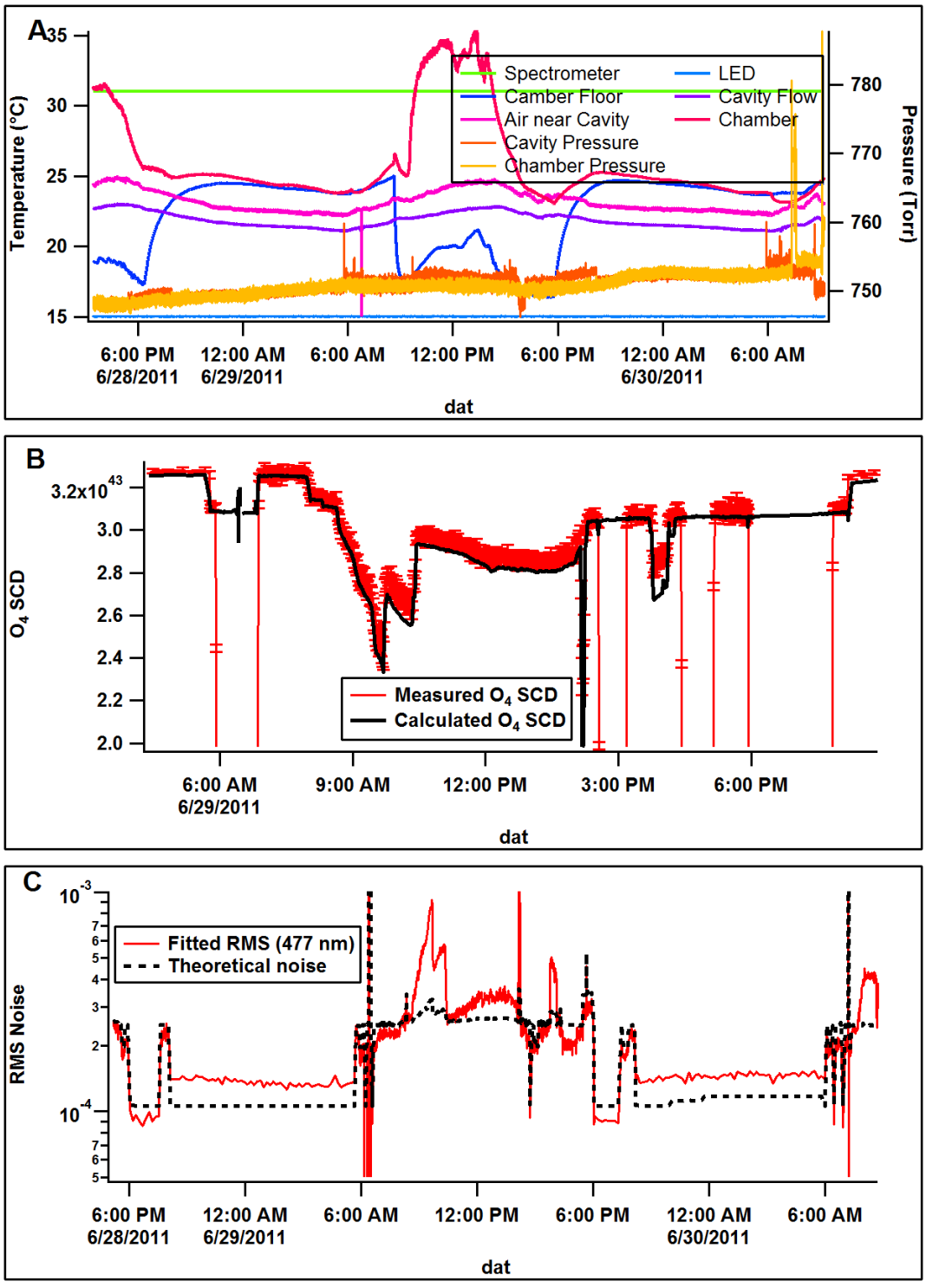

Figure A5.8: Environmental parameters (A), O_4 slant column densities (B) and theoretical/fitted noise (C) from 29 June 2011 at EUPHORE.

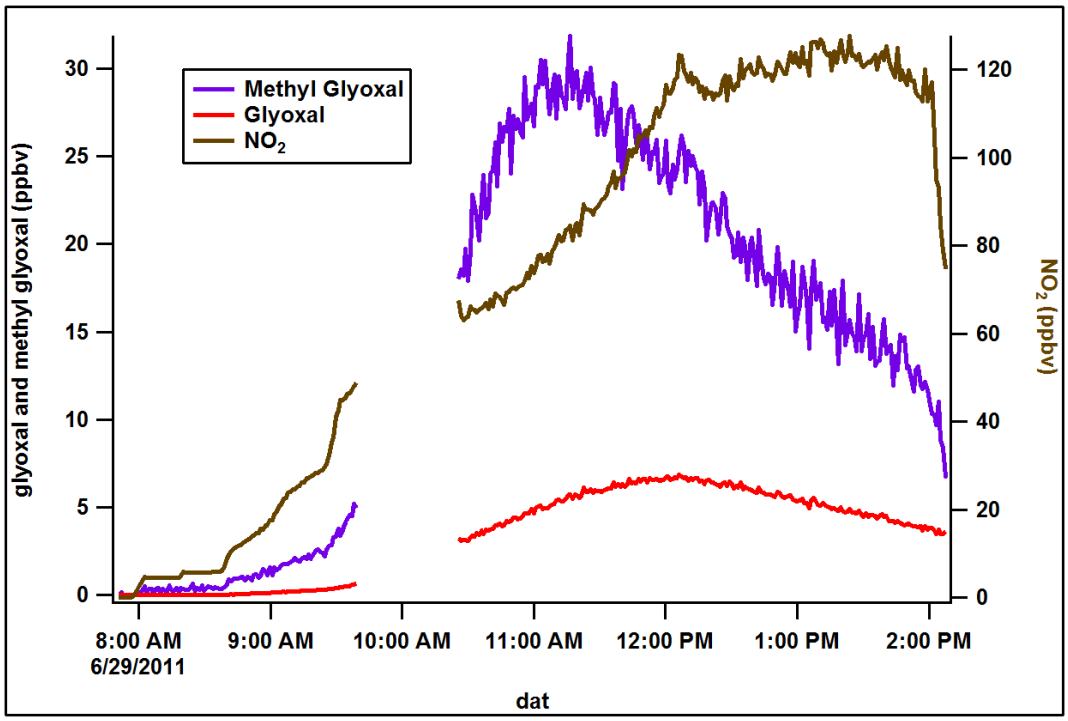

Figure A5.9: Concentrations of NO_2, glyoxal and methyl glyoxal from the oxidation of isoprene on 29 June 2011 at EUPHORE. Measurements after the gap in the data are done with the sample from the chamber diluted.

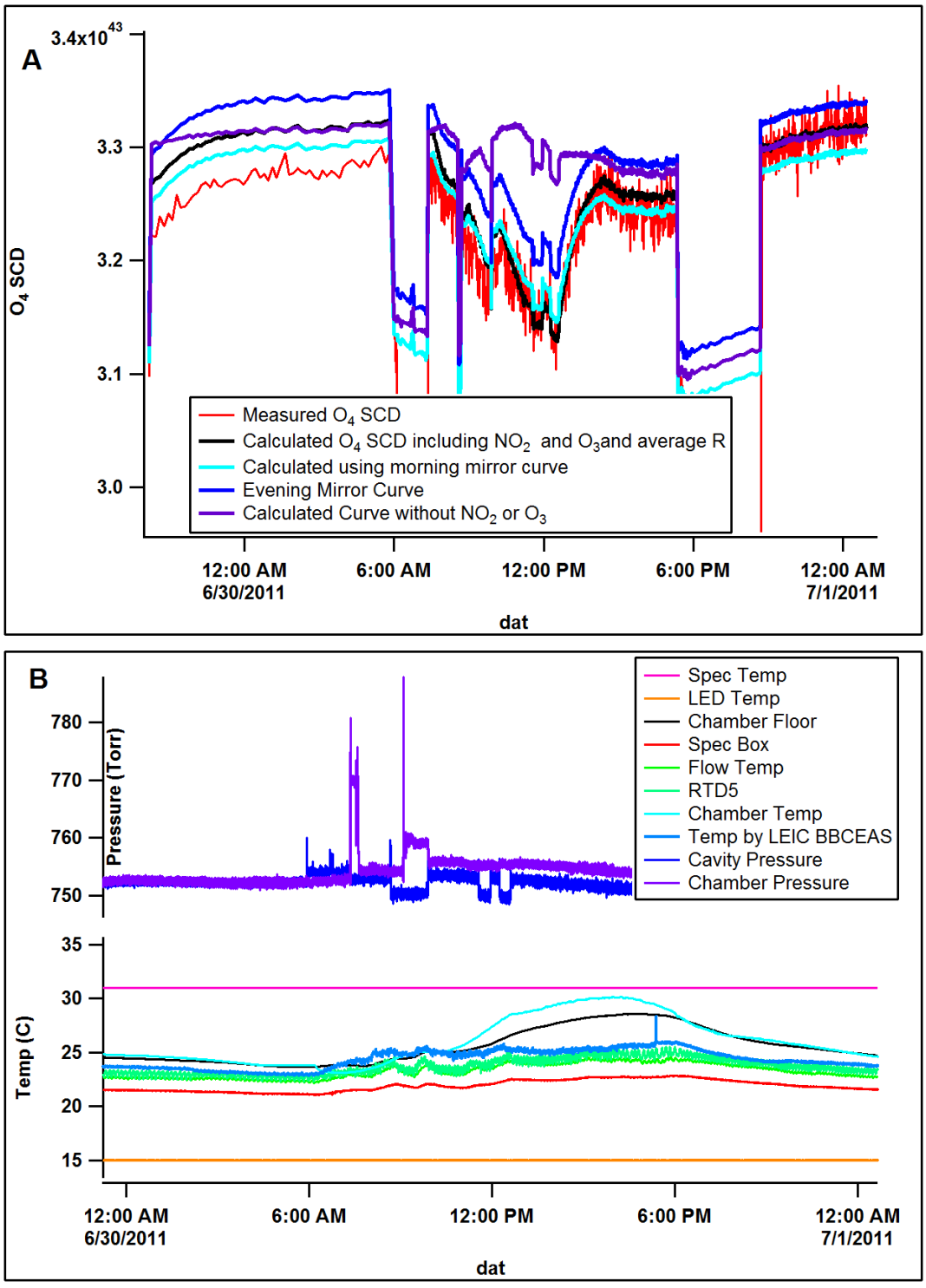

Figure A5.10: (A) O4 slant column density comparison of measured and calculated from mirror reflectivity. (B) Chamber environmental parameters from 30 June 2011 at EUPHORE.

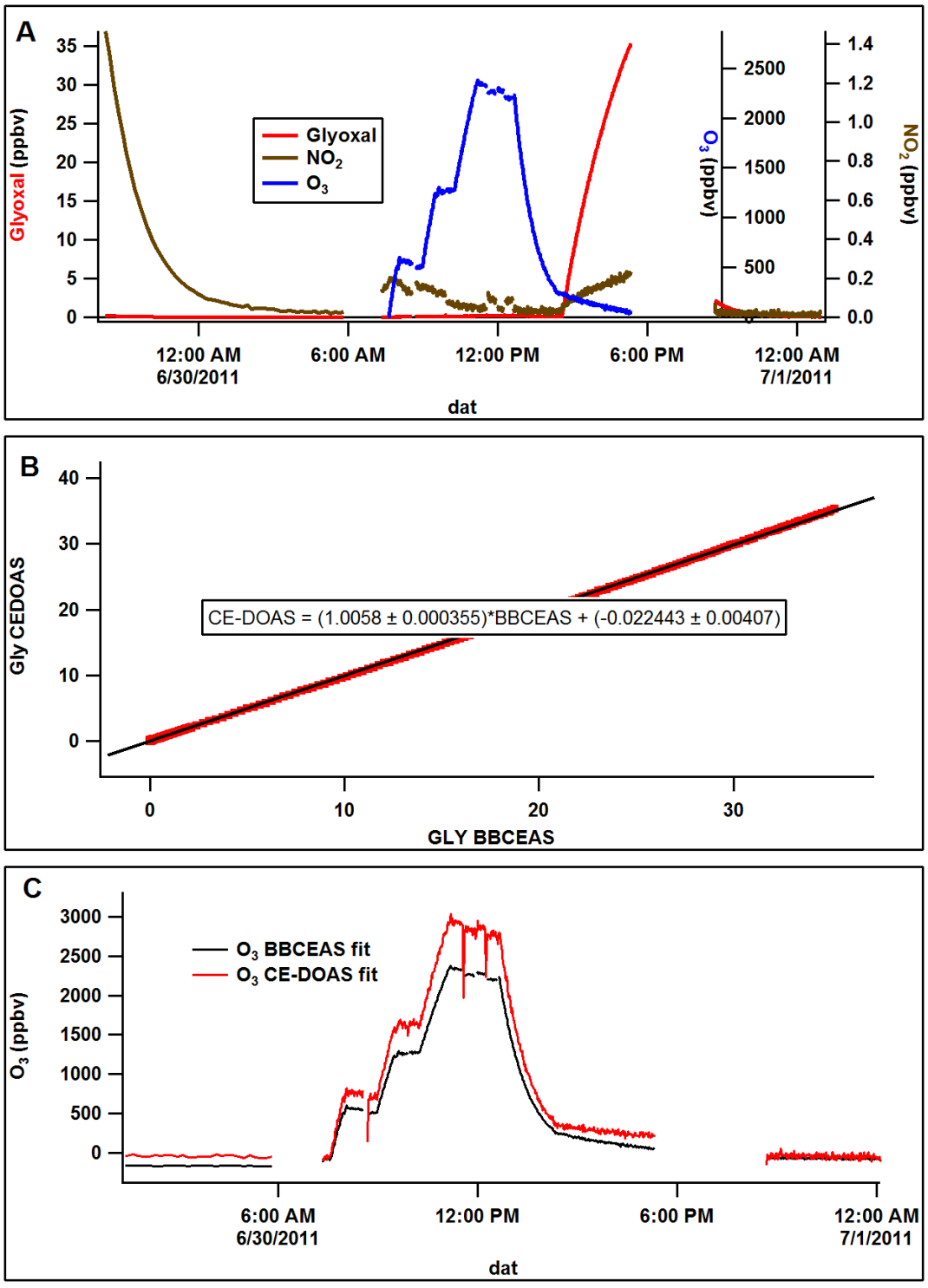

Figure A5.11: (A) Concentrations of NO_2, glyoxal and methyl glyoxal in the chamber for 30 June 2011 at EUPHORE, injected ozone followed by opening of the roof to initiate chemistry in the chamber. (B) Correlation of CE-DOAS and BBCEAS fits from CU instrument. (C) Results of different retrieval algorithms for O_3 from the same spectra.

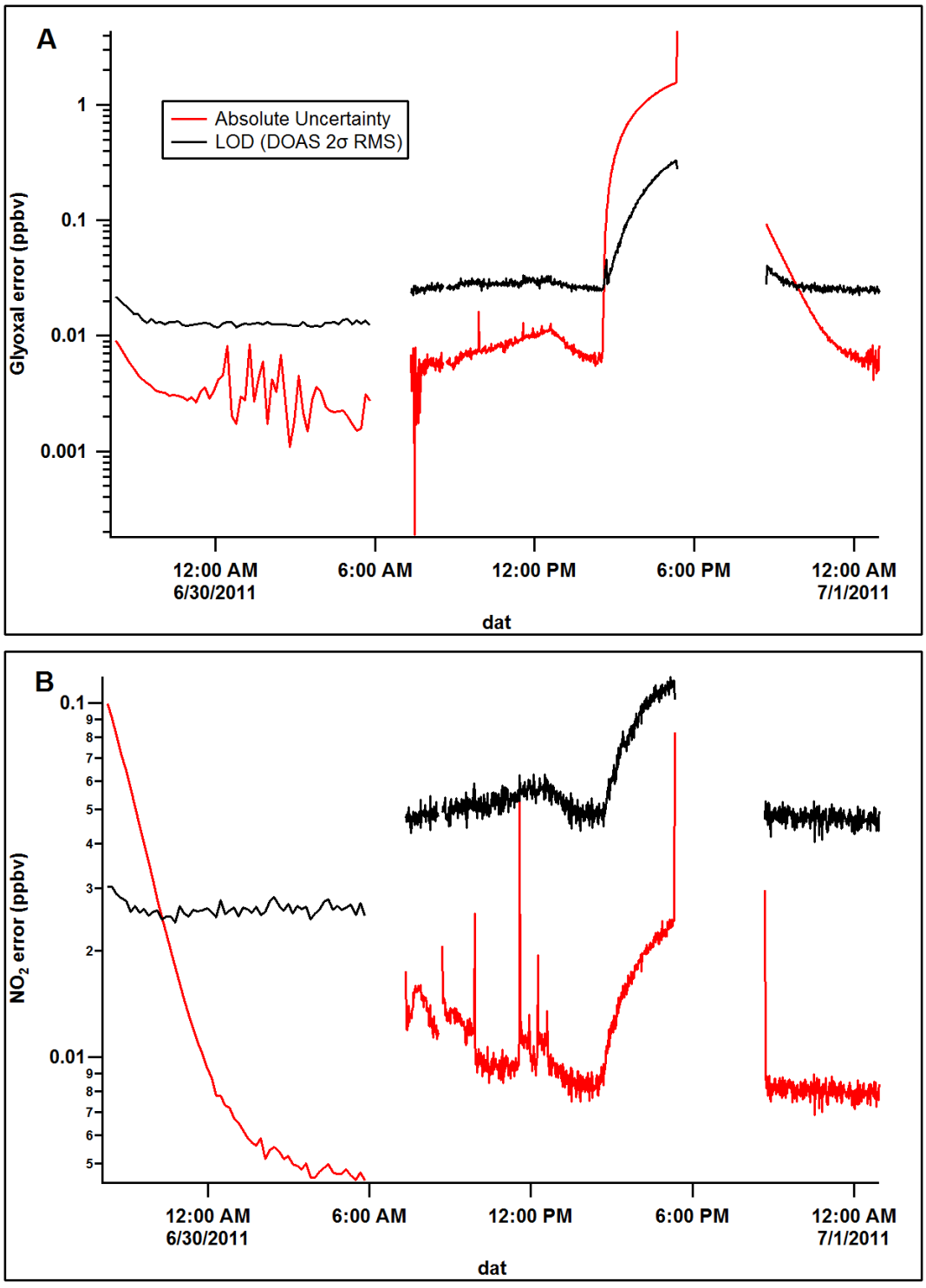

Figure A5.12: Contributions of uncertainties for glyoxal and NO_2 from 30 June 2011 at EUPHORE.

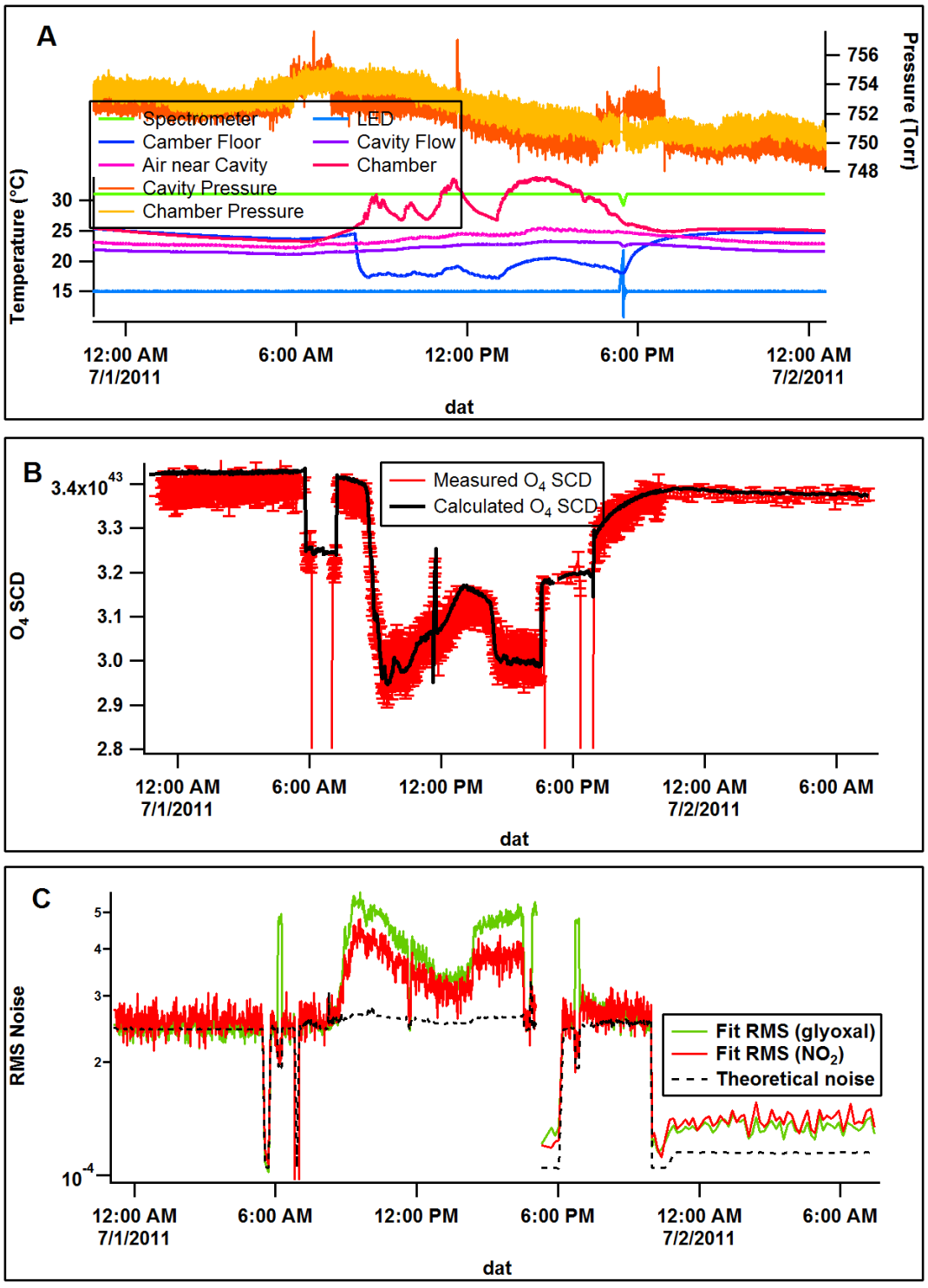

Figure A5.13: Panel A: Environmental Parameters; Panel B: O4 slant column density measured (red) compared to calculated from mirror reflectivity; Panel C: Theoretical noise (photon-shot noise) compared to measured fit residual (red) for 1 July 2011 at EUPHORE.

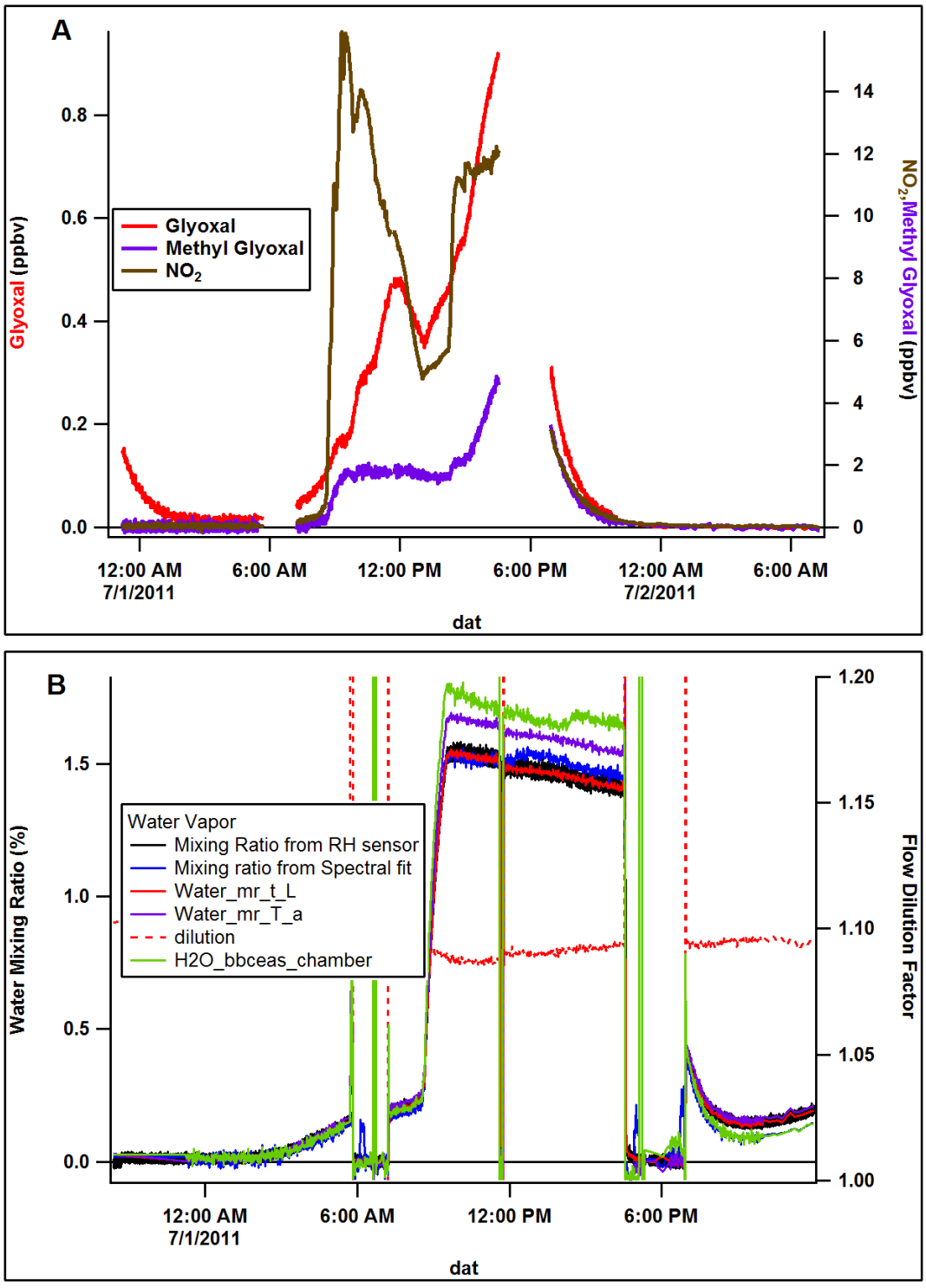

Figure A5.14: Measured species for 1 July 2011 at EUPHORE, chamber filled with ambient air. Panel B shows the comparison of the fitted water from the CE-DOAS compared to the RH probe.

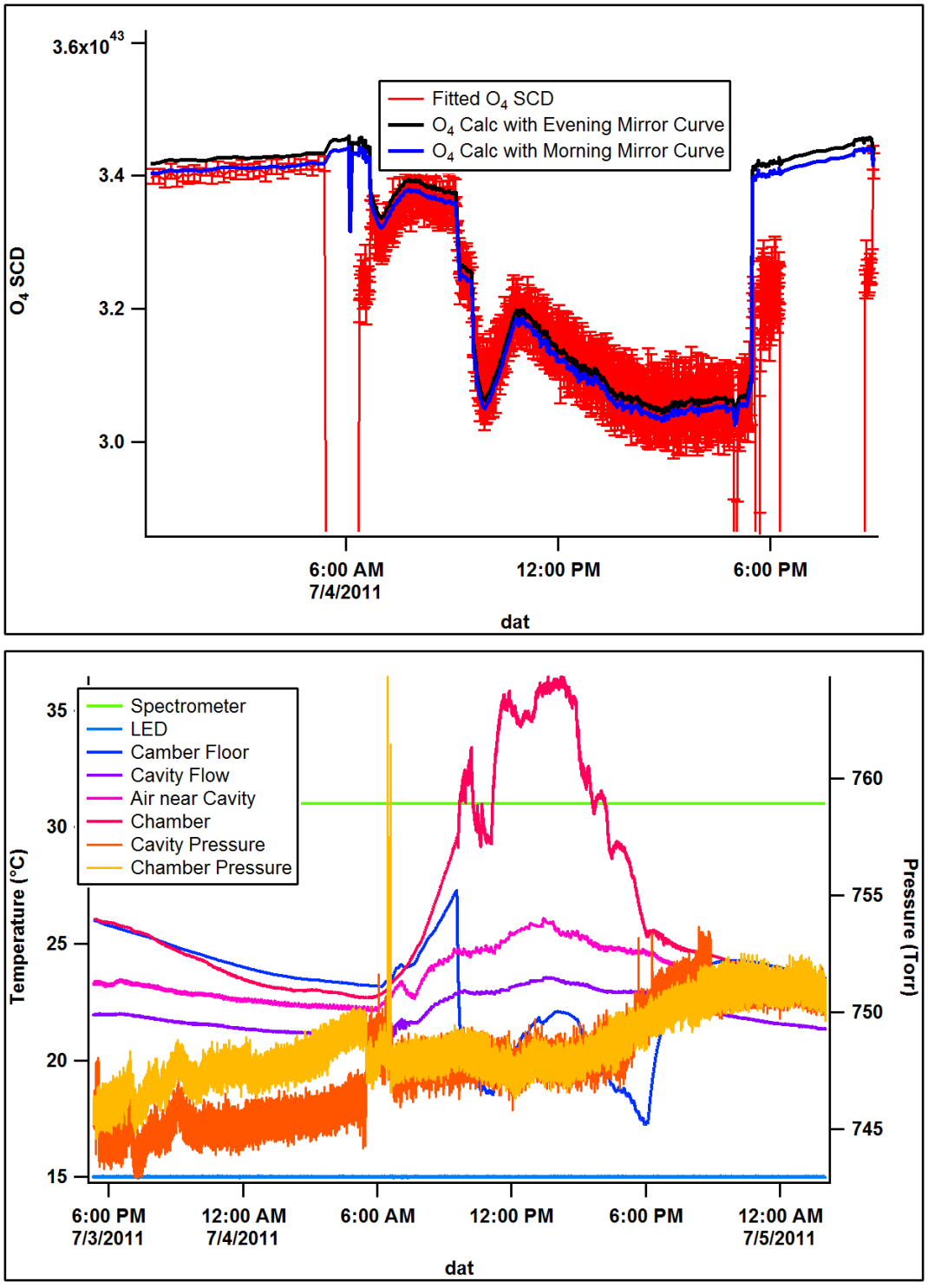

Figure A5.15: Environmental parameters for isoprene oxidation experiment on 4 July 2011 at EUPHORE. Top panel shows the measured O_4 slant column density compared to that calculated from the mirror curve.

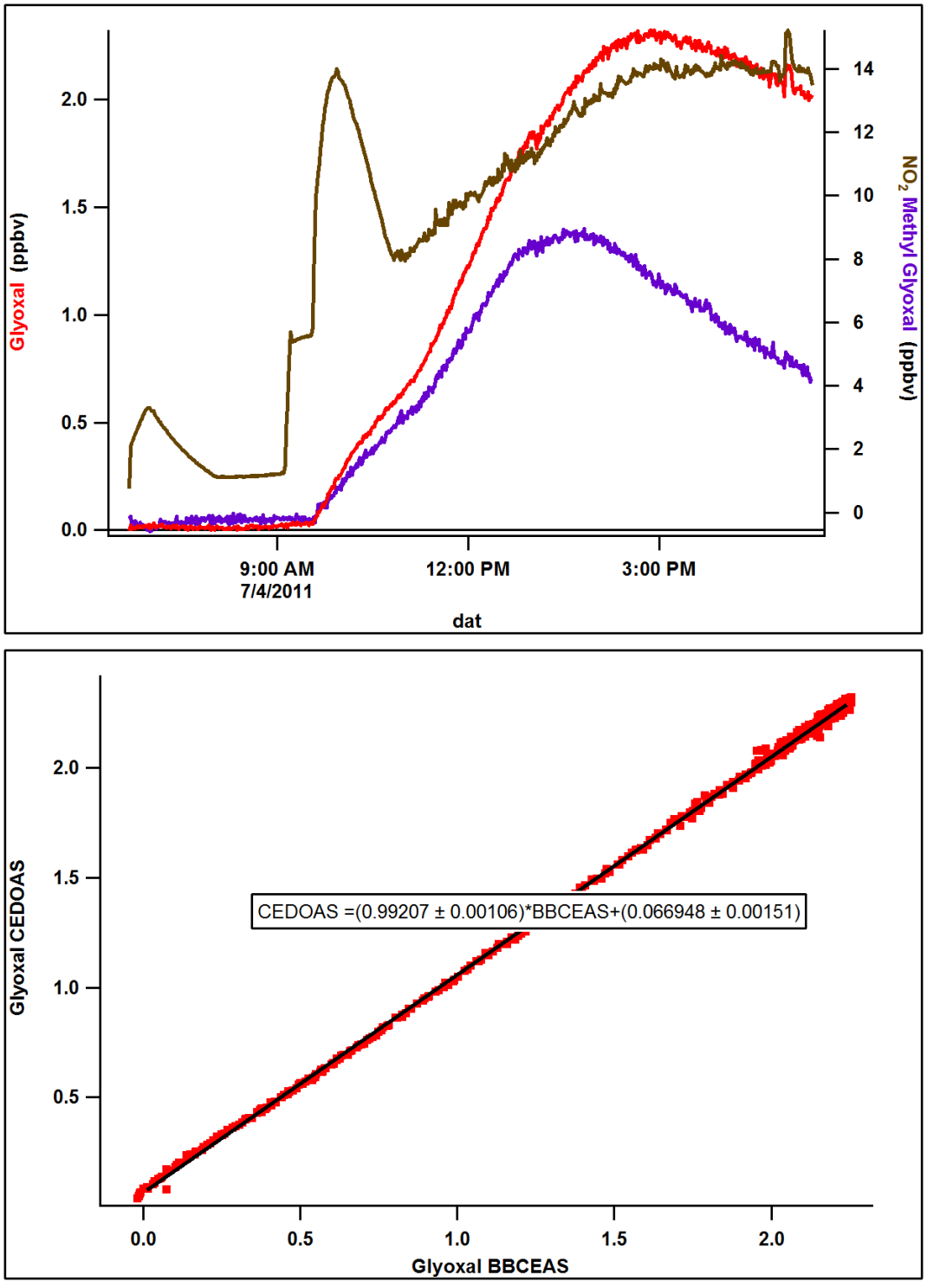

Figure A5.16: concentrations of NO_2, glyoxal and methyl glyoxal in the chamber from the oxidation of isoprene with NO_x control on 4 July 2011 at EUPHORE. Bottom panel show correlation of CE-DOAS with BBCEAS fits from the CU instrument for glyoxal.

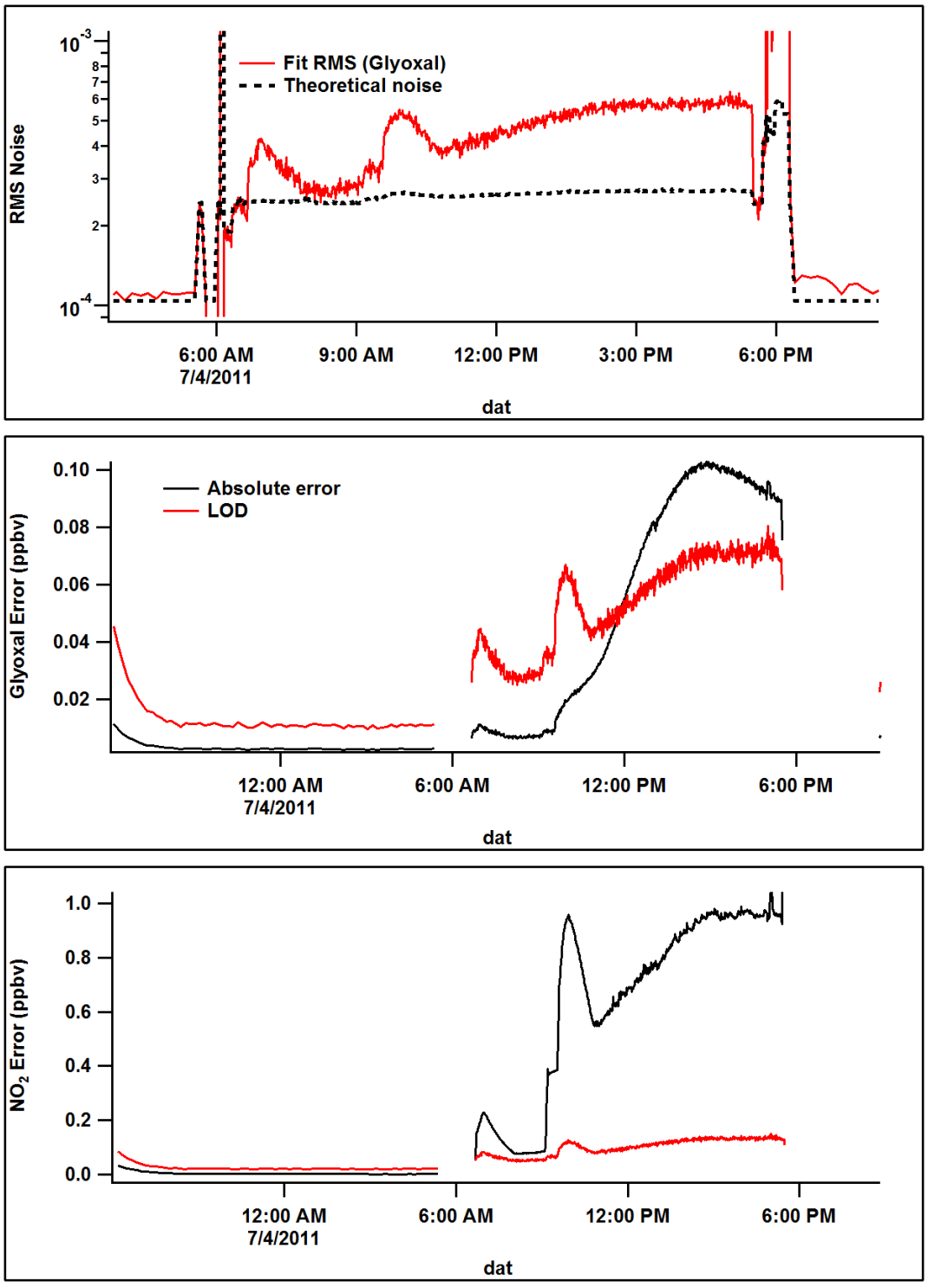

Figure A5.17: Contributing error sources for data from 4 July 2011 at EUPHORE. Top panel shows the theoretical (photon-shot) noise compared to the fit residual RMS. The bottom two panels show the contributing uncertainties for NO_2 and glyoxal.

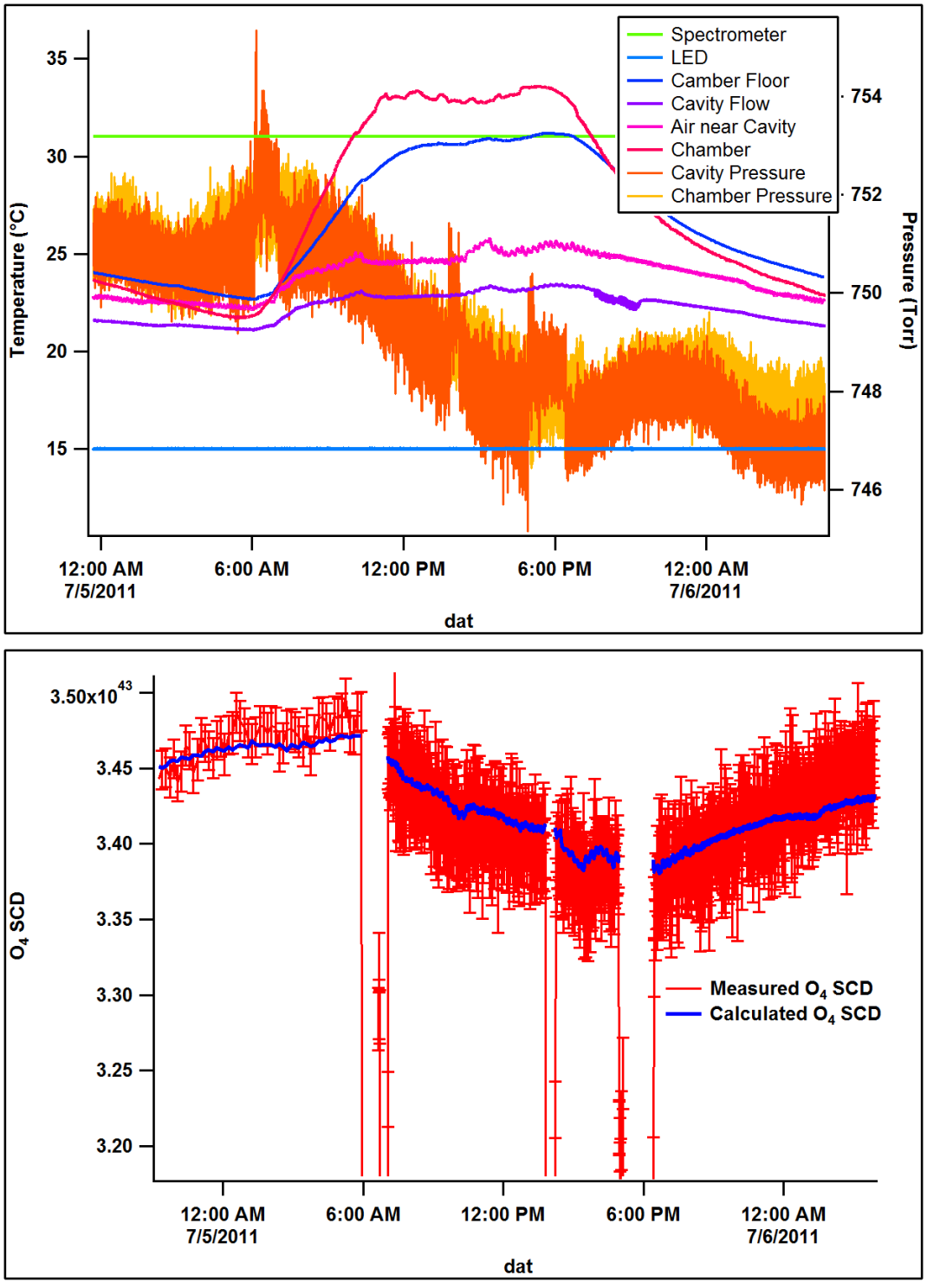

Figure A5.18: Top panel: Environmental parameters for experiments on 5 July 2011 at EUPHORE. Bottom panel: Measured O_4 slant column density compared to that calculated from the mirror reflectivity curve.

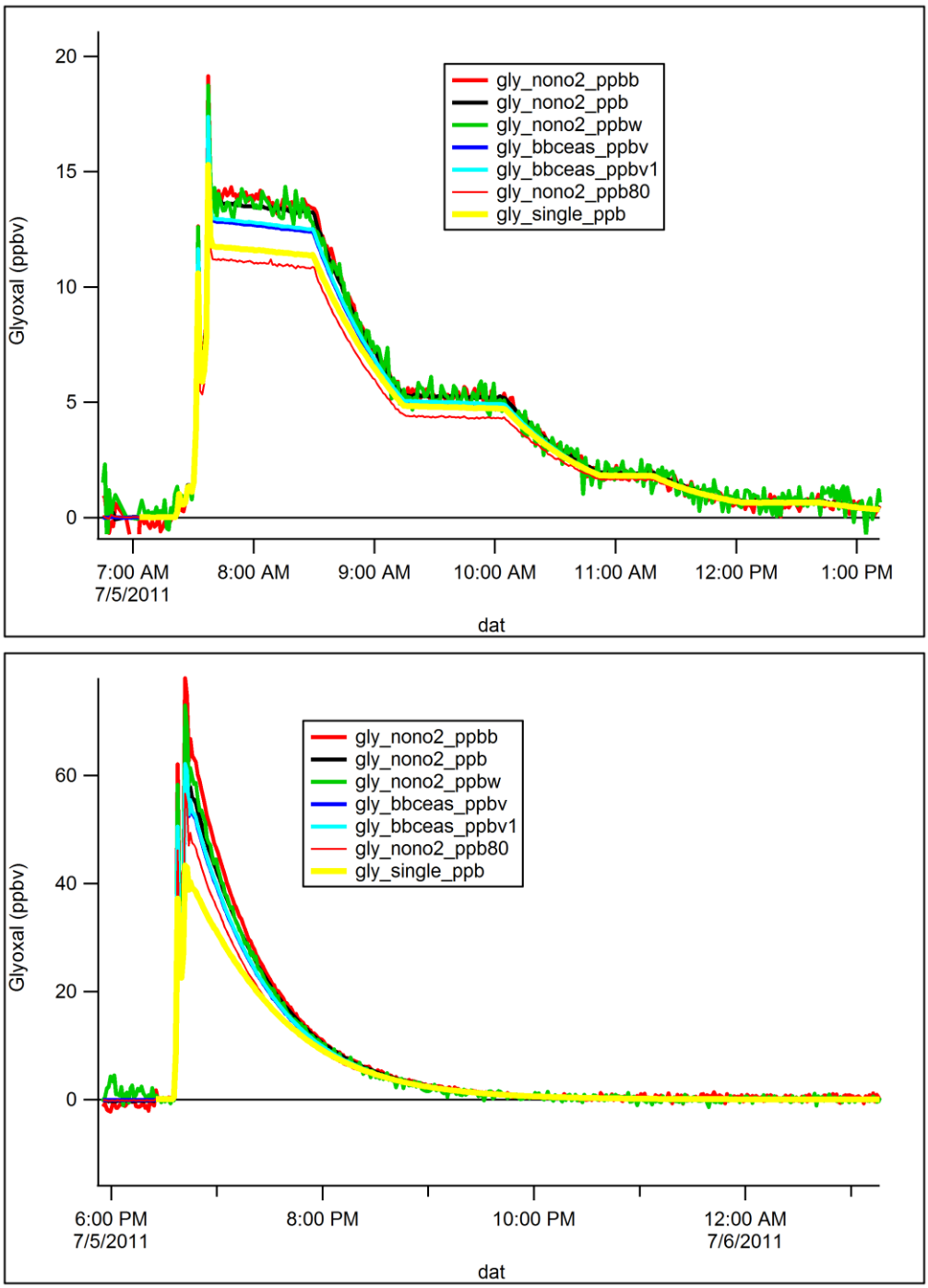

Figure A5.19: Comparison of different fitting windows and cross-sections for high concentrations of glyoxal on 5 July 2011 at EUPHORE. In each panel the letter following the label represents a different window or cross-section (b- broad region of glyoxal (short of the 455nm band); w- weak bands as described in the text; no label- standard two cross-section fit for high concentrations; v, v1 single and 80- single cross-section fits of different cross-sections; bbceas- BBCEAS fit algorithm).

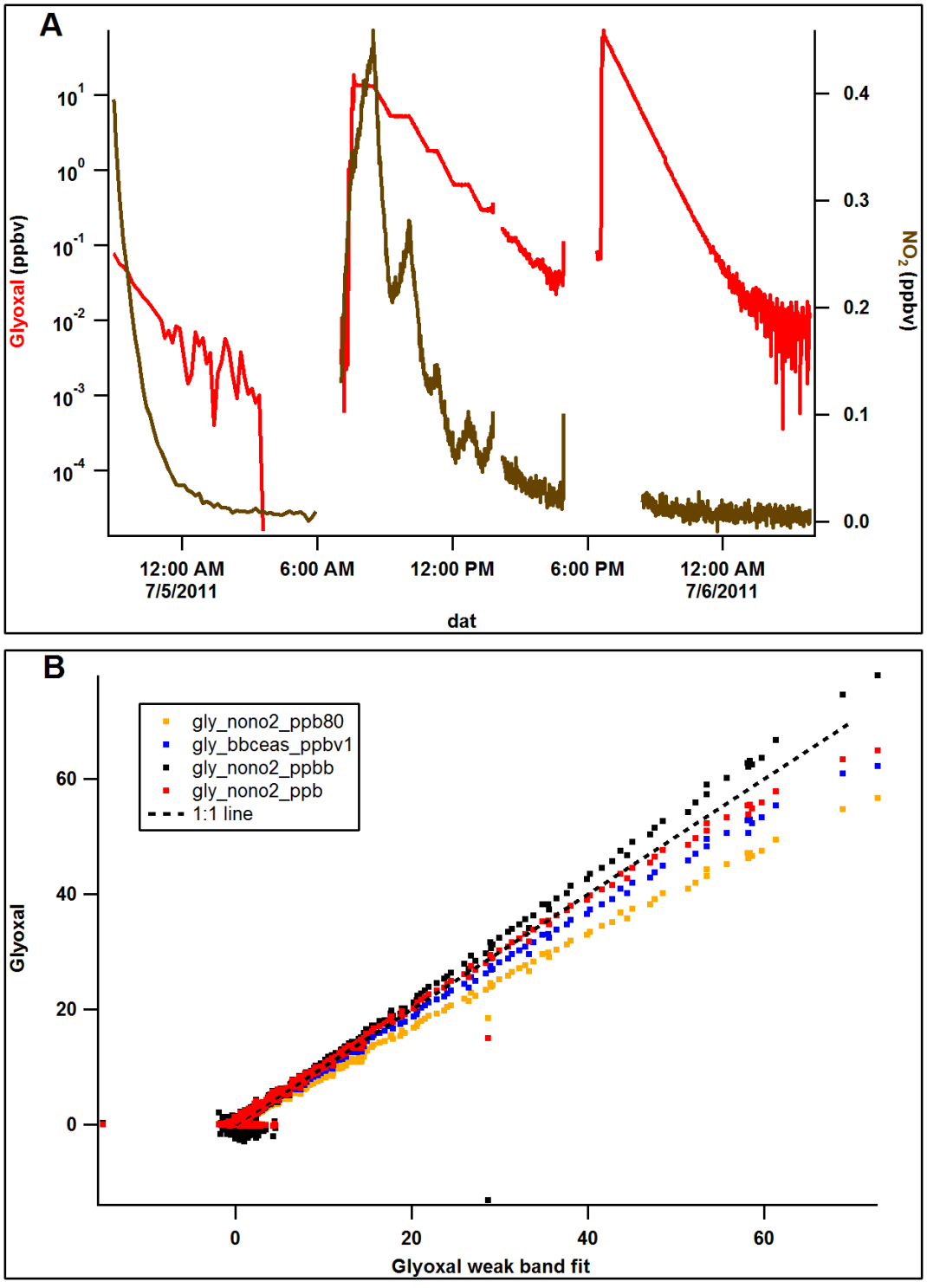

Figure A5.20: Glyoxal concentrations on a log scale to show dilution in the chamber as well as stability of low concentrations (A) for 5 July 2011 at EUPHORE. Panel B shows correlation plots of different fitting parameters (see Figure A5.19 caption).

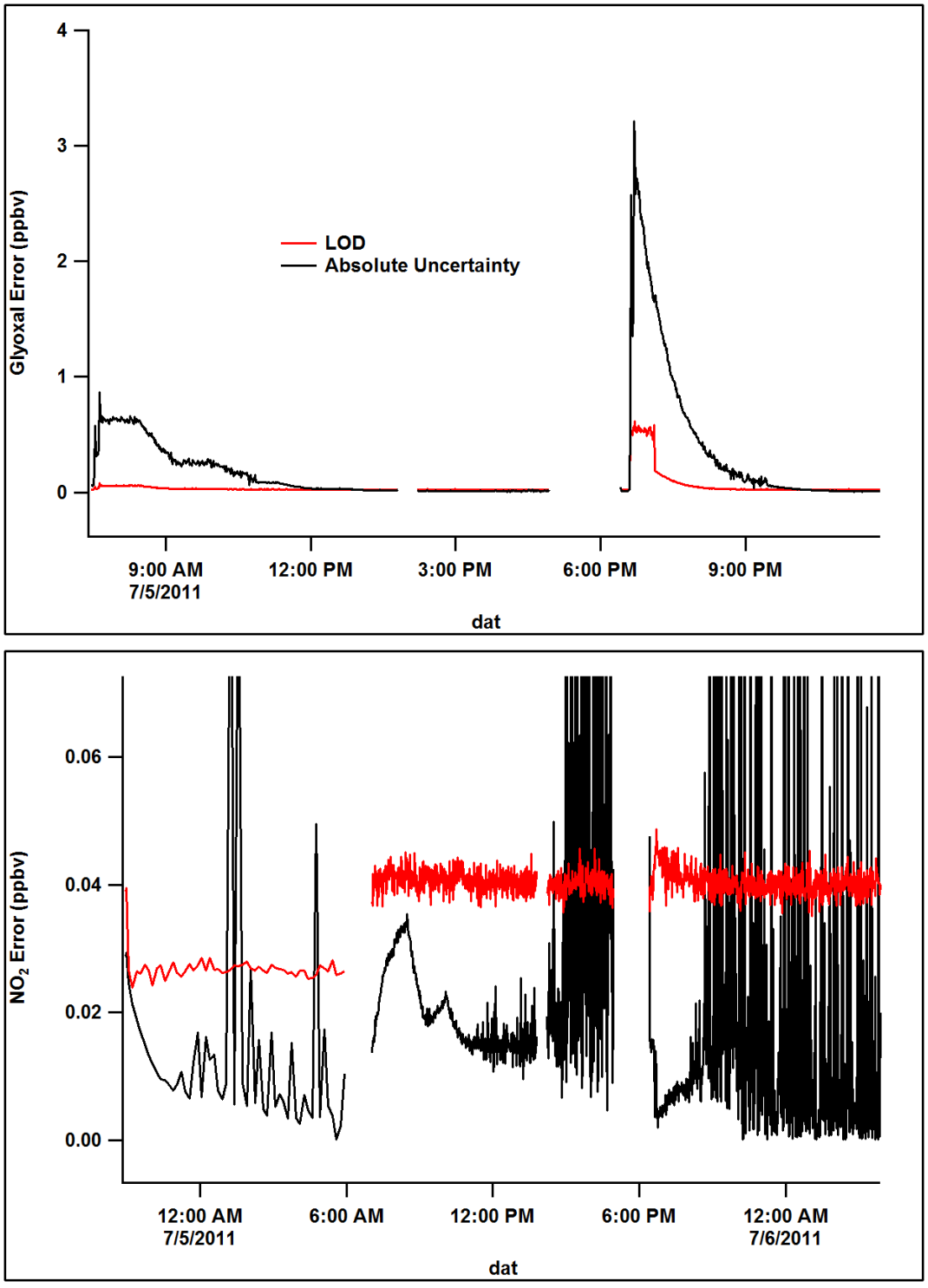

Figure A5.21: Contributing Error values for glyoxal (top panel) and NO_2 (bottom panel) for 5 July 2011 at EUPHORE. The reported error is the larger of the two values.

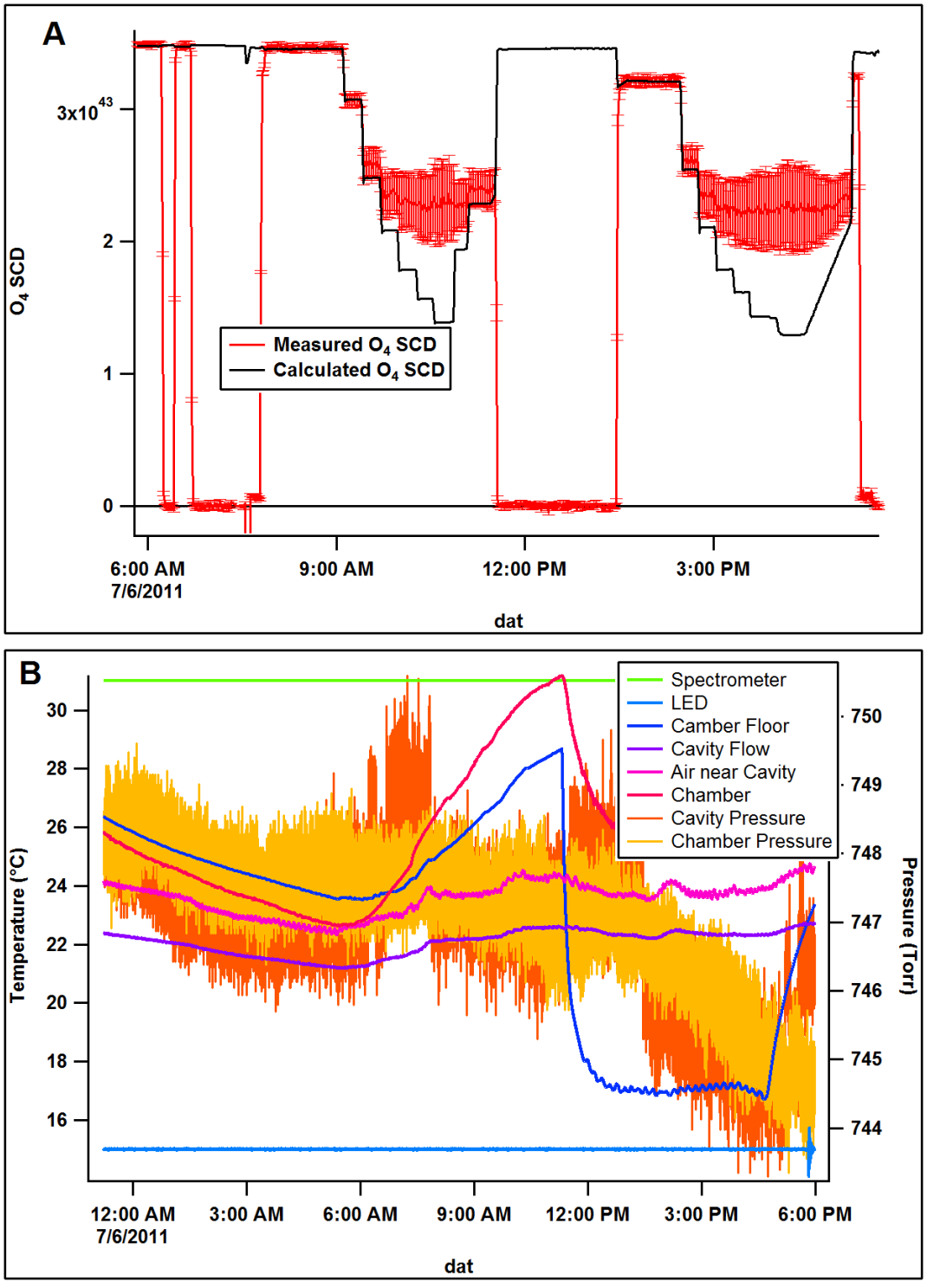

Figure A5.22: O_4 and HK data from 7 July 2011 at EUPHORE. Top panel shows measured O_4 (red) and calculated (black). As NO_2 becomes very large (>70ppbv) the O_4 fit longer does a good job fitting the feature. Panel B shows temperatures and pressures for the chamber and instrument.

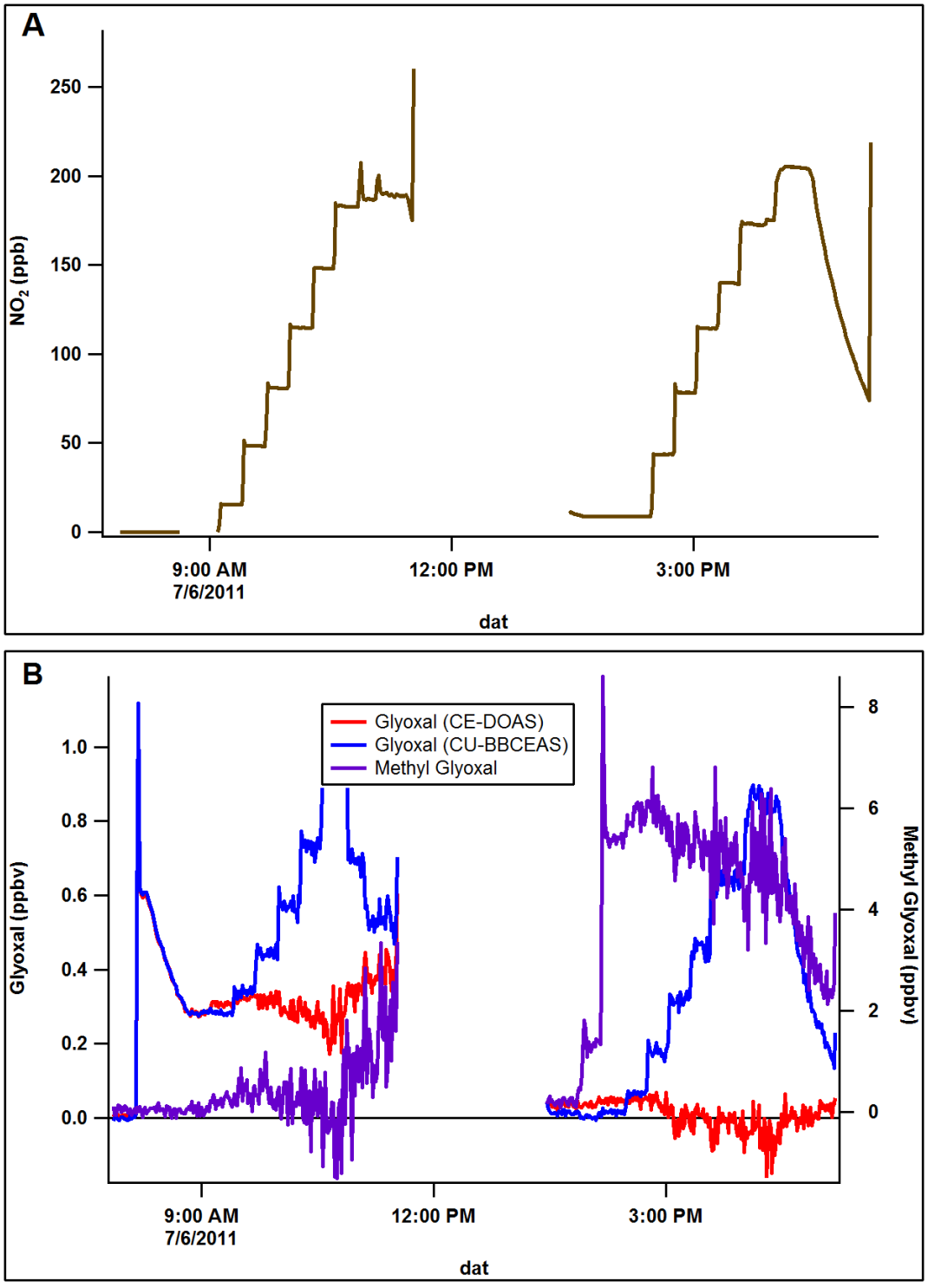

Figure A5.22: Concentrations from 7 July 2011 (Experiments 9 an 10) at EUPHORE. In panel B the fits from a BBCEAS and CE-DOAS fit for glyoxal are compared (red and blue). The BBCEAS fit shows high susceptibility to the NO_2 concentration.

Table A5.1: Correlation data for glyoxal from 24 June 2011 [a]

Y↓ X→	CE-DOAS	BBCEAS	Mad-LIP	FT-IR [b]	W-DOAS	SPME	CE-DOAS[d]
CE-DOAS							
Slope							
Int[c]	-	1.032(2)	1.301(3)	1.02(3)	1.090(4)	1.05(12)	1.02(1)
R^2		0.005(2)	-0.06(2)	-0.1(7)	0.07(1)	0.01(1)	-0.17(1)
		0.9997	0.9998	0.999	0.9998	0.996	0.998
BBCEAS							
Slope	0.970(2)	-	1.2631 (8)	0.95(2)	1.048(1)	1.02(12)	0.97(1)
Int	-0.005(2)		-0.008(2)	0.5(6)	0.029(10)	0.00(2)	0.04(18)
R^2	0.9997		0.9998	0.997	0.9998	0.996	0.999
Mad-LIP							
Slope	0.768(2)	0.7917(5)	-	0.77(2)	0.836(1)	0.74(8)	0.77(1)
Int	0.06(2)	0.006(2)		0.2(4)	0.06(1)	0.03(1)	-0.05(18)
R^2	0.9998	0.9998		0.997	0.9994	0.995	0.9996
FT-IR [b]							
Slope	0.98(3)	1.05(2)	1.31(3)	-	1.07(2)	1.1(4)	1.03(10)
Int	0.1(7)	-0.6(6)	-0.3(5)		0.0(4)	-0.3(41)	-1(3)
R^2	0.999	0.997	0.997		0.999	0.96	0.998
W-DOAS							
Slope	0.917(3)	0.955(1)	1.197(2)	0.93(2)	-	0.93(10)	0.92(2)
Int	-0.06(1)	-0.028(9)	-0.07(2)	0.0(4)		-0.08(3)	-0.02(20)
R^2	0.9998	0.9998	0.9994	0.999		0.995	0.999
SPME							
Slope	0.95(10)	0.98(11)	1.35(15)	0.9(3)	1.07(12)	-	1.0(2)
Int	-0.01(1)	-0.00(2)	-0.04(2)	0.3(36)	-0.08(4)		0.0(14)
R^2	0.996	0.996	0.995	0.96	0.995		0.994
CE-DOAS[d]							
Slope	0.98(1)	1.04(1)	1.30(2)	0.97(10)	1.08(2)	1.0(2)	-
Int	0.17(10)	-0.05(19)	0.1(0.2)	1(3)	0.02(24)	0.0(14)	
R^2	0.998	0.999	0.9996	0.998	0.999	0.994	

[a] Number in parenthesis is the 1-σ fit error of the last displayed digit
[b] Correlations for high concentration data only
[c] Units of the intercept are ppbv
[d] CE-DOAS fitting for weak band range (458.5 to 475 nm)

Table A5.2: Correlation Matrix for Glyoxal from 5 July 2011[a]

X / Y	CE-DOAS	BBCEAS	Mad-LIP	FTIR	W-DOAS	SPME
CE-DOAS						
Slope	-	1.040(3)	0.919(4)	1.01(3)	1.092(8)	1.2(1)
Int [b]		0.007(2)	-0.011(3)	0.2(1)	0.08(2)	0.00(2)
R^2		0.9998	0.998	0.992	0.998	0.998
BBCEAS						
Slope	0.962(3)	-	0.9141(9)	0.95(2)	1.027(3)	1.1(1)
Int	-0.007(2)		-0.030(2)	0.0(1)	0.02(1)	-0.01(2)
R^2	0.9998		0.998	0.992	0.997	0.998
Mad-LIP						
Slope	1.088(4)	1.094(1)	-	1.02(2)	1.057(3)	1.3(1)
Int	0.012(2)	0.033(2)		-0.1(1)	-0.05(1)	0.01(1)
R^2	0.998	0.998		0.96	0.96	0.996
FTIR						
Slope	0.99(2)	1.05(2)	0.98(2)		1.08(2)	1.3(2)
Int	-0.2(1)	0.0(1)	0.1(1)	-	0.0(1)	-0.2(3)
R^2	0.992	0.992	0.96		0.987	0.994
White-cell DOAS						
Slope	0.916(7)	0.973(3)	0.946(3)	0.93(2)	-	1.1(1)
Int	-0.07(2)	-0.02(1)	0.05(1)	0.0(1)		-0.3(1)
R^2	0.998	0.997	0.96	0.987		0.998
SPME						
Slope	0.85(8)	0.88(9)	0.75(7)	0.8(1)	0.9(1)	-
Int	0.00(1)	0.01(1)	-0.009(10)	0.1(2)	0.3(1)	
R^2	0.998	0.998	0.996	0.994	0.998	

[a] Only data from daytime experiment with defined levels; [b] Intercept in ppbv;

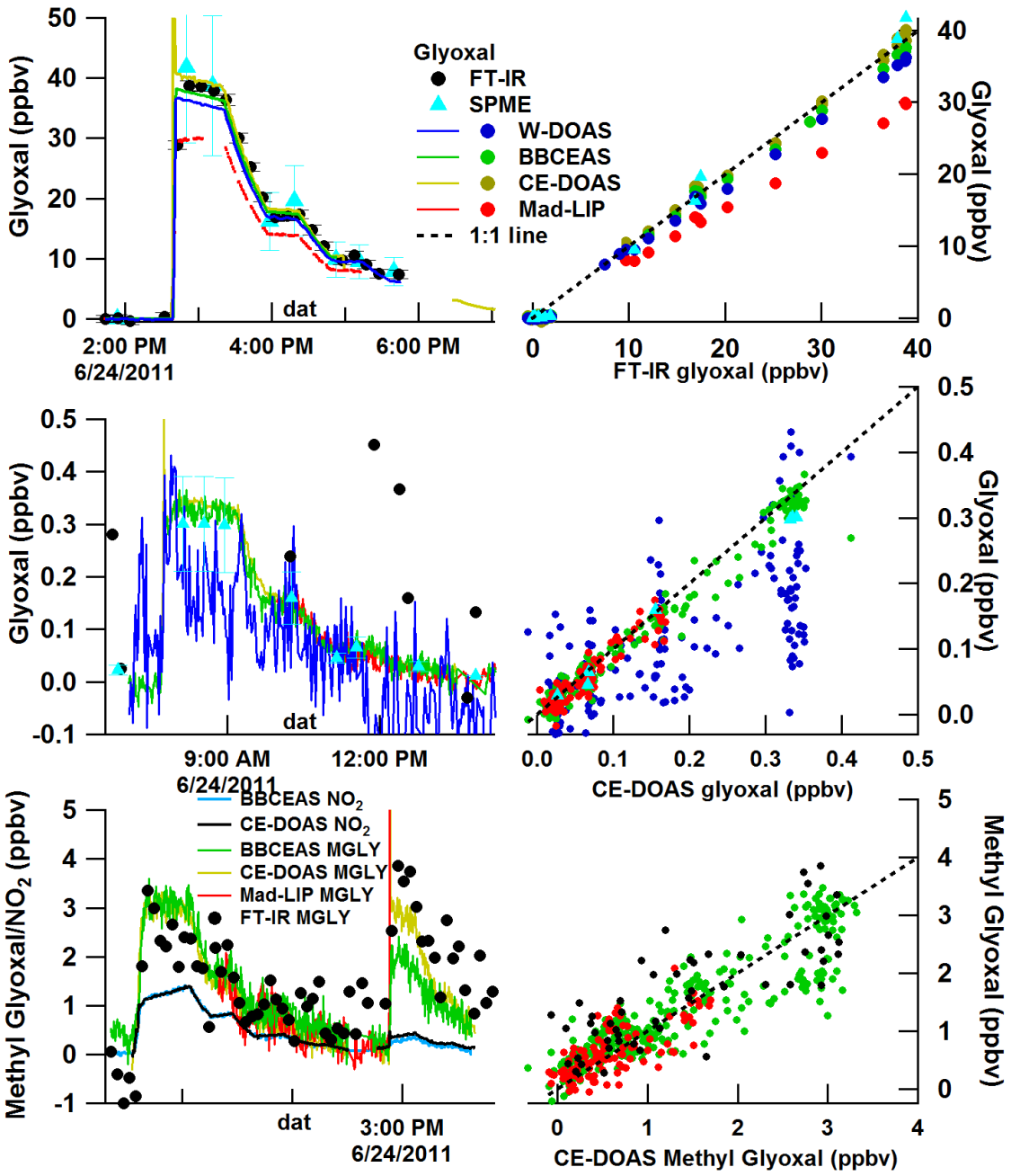

Figure A5.23: Experiment progression and correlations for Experiment 1 (24 June 2011). Fit data for glyoxal is found in Table 5.3.

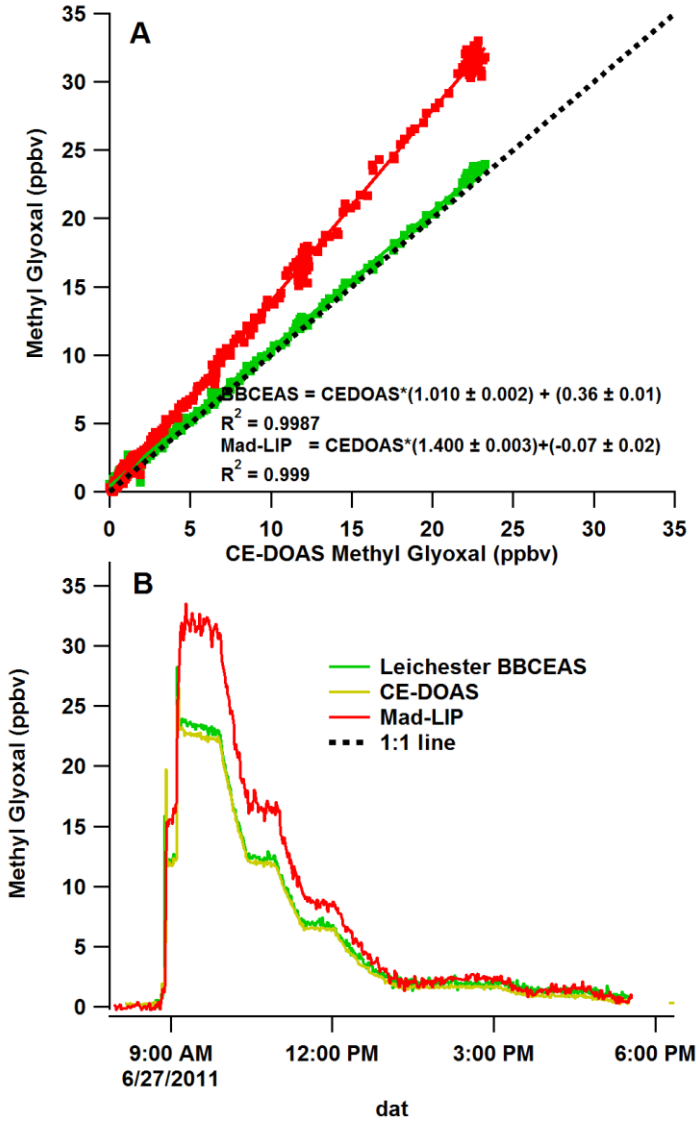

Figure A5.24: Results of EUPHORE Experiment 2, inter-comparison of measurements of methyl glyoxal. Panel A: correlation of Mad-LIP and BBCEAS plotted against CE-DOAS. Panel B: Time series of injection and dilution.

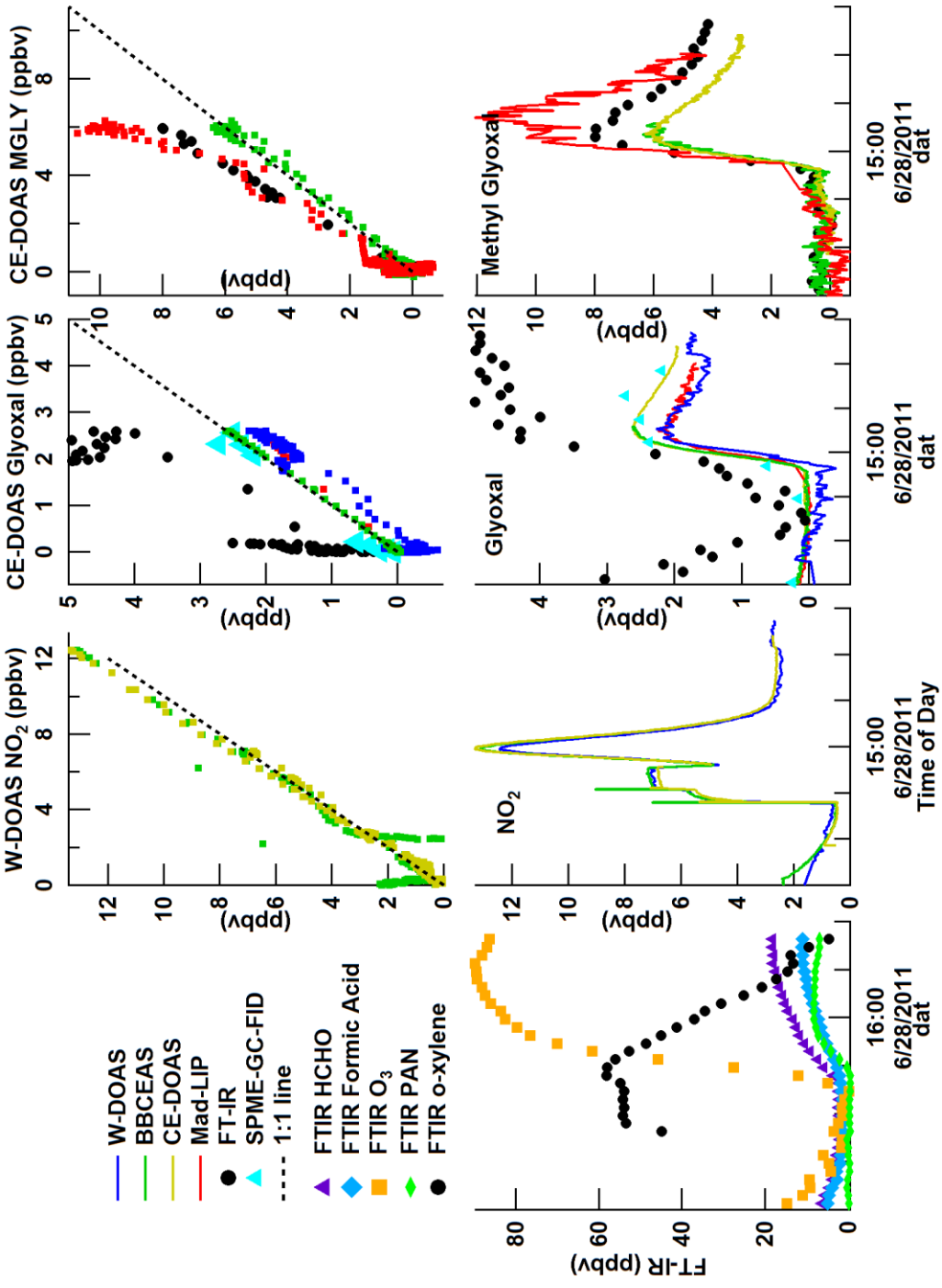

Figure 5.25: Experimental results of 28 June 2011. Upper panels contain correlation data for NO_2, glyoxal and methyl glyoxal while the bottom panels show the experiment progression for reaction species measured only by the FT-IR followed by separate panels for NO_2, glyolxal and methyl glyoxal.

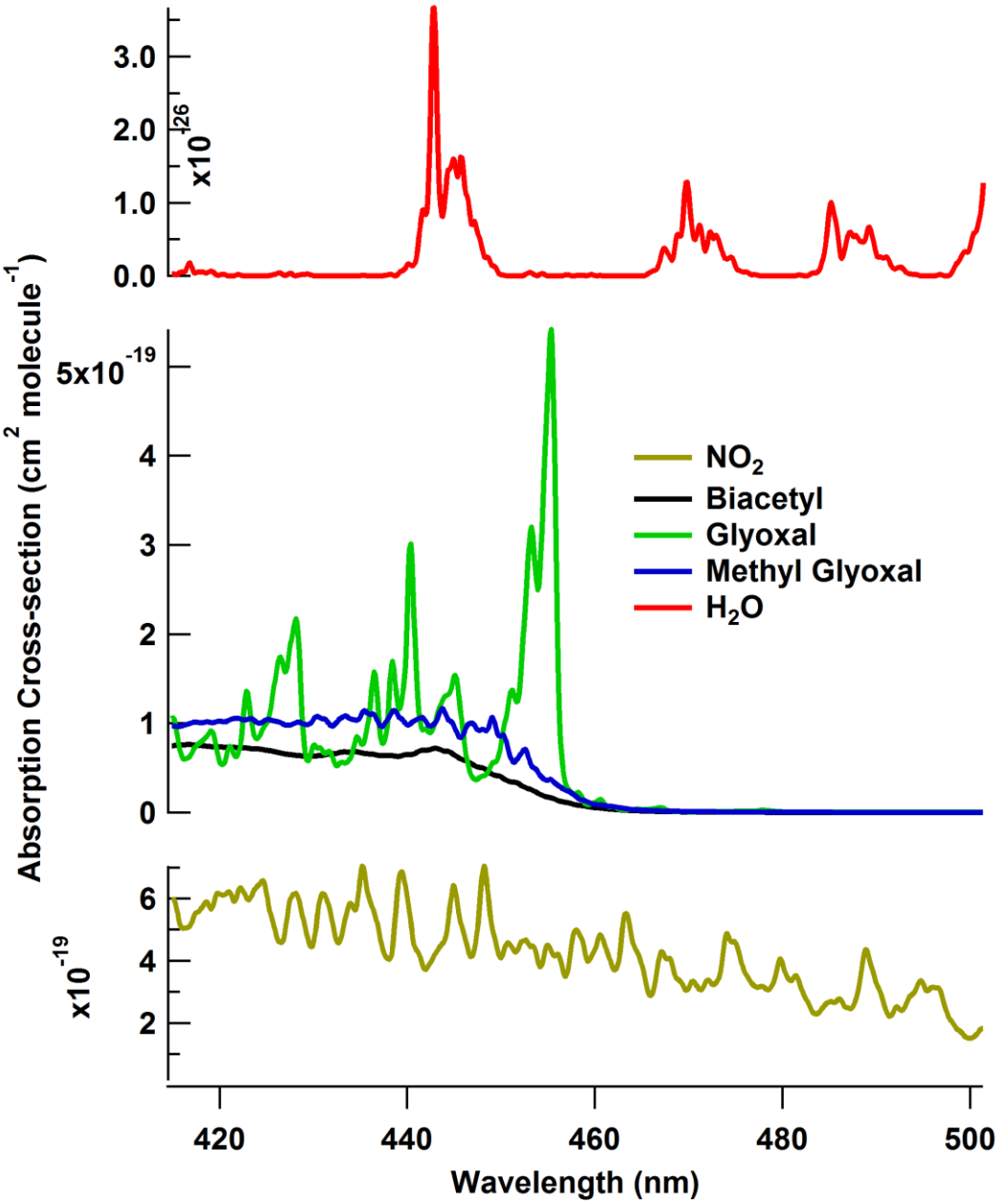

Figure A5.26: Absorption cross-section of species measured by visible light absorption spectroscopy instruments (FWHM = 0.5 nm). NO_2 and water absorb in the same region as glyoxal and methyl glyoxal.

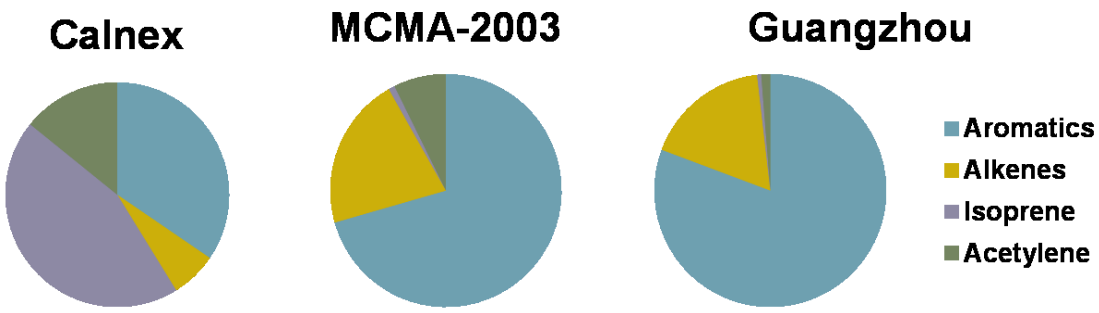

Figure A6.1: Glyoxal sources in three separate field campaigns: MCMA-2003 (Volkamer et al., 2007), Guangzhou, China (data- personal communication to R. Volkamer) and Los Angeles (CalNEX field campaign- VOC data courtesy of NOAA).

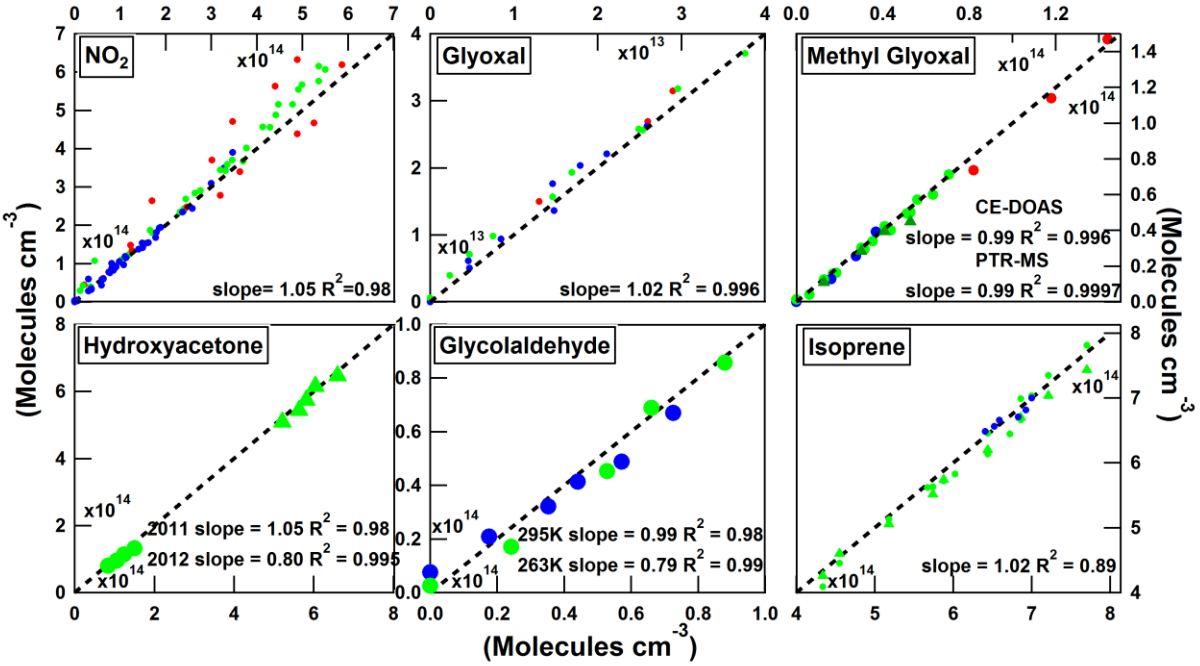

Figure A6.2: Calilbration experiments for products and reactants for isoprene oxidation experiments. Some losses are observed for glycolaldehyde at low temperatures while other compounds (glyoxal and methyl glyoxal showed better transmission from the cavity to the sampling instruments).

Table A6.1 Outline of all experiments at the NCAR chamber in 2011 and 2012.[$]

Exp #	Date	[&]Exp Type	Temp (K)	Exp description	[Reactant] ($x10^{14}$)	[NO] ($x10^{14}$)	[Oxidant][b] ($x10^{14}$)	# of photolysis steps or O_3 injections	Total photolysis time (s)	[O_3] added ($x10^{14}$)	Notes[c]
1											
2	2011.1.12	C	295	NO_2 calibration							[a], (F, C)
3	2011.1.12	C	295	NO_2 calibration							[a](F, C)
4	2011.1.12	C	295	NO_2 calibration							[a](F, C)
5	2011.1.12	-	295	O_3 + chamber							(F, C)
6	2011.1.12	L	295	TME + O_3	7.0	-	-	1	-		(F, C)
7	2011.1.13	L	295	Limonene + O_3	7.0	-	-	1	-		(F, C)
8	2011.1.13	H	295	Limonene + OH	7.0	2.0	6.0(I)				bad(F, C)
9	2011.1.13	H	295	Limonene + OH	7.0	2.14	7.14(I)	3	720	-	(F, C)
10	2011.1.13	H	295	GLYC + OH	4.2	2.28	7.28(I)	3	900	-	(F, C)
11	2011.1.14	L	295	HACET + Cl	7.0	-	7.0(C)	5	420	-	(F, C)
12	2011.1.14	C	295	C_2H_2 + Cl	14.0	-	14.0(C)	3	480	-	(F, C)
13	2011.1.14	C	295	C_2H_2 + OH	14.5	1.86	7.0(I)	5	1740	-	(F, C)
14	2011.1.18	L	295	HACET + Cl	6.3	-	7.98(C)	5	309	-	(F, C, Q, T)
15	2011.1.18	C	295	C_2H_2 + Cl	14.0	-	14.0(C)	5	495		(F, C, Q, T)
16	2011.1.18	H	295	MACR + OH	5.6	2.13	14.0(I)	4	440	-	(F, C, Q, T)
17	2011.1.19	H	295	MACR + OH	5.6	2.8	14.0(I)	-	-	-	bad
18	2011.1.19	H	295	Limonene + OH	7.0	2.14	14.6(I)	4	480		(F, C, Q, T)
19	2011.1.19	H	295	Isoprene + OH	7.0	2.16	14.0(I)	3	180		(F, C, Q, T)
20	2011.1.20	H	295	Isoprene + OH	7.0	2.15	14.1(I)	4	120		(F, C, Q, T)
21	2011.1.20	L	295	TME + O_3	7.0	-	-	1	-	1.3	(F, C, Q, T)
22	2011.1.20	L	295	Isoprene + OH	21.1	-	2.31(T)	3		1.28	(F, C, Q, T)
23	2011.1.20	L	295	Isoprene + OH	21	-	2.1(T)	1	-	1.29	(F, C, Q, T)
24	2011.1.21	L	295	MVK + OH	21.5	-	2.09(T)	2	-	0.8	(F, C, Q, T)
25	2011.1.21	L	295	T2B + O_3	7.49	-	-	2	-	1.27	(F, C, Q, T)
26	2011.1.21	L	295	Isoprene + OH	8.0	-	5.0(T2)	2	-	1.27	(F, C, Q, T)
27	2011.1.21	L	295	MACR + OH	20.0	-	(T2)	2	-	1.27	(F, C, Q, T)
28	2011.1.24	H	295	MVK + OH	7.0	2.1	7.0(I)	3	300	-	(F, C, T)
29	2011.1.24	H	295	MVK + OH	14.1	2.24	7.1(I)	6	540	-	(F, C, Q, T)
30	2011.1.24	H	295	Isoprene + OH	7.14	2.94	7.12(I)	4	120	-	(F, C, Q, T)
31	2011.1.25	H	295	Isoprene + NO_2	6.95	-	2.0(N)	-	-	-	(F, C, Q, T)
32	2011.1.25	H	295	Isoprene + OH	7.0	1.05	2.1(N)	-	-	-	d(F, C,Q, T)
33	2011.1.25	H	295	Isoprene + OH	-	-	-	-	-	-	bad
34	2011.1.26	L	295	MVK + OH	21.8	-	2.24(T2)	3	-	2.07	(F, C, Q, T)

Exp #	Date	[&]Exp Type	Temp (K)	Exp description	[Reactant] ($x10^{14}$)	[NO] ($x10^{14}$)	[Oxidant][b] ($x10^{14}$)	# of photolysis steps or O_3 injections	Total photolysis time (s)	[O_3] added ($x10^{14}$)	Notes[c]
35	2011.1.26	L	295	Limonene + O_3	7.28	-	-	2	-	1.77	(F, C, Q, T)
36	2011.1.28	H	260	Isoprene + OH	7.0	2.45	7.0(I)	4	120	-	(F, C, Q, T)
37	2011.1.28	H	260	Isoprene + OH	7.14	2.1	7.07(I)	5	300	-	(F, C, Q, T)
38	2011.1.28	H	260	Isoprene + NO_2	7.07	2.38	(N)	-	-	-	(F, C, Q, T)
39	2011.1.31	H	260	IPONO	-	2.1	7.0(I)	3	1260	-	(F, C, Q, T)
40	2011.1.31	H	260	MVK + OH	7.35	2.24	7.07(I)	5	660	-	(F, C, Q, T)
41	2011.1.31	H	260	MACR + OH	7.14	2.24	8.4(I)	2		-	(F, C, Q, T)
42	2011.2.2	H	295	IPONO	-	2.1	7(I)	4	1500	-	(F, C, Q)
43	2011.2.2	H	295	Isobutyl nitrite	7.07	-	-	3	1380	-	(F, C, Q)
44	2011.2.2	C	295	HACET + Cl	7.0	-	21.84(C)	2	120	-	(F, C, Q)
45	2011.2.3	H	295	Isobutyl nitrite	7.0	-	-	-	-	-	(F, C, Q)
46	2011.2.3	L	295	Chamber + hv	-	-	-	1	360	-	(F, C, Q)
47	2011.2.3	H	295	IBONO+Lim	10.5	-	7.0(IB)	2	1200	-	(F, C, Q)
48	2011.2.4	H	295	MVK + OH	7.0	2.31	7.42(I)	4	600	-	(F, C, Q)
49	2011.2.4	H	295	MVK + OH	7.28	2.31	14.0(I)	3	240	-	(F, C, Q)
50	2011.2.4	C	295	HACET + Cl	7.0	-	18.1(C)	2	60	-	(F, C, Q)
51	2011.2.7	H	295	Isoprene + OH	6.93	2.31	7.0(I)	4	240	-	(F, C, Q, T)
52	2011.2.7	H	295	MACR + OH	6.93	2.1	7.0(I)	7	510	-	(F, C, Q, T)
53	2011.2.7	H	295	MVK + OH	7.07	2.1	14.2(I)	3	360	-	(F, C, Q, T)
54	2011.2.8	L	295	Isoprene + OH	21.0	-	2.1(T)	2	-	0.84	(F, C, Q, T)
55	2011.2.8	L	295	Isoprene + OH	8.12	-	5.0(T2)	3	-	2.1	(F, C, Q, T)
56	2011.2.9	H	295	NO_2 in N_2	1.6	-	-	-	-	-	(F, C, Q)
57	2011.2.9	H	295	Isoprene 2°	2.1	3.0	7.35(I)	5	570	-	(F, C, Q)
58	2011.2.9	H	295	Isoprene 2°	1.4	3.5	7.2(I)	7	960	-	(F, C, Q)
59	2011.2.11	L	260	Isoprene + OH	21.0	-	2.1(T)	-	-		(F, C)
60	2011.2.11	L	260	Isoprene + O_3	21.4	-	-	3	-	1.27	(F, C, Q)
61	2011.2.11	L	260	Isoprene + OH	21.35	-	2.1(T)	3	-	1.3	(F, C, Q)
62	2011.2.14	L	260	MVK + OH	21.1	-	2.1(T)	3	-	1.31	(F, C, Q)
63	2011.2.14	L	260	MVK + OH	21.1	-	2.2(T2)	3		1.26	(F, C, Q)
64	2011.2.14	L	260	MACR + OH	-	-	-	-	-	-	(F, C, Q)
65	2011.2.15	L	295	MACR + O_3	14.1	-	-	2	-	1.42	(F, C)
66	2011.2.15	L	295	MVK + O_3	14.35	-	-	2	-	1.79	(F, C)
67	2011.2.15	H	295	Ethene + OH	3.5	4.2	17.5(I)			-	(F, C)
68	2011.3.3	H	295	Isoprene + OH	7.07	3.5	4.3(I)	4	100	-	(F, C, Q)
69	2011.3.3	C	295	MBO + OH	7.07	4.9	3.71	7	440	-	(F, C, Q)

Exp #	Date	[&]Exp Type	Temp (K)	Exp description	[Reactant] ($x10^{14}$)	[NO] ($x10^{14}$)	[Oxidant][b] ($x10^{14}$)	# of photolysis steps or O_3 injections	Total photolysis time (s)	[O_3] added ($x10^{14}$)	Notes[c]
70	2012.3.7	H	295	NO_2		-	-	-	-	-	(F, C)
71	2012.3.8	L	295	Isoprene (no rxn)	7.0	-	-	-	-	-	(F, C, Q)
72	2012.3.8	L	295	Isoprene + CCl_4	7.0	-	-		1.05 (CT)	Unk	(F, C, Q)
73	2012.3.9	C	295	C_2H_2 + Cl	14.35	-	14.6(C)	4	720	-	(F, C, Q, T)
74	2012.3.9	C	295	HACET + Cl	3.1	-	7.28(C)	4	420	-	(F, C, Q, T)
75	2012.3.9	C	295	MBO + OH	7.28	4.8	9.8(I)	4	600	-	(F, C, Q, T)
76	2012.3.12	L	295	Isoprene + OH	21.3	-	2.1(T)	3	-	1.5	(F, C, Q, T)
77	2012.3.12	L	295	Isoprene + OH	4.1	-	10.5(T2)	3	-	1.6	(F, C, Q, T)
78	2012.3.12	H	295	Isoprene + OH	7.56	8.4	7.56(I)	8	420	-	(F, C, Q, T)
79	2012.3.13	L	295	MVK + OH	18.2	-	2.1(T)	2	-	1.56	(F, C, Q, T)
80	2012.3.13	L	295	MVK + OH	21	-	2.1(T2)	3	-	2.37	(F, C, Q, T)
81	2012.3.13	L	295	MACR + OH	21	-	2.17(T2)	3	-	2.07	(F, C, Q, T)
82	2012.3.13	L	295	MACR + OH	16.8	-	2.1(T)	2	-	1.56	(F, C, Q, T)
83	2012.3.14	L	260	Isoprene + OH	21.9	-	2.17(T)	3	-	2.2	(F, C, Q, T)
84	2012.3.14	L	260	Isoprene + O_3	21.5	-	-	3	-	2.22	(F, C, Q, T)
85	2012.3.14	L	260	O_3 + chamber	-	-	-	1	-	1.33	(F, C, Q, T)
86	2012.3.14	L	260	Isoprene + OH	4.13	-	11.1(T2)	3	-	2.02	(F, C, Q, T)
87	2012.3.15	H	260	Isoprene + OH	7.1	4.2	8.9(I)	5	570	-	(F, C, Q, T)
88	2012.3.15	C	260	MBO + OH	7.0	4.2	14(I)	3	360	-	(F, C, Q, T)
89	2012.3.15	H	260	MVK + OH	7.0	5.0	15.9(I)	5	720	-	(F, C, Q, T)
90	2012.3.16	L	260	Isoprene + OH	21.0	-	2.1(T)	3	-	1.94	(F, C, Q, T)
91	2012.3.16	L	260	TME + O_3	7.7	-	-	2	-	1.23	(F, C, Q, T)
92	2012.3.16	L	260	Isoprene + OH	4.2	-	10.5(T2)	3	-	1.86	(F, C, Q, T)
93	2012.3.16	H	260	Isoprene + OH	7.0	3.5	14.77(I)	4	480	-	(F, C, Q, T)
94	2012.3.19	L	260	T2B + O_3	7.0	-	-	2	-	0.99	(F, C, Q, T)
95	2012.3.19	H	260	MACR + OH	7.0	4.2	14.35(M)	4	600	-	(F, C, Q, T)
96	2012.3.19	H	260	MVK + OH	7.0	2.1	21.0(M)	3	540	-	(F, C, Q, T)
97	2012.3.20	L	340	Isoprene + OH	21.4	-	2.31(T)	-	-	-	(F, C, Q)
98	2012.3.20	L	340	N_2	-	-	-	-	-	-	(F, C, Q)
99	2012.3.21	L	320	N_2 + O_3	-	-	-	-	-	-	(F, C, Q)
100	2012.3.21	L	320	TME + O_3	7.07	-	-	2	-	1.22	(F, C, Q)
101	2012.3.21	L	320	Isoprene + OH	21.1	-	2.1(T)	3	-	1.92	(F, C, Q)
102	2012.3.21	L	320	Isoprene + OH	4.2	-	10.4(T2)	3	-	1.86	(F, C, Q)
103	2012.3.22	H	320	Isoprene + OH	7.0	6.02	14.8(I)	5	190	-	(F, C, Q)
104	2012.3.22	C	320	MBO + OH	7.1	7.2	14.5(I)	5	360	-	(F, C, Q)

Exp #	Date	[&]Exp Type	Temp (K)	Exp description	[Reactant] ($x10^{14}$)	[NO] ($x10^{14}$)	[Oxidant][b] ($x10^{14}$)	# of photolysis steps or O_3 injections	Total photolysis time (s)	[O_3] added ($x10^{14}$)	Notes[c]
105	2012.3.22	C	320	HACET + Cl	7.0	-	20.7(C)	3	420	-	(F, C, Q)
106	2012.3.22	C	320	C_2H_2 + Cl	14.0	-	14.0(C)	3	540	-	(F, C, Q)
107	2012.3.23	H	320	Isoprene + OH	7.2	7.56	7.0(I)	4	135	-	(F, C, Q)
108	2012.3.23	H	320	MACR + OH	6.9	4.2	7.35(I)	5	705	-	(F, C, Q)
109	2012.3.23	H	320	MVK + OH	7.5	4.2	14.0(I)	3	620	-	(F, C, Q)
110	2012.4.4	H	320	Isoprene + NO_2	6.7	7.0(late)	1.5(N)	-	-	-	(F, C)
111	2012.4.5	H	320	1,3-butadiene + OH	7.35	4.3	14.1(I)	3	180	-	(F, C)
112	2012.4.5	H	320	Isoprene 2°	2.3	9.1	15.4(I)	10	1080	-	(F, C)
113	2012.4.6	L	320	Isoprene + OH	21.7	-	2.1(T)	3	-	1.56	(F, C)
114	2012.4.6	L	320	Isoprene + OH	14.0	-	2.8(T)	3	-	1.74	(F, C)
115	2012.4.6	H	320	Isoprene + OH	7.0	15.4	14.0(I)			-	(F, C)
116	2012.4.9	H	320	MVK + OH	7.28	5.74	15.4(I)	5	600	-	(F, C)
117	2012.4.9	H	320	MACR + OH	7.0	5.67	14.7(I)	5	660	-	(F, C)
118	2012.4.9	H	320	1,3-butadiene + OH	7.6	6.65	14.6(I)	5	225	-	(F, C)
119	2012.4.11	L	295	1,3-butadiene + OH	21.1	-	2.8(T)	3	-	1.9	(F, C)
120	2012.4.11	L	295	1,3-butadiene + O_3	7.1	-	-	2	-	1.2	(F, C)
121	2012.4.11	L	295	1,3-butadiene + OH	21.4	-	3.2(T)	3	-	1.8	(F, C)
122	2012.4.13	H	295	1,3-butadiene + OH	7.1	7.56	15.4(I)	7	240	-	(F, C)
123	2012.4.13	H	295	1,3-butadiene 2°	2.1	7.28	15.2(I)	7	1170	-	(F, C)
124	2012.4.13	H	295	Isoprene 2°	2.1	4.27	14.0(I)	9	1245	-	(F, C)
125	2013.2.11	H	295	Isoprene + OH	4.3	4.2		6	390	-	(F, G)
126	2013.2.11	H	295	Isoprene + OH	2.94	5.6		7	900	-	(F, G)
127	2013.2.14	H	295	1,3-butadiene + OH	4.2	4.2		6	390	-	(F, G)
128	2013.2.14	C	295	MBO + OH							(F, G)
129	2013.2.14	C	295	HACET + OH							(F, G)

[$]For more details please see spreadsheets online: (http://tinyurl.com/CU-NCAR-isp-2011; http://tinyurl.com/CU-NCAR-isp-2012) [&]C-Calibration experiment; L-Low NO_x (or Ozonolysis); H-High NO_x [a] NO_2 to check flow through MFC to CE-DOAS. [b]I-isopropyl nitrite, M-methyl nitrite., C-Cl_2, T-TME, T2- T2B, N-NO_2. [c]Instruments on-line: F: FTIR, C: CE-DOAS, Q: Quad PTR, T: PTR-ToF, G: GC-FID. [d]NO added after start of NO_2 + ISP chemistry.

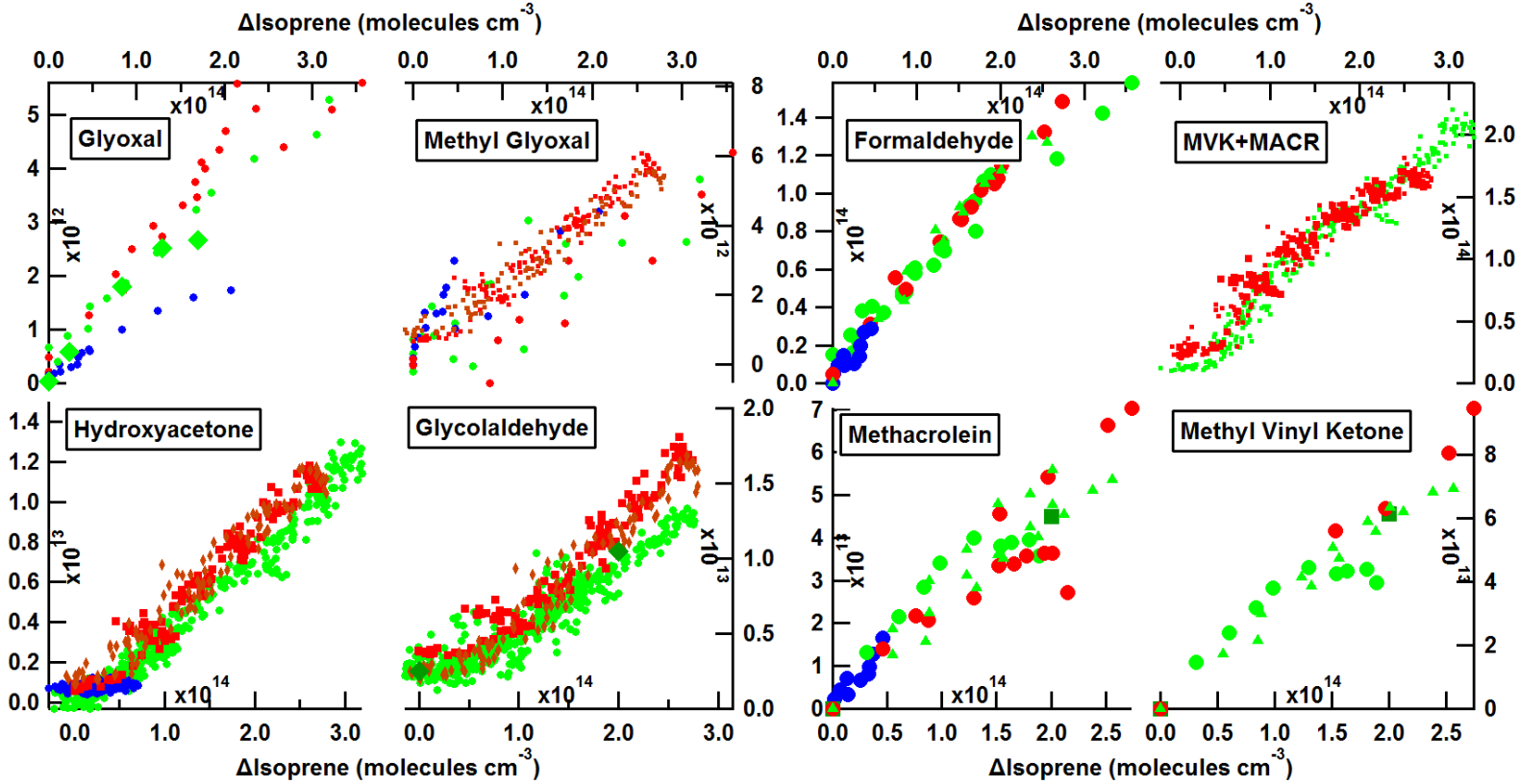

Figure A6.3: Production of major and minor products from high NO_x oxidation of isoprene as shown in Table 6.1.

Table A6.2 Primary yields (%) of 1,3-butadiene reaction with OH (range between repeat exps)

Compound	Berndt and Boge	Tuazon	Sprengnether	High NO_x		Zero NO_x
	295K	-	-	295K	320K	295K
Glyoxal	0			2.1(1)	2.1(1)	0.38
Glycolaldehyde						
Acrolein	59(6)	58(4)	54	52(2)	28(5)	30
Formaldehyde	64(8)	62(5)	58	53(1)	44(1)	-
C4-hydroxy	23(10)					
Furan	4.6(16)	3.5(5)	1.6			
Nitrates	6(2)	7(3)	11			

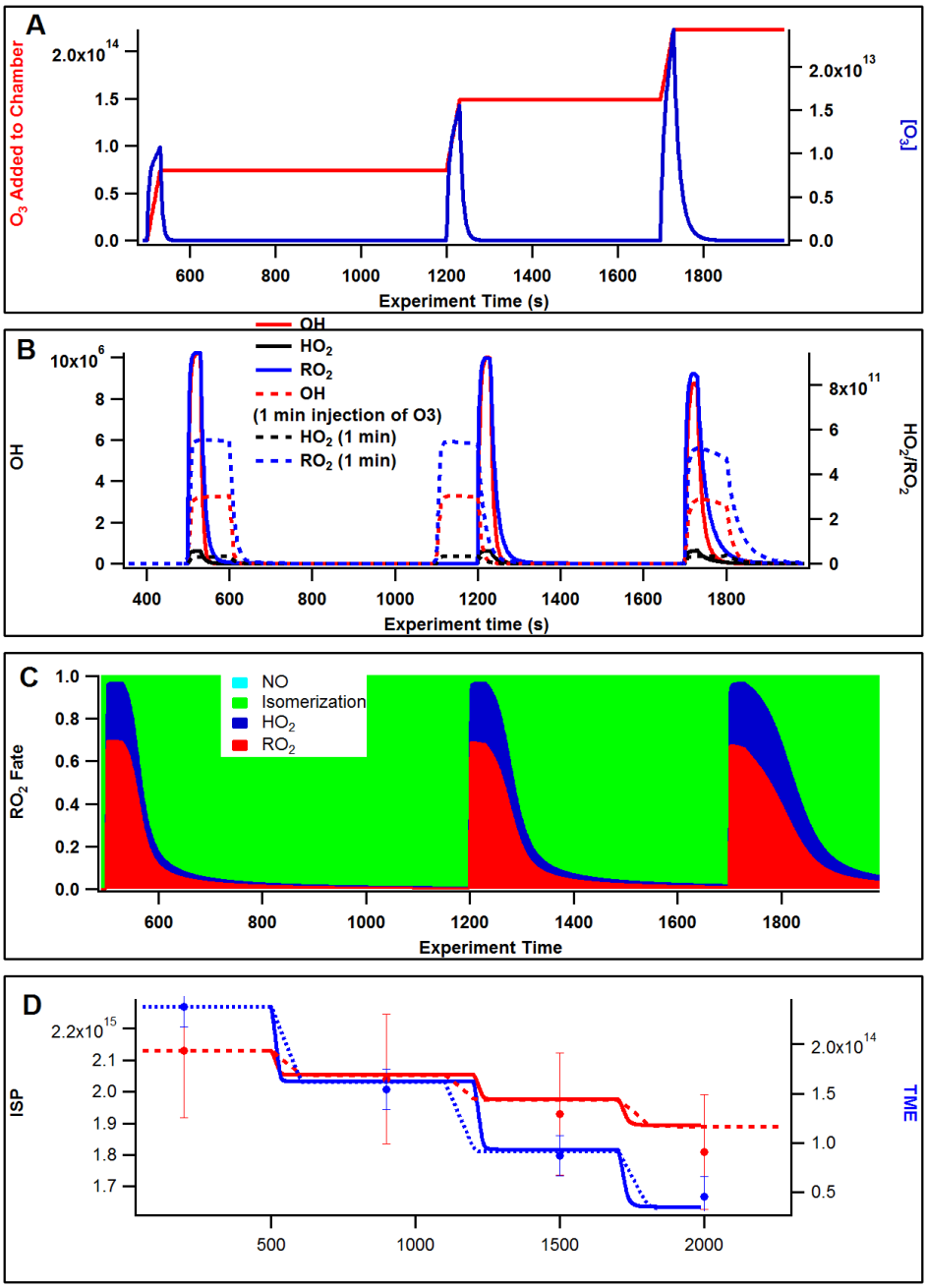

Figure A6.4: Results of MCM modeling of Experiment 76- oxidation of isoprene at room temperature using TME+O_3 source. Panel A shows O_3 accumulation and injection. Panel B shows the OH, HO_2 and RO_2 levels reached in the model for the 30 second and 1 minute injection time (in the model). The RO_2 level is 10 times that of the HO_2. Panel C shows the calculations of the RO_2 fate in the low NO_x system. RO_2+RO_2 reactions are the dominant fate, followed by HO_2 and then isomerization (0.1 s^{-1} rate). Isomerization dominates where RO_2 is low (in-between O_3 injections). Panel D shows the isoprene and TME concentrations compared to the measurements.

Table A6.3 Literature data primary yields from isoprene oxidation by OH at room temperature oxidation.

Year	H/L NOx	HCHO	MACR	MVK	Nirates	3-MF	GLYOX	HACET	GLYC	MGLOX
1988[a]	H	50	21(5)	29(7)						
1994[b]	H	57(2)	22(1)	32(3)						
1994[b]	L	34	21	17						
2000[c]	H	57	20	31						
2000[c]	L	33	18	15						
2002[d]	H	66(6)	28(2)	44(3)	12(3)	< 2				
2004e	H	-	29.3	30						
2006[f]	H	21	-	-			0.3-3			
2009[g]	H	-	26	40			-	3.8	4.2	-
2010[h]	L	-	10.9-13	8.9-15						
2011[i]	H	-	22.01(62)	30.4(13)			2.1(12)	2.90(5)	2.69(82)	-
2013[j]	H	-	28.8	41.1						
2013[j]	L	-	10.9	4.3						
MCM	H		26.5	41.5						
This work	H	53(5)	25(2)	31(1)			2.1(1)	2.3(2)	2.3(2)	1.8(2)
This work	L	-	24(1)	17(5)			0.27(3)	0.9-1.8	-	0.2-0.9

[a] Tuazon and Atkinson, 1988; [b] Miyoshi et al. 1994; [c] Ruppert and Becker 2000;[d] Spregnether et al. 2002; [e] Zhang et al. 2004; [f] Volkamer et al. 2006; [g] Paulot et al. 2009; [h] Navarro et al. 2010; [I] Galloway et al. 2011; [j] Liu et al. 2013.

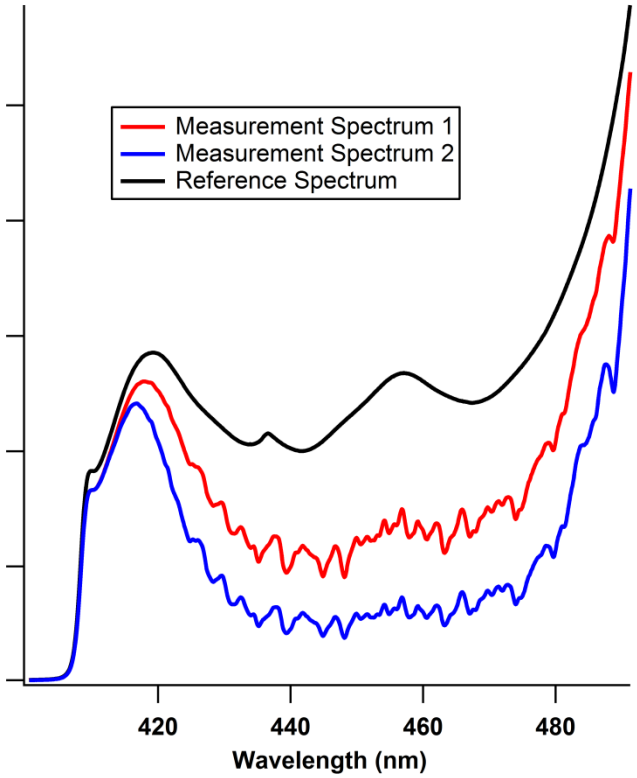

Figure A6.5: CE-DOAS measurement spectra. Intensity decrease is mostly due to extinction by NO_2. Fits for Spectra 1 and 2 are shown in Figure A6.5 with varying amounts of NO_2.

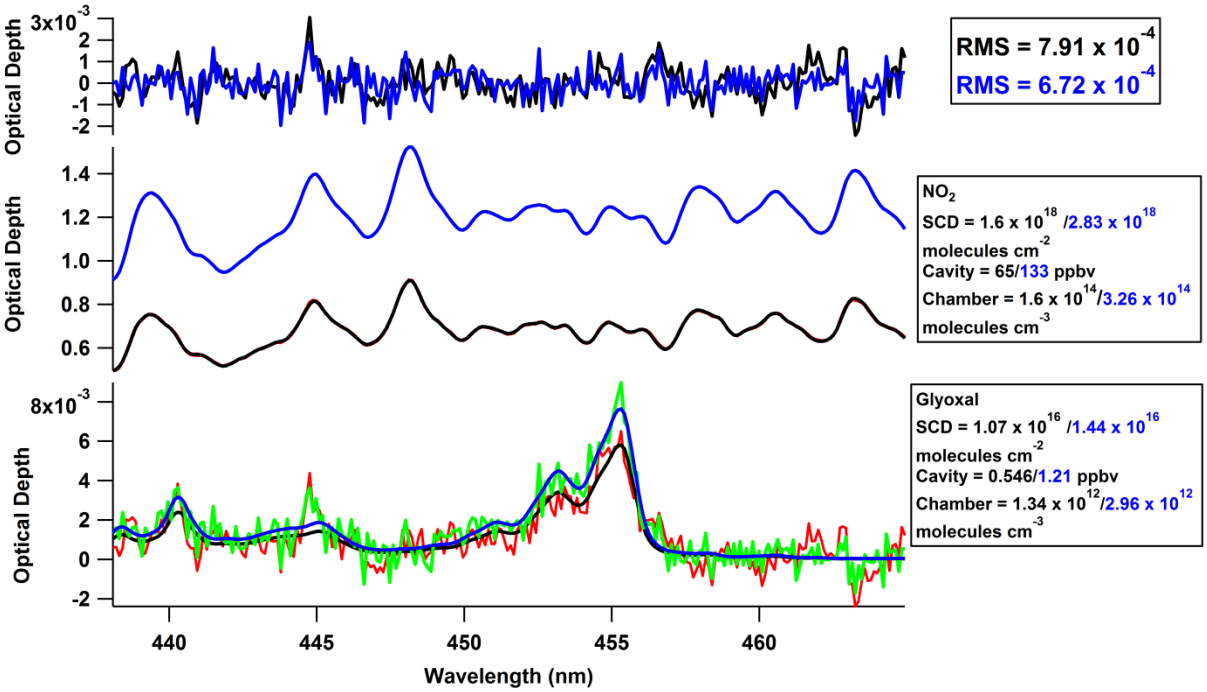

Figure A6.6: Fitted CE-DOAS from isoprene oxidation experiments showing the fitting of glyoxal on a high NO_2 background for 2 levels of NO_2 (65 and 133 ppbv).

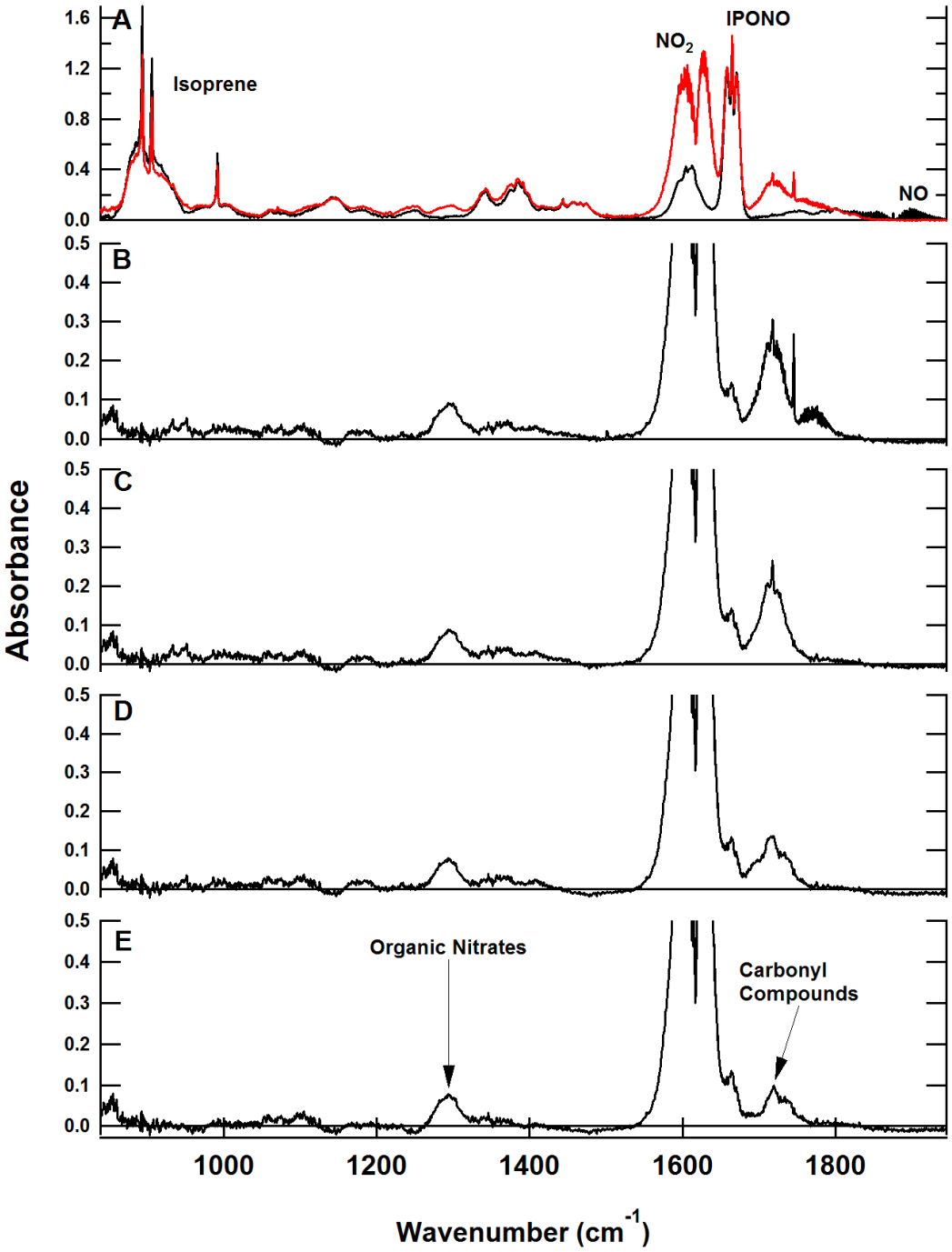

Figure A6.7: Spectra as recorded by the FT-IR for one high NO_x isoprene oxidation experiment. Panel A shows the initial spectrum before oxidation (black) and after 100 seconds of illumination (red). The isoprene is reduced by 24% and NO_2 has begun to grow in. Panel B shows the spectrum after subtraction of isoprene, isopropyl nitrite (IPONO), some methyl nitrite contamination and NO. The formaldehyde peak at 1700 cm^{-1} is subtracted next to yield panel C. Panel D shows the spectrum after subtraction of methacrolein at 1700 cm^{-1} and panel E shows the remaining unknown components of the spectrum after the subtraction of methyl vinyl ketone.

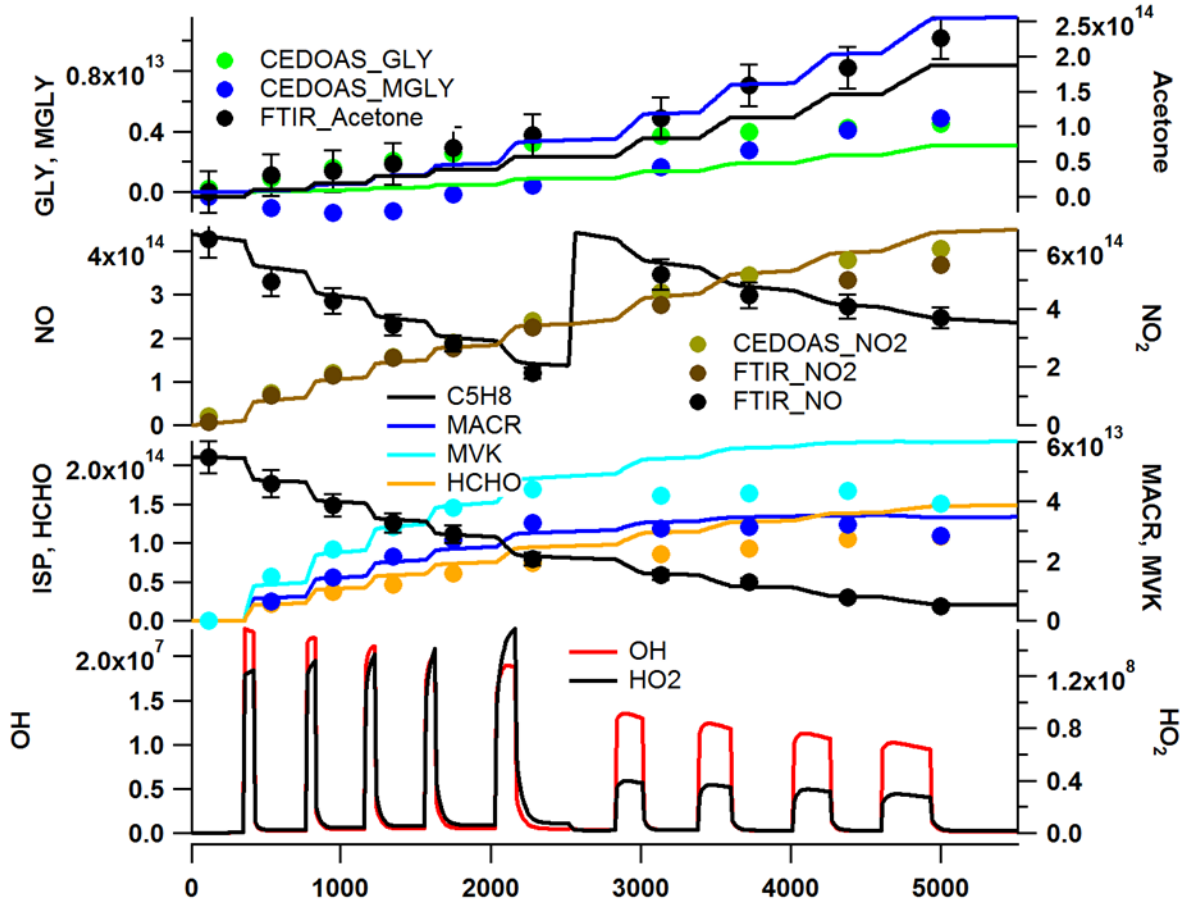

Figure A6.8: Comparison of measured data for Experiment 124 (isoprene turnover) to the Master Chemical Mechanism. The model is tuned to the turn-over of isoprene (magnitude of the OH source for each photolysis time). MACR and MVK agree very well, while HCHO and the minor products do not.

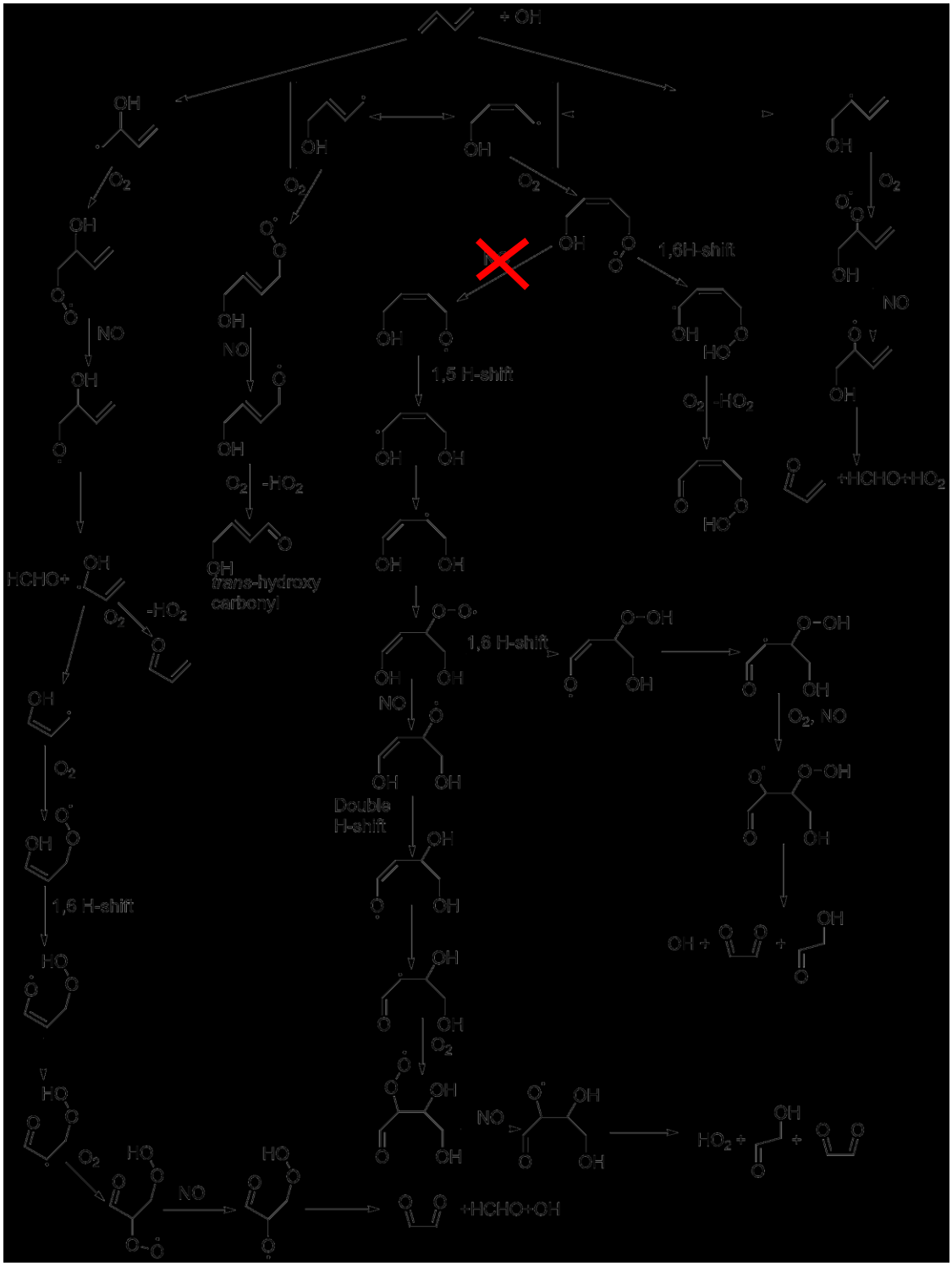

Figure A6.9: Complete mechanism for the oxidation of 1,3-butadiene under high NOx conditions. The nitrate yields at any NO step are not shown. Mechanism pathways from Berndt and Böge (2007) are included as well as proposed pathways for formation of glyoxal based on the works of Dibble (2004a; 2004b) and Peeters (2009; 2012). The less probably pathway to glyoxal formation is indicated by the red X, this is discussed in more detail in the text.

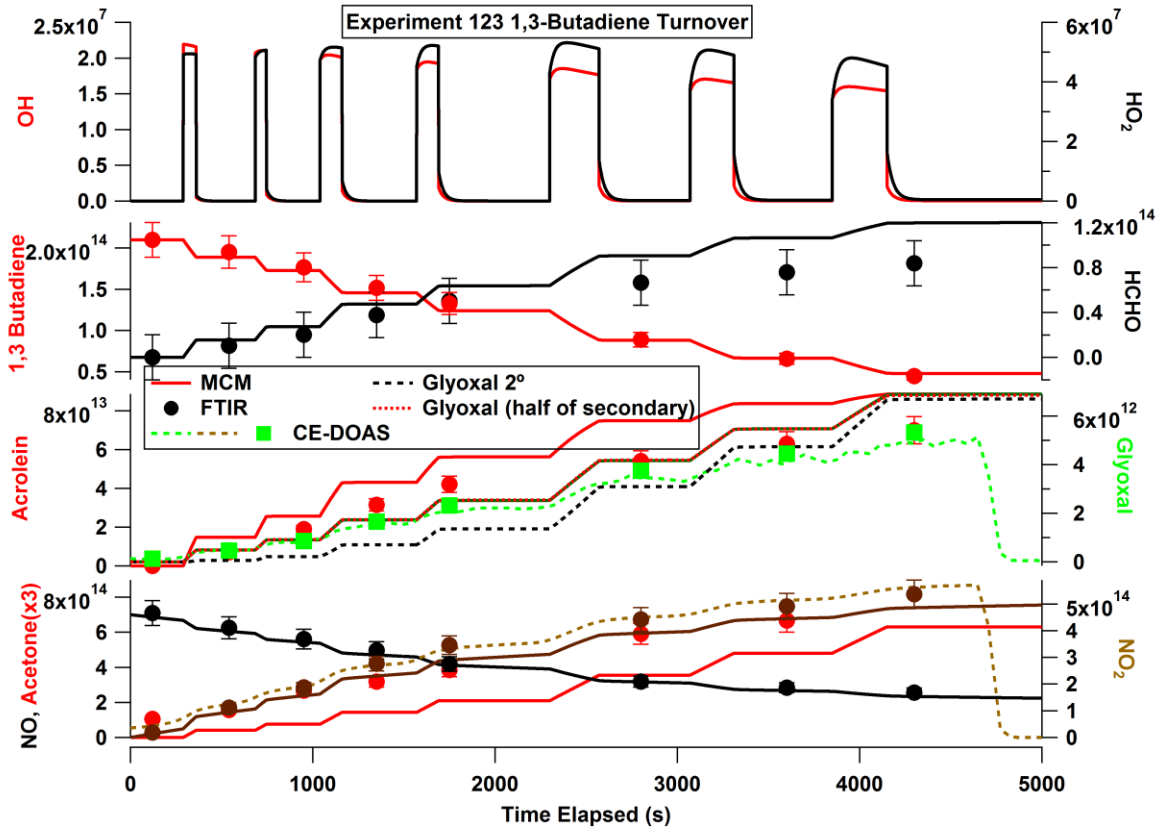

Figure A6.10: Results of Experiment 123, oxidation of 1,3-Butadiene by OH under high NOx conditions. The measurements and model compare well until more NO is added to the chamber at ~2500 seconds. The MCM 3.2 model has been modified to add a primary source of glyoxal following the mechanism in Figure A6.9 and reducing the amount of secondary glyoxal from the C4-Hydroxy Carbonyls according to the data of Berndt and Böge (2007).

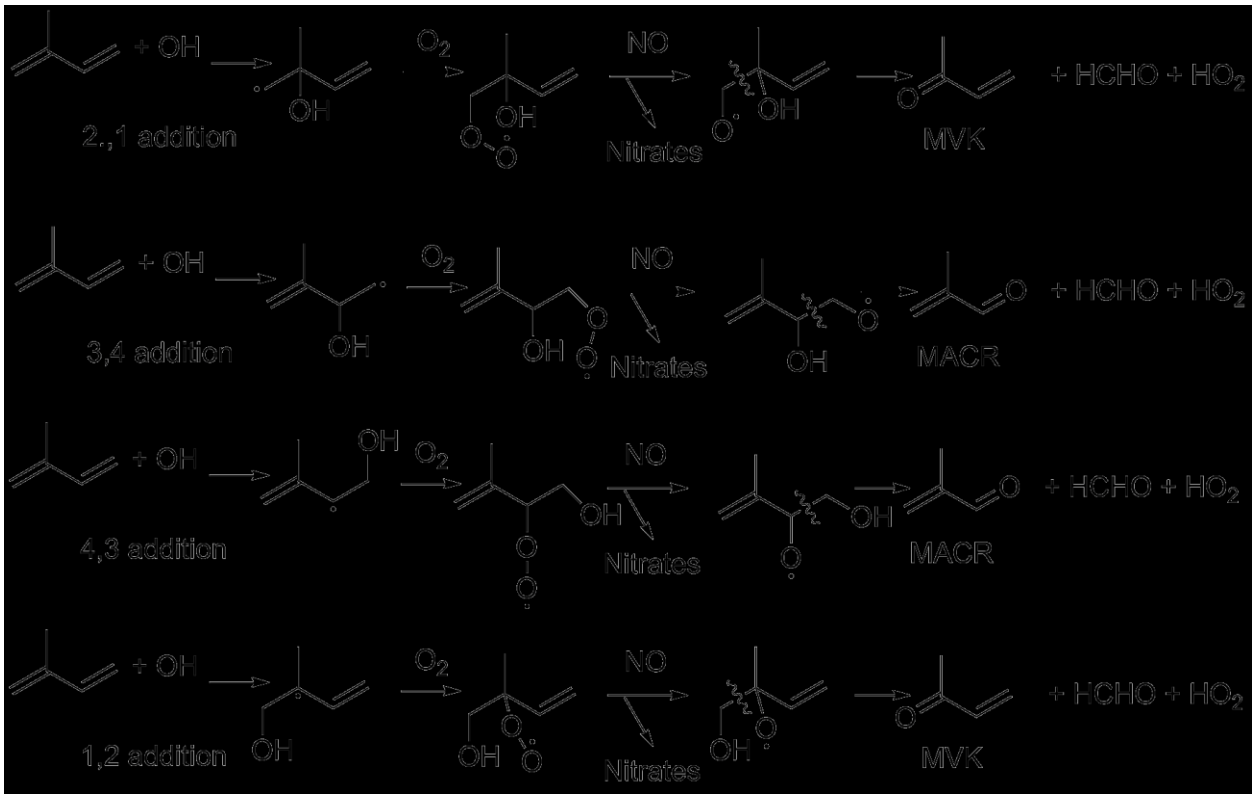

Figure A6.11: Mechanisms of major product channels of isoprene oxidation.

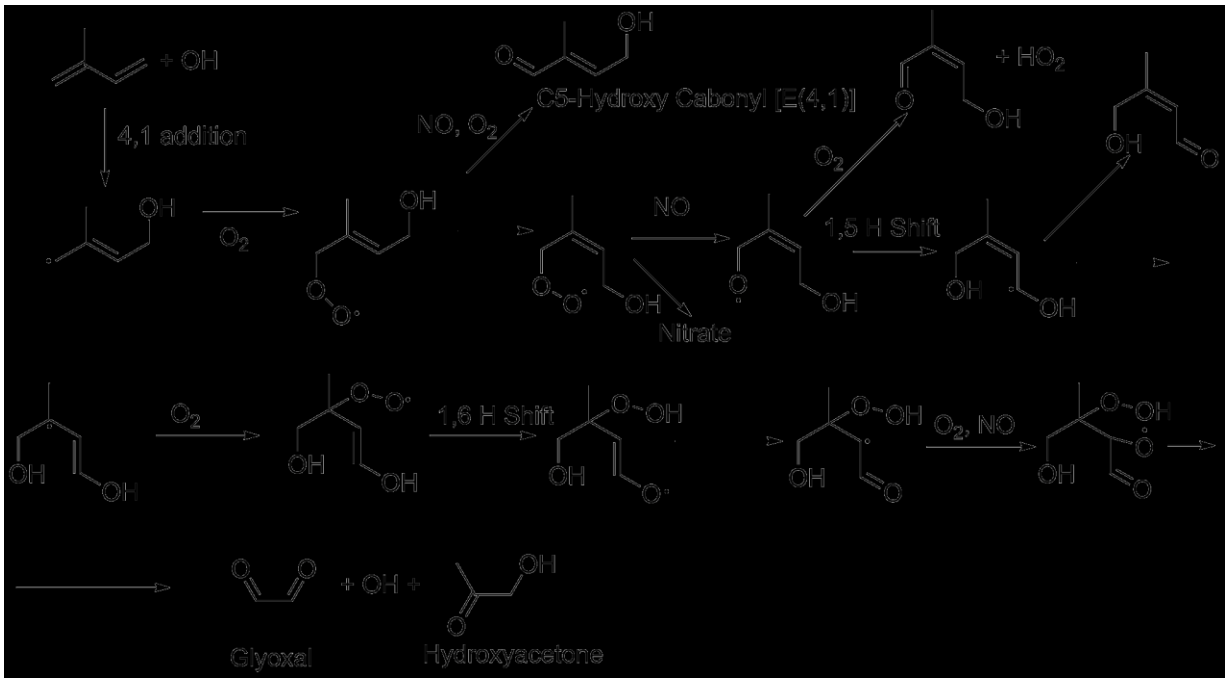

Figure A6.12: Isoprene oxidation mechanism for the 4,1 addition of OH including all possible primary products (C5-hydroxy carbonyl as well as other carbonyls, glyoxal and Hydroxyacetone).

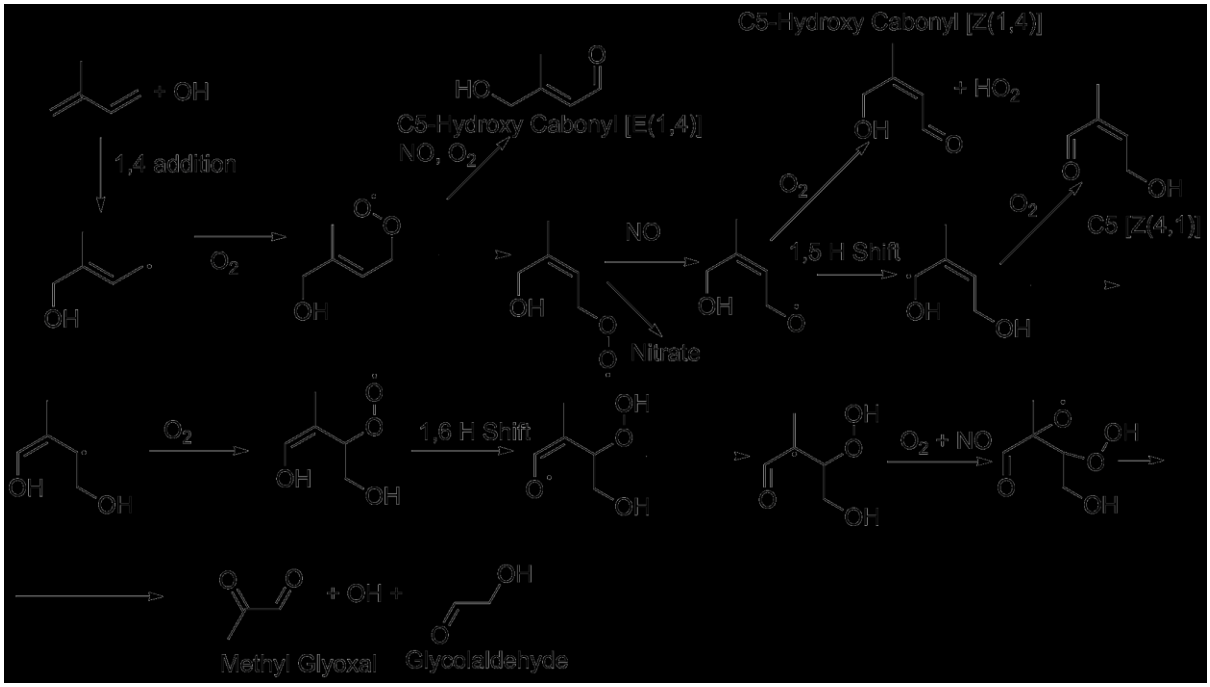

Figure A6.13: Isoprene oxidation mechanism for the 1,4 addition of OH including all possible primary products (C5-Hydroxy carbonyl compounds as well as methyl glyoxal and glycolaldehyde).

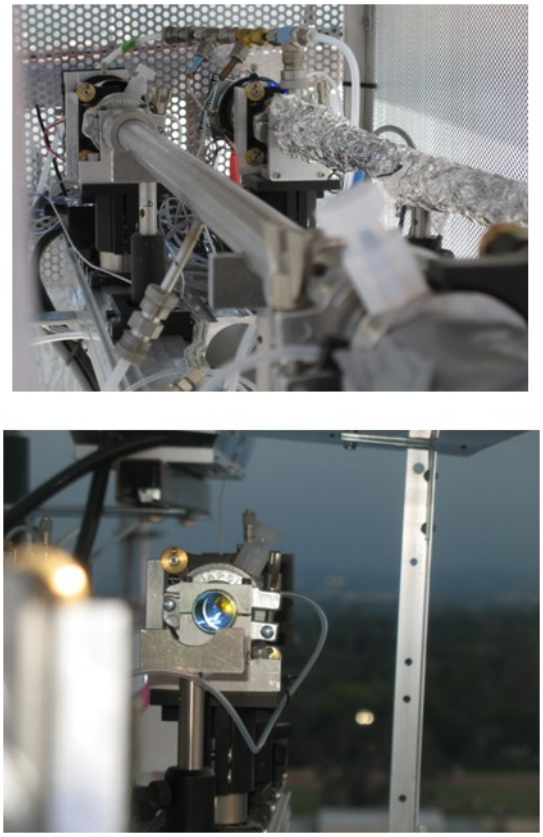

Figure A7.1: Picture of cavity setup including operation of open-cavity mode. The closed cavity (Teflon cavity enclosed in foil) was operated for the duration of the campaign. Both cavities were shaded by a roof and isolated from the elements by perforated panels except when operating the open path cavity.

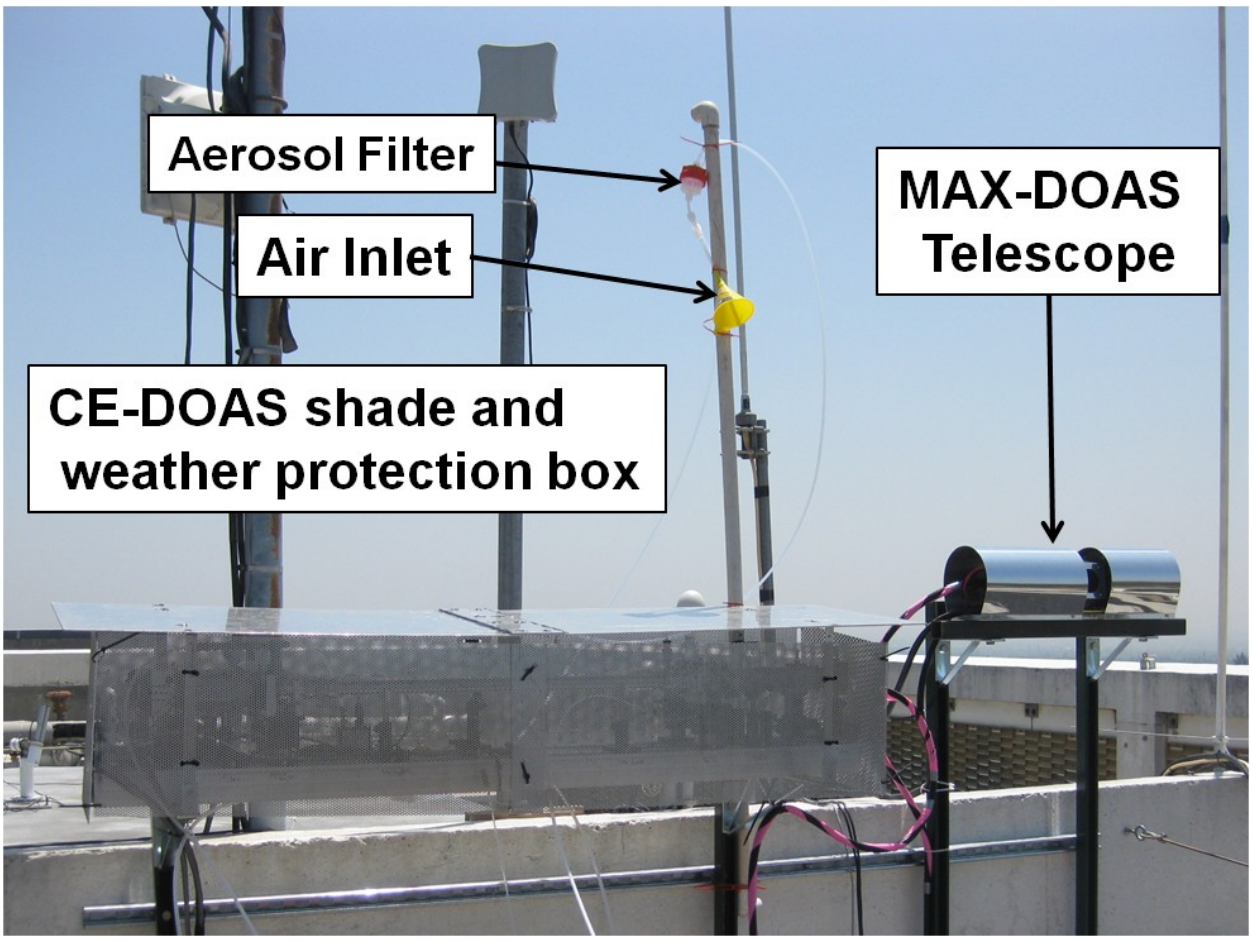

Figure A7.2: Setup of CU instruments on the Millikan library during CalNex 2010. The optical cavities were located outside to minimize inlet lengths and line losses.

Figure A7.3: Location of Four-mile Canyon fire relative to Boulder and Denver (photo from http://summitvoice.files.wordpress.com/2010/09/fourmile_tmo_2010249.jpg).

Appendix B Master Chemical Mechanism: Mechanism File

MCM mechanism extracted from mcm.leeds.uk for isoprene, trans-2-butene and 2,3 dimethylethylene and edited to include mechanisms to include additional mechanisms for OH production under low and high NOx conditions as well as the reaction of NO2 + isoprene as follows:

**********Mechanisms added to inject O3 or create OH**********
% 1 : S7 +S7 = O3 + O3;
% 4.3D-14*0.54 : S8 + S9 = OH + CH3COCH3 + NO2 ;
% 4.3D-14*0.46 : S8 + S9 = S10 + NO ;
% 4.7D-1 : S15 = NO + NO ;
**********NO2 + Isoprene mechanism, products are likely incorrect**********
% 1.3D-19*0.148 : NO2 + C5H8 = ISOPAO + NO + S11;
% 1.3D-19*0.444 : NO2 + C5H8 = ISOPBO + NO + S12;
% 1.3D-19*0.102 : NO2 + C5H8 = ISOPCO + NO + S13;
% 1.3D-19*0.306 : NO2 + C5H8 = ISOPDO + NO + S14;
********Primary source Chemistry for glyoxal production from 1,3-butadiene*********
% KDEC*0.83 : BUTDCO = ACR + HCHO + HO2 ;
% KDEC*0.17 : BUTDCO = S11 ;
% KRO2NO : S11 + NO = G4 + GLYOX + HCHO + OH
******Reduction of secondary source Chemistry for glyoxal production from C$-HC*******
% KDEC*0.60 : C41O = HOCH2CHO + HO2 ;
% KDEC*0.40 : C41O = GLYOX + HOCH2CHO + HO2 + G20 ;